Three-Dimensional Assessment of the Constitutive and Fracture Behaviors of Silica Sand at Particle-Scale Using X-ray Experiments and Finite Element Analysis

A Dissertation Presented for the
Doctor of Philosophy
Degree
The University of Tennessee, Knoxville

Wadi Habeeb Imseeh
August 2020

Copyright © 2020 by Wadi Habeeb Imseeh
All rights reserved.

DEDICATION

I am forever indebted to my parents, Habeeb and Pheobe Imseeh, for giving me the opportunities and experiences that have made me who I am today. They selflessly encouraged me to explore new directions in life and seek my own destiny. I dedicate this milestone to them.

ACKNOWLEDGEMENTS

I would like to express my sincere gratitude to my advisor Prof. Khalid Alshibli, the Department of Civil and Environmental Engineering, the University of Tennessee- Knoxville (UTK). Prof. Alshibli has always been a source of motivation, enthusiasm, and immense knowledge. His guidance and insights provided me with continual support that inspired this final product. I would also like to thank Prof. Angelica Palomino, Prof. Timothy Truster, and Prof. Claudia Rawn, for serving on my dissertation committee.

I would like to acknowledge Dr. Mark Rivers, Dr. Peter Kenesei, and Dr. Hemant Sharma, for their helpful guidance at the Advanced Photon Source (APS), Argonne National Laboratory (ANL). This dissertation used resources of the APS, an Office of Science User Facility operated for the US Department of Energy (DOE) by the ANL under Contract No. DE-AC02-06CH11357. I also acknowledge the support of GeoSoilEnviroCARS (APS, Sector 13), which is supported by the National Science Foundation, Earth Sciences (EAR-1128799), and Geosciences (DE-FG02-94ER14466).

I would like to acknowledge the help of my research colleagues at the University of Tennessee Zaher Jarrar, Dr. Andrew Druckrey, Dr. Mehmet Cil, and Maha Jarrar, for their assistant during the beamtime of Prof. Alshibli at the APS. I would also like to acknowledge my other research colleagues Amirsalar Moslehy and Dr. Siavash Amirrahmat, for their support in acquiring and analyzing some of the x-ray Diffraction data used in this dissertation.

ABSTRACT

The constitutive behavior of sand has been conventionally measured and modeled using global-scale measurements of stresses and strains at the boundaries of laboratory-sized specimens. However, acquiring global-scale measurements has originally been proposed for solid metals, while sand possesses a particulate nature with complex mechanics that we still know little about its behavior. This dissertation exploited recent advances in 3D x-ray experiments and 3D finite element (FE) computer simulations that would significantly enhance our understanding of sand constitutive behavior. Fundamental properties at different scale-levels ranging from crystal structure to laboratory-sized specimens were investigated using synchrotron micro-computed tomography (SMT), digital image processing, 3D x-ray diffraction (3DXRD), and 3D FE analysis.

It is of fundamental importance to define a specific scale-level when evaluating the constitutive behavior of silica sand. For instance, the shear strength in a slope stability problem describes the ultimate shear stress sustained by a mass of sand at a certain effective normal stress. A developer for contact models in the discrete element method (DEM) might also understand the shear strength of sand as the tangential force required to break the contact bond between two sand particles. Furthermore, the term shear strength is used within the field of crystal mineralogy and fracture to describe the critical resolved shear stress required to activate successive slip in the crystal lattice of the sand constituent mineral. Concepts even become more blurred when one finds that the yield strength of a confined silica sand specimens in 1D compression is mainly attributed to particle fracture, which is attributed to successive slips in the crystal lattice within individual silica sand particles.

There is a need for a new framework that can accurately predict the 3D constitutive behavior of silica sand through bridging the scale among fundamental material properties. The dissertation tackled this quest and introduced a new 3D FE computer simulations for the constitutive behavior of silica sand particles. The FE simulations were developed and calibrated via coding development in ABAQUS FE software and a sequence of processing modules for in-situ SMT and 3DXRD scans that were acquired for natural silica sand specimens. The FE simulations operated on a numerical specimen that closely resembled the real morphology and particle-to-particle interaction within sand specimens. The particle-to-particle interactions were modeled using appropriate FE contact models that permitted tangential force transmission and resistance to node-into-face penetration at the contact interfaces between 3D meshed particles. The dissertation also developed a material user-subroutine that numerically predicted the anisotropic constitutive and brittle fracture behavior of silica mineral. This milestone achievement uncovered a new material constitutive behavior of silica sand at the crystal scale-level of the constituent minerals. In addition, the proposed FE simulations have laid the ground for future developments of other user-subroutines that can model

additional material properties in natural silica sand particles at the crystal scale-level such as Dauphiné twins.

The results reported in this dissertation addressed many fundamental outcomes that have a broad impact on the constitutive behavior of silica sands. To mention few examples: (i) the incompleteness of the critical state theory in cohesionless soils was attributed to the much higher dilative behavior that internally occurs within sheared sand specimens along localized zones of intensive distortion (shear bands); (ii) Natural sand morphology was proven to improve inter-particle coordination, embracement, and interlocking when compared with specimens composed of spherical particles. Prior to extensive particle fracture, these improvements imply higher stiffness in the oedometer test for specimens composed of sand particles other than spherical particles; (iii) Particle fracture was found to give rise for sand yielding in oedometer compression under high effective stresses; (iv) The resistance of sand particles to fracture decreases as the particle shape deviates from a sphere or when the particle exhibits fewer contacts with its neighboring particles; and (v) the fracture behavior of silica sand particles depends on the direction of applied stresses relative to the crystal lattice plane within the particle. All these insights advocate for rather complex constitutive behavior of silica sands and make a strong case for continuing research for a better understanding of the sand behavior.

TABLE OF CONTENTS

Chapter One General Introduction 1
Motivational Background 1
Dissertation Objectives 3
Literature Review 4
Global-Scale Response of Sand Material 5
Particle-Scale Behavior 6
Crystalline-Scale 10
Dissertation Outline 12
References 13
Appendix A: Figures 25
Chapter Two Discrepancy in the Critical State Void Ratio of Poorly-Graded Sand due to Shear Strain Localization 26
Introduction 27
CTC Experiments on Laboratory-Size Specimens 29
Experiments 29
Critical State (CS) Assessment 30
Discussion 31
In-Situ SMT Scans for CTC Experiments 32
In-situ Scanning 32
Image Processing and Data Analysis 33
Discussion 34
Oedometer Experiments 35
Experiments 35
Critical State (CS) Assessment 36
Discussion 37
Summary and Conclusions 38
Acknowledgments 38
References 39
Appendix A: Tables 45
Appendix B: Figures 50
Chapter Three 3D Finite Element Modeling of Force Transmission and Particle Fracture in Sand 68
Introduction 68
Experiment Description and Image Acquisition 71
Finite Element (FE) Model Description 72
Results 76
Force chains 76
Fracture Mode 77
Stress-Strain Relationships within Individual Particles 78
Summary and Conclusions 79
Acknowledgments 80
References 81

Appendix A: Figures 86
Chapter Four Influence of Sand Morphology on Inter-Particle Force and Stress Transmission Using 3D Discrete and Finite Element Methods 96
Introduction 97
Experiment and In-Situ SMT Scans 99
3D DEM and FEM Simulations 100
Finite Element Method (FEM) 101
Discrete Element Method (DEM) 102
Results and Discussion 103
Boundary Load-Displacement and Averaged Coordination Number 103
Distribution of Inter-Particle Contact Forces and Stresses within Particles 104
Correlation between the Inter-Particle Contact Forces and Coordination Number (CN) 106
Development of Force Chains 107
Conclusions 108
Acknowledgments 110
References 111
Appendix A: Tables 117
Appendix B: Figures 118
Chapter Five Influence of Crystal Structure on Constitutive Anisotropy of Silica Sand at Particle-Scale 128
Introduction 128
Experiments and Modeling of Synthetic Silica Cubes 131
Powder and Laue x-ray Diffraction 131
Combined In-Situ SMT and 3DXRD 132
3D FE Analysis of the Silica Cube Experiments 134
Discussion of Results 135
Experiments and Modelling of Natural Silica Sand Particles 137
Crystal Structure of Natural Silica Sand Particles 139
3D FE Simulations of the Confined Uniaxial Compression Experiment 139
Discussion of FE Simulation Results 141
Conclusions 142
Acknowledgments 144
References 145
Appendix A: Description of the 3D Finite Element (FE) Simulations 151
3D Finite Element (FE) Solver 151
Contact Model 152
Appendix B: Assessment of Local Crystal Orientations for Sand Particles with Multiple 3DXRD Measurements 153
Appendix C: Tables 155
Appendix D: Figures 157
Chapter Six Influence of Micro- and Crystalline- Scale Properties on the Fracture of Silica Sand Particles Using 3D Finite Element Analysis 174
Introduction 175

Formulation of the Material User-Subroutines for Silica Mineral 178
Constitutive Relationship 178
Failure Criterion 180
Degradation of Stiffness and Damage Evolution 181
Implementation of User-Subroutines for Silica Material 182
Single particle Crushing FE Simulations 183
3D FE Simulations of a Confined 1D Compression Experiment 187
Summary and Conclusions 189
Acknowledgments 190
References 191
Appendix A: Tables 196
Appendix B: Figures 197
Chapter Seven Conclusions and Recommendations 211
Summary of Major Conclusions 211
Recommendations for Future Work 212
Vita 214

LIST OF TABLES

Table 2-1. Properties of tested granular material (Alshibli et al., 2014b). 45
Table 2-2. Summary of the 50 CTC experiments reported by (Alshibli and Cil, 2017). 46
Table 2-3. Summary of the regression model results fitted in Figure 2-4. Values in parentheses denote the 95% confidence limits of the parameter. 47
Table 2-4. Summary of the SMT scans that were acquired during the CTC experiments on specimens of the tested granular materials. 47
Table 2-5. Summary of the oedometer tests. 48
Table 2-6. Summary of common models used in the literature to describe the yield locus of sand in the stress plane $(q - p)$. Equations are plotted in Figure 2-15. 48
Table 2-7. Summary of the regression model results fitted in Figure 2-16. Values in parentheses denote the 95% confidence limits of the parameter. 49
Table 2-8. Summary of the CS parameters for tested granular materials. Values in parentheses denote the 95% confidence limits of the parameter. 49
Table 4-1. *P*-values for Kolmogorov-Smirnov goodness of fit test for the inter-particle contact forces. 117
Table 4-2. *P*-value for Kolmogorov-Smirnov goodness of fit test for the major principal stress of particles $(\sigma 1)$. 117
Table 5-1. x-ray powder diffraction results on silica cubes. Values in parentheses are provided by MaTecK. Values in this table were obtained with the help of my research colleague Amirsalar Moslehy. 155
Table 5-2. Summary of the major principal strain measured for silica cubes using 3DXRD. Layers 1 to 5 denote sequential and equal vertical layers along the cube $1\ mm$ height, in which layer 1 represents the top one-fifth portion of the cube that is in contact with the top loading platen. 155
Table 5-3. Elastic constants of crystal quartz (Heyliger et al., 2003) 156
Table 5-4. Comparison between experimental (3DXRD), simulated (3D FE), and calculated (closed-form) major principal strain for the silica cubes. 156
Table 6-1. Input parameters adopted in the material user-subroutines for silica mineral. 196
Table 6-2. Summary of the experiments that were simulated using 3D FE. 196
Table 6-3. Micro-scale properties of the two particles that were tested and simulated in single particle crushing, as well as the simulated equivalent sphere. 196

LIST OF FIGURES

Figure 1-1. Summary of dissertation objectives 25
Figure 2-1. Evolution of q/p' versus $\varepsilon 1$ for the 50 CTC experiments listed in Table 1-2 50
Figure 2-2. Evolution of e versus $\varepsilon 1$ for the 50 CTC experiments listed in Table 1-2 51
Figure 2-3. The CSL modeled in the stress plane $(q - p')$ using the 50 CTC experiments listed in Table 1-2, which were conducted on specimens of (a) F35, (b) DG, (c) GS40, and GB..... 52
Figure 2-4. The CSL modeled in the compression plane $e - p'$ using the 50 CTC experiments listed in Table 1-2, which were conducted on specimens of (a) F35, (b) DG, (c) GS40, and GB..... 53
Figure 2-5. The change in $elocal$ versus REV size for (a) F35_D_400_SMT; (b) F35_D_15_SMT; (c) F35_MD_15_SMT; (d) DG_D_400_SMT; (e) DG_D_15_SMT; (f) DG_MD_15_SMT; (g) GS40_D_400_SMT; (h) GS40_D_15_SMT; (i) GB_D_400_SMT; and (j) GB_D_15_SMT experiments. Refer to Table 1-4 for labels of experiments. 54
Figure 2-6. Distribution fields of e versus $\varepsilon 1$ at central Y-Z cuts across the SMT scans collected during the F35_D_400_SMT experiment. Refer to Table 1-4 for labels of experiments. 55
Figure 2-7. Distribution fields of e versus $\varepsilon 1$ at central Y-Z cuts across the SMT scans collected during the F35_D_15_SMT experiment. Refer to Table 1-4 for labels of experiments. 56
Figure 2-8. Distribution fields of e versus $\varepsilon 1$ at central Y-Z cuts across the SMT scans collected during the F35_MD_15_SMT experiment. Refer to Table 1-4 for labels of experiments. 57
Figure 2-9. Comparison between the evolution of $eglobal$ and $elocal$ versus $\varepsilon 1$ for (a) F35; (b) DG, (c) GS40; and (d) GB experiments. Refer to Table 1-4 for labels of experiments. 58
Figure 2-10. Boxplots of $elocal$ at the last loading step for the (a) F35; (b) DG; (c) GS40; and (d) GB experiments. Refer to Table 1-4 for labels of experiments. 59
Figure 2-11. Distribution fields of RPTG and $elocal$ calculated using the processed SMT images that were collected at the last loading steps for (a) F35_D_400_SMT; (b) F35_D_15_SMT; (c) F35_MD_15_SMT; (d) GS40_D_400_SMT; (e) GS40_D_15_SMT. Refer to Table 1-4 for labels of experiments..... 60
Figure 2-12. Distribution fields of RPTG and $elocal$ calculated using the processed SMT images that were collected at the last loading steps for (a) DG_D_400_SMT; (b) DG_D_15_SMT; (c) DG_MD_15_SMT; (d) GB_D_400_SMT; (e) GB_D_15_SMT. Refer to Table 1-4 for labels of experiments..... 61

Figure 2-13. The discrepancy in the evolution of e toward the CS for the experiments presented in Figure 2-11 and conducted on F35 and GS40 sand. 62
Figure 2-14. The evolution of e versus $\sigma 1$ for the 12 oedometer experiments listed in Table 1-5, which were conducted on specimens of (a) F35, (b) DG, (c) GS40, and GB. 63
Figure 2-15. Illustration of common models used in the literature to fit a yield locus for sand in the stress plane $q - p'$. Refer to Table 1-6 for more details on each model. 64
Figure 2-16. The CSL modeled in the compression plane $(e - p')$ using the 12 oedometer experiments listed in Table 1-5, which were conducted on specimens of (a) F35, (b) DG, (c) GS40, and GB. 65
Figure 2-17. The CSL modeled in the compression plane $(e - p')$ using the 50 CTC experiments summarized in Table 1-2, which were conducted on (a) loose, (b) medium dense, and (c) dense specimens. 66
Figure 2-18. Yield locus for (a) F35, (b) DG, (c) GS40, and GB. 67
Figure 3-1. Axial slice through the initial SMT scan: (a) grayscale image; (b) labeled image; and (c) 3D view of the generated surface mesh. 86
Figure 3-2. Global compressive displacement versus force calibration curve of the top end cap. 86
Figure 3-3. Specimen behavior using FE simulation in which surrounding mold is hidden for better visualization ($\varepsilon 1$ refers to the global axial strain). 87
Figure 3-4. Illustrative example of equivalent contact force calculations between particle 10 and 11 at about 7% global axial strain. 88
Figure 3-5. Evolution of (a) force chain I; (b) fracture in particle 6; (c) force chain II; and (d) fracture in particle 31. Surrounding mold is hidden for better visualization ($\varepsilon 1$ refers to the global axial strain). 89
Figure 3-6. Comparison between (a) experimental force chain I; (b) model force chain I; (c) experimental force chain II; and (d) model force chain II. 90
Figure 3-7. Visualization of interaction between force chain I and II through a common supporting particle #26 at about 7% global axial strain. 90
Figure 3-8. (a) Nodal contact forces between particle 11 and its surrounding particles and (b) stress flow in an assembly associated with force chain I and another assembly not associated with any of the detected force chains at about 7% global axial strain. 91
Figure 3-9. Visualization and comparison between experimental versus model fracture of (a) Particle 6; (b) Particle 31; (c) Particle 13; (d) Particle 27; and (e) Particle 28. 92
Figure 3-10. FE model fracture assessment for (a) Particle 6 (b) Particle 31. 93
Figure 3-11. Evolution of principal stresses and strains within Particles 6 and 31. 94
Figure 3-12. Histogram of maximum tensile principal stress distribution of particles 6 and 31. 95

Figure 4-1. (a) Schematic sketch of the experimental setup; (b) displacement versus vertical load relationship at the top loading platen; and (c) 3D volume rendering of the processed SMT images showing the onset of particle breakage within the specimen. 118
Figure 4-2. (a) Grain size distribution of the scanned sand specimen; (b) histogram plot of the aspect ratio of the sand particles in the scanned specimen; and (c) 3D volume rendering of a few representative sand particles with different aspect ratio along with their equivalent diameter spheres.(The wired-meshes disappear when they overlap with the sand particles). 119
Figure 4-3. (a) 3D volume rendering of the scanned sand specimen; (b) 3D particle meshes used in FEM-Sand simulations; (c) 3D particle clumps used in DEM-Sand simulations; (d) 3D particle meshes used in FEM-Sphere simulations; and (e) spherical particles used in DEM-Sphere simulations. 120
Figure 4-4. The 3D numerical simulations of the uniaxial compression experiment (a) FEM-Sand; (b) FEM-Spheres; (c) DEM-Sand; and (d) DEM-Spheres. 121
Figure 4-5. Evolution of the averaged coordination number (CN) with the global vertical compressive load. 122
Figure 4-6. Illustration of the procedure used to calculate inter-particle contact forces for simulations of (a) FEM-Sand; (b) FEM-Spheres; (c) DEM-Sand; (e) and DEM-Spheres. 123
Figure 4-7. The distribution of inter-particle contact forces within the simulated specimens at global vertical compressive loads of 200 and 500 N. 124
Figure 4-8. Weibull fit parameters for the distribution of (a) inter-particle contact forces; and (b) particles' major principal stress $(\sigma 1)$ within the specimen at multiple steps of the global vertical compressive load. 125
Figure 4-9. Inverse trend between the mean of inter-particle contact forces acting on highly stresses particles and the associated coordination number. 126
Figure 4-10. Influence of particle morphology on the development of force chains: DEM versus FEM. 127
Figure 5-1. Illustrative diagrams of (a) left- and (b) right-handed crystal quartz. The crystal diagrams are a modified version of Figure 6 in Akhavan (2013). ... 157
Figure 5-2. (a) Uniaxial global load versus displacement relationships for the weak and strong cube experiments as recorded by the testing sensors. Central vertical Y-Z slice in SMT scans visualizing the evolution of lattice strains versus compression as quantified from 3DXRD measurements for the (b) strong and (c) weak cube experiments. 158
Figure 5-3. 3D FE modeling of the (a) strong; (b) weak; and (c) isotropic cubes using a single 20-noded hexahedral element. (d) Relationships between the major principal strains and the major principal stresses for the hexahedral element. 159
Figure 5-4. Demonstration of the closed-form solution for the (a) strong; (b) weak; and (c) isotropic cubes under uniaxial compression loading conditions. ... 160

Figure 5-5. Synthesis of the experimental (3DXRD), simulated (3D FE), and calculated (closed-form) major principal strain for the cube under uniaxial compression conditions. 161
Figure 5-6. Evolution of the major principal strain versus compression in the 3D FE simulations of (a) strong; (b) weak; and (c) isotropic cube at load steps similar to the experiments. 162
Figure 5-7. (a) Central vertical Y-Z slice in the SMT greyscale image; (b) 3D volume rendering of AVIZO processed image; and (c) centroids of crystal lattices from 3DXRD measurements for the natural sand specimen composed of 2705 silica particles. 163
Figure 5-8. 3D volume rendering in greyscale SMT image for particle 111 showing the wire-frame mesh used in 3D FE analysis and the crystal local orientation as quantified from 3DXRD measurements. 163
Figure 5-9. Histogram of the number of 3DXRD measurements matched to the SMT particles. 164
Figure 5-10. Histogram of the crystal structure of sand particles. 164
Figure 5-11. Configurations of crystal local orientations pre-assigned to individual particle meshes in (a) strong; (b) weak; and (c) experimental simulations. The blue, green, and red vectors, respectively, denote the [0 0 0 1] (c-axis), [0 1 -1 0], and [2 -1 -1 0] (a-axis) crystal local axes. Confining tube surrounding the specimen is hidden for better visualization of the specimen internal fabric. 165
Figure 5-12. 3D spherical distribution on a unit radius semi-sphere of the pre-assigned [0 0 0 1] crystal local axis (c-axis) for the 2705 sand particles in the (a) strong; (b) weak; and (c) experimental simulations. 166
Figure 5-13. Evolution of global uniaxial strain versus global uniaxial stress for 3D FE simulations. 167
Figure 5-14. Histograms of major principal stress of sand particles in (a) experimental versus isotropic and (b) strong versus weak simulations at 3% global uniaxial strain. 167
Figure 5-15. FE fringe plot for the major principal stress in the isotropic simulations at 3% global uniaxial strain. Side particles compare major principal stress and crystal local orientations among the four conducted 3D FE simulations (strong, weak, experimental, and isotropic). 168
Figure 5-16. Evolution of major principal strain versus stress in the 3D FE simulations (strong, weak, experimental, and isotropic) for particles (a) 476; (b) 675; (c) 828; (d) 1445; (e) 2266, and (f) 2500. 169
Figure 5-17. Dynamic explicit model of the cube experiments using (a) 100 μm, and (b) $50\ \mu m$ mesh size. Static implicit model of the cube experiments using (c) 100 μm, and (d) $50\ \mu m$ mesh size. (e) Assessment of mesh sensitivity and quasi-static response for (a)–(d) models. 170
Figure 5-18. Illustrative examples of sand particles matched with multiple 3DXRD measurements but possessed a single crystal structure. 171

Figure 5-19. Illustrative examples of sand particles matched with multiple 3DXRD measurements and possessed Dauphiné twins. 172
Figure 5-20. Illustrative example of particle 272 matched with four 3DXRD measurements and possessed Dauphiné twins. 173
Figure 5-21. Illustrative examples of sand particles with poly crystal structures. 173
Figure 6-1. (a) Illustration of the failure criterion and (b) damage evolution that were implemented in the material user-subroutines to model the brittle fracture of silica sand particles. 197
Figure 6-2. Illustration of the acquired in-situ SMT scans and conducted FE simulations for (a) Particle-1; (b) Particle-2; and (c) Sphere-Eq. 198
Figure 6-3. (a) Evolution of vertical load (Fz) versus displacement (UZ) at the top loading platen for the single particle crushing simulations and experiments; and (b) evolution of the particle major principal stress $(\sigma 1)$ versus strain $(\epsilon 1)$. 199
Figure 6-4. Fracture patterns in the FE simulations of (a) Particle-1; (b) Particle-2; and (c) Sphere-Eq. 200
Figure 6-5. Relationship between the particle major principal stress $(\sigma 1)$ and applied vertical load (FZ) prior to fracture in the single particle crushing FE simulations. 201
Figure 6-6. Distribution of stress within the Sphere-Eq simulations prior to fracture. *Value of force used to evaluate the theoretical closed-form solution per Hiramatsu and Oka (1966). 202
Figure 6-7. (a) 3D SMT image and (b) 3D FE numerical meshes of the sand specimen tested in confined 1D compression. 203
Figure 6-8. Illustration of the FEM-Experimental simulations at vertical axial strain (εZ) of (a) 10%; (b) 20%; and (c) 30%. 204
Figure 6-9. Configurations of local crystal orientations assigned to each particle in the FE simulations of (a) FEM-Strong; (b) FEM-Weak; and (c) FEM-Experiment. 205
Figure 6-10. Evolution of the specimen void ratio (e) versus vertical compressive stress σZ for the confined 1D compression FE simulations and experiment. 206
Figure 6-11. Examples of stress-strain relationships for 6 fractured particles that were selected from different regions within the specimen. 207
Figure 6-12. Relationships between particle von Mises (σvf) and hydrostatic mean stress (σhf) at fracture. 208
Figure 6-13. Correlation between the particle coordination number (CN) and fracture stress. 209
Figure 6-14. Correlation between the particle aspect ratio (AR) and fracture stress. 210

CHAPTER ONE

GENERAL INTRODUCTION

Motivational Background

The abundance and excellent physical properties of sand make it a suitable material for many engineering applications. In addition, the fine particulate nature of sand provides excellent drainage, immediate settlement, and enhanced bearing capacity compared to soft clayey soils. Therefore, sand has been frequently recommended for use as a foundation material in many civil engineering applications. The frictional resistance of sand has also made it useful for pile foundations as well as military barriers. The most common constituent of sand particles is quartz mineral (silicon oxide), which is well-known for its high compressive strength that makes sand an excellent proppant for high-pressure hydraulic fracturing in the oil and gas industry. These excellent properties have drawn the attention of many researchers seeking to establish a comprehensive understanding of sand constitutive behavior and particle fracture to improve the performance of relevant engineering applications.

Critical State (CS) soil mechanics is the conventional framework that governs the constitutive behavior of sand within the theory of frictional plasticity (Coulomb, 1776) and stress-dilatancy relationships (Roscoe et al., 1958). However, the critical state theory (CST) was originally proposed for cohesive soils (Schofield and Wroth, 1968), and the theory applicability for sand specimens has widely been questioned in the published literature. Wood (1990) evaluated the CS for sand specimens tested in the conventional triaxial compression apparatus of constant mean stress and stated that "*from the tests on loose sands, a critical void ratio would imply a volumetric expansion of 17% for the initially dense specimens*". He also added that 17% is an unrealistic amount of volumetric expansion, and "*testing difficulties have prevented the dense specimen from attaining an ultimate condition with shearing continuing at constant volume."* The non-convergence of dense and loose sand specimens to a unique CS is well documented in the literature and the term "*transitional sand"* has been introduced to describe this mode of behavior (Martins et al., 2001, Ferreira and Bica, 2006, Shipton and Coop, 2012, Coop, 2015). This dissertation postulates that the transitional behavior of sand is fundamentally caused by the complex micro-scale deformations that develop throughout the hardening regime of sheared sand under conventional triaxial compression (CTC). The dissertation uncovers these micro-scale deformations through 3D digital image processing of in-situ synchrotron micro-computed tomography (SMT) scans for a series of CTC experiments on different types of silica sands and glass beads.

In-situ SMT images have recently characterized several micro-scale deformations in sand specimens, including particle kinematics, rearrangement, frictional sliding/rotation, fracture, and fabric reconstruction. These micro-scale

deformations appear rather complex for the CST to address in a theoretical framework. This fundamental limitation was reported in the literature as early as the controversial statement published by Terzaghi (1920): "*The fundamental error was introduced by Coulomb, who purposely ignored the fact that sand consists of individual grains, and who dealt with sand as if it were a homogenous mass with certain mechanical properties … The way out of the difficulty lies in dropping the old fundamental principles and starting again from the elementary fact that sand consists of individual grain*s". Following Terzaghi's statement, several efforts have been made in the literature to re-establish the stress-dilatancy relationships for an ideal packing of particles with regular geometries, such as spherical and ellipsoidal particles (Rowe, 1962, Bolton, 1986). Alternatively, the Discrete Element Method (DEM) (Cundall and Strack, 1979) has fundamentally acknowledged the particulate nature of sand by numerically modeling the static balance of individual particles that interact with each other in the granular assembly according to appropriate contact models.

In the second half of the 20th century, the quantitative description of morphology, fabric, and particle interaction in 2D granular materials has been the subject matter of extensive geotechnical research (Oda, 1972, Kanatani, 1984). Yet, similar 3D measurements are still very limited for natural sand specimens. For instance, Cho et al. (2006) investigated the influence of particle morphology on stiffness and strength for a large experimental database of sand specimens. Sphericity and roundness were visually characterized using 2D microscopic images of sand particles. They concluded that increasing particle irregularity causes a decrease in the stability of contact interfaces between sand particles, and thus a reduction in the material stiffness when measured using oedometer tests. Cho et al. (2006) further stated that *"Particle shape emerges as a significant soil index property that needs to be properly characterized and documented, particularly in clean sands and gravel. The systematic assessment of particle shape will lead to a better understanding of sand behavior".* While the dissertation outcomes would agree with the latter statement, they would challenge the conclusion by Cho et al. (2006) that suggested a decrease in the material stiffness due to more shape irregularities in granular materials. Namely, the dissertation proposes that a certain level of shape irregularities, such as the natural particle morphology of the standard Ottawa ASTM 20-30 sand, can cause a higher degree of particle interlocking and embracement that would lead to an increase in the global material stiffness.

In a recent scientific achievement, Alshibli et al. (2013) demonstrated that 3D x-ray diffraction (3DXRD) could accurately measure the lattice strain within silica sand particles. This achievement marked a milestone since it uncovered a massive gap regarding the constitutive behavior of silica sand particles from the perspective of deformations in the crystal lattice of the constituent minerals. Furthermore, the DEM fundamentally ignores these crystal deformations since it assumes rigid particles. This dissertation alleviates these concerns about DEM limitations through the development of an alternative 3D FE approach that still captures the discrete nature of sand particles. The proposed FE simulations operated on

numerical 3D meshes of particle shapes that closely resembled the natural morphology of sand specimens. The transmission of inter-particle contact stresses was simulated using the slip-stick frictional models that are established for penetrating nodes between touching 3D meshes in FE analysis. The principal motivation for the proposed FE simulations emerges from the new ability to predict the lattice strains and stresses within individual silica sand particles through the implementation of a user-subroutine that describes the material behavior of the constituent mineral.

From a crystalline-scale point of view, little is known about the constitutive behavior of silica sand particles. This dissertation would advocate for the hypothesis that the crystal structure of silica sand particles is a major contributor to their fracture and constitutive behaviors. The hypothesis was investigated through experimental insights into the crystal structure and lattice strains of natural silica sand particles using an in-situ scanning technique that combines SMT and 3DXRD. These state-of-the-art measurements were then adopted to calibrate a material user-subroutine that models the constitutive behavior of silica sand particles assuming anisotropic linear elastic behavior of quartz. The user-subroutine adopted the concept of continuum damage mechanics to simulate the brittle fracture of sand particles when subjected to high effective stresses. Outcomes of this dissertation are expected to stimulate many efforts in the geotechnical research community toward the development of material user-subroutines that would incorporate additional crystal characteristic when modeling the constitutive behavior of silica sands, such as the fracture along preferred slip systems in mono-crystal particles or along the lattice boundaries/domains in particles compose of poly-crystals and crystal twins.

Dissertation Objectives

This dissertation investigated the 3D constitutive behavior of sand at multiple scale-levels, as illustrated in Figure 1-1 (note that Figures and Tables in this dissertation are presented in Appendices at the end of each Chapter):

1. Global scale (*Chapter 2*)

At the global scale-level, the CS concept was assessed using results of CTC and oedometer experiments that were conducted on laboratory-sized specimens of natural silica sands. This assessment was coupled with insights from digital image processing of in-situ SMT images that were acquired for CTC experiments on natural silica sand specimens. Analyses of the rich experimental datasets searched for:

- The notion of a unique CS locus for sand specimens that are tested in the CTC apparatus under a wide range of confining pressures (15 to 400 kPa) and initial density states.
- Micro-scale deformations within the CTC specimen that would explain possible reasons for the transitional behavior of sand. Recall that the transitional behavior of sand is defined as the non-convergence of CTC stress paths to a unique CS locus in the compression plane depending on the initial specimen density.

2. Particle-scale (Chapters 3 & 4)

At the particle-scale level, sand was treated as an assembly of discrete deformable particles. In-situ SMT images for natural sand specimens were processed to produce 3D FE simulations for the confined 1D compression experiment. Compared to DEM, the proposed 3D FE simulations enhanced the numerical resemblance of natural sand morphology, particle-to-particle interaction, and particle breakage. 3D FE simulations studied:

- Fundamental mechanisms causing particle fracture within specific regions associated with the evolving force chains in sand specimens when loaded under confined 1D compression. The dissertation answered research questions such as: *what intrinsic properties would cause a specific sand particle to fracture before other particles within a loaded mass of sand?*
- The onset and evolution of force chains in granular specimens loaded in confined 1D compression and composed of spherical versus natural-shaped sand particles. The dissertation accurately evaluated the influence of natural sand morphology on the force and stress transmission between particles associated with the force chains.

3. Crystalline scale *(Chapters 5 & 6)*

This scale-level treated sand as mineral particles composed of crystal quartz. The unique properties of quartz crystal structure were represented with their corresponding influence on the constitutive behavior of silica sand particles. The crystal structure was examined for natural silica sand particles using powder x-ray diffraction, Laue x-ray diffraction, and 3DXRD. The following is a list of objectives related to the crystalline-scale level:

- Determine the crystal structure of natural silica sand particles and compare it with the structure of synthetic silica cubes. The cubes represent a baseline geometry that would be loaded in unconfined 1D compression to uncover the effects of crystalline-scale properties on the constitutive behavior of silica sand particles.
- Discuss unique 3DXRD patterns for natural silica sand particles that would suggest the notion of crystal twins and poly-crystal structure.
- Develop a material user-subroutine to simulate the crystal-based anisotropy in the constitutive and fracture behaviors of silica sand particles. The user-subroutine would implement the anisotropic linear elastic model for crystal quartz, coupled with an exponential degradation in the material point stiffness to simulate brittle fracture appropriately.
- Utilize the material user-subroutine to investigate the influence of crystalline-scale properties on the constitutive and fracture behaviors of silica sand particles, such as the direction of applied particle stresses relative to the local crystal orientation of the sand particle.

Literature Review

This dissertation is structured into five major chapters that are published in peer-reviewed journals, or in the process of being published. Each chapter begins with

an “Introduction” Section that presents a thorough literature review about the corresponding subject matter. The following sub-sections give a top-level summary of the thorough literature that was reviewed for the five chapters.

Global-Scale Response of Sand Material

Critical State (CS) Soil Mechanics

Studies reporting on the constitutive behavior of sand have traditionally recognized global-scale input measurements such as stresses and strains at boundaries of laboratory-size specimens to describe Mohr-Coulomb failure (Coulomb, 1773). Understanding the stress-dilatancy relationship (Roscoe et al., 1958) added a major enhancement to the Mohr-Coulomb criterion and motivated the CST in soil mechanics as a benchmark framework. The CS concept was originally proposed for clays by Schofield and Wroth (1968) and theoretically postulated the notion of a material yield surface, as well as a unique post-failure state known as the CS. This unique post-failure state was attributed to the conditions of ultimate shear deformation without changes in volume or effective stresses and theoretically represented by the Critical State Line (CSL) tracing the top of yield locus in $p' - q - e$ space where p', q, and e are the mean effective principal stress, deviatoric stress, and void ratio; respectively. Constructing the CSL in the stress plane ($p' - q$) and compression plane ($p' - e$) separately has been a common practice since this has enhanced the understanding of general triaxial stress paths when superimposed in planes versus 3D space representation (Poorooshasb et al., 1966, Wood, 1990).

1D compression experiments on sands have confirmed a similar pattern of response to clays in which normal compression lines (NCLs) and CSL are parallel when plotted in the compression plane (Been and Jefferies, 1985, Coop, 1990, McDowell and Bolton, 1998a) with certain allowance for the effects of particle breakage (Coop and Lee, 1993). Yet, the convergence to a unique CSL is still questionable (Martins et al., 2001, Nocilla et al., 2006) and recent research has introduced the term “transitional” describing the non-convergence to a unique CSL in sand (Ferreira and Bica, 2006, Shipton and Coop, 2012, Coop, 2015). Several studies have investigated the transitional behavior of sands that was directly related to the high stresses required for CS attainment and the synchronous particle breakage (Altuhafi and Coop, 2011, Shipton and Coop, 2012, Xiao et al., 2015), as well as the associated influence of particle-scale properties such as grain sizes (Nocilla et al., 2006, Shipton and Coop, 2014, Zuo and Baudet, 2015), particle morphology (Santamarina and Cho, 2004, Yang and Luo, 2015, Alshibli and Cil, 2017, Kandasami and Murthy, 2017), and fabric reconstruction (Li and Dafalias, 2011, Coop, 2015, Dafalias, 2016, Todisco et al., 2018). Although there is still active quest trying to integrate fabric reconstruction, for example, as an essential state parameter in the conventional CST (Dafalias and Manzari, 2004, Fu and Dafalias, 2011, Gao et al., 2014, Theocharis et al., 2016, Wang et al., 2017, Petalas et al., 2019), the notion of a theoretical yield surface for sand material is

fundamentally problematic due to the particulate nature of sand and rather complex particle-to-particle interaction.

Shear Strain Localization

Studies reported in the literature relied on the global change in volume to calculate the evolution of e toward the CS with limited research investigating the accuracy of conventional triaxial testing procedures (Garga and Zhang, 1997, Jefferies and Been, 2000, Rocchi and Coop, 2013). In recent years, excellent in-situ x-ray computed tomography (CT) scans were collected for sand specimens loaded in conventional triaxial compression (CTC) (Alshibli et al., 2016, Andò et al., 2017), and the scans exposed rather complex internal shearing pattern called micro shear bands (MSBs) that developed during the hardening phase of the experiment (Amirrahmat et al., 2019). Therefore, the transitional behavior of sand can be mainly caused by the misleading global measurement of volume change that has traditionally been used to calculate the evolution of e in the compression plane instead of e within the MSBs (Salvatore et al., 2017). Overall, advances in in-situ x-ray computed tomography (CT) and image processing techniques have exposed micro-level characterization of particle kinematics (Druckrey et al., 2017) that broadly challenged the ability of CST to interpret the complex deformation mechanisms at the particle-scale during CTC experiments (Desrues et al., 2018).

Particle-Scale Behavior

Distinct Element Method (DEM)

DEM is a modern approach that has been widely utilized to model the mechanical response of sand and granular materials in general. Originally proposed by Cundall and Strack (1979), DEM has numerically modeled the movement and interaction between spheres. Since then, advances in particle kinematics and contact models have extensively evolved by means of explicit time integration and particle force-moment balance algorithms (Pande et al., 1990, Shi, 1992, Munjiza, 2004, Williams et al., 2014). Many researchers used DEM to numerically simulate loading conditions for specific engineering applications, as well as standard laboratory experiments such as CTC fluid pressure (Ng, 2004), latex membrane effects (Cheung and O'Sullivan, 2008, Cil and Alshibli, 2014b), and interactions between sand and rigid bodies (Yang et al., 2011).

The mechanical response of sands is essentially related to the rheology of granular materials. DEM provided an invaluable tool to investigate these mechanics since it captures the particulate nature of sands. To mention few example studies, Belheine et al. (2009) reported high peak stresses under triaxial compression conditions caused by the rolling resistance between particles in DEM simulations with an enhanced contact model to account for particle roughness. O'Sullivan and Cui (2009) simulated loading-unloading cycles on specimens composed of steel spheres (~15,000 particles) loaded in quasi-static triaxial compression conditions and examined changes in mechanisms of particle-scale deformation during load reversals. Yimsiri and Soga (2010) utilized DEM to prepare multiple specimens of

spheres with non-uniform sizes and different distribution of normal to contact vectors between particles. Results in Yimsiri and Soga (2010) advocated for the profound effect of contact fabric on the mechanical response of sands under extension and compression triaxial loading conditions. Jiang et al. (2011) examined shear band localization and inhomogeneity fields of e during DEM simulations on 2D discs loaded in biaxial compression. de Bono and McDowell (2014) reported on the importance of particle fracture in modeling the volumetric contraction of sands via simulations of high-pressure triaxial shear experiments on crushable spheres featuring flexible membrane boundary conditions. Guo and Zhao (2014) introduced a hierarchical multi-scale modeling framework in which DEM-calibrated loading histories for representative elementary volumes (REVs) of sand were implemented in the stress-strain calculations at the Gaussian integration points of a finite element mesh representing the granular media. The industrial and practical use of DEM in relatively large-scale engineering applications (Marigo and Stitt, 2015) is also promising due to the rapid advancements in numerical models, computational power, and parallel computing (Yan and Regueiro, 2018a, Yan and Regueiro, 2018b).

Force Chains in Sands

Realizing the particulate nature of sands has emerged as a milestone in understanding their mechanics. Global compressive loads applied at boundaries of a sand mass are internally supported by a skeleton of particles piling and jamming into a complex network of mutual compressive forces. There are regions of high contact stresses transmitted through some interfaces between particles to form what is commonly known as force chains. Force chains have been visualized in photo-elastic granular materials (Dantu, 1957, Wakabayashi, 1957, Dantu, 1968, Jong and Verruijt, 1969, Behringer et al., 1999, Howell et al., 1999, Geng et al., 2003, Majmudar and Behringer, 2005, Clark et al., 2012). Besides photo-elasticity, many methods were employed to characterize and visualize force chains in granular material. For instance, Coppersmith et al. (1996) introduced the scaler q model to characterize force chains within a specimen composed of spheres in which the dominant physical mechanism altering force chains was concluded to be the variations in the contact angles and constraints imposed by the force balance on each sphere (Liu et al., 1995, Eloy and Clément, 1997, Socolar, 1998). Bouchaud et al. (1995) described the propagation of force chains in compacted granular material using phenomenological equations, which are also known as the oriented stress linearity model. Radjai et al. (1996), (1999) implemented contact dynamics simulation to evaluate the statistical distribution of contact forces between 2D rigid disks subjected to uniaxial compression. Edwards and Grinev (2003) proposed an approach that utilized statistical and mechanical concepts to characterize force chains in granular material.

DEM has emerged as a powerful tool in modern characterization and visualization of force chains in sand-sized granular material. Peters et al. (2005) developed an algorithm that used contact forces and trajectories of the major principal stress to characterize force chains in DEM simulations of flat punch indentation through an

assembly of 2D discs. Tordesillas (2007) examined force chain buckling and shear banding during DEM simulations of 2D densely-packed discs subjected to quasi-static biaxial compression. Zhang et al. (2016) applied DEM to investigate the evolution of force chains in 2D discs loaded under quasi-static biaxial compression, as well as 3D spheres subjected to dynamic impact loading. In summary, most of the studies reported in the literature used either 2D disks or 3D spheres to characterize and study the force chains in sands (Andrade and Avila, 2012, Hurley et al., 2014, Brodu et al., 2015, Hall and Wright, 2015b, Hurley et al., 2016). Yet, there is limited knowledge about the behavior of particles with complex morphology like natural sands.

Sand Particle Morphology

During shearing/compression, sand particles may translate and rotate as they interact with each other in a complex fashion. Published literature has repeatedly acknowledged the influence of sand morphology on particle friction (Yousuff and Page, 1993, Santamarina and Cho, 2004, Vangla and Latha, 2015, Vangla and Gali, 2016), rearrangement (Pena et al., 2007, Shin and Santamarina, 2012, Kandasami and Murthy, 2017), interlocking (Guo and Su, 2007, Azéma et al., 2013), and fracture (Nakata et al., 2001, Cavarretta and O'sullivan, 2012, Wang and Coop, 2016). Sand morphology has been characterized using 2D imaging (Kwan et al., 1999, Wang et al., 2005, Al-Rousan et al., 2007, Cox and Budhu, 2008, Bessa et al., 2012, Sun et al., 2012), 3D x-ray CT (Fonseca et al., 2012, Garboczi and Bullard, 2013, Garbout et al., 2013), and 3D laser scanning (Komba et al., 2013). For instance, Cho et al. (2004) quantified particle morphology by means of sphericity, roundness, and surface roughness using 2D images and experimentally confirmed a global decrease in stiffness as well as an increase in compressibility for sand specimens with fewer irregularities in particle shape. Advances in x-ray CT and image processing have also served as valuable tools in the 3D characterization of sand morphology. Alshibli et al. (2014a) proposed robust 3D definitions of particle roundness and sphericity indices quantified using x-ray CT as well as a surface roughness index measured using an optical surface profiler. The indices were significantly correlated to the volumetric change, dilatancy, peak, and CS strength of laboratory-size specimens tested in CTC conditions (Alshibli and Cil, 2017).

Recognizing the importance of sand morphology has motivated many efforts in DEM to alter the spherical shape of particles into more realistic sand-like shapes. Efforts included the numerical formulation of particle kinematics and contact models for ellipsoids (Yan et al., 2010) and poly-ellipsoids (Zhang et al., 2018). Still, sand particles have much more complex morphology in comparison to ellipsoidal shapes. DEM clumping of sub-spheres into unbreakable 2D (Lu and Frost, 2010) and 3D (Salot et al., 2009, Hasan and Alshibli, 2010) particles enhanced the resemblance of angularity in sand particles. However, clumping produced surface aliasing that can undoubtedly influence the particle-to-particle interaction even when tiny sub-spheres are clumped into a relatively large base sphere (Ferellec and McDowell, 2010, Gao et al., 2012, Li and McDowell, 2018).

Surface meshes that closely match the complex morphology of sand particles were filled in DEM with agglomerates of bonded spheres (Cil and Alshibli, 2015, Fu et al., 2017). Nonetheless, agglomerates were originally proposed to simulate particle fracture in DEM, ignoring the major drawback in creating porous particles while sands consist of discrete solid-filled particles. Level-set (LS) functions have recently proven powerful in tracing the complex surface of sand particles with the help of in-situ x-ray CT (Kawamoto et al., 2016). LS functions were implemented in DEM (LS-DEM) and appeared effective in predicting shear bands during simulations of CTC experiments (Kawamoto et al., 2018).

Particle Fracture in Sand

Deformation mechanisms in sand specimens are essentially altered by particle breakage due to high effective stresses. Particle breakage in sand influences stress-dilatancy relationship (Bolton, 1986), leads to the development of NCLs in uniaxial compression (Coop and Lee, 1993, McDowell and Bolton, 1998a), correlates to plastic yielding (McDowell and Bolton, 1998b, McDowell and Harireche, 2002b), affects strain accumulation in cyclic loading (Harireche and McDowell, 2003) , and impacts CSL location in the compression plane (Cheng et al., 2005, Xiao et al., 2016).

Several numerical models have been developed in DEM to simulate particle breakage. In the agglomerates approach (Robertson and Bolton, 2001, McDowell and Harireche, 2002b, Cheng et al., 2003), individual particles were filled with bonded sub-spheres while bonds between sub-spheres can break according to appropriate contact models (Cil and Alshibli, 2014c). Particle substitution method (Tsoungui et al., 1999, Lobo-Guerrero and Vallejo, 2005b) proposed a critical loading history at which spheres in DEM replaced by smaller sub-spheres. DEM has also modeled particle breakage in sand using Hoek-Brown fracture criterion, a common criterion that numerically simulated brittle fracture in rocks (Hoek and Martin, 2014, Zhang et al., 2015). However, these mentioned models lack the concepts of fracture mechanics in brittle crystalline material (sand particles), which is primarily induced by a successive breakage of atomic bonds along specific crystallographic planes commonly known as slip planes or slip systems (Callister, 2007, Quintana-Alonso and Fleck, 2009).

Single Particle Fracture and Single Contact Interface

Hydraulic fracturing and the relevance of particle breakage to many engineering applications has led many geotechnical researchers to investigate the fracture characteristics of silica sand at the scale of single-particle crushing experiments. Cil and Alshibli (2012) examined the tensile strength of 87 silica sand particles and surprisingly reported a wide variation in the particle fracture stress with a mean of $118.43\ MPa$ and a standard deviation of $37.89\ MPa$. Much less variation in the fracture stress was expected since Cil and Alshibli (2012) tested particles of ASTM 20-30 Ottawa sand; a standard type of sand commonly used in geotechnical testing and known for having 99.9% silica constituent as well as uniform grain sizes (between US sieve #20 and #30). In-situ x-ray CT images with excellent resolution

were acquired for single-particle crushing experiments (Cil and Alshibli, 2012, Zuo and Baudet, 2015), and the scans exposed complex particle morphology causing different loading conditions at contact interfaces between the loading platens and the individual sand particle. 3D DEM (Cil and Alshibli, 2014c) and FE simulations (Druckrey and Alshibli, 2015) have also advocated for the influence of sand morphology and particle-to-platen interactions on the fracture strength of single-particle crushing experiments.

Particle-to-particle interaction has widely been recognized as a key factor in determining the mechanical response of sands. For instance, Otsubo et al. (2015) demonstrated how surface roughness at contact interfaces between particles tended to decrease global stiffness. Studies investigating contact interfaces between sand particles have recently emerged at the scale of a single particle-to-particle contact, which provided concrete measurements of frictional/normal contact force (Cole, 2015). A three-axis loading apparatus was fabricated by Nardelli et al. (2017) to experimentally measure normal and shear contact forces at a single sand particle-to-particle contact interface. The three-axis loading apparatus experimentally validated the elastic contact models implemented in DEM (Nardelli and Coop, 2018).

Crystalline-Scale

Particle to Crystal

Sand is a granular material composed of finely weathered rock and mineral particles. The composition of sand particles is mainly inherited from local rock sources and weathering conditions (Pettijohn et al., 1972). Quartz is the most common constituent mineral in sands since it has the lowest potential for weathering, according to Goldich dissolution series (Goldich, 1938). In general, minerals have unique physical (e.g., hardness), chemical (e.g., reaction to acids), and mechanical (e.g., constitutive response) properties that are fundamentally governed by their crystal structure (Reynolds et al., 2016). Molecules in a crystal are arranged in a periodic manner (lattice), which defines the symmetry properties (Hahn et al., 1983) and determines the constitutive isotropy/anisotropy of the material (Roters et al., 2010). A crystalline material is called anisotropic when it deforms differently depending on the direction of external loading with respect to the crystal planes.

Quartz Crystal Structure

The building block (unit cell) of quartz crystal is silicon oxide tetrahedra (SiO_4) with each oxygen atom shared between two tetrahedra. This gives quartz an overall chemical formula of silicon dioxide (SiO_2), commonly known as silica. In crystallography, quartz has a hexagonal lattice system, trigonal crystal system, and rhombohedral unit cell (Dušek et al., 2001, Nikitin et al., 2007). Thorough description of quartz crystal structure can be found in (Akhavan, 2013). Briefly, the trigonal crystal structure of quartz is spanned by a four-axis system: a_1,a_2, a_3, and c. The three a-axes correspond to a and b lattice parameters that have equal

length, span the hexagonal plane of the trigonal system, intersect at 60^o angles, and usually referred to as the a-axis for simplification. On the other hand, the c-axis runs perpendicular to the hexagonal plane and corresponds to the c lattice parameter which is 1.1 times the length of a or b. This nontrivial crystal structure of quartz has drawn the attention of many researchers in material science and certainly produced directional anisotropy in the constitutive response (Bechmann, 1958, Gregoryanz et al., 2000, Ogi et al., 2006, Cady, 2018).

Crystal quartz is well-known to form different types of penetration and contact twinning, such as Dauphiné, Brazil, and Japan (Gault, 1949). Crystal twinning forms when two or more separate sub-domain crystals share some of the lattice points. This results in an intergrown structure of the sub-domain crystals in specific configurations known as twin laws (Tilley, 1961). In contact twinning, the sub-domain crystals share a single composition surface that is often displayed in electron crystal microscopy as mirror distortion across the crystal boundaries (Sunagawa and Yasuda, 1983). Penetration twinning forms when two or more sub-domain crystals interpenetrate each other with the surface between the sub-domains being indefinable and irregular. For instance, Dauphiné is a penetration twinning that forms when sub-domain crystals of either right- or left-handed quartz are combined in the same structure. The sub-domain crystals share the same c-axis and rotated about the common c-axis by 60° relative to each other (Eder et al., 2015). Dauphiné twinning is recognized to influence stress concentrations and the onset of lattice fracture near crystal boundaries (Lloyd, 2000, Barton and Wenk, 2007). Recently, Hurley et al. (2018c) reported on the notion of Dauphiné twinning in a specimen composed of synthetic silica particles scanned using in-situ x-ray CT and 3DXRD. Yet, little is known about crystal twinning of silica sand particles in the geotechnical research.

Crystalline-Scale in Geotechnical Research

Most of the recent studies in geotechnical research focus on the effects of sand morphology and particle-to-particle interaction on the constitutive behavior of sand at a scale of individual or multiple particle fracture (Bolton et al., 2008, Cil and Alshibli, 2012, Cil and Alshibli, 2015, Zhao et al., 2015, Druckrey and Alshibli, 2016) and single contact interface (Cole and Hopkins, 2016, Nardelli and Coop, 2018, Sandeep et al., 2018). However, lattice stresses and strains within individual silica sand particles are fundamentally governed by the constitutive response at the scale of the constituent mineral (Alshibli et al., 2013).

In-situ scanning techniques have lately combined x-ray CT with 3DXRD (Cil et al., 2014, Hall and Wright, 2015a), which provided experimental measurements of lattice strains in synthetic (Hurley et al., 2017) and natural (Cil et al., 2017) silica sand particles. Although the combined x-ray CT and 3DXRD technique has acknowledged the crystal structure of quartz, these studies investigated the force chains in sands (Hurley et al., 2018) while there is still much unknown about the contribution of crystalline-scale characteristics. The combined in-situ scanning technique of x-ray CT and 3DXRD needs a synchrotron radiation source, as well

as expensive equipment that is only available in a few facilities. DEM also fails to model crystalline-scale characteristics as they are considered beyond the capability of particle flow simulations. This dissertation substantially contributes to our knowledge regarding the influence of quartz crystal structure on the constitutive behavior of silica sand particles.

Dissertation Outline

The dissertation consists of six chapters that present a comprehensive investigation and assessment of fundamental properties that exist at multiple scale-levels and contribute to the overall constitutive behavior of silica sand particles:

Chapter 2 assessed the critical state and yield locus of four different types of granular materials based on conventional laboratory experiments and in-situ SMT images. It shed the light on a discrepancy in measuring the evolution of the void ratio toward the critical state using the conventional triaxial apparatus due to shear strain localization within granular specimens.

Chapter 3 introduced 3D FE simulations that can numerically model the stress-strain and fracture mode of silica sand particles in light of their complex morphology and particle-to-particle interaction. The FE simulations were implemented to examine the evolution of force chains and the onset of particle fracture within a natural sand specimen composed of 35 particles and loaded in confined 1D compression.

Chapter 4 covered the implementation of the 3D FE simulations to assess the influence of sand morphology and coordination on inter-particle force and stress transmission, as well as the development of force chains. Analogous simulations were executed and compared for two granular specimens loaded in confined 1D compression and composed of 236 spherical versus natural-shaped sand particles.

Chapter 5 utilized x-ray diffraction experiments and SMT images to characterize the crystal structure and measure lattice strains within synthetic silica cubes loaded in unconfined uniaxial compression. The crystal structure was also characterized for a natural sand specimen loaded in confined 1D compression and composed of 2705 particles.

Chapter 6 employed the rich experimental data of 3DXRD and SMT to develop a material user-subroutine that can numerically model the constitutive behavior and fracture mode of silica sand particles, in light of their non-trivial crystal structure. The user-subroutine was then used to simulate single-particle crushing experiments, as well as the confined 1D compression experiment from Chapter 5.

Chapter 7 highlights the major conclusions from this dissertation and suggests recommendations for future research.

References

Coulomb, C. A. (1773) Essai sur une application des regles de maximis et minimis a quelques problemes de statique relatifs a l'architecture (essay on maximums and minimums of rules to some static problems relating to architecture).

Coulomb, C. (1776) An attempt to apply the rules of maxima and minima to several problems of stability related to architecture. *Mémoires de l'Académie Royale des Sciences* **7**:343-382.

Terzaghi, K. (1920) Old earth-pressure theories and new test results. *Engineering News-Record* **85(14)**.

Goldich, S. S. (1938) A study in rock-weathering. *The journal of Geology* **46(1)**:17-58.

Gault, H. (1949) The frequency of twin types in quartz crystals. *American Mineralogist: Journal of Earth and Planetary Materials* **34(3-4)**:142-162.

Dantu, P. (1957). In *The 4th international conference on soil mechanics and foundation engineering*.) Butterworths Scientific Publication, London, vol. vol 1, pp. p 133.

Wakabayashi, T. (1957) Photoelastic method for determination of stress in powdered mass. In *Japan National Congress for Appl. Mech.*), pp. p. 153.

Bechmann, R. (1958) Elastic and piezoelectric constants of alpha-quartz. *Physical Review* **110(5)**:1060.

Roscoe, K. H., Schofield, A. & Wroth, C. (1958) On the yielding of soils. *Geotechnique* **8(1)**:22-53.

Tilley, C. E. (1961) Leonard James Spencer, 1870-1959.) The Royal Society London.

Rowe, P. W. (1962) The stress-dilatancy relation for static equilibrium of an assembly of particles in contact. In *Proceedings of the Royal Society of London A: Mathematical, Physical and Engineering Sciences*.) The Royal Society, vol. 269, pp. 500-527.

Poorooshasb, H., Holubec, I. & Sherbourne, A. (1966) Yielding and flow of sand in triaxial compression: Part I. *Canadian Geotechnical Journal* **3(4)**:179-190.

Dantu, P. (1968) Etude statistique des forces intergranulaires dans un milieu pulvérulent. *Geotechnique* **18(1)**:50-55.

Schofield, A. & Wroth, P. (1968) Critical state soil mechanics.

Jong, G. D. J. D. & Verruijt, A. (1969) étude photo-étlastique d'un empilement de disques. .

Oda, M. (1972) Initial fabrics and their relations to mechanical properties of granular material. *Soils and Foundations* **12(1)**:17-36.

Pettijohn, F. J., Potter, P. E. & Siever, R. (1972) Introduction and Source Materials. In *Sand and Sandstone*.) Springer, pp. 1-23.

Cundall, P. A. & Strack, O. D. (1979) A discrete numerical model for granular assemblies. *Geotechnique* **29(1)**:47-65.

Hahn, T., Shmueli, U. & Wilson, A. J. C. (1983) *International tables for crystallography.* Reidel Dordrecht.
Sunagawa, I. & Yasuda, T. (1983) Apparent re-entrant corner effect upon the morphologies of twinned crystals; A case study of quartz twinned according to Japanese twin law. *Journal of Crystal Growth* **65(1-3)**:43-49.
Kanatani, K.-I. (1984) Distribution of Directional Data and Fabric Tensors. *Int. J. Engng Sci.* **22(2)**:149-164.
Been, K. & Jefferies, M. G. (1985) A state parameter for sands. *Geotechnique* **35(2)**:99-112.
Bolton, M. D. (1986) The strength and dilatancy of sands. *Geotechnique* **36**:65-78.
Coop, M. (1990) The mechanics of uncemented carbonate sands. *Geotechnique* **40(4)**:607-626.
Pande, G., Beer, G. & Williams, J. (1990) Numerical methods in rock mechanics.
Wood, D. M. (1990) *Soil behavior and critical state soil mechanics.* New York, NY 10011, USA, Press Syndicate of the University of Cambridge the Pitt Building.
Shi, G.-H. (1992) Discontinuous deformation analysis: a new numerical model for the statics and dynamics of deformable block structures. *Engineering computations* **9(2)**:157-168.
Coop, M. & Lee, I. (1993) The behavior of granular soils at elevated stresses. *Predictive soil mechanics*:186-198.
Yousuff, M. & Page, N. (1993) Particle material, morphology and load effects on internal friction in powders. *Powder Technology* **76(2)**:155-164.
Bouchaud, J.-P., Cates, M. & Claudin, P. (1995) Stress distribution in granular media and nonlinear wave equation. *Journal de Physique I* **5(6)**:639-656.
Liu, C., Nagel, S. R., Schecter, D., Coppersmith, S. & Majumdar, S. (1995) Force fluctuations in bead packs. *Science* **269(5223)**:513.
Coppersmith, S., Liu, C.-H., Majumdar, S., Narayan, O. & Witten, T. (1996) Model for force fluctuations in bead packs. *Physical Review E* **53(5)**:4673.
Radjai, F., Jean, M., Moreau, J.-J. & Roux, S. (1996) Force distributions in dense two-dimensional granular systems. *Physical Review Letters* **77(2)**:274.
Eloy, C. & Clément, É. (1997) Stochastic aspects of the force network in a regular granular piling. *Journal de Physique I* **7(12)**:1541-1558.
Garga, V. K. & Zhang, H. (1997) Volume changes in undrained triaxial tests on sands. *Canadian Geotechnical Journal* **34(5)**:762-772.
Mcdowell, G. & Bolton, M. (1998a) On the micromechanics of crushable aggregates. *Geotechnique* **48(5)**:667-679.
Mcdowell, G. R. & Bolton, M. D. (1998b) On the micromechanics of crushable aggregates. In *Geotechnique*.), vol. 48, pp. 667-679.
Socolar, J. E. (1998) Average stresses and force fluctuations in noncohesive granular materials. *Physical Review E* **57(3)**:3204.
Behringer, R., Howell, D., Kondic, L., Tennakoon, S. & Veje, C. (1999) Predictability and granular materials. *Physica D: Nonlinear Phenomena* **133(1)**:1-17.

Howell, D., Behringer, R. & Veje, C. (1999) Stress fluctuations in a 2D granular Couette experiment: a continuous transition. *Physical Review Letters* **82(26)**:5241.

Kwan, A. K., Mora, C. & Chan, H. (1999) Particle shape analysis of coarse aggregate using digital image processing. *Cement and Concrete Research* **29(9)**:1403-1410.

Radjai, F., Roux, S. & Moreau, J. J. (1999) Contact forces in a granular packing. *Chaos: An Interdisciplinary Journal of Nonlinear Science* **9(3)**:544-550.

Tsoungui, O., Vallet, D. & Charmet, J.-C. (1999) Numerical model of crushing of grains inside two-dimensional granular materials. *Powder Technology* **105(1-3)**:190-198.

Gregoryanz, E., Hemley, R. J., Mao, H.-K. & Gillet, P. (2000) High-pressure elasticity of α-quartz: instability and ferroelastic transition. *Physical Review Letters* **84(14)**:3117.

Jefferies, M. & Been, K. (2000) Implications for critical state theory from isotropic compression of sand. *Geotechnique* **50(4)**:419-429.

Lloyd, G. E. (2000) Grain boundary contact effects during faulting of quartzite: an SEM/EBSD analysis. *Journal of Structural Geology* **22(11-12)**:1675-1693.

Dušek, M., Petříček, V., Wunschel, M., Dinnebier, R. & Van Smaalen, S. (2001) Refinement of modulated structures against X-ray powder diffraction data with JANA2000. *Journal of Applied Crystallography* **34(3)**:398-404.

Martins, F. B., Bressani, L. A., Coop, M. R. & Bica, A. V. D. (2001) Some aspects of the compressibility behavior of a clayey sand. *Canadian Geotechnical Journal* **38(6)**:1177-1186.

Nakata, Y., Kato, Y., Hyodo, M., Hyde, A. F. & Murata, H. (2001) One-dimensional compression behavior of uniformly graded sand related to single particle crushing strength. *Soils and Foundations* **41(2)**:39-51.

Robertson, D. & Bolton, M. (2001) DEM simulations of crushable grains and soils. *Powders and grains. Lisse. The Netherlands: Balkema*:623-6.

Mcdowell, G. & Harireche, O. (2002) Discrete element modelling of yielding and normal compression of sand. *Geotechnique* **52(4)**:299-304.

Cheng, Y., Nakata, Y. & Bolton, M. (2003) Discrete element simulation of crushable soil. *Geotechnique* **53(7)**:633-641.

Edwards, S. & Grinev, D. (2003) Statistical mechanics of granular materials: stress propagation and distribution of contact forces. *Granular Matter* **4(4)**:147-153.

Geng, J., Reydellet, G., Clément, E. & Behringer, R. (2003) Green's function measurements of force transmission in 2D granular materials. *Physica D: Nonlinear Phenomena* **182(3)**:274-303.

Harireche, O. & Mcdowell, G. (2003) Discrete element modelling of cyclic loading of crushable aggreates. *Granular Matter* **5(3)**:147-151.

Cho, G., Dodds, J. & Santamarina, J. (2004) Particle Shape Effects on Packing Density. *Stiffness and Strength of Natural and Crushed Sands-Internal Report, Georgia Institute of Technology, 33pp*.

Dafalias, Y. F. & Manzari, M. T. (2004) Simple plasticity sand model accounting for fabric change effects. *Journal of Engineering Mechanics* **130(6)**:622-634.
Munjiza, A. A. (2004) *The combined finite-discrete element method.* John Wiley & Sons.
Ng, T.-T. (2004) Triaxial test simulations with discrete element method and hydrostatic boundaries. *Journal of Engineering Mechanics* **130(10)**:1188-1194.
Santamarina, J. & Cho, G.-C. (2004) Soil behavior: The role of particle shape. In *Advances in geotechnical engineering: The skempton conference*.) Citeseer, vol. 1, pp. 604-617.
Cheng, Y., Bolton, M. & Nakata, Y. (2005) Grain crushing and critical states observed in DEM simulations. *P&G05* **2**:1393-1397.
Lobo-Guerrero, S. & Vallejo, L. E. (2005) Discrete element method evaluation of granular crushing under direct shear test conditions. *Journal of Geotechnical and Geoenvironmental Engineering* **131(10)**:1295-1300.
Majmudar, T. S. & Behringer, R. P. (2005) Contact force measurements and stress-induced anisotropy in granular materials. *Nature* **435(7045)**:1079.
Peters, J., Muthuswamy, M., Wibowo, J. & Tordesillas, A. (2005) Characterization of force chains in granular material. *Physical Review E* **72(4)**:041307.
Wang, L., Wang, X., Mohammad, L. & Abadie, C. (2005) Unified method to quantify aggregate shape angularity and texture using Fourier analysis. *Journal of Materials in Civil Engineering* **17(5)**:498-504.
Cho, G.-C., Dodds, J. & Santamarina, J. C. (2006) Particle shape effects on packing density, stiffness, and strength: natural and crushed sands. *Journal of Geotechnical and Geoenvironmental Engineering* **132(5)**:591-602.
Ferreira, P. & Bica, A. (2006) Problems in identifying the effects of structure and critical state in a soil with a transitional behavior. *Geotechnique* **56(7)**:445-454.
Nocilla, A., Coop, M. & Colleselli, F. (2006) The mechanics of an Italian silt: an example of 'transitional'behavior. *Geotechnique* **56(4)**:261-271.
Ogi, H., Ohmori, T., Nakamura, N. & Hirao, M. (2006) Elastic, anelastic, and piezoelectric coefficients of α-quartz determined by resonance ultrasound spectroscopy. *Journal of Applied Physics* **100(5)**:053511.
Al-Rousan, T., Masad, E., Tutumluer, E. & Pan, T. (2007) Evaluation of image analysis techniques for quantifying aggregate shape characteristics. *Construction and Building Materials* **21(5)**:978-990.
Barton, N. R. & Wenk, H.-R. (2007) Dauphiné twinning in polycrystalline quartz. *Modelling and Simulation in Materials Science and Engineering* **15(3)**:369.
Callister, W. D. (2007) *Materials science and engineering-an introduction.* John wiley & sons.
Guo, P. & Su, X. (2007) Shear strength, interparticle locking, and dilatancy of granular materials. *Canadian Geotechnical Journal* **44(5)**:579-591.

Nikitin, A., Markova, G., Balagurov, A., Vasin, R. & Alekseeva, O. (2007) Investigation of the structure and properties of quartz in the α-β transition range by neutron diffraction and mechanical spectroscopy. *Crystallography Reports* **52(3)**:428-435.

Pena, A., Garcia-Rojo, R. & Herrmann, H. J. (2007) Influence of particle shape on sheared dense granular media. *Granular Matter* **9(3-4)**:279-291.

Tordesillas, A. (2007) Force chain buckling, unjamming transitions and shear banding in dense granular assemblies. *Philosophical Magazine* **87(32)**:4987-5016.

Bolton, M., Nakata, Y. & Cheng, Y. (2008) Micro-and macro-mechanical behavior of DEM crushable materials. *Geotechnique* **58(6)**:471-480.

Cheung, G. & O'sullivan, C. (2008) Effective simulation of flexible lateral boundaries in two-and three-dimensional DEM simulations. *Particuology* **6(6)**:483-500.

Cox, M. R. & Budhu, M. (2008) A practical approach to grain shape quantification. *Engineering Geology* **96(1–2)**:1-16.

Belheine, N., Plassiard, J.-P., Donzé, F.-V., Darve, F. & Seridi, A. (2009) Numerical simulation of drained triaxial test using 3D discrete element modeling. *Computers and Geotechnics* **36(1)**:320-331.

O'sullivan, C. & Cui, L. (2009) Micromechanics of granular material response during load reversals: combined DEM and experimental study. *Powder Technology* **193(3)**:289-302.

Quintana-Alonso, I. & Fleck, N. A. (2009) Fracture of brittle lattice materials: A review. In *Major accomplishments in composite materials and sandwich structures*.) Springer, pp. 799-816.

Salot, C., Gotteland, P. & Villard, P. (2009) Influence of relative density on granular materials behavior: DEM simulations of triaxial tests. *Granular Matter* **11(4)**:221-236.

Ferellec, J.-F. & Mcdowell, G. R. (2010) A method to model realistic particle shape and inertia in DEM. *Granular Matter* **12(5)**:459-467.

Hasan, A. & Alshibli, K. A. (2010) Discrete element modeling of strength properties of Johnson Space Center (JSC-1A) lunar regolith simulant. *Journal of Aerospace Engineering* **23(3)**:157-165.

Lu, Y. & Frost, D. (2010) Three-dimensional DEM modeling of triaxial compression of sands. In *Soil Behavior and Geo-Micromechanics*.), pp. 220-226.

Roters, F., Eisenlohr, P., Hantcherli, L., Tjahjanto, D. D., Bieler, T. R. & Raabe, D. (2010) Overview of constitutive laws, kinematics, homogenization and multiscale methods in crystal plasticity finite-element modeling: Theory, experiments, applications. *Acta Materialia* **58(4)**:1152-1211.

Yan, B., Regueiro, R. A. & Sture, S. (2010) Three-dimensional ellipsoidal discrete element modeling of granular materials and its coupling with finite element facets. *Engineering Computations* **27(4)**:519-550.

Yimsiri, S. & Soga, K. (2010) DEM analysis of soil fabric effects on behavior of sand. In *Geotechnique*.), vol. 60, pp. 483-495.

Altuhafi, F. & Coop, M. R. (2011) Changes to particle characteristics associated with the compression of sands. *Geotechnique* **61(6)**:459-471.
Fu, P. & Dafalias, Y. F. (2011) Fabric evolution within shear bands of granular materials and its relation to critical state theory. *International Journal for Numerical and Analytical Methods in Geomechanics* **35(18)**:1918-1948.
Jiang, M., Yan, H., Zhu, H. & Utili, S. (2011) Modeling shear behavior and strain localization in cemented sands by two-dimensional distinct element method analyses. *Computers and Geotechnics* **38(1)**:14-29.
Li, X. & Dafalias, Y. (2011) Anisotropic Critical State Theory: Role of Fabric. *Journal of Engineering Mechanics* **138(3)**:263-275.
Yang, G., Yu, T. & Hanlong, L. (2011) Numerical simulation of undrained triaxial test using 3D discrete element modeling. In *Instrumentation, Testing, and Modeling of Soil and Rock Behavior*.), pp. 99-106.
Andrade, J. E. & Avila, C. F. (2012) Granular element method (GEM): linking inter-particle forces with macroscopic loading. *Granular Matter* **14(1)**:51-61.
Bessa, I. S., Branco, V. T. C. & Soares, J. B. (2012) Evaluation of different digital image processing software for aggregates and hot mix asphalt characterizations. *Construction and Building Materials* **37**:370-378.
Cavarretta, I. & O'sullivan, C. (2012) The mechanics of rigid irregular particles subject to uniaxial compression. *Geotechnique* **62(8)**:681-692.
Cil, M. & Alshibli, K. (2012) 3D assessment of fracture of sand particles using discrete element method. *Géotechnique Lett* **2(3)**:161-166.
Clark, A. H., Kondic, L. & Behringer, R. P. (2012) Particle scale dynamics in granular impact. *Physical Review Letters* **109(23)**:238302.
Fonseca, J., O'sullivan, C., Coop, M. R. & Lee, P. D. (2012) Non-invasive characterization of particle morphology of natural sands. *Soils Found.* **52**:712.
Gao, R., Du, X., Zeng, Y., Li, Y. & Yan, J. (2012) A new method to simulate irregular particles by discrete element method. *Journal of Rock Mechanics and Geotechnical Engineering* **4(3)**:276-281.
Shin, H. & Santamarina, J. (2012) Role of particle angularity on the mechanical behavior of granular mixtures. *Journal of Geotechnical and Geoenvironmental Engineering* **139(2)**:353-355.
Shipton, B. & Coop, M. R. (2012) On the compression behavior of reconstituted soils. *Soils and Foundations* **52(4)**:668-681.
Sun, W., Wang, L. & Tutumluer, E. (2012) Image analysis technique for aggregate morphology analysis with two-dimensional Fourier transform method. *Transportation Research Record: Journal of the Transportation Research Board***(2267)**:3-13.
Alshibli, K., Cil, M., Kenesei, P. & Lienert, U. (2013) Strain tensor determination of compressed individual silica sand particles using high-energy synchrotron diffraction. *Granular Matter*:1-14.

Azéma, E., Radjai, F., Saint-Cyr, B., Delenne, J.-Y. & Sornay, P. (2013) Rheology of three-dimensional packings of aggregates: Microstructure and effects of nonconvexity. *Physical Review E* **87(5)**:052205.
Garboczi, E. J. & Bullard, J. W. (2013) Contact function, uniform-thickness shell volume, and convexity measure for 3D star-shaped random particles. *Powder Technology* **237**:191-201.
Garbout, A., Munkholm, L. J. & Hansen, S. B. (2013) Temporal dynamics for soil aggregates determined using X-ray CT scanning. *Geoderma* **204**:15-22.
Komba, J. J., Anochie-Boateng, J. K. & Steyn, W. V. (2013) Analytical and Laser Scanning Techniques to Determine Shape Properties of Aggregates. *Transportation Research Record* **(2335)**:60-71.
Rocchi, I. & Coop, M. (2013) Experimental accuracy of the initial specific volume. *Geotechnical Testing Journal* **37(1)**:169-175.
Alshibli, K., Druckrey, A., Al-Raoush, R., Weiskittel, T. & Lavrik, N. (2014) Quantifying Morphology of Sands Using 3D Imaging. *Journal of Materials in Civil Engineering*:04014275.
Cil, M. B., Alshibli, K., Kenesei, P. & Lienert, U. (2014) Combined high-energy synchrotron X-ray diffraction and computed tomography to characterize constitutive behavior of silica sand. *Nuclear Instruments and Methods in Physics Research Section B: Beam Interactions with Materials and Atoms* **324**:11-16.
Cil, M. B. & Alshibli, K. A. (2014a) 3D analysis of kinematic behavior of granular materials in triaxial testing using DEM with flexible membrane boundary. *Acta Geotechnica* **9(2)**:287-298.
Cil, M. B. & Alshibli, K. A. (2014b) 3D evolution of sand fracture under 1D compression. *Geotechnique* **64**:351.
De Bono, J. P. & Mcdowell, G. R. (2014) DEM of triaxial tests on crushable sand. *Granular Matter* **16(4)**:551-562.
Gao, Z., Zhao, J., Li, X. S. & Dafalias, Y. F. (2014) A critical state sand plasticity model accounting for fabric evolution. *International Journal for Numerical and Analytical Methods in Geomechanics* **38(4)**:370-390.
Guo, N. & Zhao, J. (2014) A coupled FEM/DEM approach for hierarchical multiscale modelling of granular media. *International Journal for Numerical Methods in Engineering* **99(11)**:789-818.
Hoek, E. & Martin, C. (2014) Fracture initiation and propagation in intact rock–a review. *Journal of Rock Mechanics and Geotechnical Engineering* **6(4)**:287-300.
Hurley, R., Marteau, E., Ravichandran, G. & Andrade, J. E. (2014) Extracting inter-particle forces in opaque granular materials: beyond photoelasticity. *Journal of the Mechanics and Physics of Solids* **63**:154-166.
Shipton, B. & Coop, M. R. (2014) Transitional behavior in sands with plastic and non-plastic fines. *The japanese geotechnical society*.
Williams, J. R., Hocking, G. & Mustoe, G. G. (2014) The theoretical basis of the discrete element method.

Brodu, N., Dijksman, J. A. & Behringer, R. P. (2015) Spanning the scales of granular materials through microscopic force imaging. *Nature communications* **6**.

Cil, M. B. & Alshibli, K. A. (2015) Modeling the influence of particle morphology on the fracture behavior of silica sand using a 3D discrete element method. *Comptes Rendus Mécanique* **343(2)**:133-142.

Cole, D. M. (2015) Laboratory observations of frictional sliding of individual contacts in geologic materials. *Granular Matter* **17(1)**:95-110.

Coop, M. (2015) Limitations of a Critical State framework applied to the behavior of natural and "transitional" soils. In *Proceedings of 6th International Symposium on Deformation Characteristics of Geomaterials, IS-Buenos Aires*.), pp. 115-155.

Druckrey, A. M. & Alshibli, K. A. (2015) 3D finite element modeling of sand particle fracture based on in situ X-Ray synchrotron imaging. *International Journal for Numerical and Analytical Methods in Geomechanics*.

Eder, S. D., Fladischer, K., Yeandel, S., Lelarge, A., Parker, S. C., Søndergård, E. & Holst, B. (2015) A giant reconstruction of α-quartz (0001) interpreted as three domains of nano dauphine twins. *Scientific reports* **5**:14545.

Hall, S. & Wright, J. (2015a) Three-dimensional experimental granular mechanics. *Géotechnique Letters* **5(4)**:236-242.

Hall, S. A. & Wright, J. (2015b) Three-dimensional experimental granular mechanics. *Geotech. Lett.* **5**:236.

Marigo, M. & Stitt, E. H. (2015) Discrete element method (DEM) for industrial applications: Comments on calibration and validation for the modelling of cylindrical pellets. *KONA Powder and Particle Journal* **32**:236-252.

Otsubo, M., O'sullivan, C., Sim, W. & Ibraim, E. (2015) Quantitative assessment of the influence of surface roughness on soil stiffness.

Vangla, P. & Latha, G. M. (2015) Influence of particle size on the friction and interfacial shear strength of sands of similar morphology. *International Journal of Geosynthetics and Ground Engineering* **1(1)**:6.

Xiao, Y., Liu, H., Ding, X., Chen, Y., Jiang, J. & Zhang, W. (2015) Influence of particle breakage on critical state line of rockfill material. *International Journal of Geomechanics* **16(1)**:04015031.

Yang, J. & Luo, X. (2015) Exploring the relationship between critical state and particle shape for granular materials. *Journal of the Mechanics and Physics of Solids* **84**:196-213.

Zhang, B., Herbold, E. B., Homel, M. & Regueiro, R. A. (2015) *DEM Particle Fracture Model*.

Zhao, B., Wang, J., Coop, M., Viggiani, G. & Jiang, M. (2015) An investigation of single sand particle fracture using X-ray micro-tomography. *Geotechnique* **65(8)**:625-641.

Zuo, L. & Baudet, B. A. (2015) Determination of the transitional fines content of sand-non plastic fines mixtures. *Soils and Foundations* **55(1)**:213-219.

Alshibli, K. A., Jarrar, M. F., Druckrey, A. M. & Al-Raoush, R. I. (2016) Influence of Particle Morphology on 3D Kinematic Behavior and Strain Localization of Sheared Sand. *Journal of Geotechnical and Geoenvironmental Engineering* **143(2)**:04016097.

Cole, D. M. & Hopkins, M. A. (2016) The contact properties of naturally occurring geologic materials: experimental observations. *Granular Matter* **18(3)**:62.

Dafalias, Y. F. (2016) Must critical state theory be revisited to include fabric effects? *Acta Geotechnica* **11(3)**:479-491.

Druckrey, A. M. & Alshibli, K. A. (2016) 3D finite element modeling of sand particle fracture based on in situ X-ray synchrotron imaging. *Int. J. Numer. Anal. Methods Geomech.* **40**:105.

Hurley, R., Hall, S., Andrade, J. & Wright, J. (2016) Quantifying interparticle forces and heterogeneity in 3D granular materials. *Physical Review Letters* **117(9)**:098005.

Kawamoto, R., Andò, E., Viggiani, G. & Andrade, J. E. (2016) Level set discrete element method for three-dimensional computations with triaxial case study. *Journal of the Mechanics and Physics of Solids* **91**:1-13.

Reynolds, S. J., Johnson, J. K., Morin, P. J. & Carter, C. (2016) *Exploring geology.* McGraw-Hill Education.

Theocharis, A. I., Vairaktaris, E., Dafalias, Y. F. & Papadimitriou, A. G. (2016) Proof of Incompleteness of Critical State Theory in Granular Mechanics and Its Remedy. *Journal of Engineering Mechanics*:04016117.

Vangla, P. & Gali, M. L. (2016) Effect of particle size of sand and surface asperities of reinforcement on their interface shear behavior. *Geotextiles and Geomembranes* **44(3)**:254-268.

Wang, W. & Coop, M. (2016) An investigation of breakage behavior of single sand particles using a high-speed microscope camera. *Geotechnique* **66(12)**:984-998.

Xiao, Y., Coop, M., Liu, H., Liu, H. & Jiang, J. (2016) Transitional behaviors in well-graded coarse granular soils. *Journal of Geotechnical and Geoenvironmental Engineering* **142(12)**:06016018.

Zhang, L., Nguyen, N. G. H., Lambert, S., Nicot, F., Prunier, F. & Djeran-Maigre, I. (2016) The role of force chains in granular materials: from statics to dynamics. *European Journal of Environmental and Civil Engineering*:1-22.

Alshibli, K. & Cil, M. (2017) Influence of Particle Morphology on the Friction and Dilatancy of Sand. *Journal of Geotechnical and Geoenvironmental Engineering*.

Andò, E., Salvatore, E., Desrues, J., Charrier, P., Toni, J.-B., Modoni, G. & Viggiani, G. (2017) Strain Localisation in Sand in Cycles of Triaxial Compression and Extension: Continuum and Grain-Scale Analysis. In *International Workshop on Bifurcation and Degradation in Geomaterials*.) Springer, pp. 489-497.

Cil, M. B., Alshibli, K. A. & Kenesei, P. (2017) 3D Experimental Measurement of Lattice Strain and Fracture Behavior of Sand Particles Using Synchrotron

X-Ray Diffraction and Tomography. *Journal of Geotechnical and Geoenvironmental Engineering* **143(9)**.
Druckrey, A., Alshibli, K. & Al-Raoush, R. (2017) Discrete particle translation gradient concept to expose strain localisation in sheared granular materials using 3D experimental kinematic measurements. *Geotechnique*:1-9.
Fu, R., Hu, X. & Zhou, B. (2017) Discrete element modeling of crushable sands considering realistic particle shape effect. *Computers and Geotechnics* **91**:179-191.
Hurley, R., Hall, S. & Wright, J. (2017) Multi-scale mechanics of granular solids from grain-resolved X-ray measurements. *Proceedings of the Royal Society A: Mathematical, Physical and Engineering Sciences* **473(2207)**:20170491.
Kandasami, R. K. & Murthy, T. G. (2017) Manifestation of particle morphology on the mechanical behavior of granular ensembles. *Granular Matter* **19(2)**:21.
Nardelli, V., Coop, M., Andrade, J. & Paccagnella, F. (2017) An experimental investigation of the micromechanics of Eglin sand. *Powder Technology* **312**:166-174.
Salvatore, E., Modoni, G., Andò, E., Albano, M. & Viggiani, G. (2017) Determination of the critical state of granular materials with triaxial tests. *Soils and Foundations* **57(5)**:733-744.
Wang, R., Fu, P., Zhang, J.-M. & Dafalias, Y. F. (2017) Evolution of Various Fabric Tensors for Granular Media toward the Critical State. *Journal of Engineering Mechanics* **143(10)**:04017117.
Cady, W. G. (2018) *Piezoelectricity: Volume Two.* Courier Dover Publications.
Desrues, J., Andò, E., Mevoli, F. A., Debove, L. & Viggiani, G. (2018) How does strain localise in standard triaxial tests on sand: Revisiting the mechanism 20 years on. *Mechanics Research Communications* **92**:142-146.
Hurley, R. C., Herbold, E. B. & Pagan, D. C. (2018) Characterization of the crystal structure, kinematics, stresses and rotations in angular granular quartz during compaction. *Journal of Applied Crystallography* **51(4)**.
Kawamoto, R., Andò, E., Viggiani, G. & Andrade, J. E. (2018) All you need is shape: Predicting shear banding in sand with LS-DEM. *Journal of the Mechanics and Physics of Solids* **111**:375-392.
Li, H. & Mcdowell, G. R. (2018) Discrete element modelling of under sleeper pads using a box test. *Granular Matter* **20(2)**:26.
Nardelli, V. & Coop, M. R. (2018) The experimental contact behavior of natural sands: normal and tangential loading. *Geotechnique*:1-15.
Sandeep, C., He, H. & Senetakis, K. (2018) An experimental micromechanical study of sand grain contacts behavior from different geological environments. *Engineering Geology* **246**:176-186.
Todisco, M., Coop, M. & Pereira, J.-M. (2018) Fabric characterisation in transitional soils. *Granular Matter* **20(2)**:20.
Yan, B. & Regueiro, R. (2018a) Large-scale dynamic and static simulations of complex-shaped granular materials using parallel three-dimensional

discrete element method (DEM) on DoD supercomputers. *Engineering Computations* **35(2)**:1049-1084.

Yan, B. & Regueiro, R. A. (2018b) Superlinear speedup phenomenon in parallel 3D Discrete Element Method (DEM) simulations of complex-shaped particles. *Parallel Computing* **75**:61-87.

Zhang, B., Regueiro, R., Druckrey, A. & Alshibli, K. (2018) Construction of poly-ellipsoidal grain shapes from SMT imaging on sand, and the development of a new DEM contact detection algorithm. *Engineering Computations* **35(2)**:733-771.

Amirrahmat, S., Druckrey, A., Alshibli, K. & Al-Raoush, R. (2019) Micro shear bands: Precursor for strain localization in sheared granular materials. *Journal of Geotechnical and Geoenvironmental Engineering* **145(2)**:04018104.

Petalas, A. L., Dafalias, Y. F. & Papadimitriou, A. G. (2019) SANISAND-FN: An evolving fabric-based sand model accounting for stress principal axes rotation. *International Journal for Numerical and Analytical Methods in Geomechanics* **43(1)**:97-123.

Appendix

Appendix A: Figures

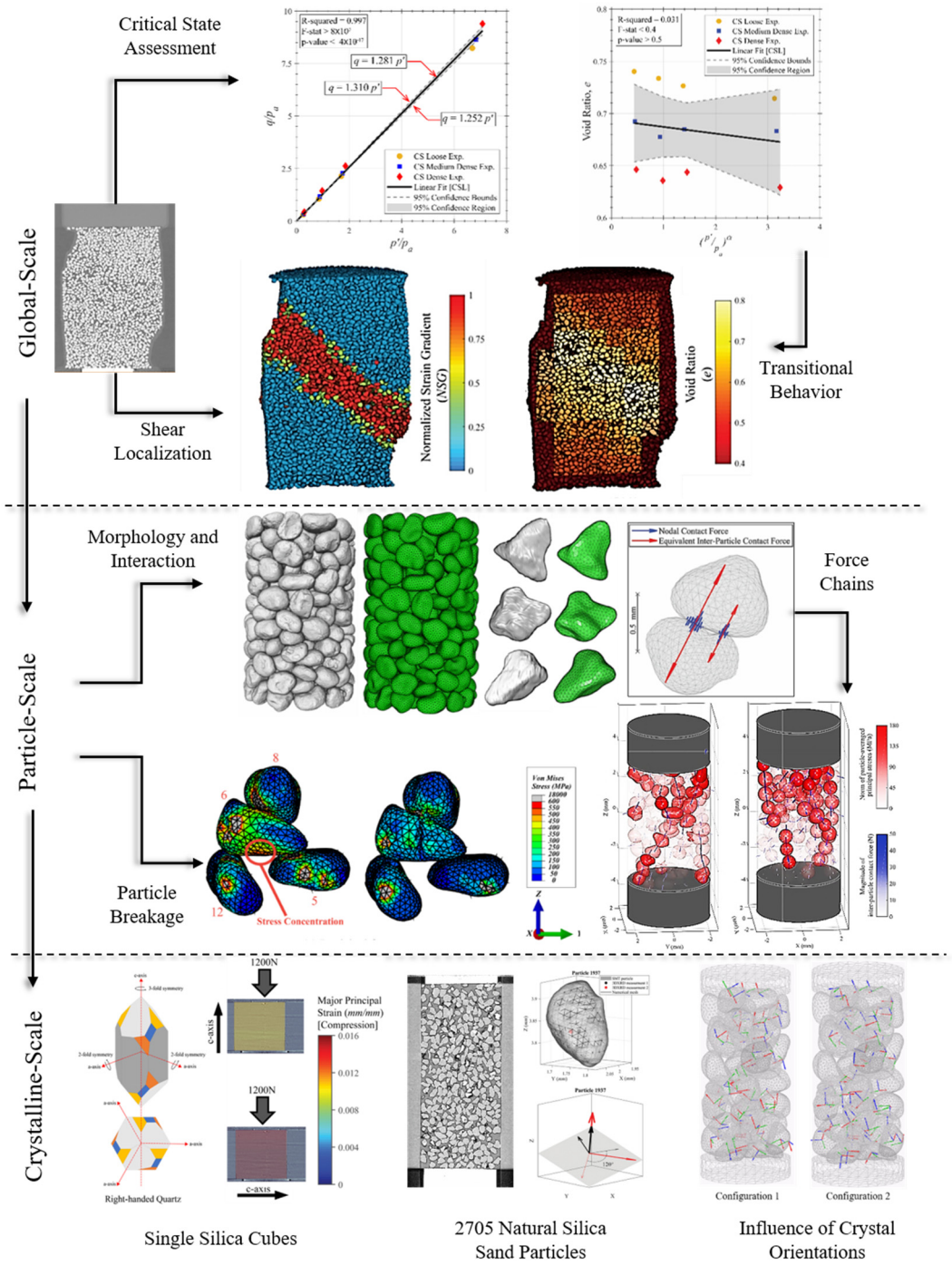


Figure 1-1. Summary of dissertation objectives

CHAPTER TWO

DISCREPANCY IN THE CRITICAL STATE VOID RATIO OF POORLY-GRADED SAND DUE TO SHEAR STRAIN LOCALIZATION

A version of this chapter was published as Imseeh, W. H., Alshibli, K. A. & Al-Raoush R. I. (2020) “Discrepancy in the Critical State Void Ratio of Poorly-Graded Sand due to Shear Strain Localization”. *ASCE, Journal of Geotechnical and Geoenvironmental Engineering*.
https://doi.org/10.1061/(ASCE)GT.1943-5606.0002280

Abstracts: The critical state (CS) concept is a theoretical framework that models the constitutive behavior of soils, including sand and other granular materials. It supports the notion of a unique post-failure state, where the soil ultimately experiences continuous shearing with no change in the plastic volumetric strain. However, the published literature has frequently noted the non-convergence of sand specimens with different initial densities to a unique CS in the compression plane due to many factors such as specimen fabric, particle morphology, breakage, and grain size distribution. This chapter examines the CS for poorly-graded (uniform) glass beads and three different types of silica sands using 50 conventional triaxial compression (CTC) experiments, 12 oedometer tests, and in-situ synchrotron micro-computed tomography (SMT) scans for 10 CTC experiments. Results of the 50 CTC experiments exposed a diffused CS zone in the compression plane, which was further examined using the in-situ SMT scans. A thorough 3D image analysis of the SMT scans has accurately quantified the evolution of the local void ratio (e_{local}) versus axial compression within zones of intensive shearing toward the center of the specimen. The evolution of the void ratio was also measured using the entire volume of the specimen (e_{global}). At the CS, the ratio $\frac{e_{local}}{e_{global}}$ was assessed to be ~ 1.25 when a single shear band developed within the scanned specimens and ~1.1-1.15 for specimens that failed via external bulging that was internally manifested by the development of multiple shear bands. This finding suggests that the CS zone in the compression plane can be attributed to the common wrong consideration of e_{global} evolution in lieu of e_{local} within the developing shear bands. Furthermore, the lack of shear band development in uniaxial compression has made the results of the oedometer test reliable in quantifying the CS parameters in the compression plane.

Key Words: Sand, critical state, shear bands, void ratio, micro-computed tomography, conventional triaxial compression, oedometer tests.

Introduction

In engineering practice, the constitutive behavior of sand has been traditionally modeled using global-scale measurements of stress and strain at the boundaries of laboratory-size specimens. The development of the stress-dilatancy relationship (Roscoe et al., 1958) offered a major enhancement to the Mohr-Coulomb criterion and inspired the development of the critical state (CS) theory in soil mechanics. The CS theory was originally proposed for clays by Schofield and Wroth (1968), who postulated a material failure surface known as yield locus, and a unique post-failure state known as the CS. The unique post-failure CS is attributed to the conditions of ultimate shear distortion without changes in the volume or effective stress, and theoretically represented by the Critical State Line (CSL) tracing the top of yield locus in $p' - q - e$ space where p', q, and e are the mean effective principal stress, deviatoric stress, and void ratio, respectively. The CSL has conventionally been established in the stress plane $(p' - q)$ and compression plane $(p' - e)$ separately, since this procedure enhances the understanding of general triaxial stress and compression paths when superimposed in planes versus 3D space representation (Poorooshasb et al., 1966, Wood, 1990). Many 1D compression experiments on sand have confirmed a similar response to clayey soil in which the CSL and normal compression lines (NCLs) are parallel when plotted in the compression plane (Been and Jefferies, 1985, Coop, 1990, McDowell and Bolton, 1998a) with a certain allowance for the influence of particle breakage (Coop and Lee, 1993). However, the convergence of sand specimens to a unique CSL in the compression plane has been controversial in the current literature. To mention a few studies, Martins et al. (2001) examined the compression behavior of residual clayey sand specimens using oedometer tests, and the location of NCLs in the compression plane was found to be a function of the specimen's initial e. Ferreira and Bica (2006) assessed the CS for sand-kaolin mixtures using triaxial compression experiments, and reported a family of parallel critical state lines (CSLs) in the compression plane depending on the specimen's initial density state.

The non-convergence of compression paths (NCLs and CSLs) has been acknowledged when describing the constitutive behavior of sand, and published literature has introduced the term "transitional" to describe this mode of behavior (Nocilla et al., 2006). Several studies have demonstrated that the transitional behavior of sand is caused by particle breakage (Altuhafi and Coop, 2011, Shipton and Coop, 2012, Xiao et al., 2015), inherent effects of the specimen's initial density state (Shipton and Coop, 2012, Coop, 2015, Xiao et al., 2016, Xu and Coop, 2017), the complex morphology of natural sand particles (Santamarina and Cho, 2004, Yang and Luo, 2015, Alshibli and Cil, 2017, Kandasami and Murthy, 2017), influences of grain size distribution (Altuhafi et al., 2010, Altuhafi and Coop, 2011), variation in the mineralogy of sand-fine mixtures (Shipton and Coop, 2015, Ponzoni et al., 2017), and the percentage of fine content in sand specimens (Zuo and Baudet, 2015, Kwa and Airey, 2016). The transitional behavior of sand has also been attributed to the strong forms of microscale fabric that are difficult to

break even at high applied strains. For instance, Todisco et al. (2018) used mercury intrusion porosimetry to investigate the evolution of pore structure within sand specimens subjected to conventional triaxial and uniaxial compression tests. Todisco et al. (2018) advocated for the complex evolution of pore void distribution, causing the transitional behavior of sand due to initial differences in the void structure that could not be erased during conventional testing. Although there are still active quests for integrating fabric evolution as an essential state parameter in the CS theory (Dafalias and Manzari, 2004, Fu and Dafalias, 2011, Gao et al., 2014, Theocharis et al., 2016, Imseeh et al., 2017, Wang et al., 2017, Petalas et al., 2019), the development of these constitutive models is still incomplete because laboratory sand specimens tested in the conventional biaxial (Finno and Rechenmacher, 2003) and triaxial (Alshibli and Cil, 2017) apparatuses fail to deliver a unique CSL in the compression plane.

Most of the studies reported in the literature relied on global change in the specimen's volume to measure the evolution of e toward the CS with limited research investigating the accuracy of conventional triaxial or biaxial testing procedures (Garga and Zhang, 1997, Jefferies and Been, 2000). Mooney et al. (1998) conducted a series of biaxial compression tests in quest for a unique CSL when locally assessed for the zone affected by a high shear distortion, which is also known as the shear band. Their tests were conducted using a special biaxial apparatus (Harris et al., 1995) that provided a local estimate of the volumetric strain within the shear band via several displacement sensors attached to the specimen surface at multiple vertical levels. The apparatus side walls and loading platens were also lubricated to minimize friction, and the bottom loading platen was connected to a free-sliding base that allowed for the onset and growth of the shear band by minimizing the influence of boundary constraints. Furthermore, one of the apparatus side walls was made of clear Plexiglas, which permitted monitoring shear strain localization from the specimen side using digital photographs. Mooney et al. (1998) reported a significantly higher local e when measured near the shear band region compared to e measured using the global volume change. Furthermore, they advocated for the notion of a CSL, but the CSL in the compression plane was found to depend on the initial e and subsequent consolidation history of the specimens (Finno and Rechenmacher, 2003). Localization of e at higher values was also detected by optical microscopy near the center of sand specimens loaded in drained triaxial (Frost and Jang, 2000) and biaxial (Evans and Frost, 2010) compression using epoxy resin impregnation and 2D section microscopy. Numerous DEM studies have also demonstrated the localization of e at higher values within the shear band that develops within specimens composed of 2D discs (Iwashita and Oda, 1998, Iwashita and Oda, 2000, Jiang et al., 2011, Gu et al., 2014) and 3D clumped spheres (Lu and Frost, 2010) loaded in biaxial compression.

In-Situ (i.e., in-position scanning during the experiment) x-ray CT has recently offered a powerful non-destructive technique that imaged through the 3D internal structure (e.g., particles and voids) of sand specimens, and confirmed the

localization of e at high values within the developed shear band in sand specimens loaded under biaxial compression (Desrues and Viggiani, 2004, Alshibli and Hasan, 2008). However, sand specimens tested in biaxial compression exhibit much less volumetric strain at the CS in comparison to specimens loaded in triaxial compression (Alshibli et al., 2003). Tagliaferri et al. (2011) collected in-situ x-ray scans for conventional triaxial compression (CTC) experiments on two sand specimens: bio-cemented and non-cemented. Images of the non-cemented specimen reaffirmed the localization of e at high values within the shear band that gradually developed with axial compression. In recent advances, sets of in-situ x-ray CT scans with excellent image quality were acquired for sand specimens subjected to CTC experiments (Alshibli et al., 2016, Andò et al., 2017). Compared to biaxial compression, the scans for CTC specimens exposed rather complex internal shearing patterns named micro shear bands (MSBs) that developed during the hardening stage of the experiments (Amirrahmat et al., 2019). Furthermore, in-situ x-ray CT scans for conventional triaxial extension and compression experiments on sand specimens in Salvatore et al. (2017) revealed a unique trace of the CSL in the compression plane when e measured from the scans was limited to the zones affected by the largest distortion (shear bands).

The main objective of this chapter is to accurately establish the CSL and yield locus for four different types of poorly-graded granular materials based on conventional laboratory experiments. The chapter sheds light on a discrepancy in measuring the evolution of e toward the CS using the conventional triaxial apparatus due to the development of internal shear bands within the specimens.

CTC Experiments on Laboratory-Size Specimens

Experiments

This chapter uses the results of 50 CTC experiments that were reported in Alshibli and Cil (2017) on specimens composed of spherical glass beads (labeled as GB) and three types of silica sands known as F-35 Ottawa sand (labeled as F35), #1 Dry Glass sand (labeled as DG), and GS#40 Columbia Grout sand (labeled as GS40). Table 2-1 summarizes the properties of tested materials. The glass beads and three silica sands represent poorly-graded (uniform) granular materials with grain-size between US sieve #40 (0.420) and #50 (0.297 mm), and have different particle morphologies ranging from rounded to angular classes. Poorly-graded granular materials were selected in this study because the uniform grain sizes limit the experimental parameters and significantly increase the quality of the x-ray CT image as well as the efficiency of image processing procedures (e.g., algorithms for particle segmentation and tracking). A detailed description of particle morphology for each material can be found in Alshibli et al. (2014b), including scanning electron microscope (SEM) images.

The CTC experiments were conducted on dry cylindrical specimens measuring 70 mm in diameter $\times$ 140 mm in height under drained conditions. The specimens were tested at constant confining pressures (σ_3) of 15, 25, 50, 100, and 400 kPa

as well as different initial relative density (D_r) states: loose ($D_r < 30\%$), medium dense ($30\% \leq D_r \leq 70\%$), and dense ($D_r > 70\%$) (see Table 1-2). Alshibli and Cil (2017) presented a detailed description of the specimen preparation and testing procedures. Briefly, dry sand was deposited using air-pluviation to prepare the cylindrical specimens with different initial D_r. Water was used to apply a constant confining pressure (σ_3) via a standard triaxial cell, then specimens were sheared under axial compression at a constant displacement rate of 0.5 mm/min. The CTC apparatus was connected to a data acquisition system that recorded accurate measurements of σ_3, bulk volume change (δv), axial stress (σ_1), and axial strain (ε_1). δv was measured by continuously recording the change in the volume of water pumped in/purged out of the confining chamber. Figures 1-1 and 1-2 display the evolution of ${}^{q}/_{p'}$ and e versus ε_1 for the experiments; respectively, where:

$$deviator\ stress\ (q) = \sigma_1' - \sigma_3' \tag{2-1}$$

$$effective\ mean\ stress\ \ (p') = \frac{\sigma_1' + 2\sigma_3'}{3} \tag{2-2}$$

$$e = \frac{(V_0 - \delta v)\ - (\frac{w_s}{\gamma_w G_s})}{(\frac{w_s}{\gamma_w G_s})} \tag{2-3}$$

where the effective stresses σ_1' and σ_3' are equal to the total stresses σ_1 and σ_3 since dry specimens were tested in drained conditions (no pore water pressure), V_0 is the initial volume of the specimen calculated using caliper measurements of the specimen's initial diameter and height, w_S is the weight of solids, γ_w is the unit weight of water, and G_s is the specific gravity of solids (Table 2-1). Referring to Figures 1-1d and 1-2d, one can notice that the curves describing the glass bead experiments exhibited an oscillatory behavior caused by slip-stick that occurs between particles as they roll/slide against each other. This sudden slip-stick behavior is attributed to the high-uniformity in the roundness and sphericity of the glass beads (manufactured material) as well as their smooth surface texture. Alshibli and Roussel (2006) presented a detailed experimental study of the slip-stick behavior in specimens composed of glass beads.

Critical State (CS) Assessment

Results of the 50 CTC experiments were examined to establish the CSL for the tested materials. The CS attainment is mathematically described by the conditions at which (Wood, 1990):

$$\frac{\partial p'}{\partial \varepsilon_q} = \frac{\partial q}{\partial \varepsilon_q} = \frac{\partial e}{\partial \varepsilon_q} = 0\ ,\ \ \varepsilon_q = \frac{2(\varepsilon_1 - \varepsilon_3)}{3} \tag{2-4}$$

where ε_q and ε_3 are the deviatoric and radial strains for CTC conditions, respectively. $\partial \varepsilon_q$ in Equation 1-4. degenerates to $\partial \varepsilon_1$ since $\varepsilon_1 = -2\varepsilon_3$ for the specific condition of ultimate shear distortion at a constant volume, which is postulated by the CS theory. Therefore, tested specimens are assumed to reach the CS when curves in Figures 1-1 and 1-2 relatively approach a constant slope

($\sim\varepsilon_1$ >15%). For each set of curves/material in Figures 1-1 and 1-2, constant p', q, and e at the CS were determined and plotted in the stress and compression planes as depicted in Figures 1-3 and 1-4, respectively. In the stress plane (Figure 2-3), the CSL is modeled using the CS parameter M as:

$$q = Mp' \tag{2-5}$$

In the compression plane (Figure 2-4), several analytical models were proposed in the literature to fit a linear yield locus including the CSL ($e_\lambda = \Gamma$ for the CSL):

$$e = e_\lambda - \lambda \, ln \, p' \rightarrow \quad \text{Cam Clay Model (Schofield and Wroth, 1968)} \tag{2-6}$$

$$e = e_\lambda - \lambda \left(\frac{p'}{p_a}\right)^{\alpha} \rightarrow \quad \text{Linear Model (Li and Wang, 1998)} \tag{2-7}$$

where p_a is the atmospheric pressure, and $\alpha = 0.6$ is a model fit parameter. This chapter adopts Li and Wang (1998) model since it has been widely recommended to enhance the linear representation of the CSL in the compression plane for granular materials. Furthermore, the normalization of p' with respect to p_a in Equation (2-7 makes the intercept parameter e_λ independent of the unit chosen for the measurement of stress, unlike the case for the Cam clay model (Equation (2-6).

Discussion

For each tested material, the CTC results showed a distinctive CSL in the stress plane as depicted in Figure 2-3. Still, a trend can be noticed in Figure 2-3 in which dense specimens tend to have a slightly higher slope (M). This trend was also reported by Alshibli and Cil (2017) and correlated well to the applied σ_3 as well as specimen's initial D_r. Overall, the linear regression models in Figure 2-3 show significant statistical correlations: R-squared~1, p-value < 0.05 for the F-statistics (the regression model is significant), and narrow 95% confidence limits for the estimate of M. However, the CSL appeared as a diffused stress-dependent zone in the compression plane (Figure 2-4 and Table 2-3) rather than a linear representation (low R-squared values, p-value>0.05 for the F-statistics, wide 95% confidence interval for the estimates Γ and λ. Extensive published literature has reported a similar pattern of response in the compression plane in which sand specimens with different initial e do not approach a unique CSL when tested under general triaxial compression paths. For instance, Marschi et al. (1972) conducted drained CTC experiments on Pyramid Dam rockfill granular material and reported that the CTC paths in the compression plane of dense versus loose specimens did not approach the same CSL. Wood (1990) examined results of constant p' triaxial compression experiments on Chattahoochee River sand (Vesic and Clough, 1968), and the results showed different e for initially dense versus loose specimens at the CS. Namely, Wood (1990) reported that dense specimens needed ~17% dilation by volume to attain the same e as the loose specimens at the CS, which is unlikely to occur due to testing difficulties (e.g., rigid loading endplates, rubber

membrane, etc.) hinder the ultimate dilation of the specimens. Although the testing difficulties were fairly alleviated by the special biaxial compression apparatus used by Mooney et al. (1998), they still failed to deliver a unique CSL in the compression plane. In fact, similar findings to Figure 2-4 were reported by Mooney et al. (1998) and Finno and Rechenmacher (2003) based on the results of biaxial compression experiments. In summary, they characterized the CS zone by multiple CSLs depending on the initial e of the specimen.

Visual observation of the specimen failure at the CS manifested different modes for the 50 CTC experiments depending on the applied σ_3 and the specimen's initial D_r (see Table 2-2). In summary, loose specimens exhibited slight bulging with no externally-observed shear bands, whereas medium dense and dense specimens failed via apparent single or multiple shear bands. Characterizing the failure mode of specimens by visual observations on their surfaces can be misleading as they are just an external manifestation of more complex internal shearing patterns that causes a non-uniform distribution of e within the sheared specimens. Therefore, the diffused CS zone in the compression plane can be attributed to the false reliance on the global volume change (δv) (Equation 1-3) to measure e at failure. The following section evaluates the latter hypothesis that would explain the formation of the CS zone in the compression plane using accurate measurements of e based on in-situ synchrotron micro-computed tomography (SMT) scans that were collected for a series of CTC experiments on the tested materials.

In-Situ SMT Scans for CTC Experiments

In-situ Scanning

Alshibli et al. (2016) collected sets of in-situ SMT scans for ten drained CTC experiments on dry specimens composed of the four granular materials studied in this chapter (Table 2-1). The CTC experiments were conducted using a special-fabricated triaxial compression apparatus, which was described in (Hasan and Alshibli, 2012, Druckrey and Alshibli, 2014) and had capabilities to test 10 mm (diameter) $\times$ 20 mm (height) specimens under drained CTC conditions similar to a conventional laboratory apparatus. The special apparatus was mounted on the SMT scanner stage of beamline station 13BMD, Advanced Photon Source (APS), Argonne National Laboratory (ANL), Illinois, USA. The specimens were confined at a constant σ_3 inside an air-presssurized chamber, then axial compression was applied by a stepper motor at a displacement-controlled loading rate of 0.2 mm/min. The axial compression was paused at certain loading steps, then the special apparatus was rotated over 180° at 0.2° rotational increments to acquire 900 radiographs using a monochromatic x-ray beam at an enegry of 33 keV. The radiographs were reconstructed into 3D images with an excellent spatial resolution ranging between 8.16 and 11.18 μm/pixel.

The set of scans collected by Alshibli et al. (2016) has an excellent resolution (see Table 2-4) and sharp grayscale contrast discerning the solid and air phases inside the specimens. The ability to image through the internal structure of sand

specimens at this high-quality have offered deep experimental insights into the evolution of 3D particle-scale characteristics in the course of CTC such as the fabric of the normal to contact vectors between particles (Imseeh et al., 2017) and localization of shear strain into MSBs (Amirrahmat et al., 2019). This chapter exploits the rich 3D experimental data in this set of scans, and processed the scans to accurately examine the evolution of e toward the CS within the CTC specimens in light of potential reasons for the CS zone in the compression plane (Figure 2-4). Table 2-4 summarizes the scans collected for the 10 experiments, which were tested on medium dense and dense specimens at $\sigma_3 = 15\ kPa$ and $400\ kPa$.

Image Processing and Data Analysis

The SMT scans provided excellent grayscale images with crisp boundaries that separate the solid and air phases within the specimens. The grayscale images were processed using AVIZO 9.7.0; a commercial computer software developed by Thermo Fisher Scientific for high-performance 3D image visualization and processing. An anisotropic filter module was executed on grayscale images to reduce image noise, then the solid and air phases were segmented using an interactive thresholding module. Voxels belonging to the solid and air phases were assigned a value of 1 and 0, respectively. A detailed description of image acquisition and processing modules can be found in Druckrey et al. (2016). Processed images were used to accurately measure the volume of solid and air phases within the scanned specimens at a μm level accuracy. For each processed image, e_{global} was calculated as the volume ratio between the air and solid phases within the entire specimen and the evolution of e_{global} versus ε_1 was plotted in Figure 2-2 for the scanned specimens to compare with the behviour of laboratory-size CTC experiments presented earlier in Section 2.

A cubical representative elementary volume (REV) was partitioned at the center of each processed image and e was calculated for the REV to investigate the evolution of e_{local} versus ε_1 within the scanned specimens. REV sizes were gradually increased from 0.05 to 5 mm at $0.1\ mm$ increments of the REV side length to examine the effect of the REV size on e_{local} measurement. The change in e_{local} value versus the REV size is displayed in Figure 2-5, which shows REV sizes >2 mm relatively having a constant e_{local} for the processed images. Therefore, the REV size of 2 mm was selected to generate local distribution fields of e within the scanned specimens as illustrated in Figures 1-6 through 1-8 at a central axial (Y-Z) section across the 3D images acquired for the F35_D_400_SMT, F35_D_15_SMT, and F35_MD_15_SMT experiments, respectively. Furthermore, e_{local} values corresponding to 2 mm REV sizes were averaged for each image to generate the evolution curves of e_{local} versus ε_1 in Figure 2-9 with error bars displaying the interquartile range (IQR) of e_{local} with respect to different REV sizes, whereas dashed curves represent the evolution of e_{global}.

Discussion

Figures 1-6 through 1-8 show a clear evidence that e within the scanned specimens was non-uniformly distributed, particularly when the specimens approached the CS ($\varepsilon_1 > 15\%$). Higher e values can be seen in Figures 1-6 through 1-8 at the center of the specimens, which is expected due to the effects of the rigid loading endplates and the flexible latex membrane surrounding the specimens. Moreover, the evolution of e_{local} versus ε_1 in Figure 2-9 is significantly different from the evolution of e_{global}, simillar to findings reported on sand specimens loaded in biaxial compression (Mooney et al., 1998, Finno and Rechenmacher, 2003). In quest to assess the uniqueness of the CSL in the compression plane using e_{local}, Figure 2-10 diplays boxplots of e_{local} for the scanned specimens at failure (last loading step) with the scattered points representing the variation in e_{local} versus the REV size (2-5 mm). Regarding the boxplot components, the green diamond symbol represents the mean; the red line marks the median; the blue box represents the IQR; and the black whisker bounds the data points within $1.5 \times$ IQR of the upper and lower quartiles. Interestingly, equal e_{local} was assessed at failure for the F35_MD_15_SMT and F35_D_15_SMT specimens in Figure 2-10a as well as the DG_MD_15_SMT and DG_D_15_SMT specimens in Figure 2-10b, which are the specimens with different initial e tested at the same σ_3. The equality in e_{local} for these two pair of specimens was assessed via the Wilcoxon Rank Sum (WRS) Test, which tested the null hypothesis (H_o) of equal median for the two specimens' data of e_{local}. In statistical hypothesis testing, the failure to reject H_o is assessed by the test probability value (p-value) and a pre-defined significance limit ($\alpha_s = 0.05$). Namely, a p-value>α_s indicates a failure to reject H_0, and one can conclude equal medians for the two specimens' data of e_{local}. The WRS test exhibited a p-value > 0.8 for the F35_MD_15_SMT and F35_D_15_SMT boxplots in Figure 2-10a, and > 0.1 for the DG_MD_15_SMT and DG_D_15_SMT boxplots in Figure 2-10b. The equality between e_{local} for the medium dense and dense specimens in Figure 2-10a and b advocates for the notion of a unique CSL in the compression plane, which confirms the findings reported in Salvatore et al. (2017), and emerges a step beyond the conclusions reported in (Mooney et al., 1998) and Finno and Rechenmacher (2003) of multiple CSLs depending on the initial e of the specimens tested in biaxial compression.

Amirrahmat et al. (2019) used the relative particle translation gradient (RPTG) concept proposed by Druckrey et al. (2017) to provide a thorough assessment of the internal shearing patterns that developed within the scanned specimens reported in this chapter. Briefly, RPTG refers to the incremental displacement of each particle relative to its neighboring particles and normalized with respect to the global axial compression. When a shear band develops within a specimen, particles within the shear band rotate and translate as if the bulk specimen is divided into multiple frictionally sliding wedges, which produces higher RPTG values along the developed shear band and constant volume flow as postulated by the CS theory. Figures 1-11 and 1-12 presents side-by-side color maps for

RPTG and e distribution within the same central Y-Z vertical cut across the images acquired at the last loading step for the 10 scanned specimens. RPTG clearly exposed the development of a single shear band in the F35_D_400_SMT (Figure 2-11a), GS40_D_400_SMT (Figure 2-11d), and GB_D_400_SMT (Figure 2-12d) specimens, while external surface bulging in the other specimens was internally manifested by the development of multiple shear bands in opposite directions. In order to quantify the influence of failure mode (single versus multiple shear band) on the discrepancy in e at the CS, Figure 2-13 depicts the evolution of e_{local}/e_{global} versus ε_1 for the specimens presented in Figure 2-11. The discrepancy curves in Figure 2-13 represent the solid curves/errorbars (e_{local}) from Figure 2-9a and c normalized by their respective dashed curves (e_{global}). Initially, e_{local}/e_{global} was $\sim 1-1.05$ since isotropic normal compression under σ_3 produces no shear (no shear strain localization), then the difference between e_{local} and e_{global} gradually increased with ε_1. At the CS (last loading step scans), e_{local}/e_{global} was ~1.25 for the F35_D_400_SMT (Figure 2-11a) and GS40_D_400_SMT (Figure 2-11d) specimens, which failed via a single shear band. On the other hand, e_{local}/e_{global} was less throughout compression for specimens that exhibited external bulging (~1.10-1.15 at the CS). This discrepancy between e_{global} and e_{local} can actually explain the formation of the CS zone in the compression plane in Figure 2-4. Furthermore, the slight bulging in the F35_MD_15_SMT specimen (Figure 2-11c) produced the least severe discrepancy as the curve of e_{local}/e_{global} was the closest to unity in Figure 2-13. The less deviation between e_{local} and e_{global} for the F35_MD_15_SMT specimen can also be noticed in Figure 2-11c as the distribution field of e shows less variation, and RPTG reveals a dispersed development of multiple shear bands within the specimen. Therefore, the loose laboratory-size CTC specimens that manifested slight surface bulging at failure (Table 2-2) supposedly provided a more accurate (representative of the whole specimen) measurement of e at the CS than the dense specimens.

Oedometer Experiments

Experiments

The in-situ SMT scans have uncovered a discrepancy in measuring the evolution of e using the CTC apparatus due to shear strain localization within sand specimens at the CS. Alternatively, the CSL in the compression plane can be determined using the oedometer test. The restriction of lateral expansion in the oedometer test hinders the development of shear bands, which results in a relatively uniform distribution of e within the specimen and allows accurate quantification of NCLs in the compression plane. 12 oedometer tests were conducted on dry specimens of the same granular materials studied in this chapter (Table 2-1). The specimens were prepared by depositing the granular materials in four lifts using a funnel into a thick-wall cylindrical steel mold that has an inner diameter (D) of 50 mm and a height (H_o) of 25 mm. For each material, three

specimens were tested at different initial D_r (dense, medium dense, and loose) as summarized in Table 2-1. Specimens with different initial D_r were prepared by controlling the deposition height (small deposition height for loose specimens) and slightly tapping on the mold sides with a rubber mallet after depositing each lift (no tapping for loose specimens, 4 taps for medium dense specimens, 8 taps for dense specimens). The specimens were also capped with a cylindrical steel spacer measuring 49 mm in diameter $\times$ $7\,mm$ in thickness to provide a level contact surface when loading the specimen in uniaxial compression.

The oedometer experiments were performed using a universal testing machine (UTS) with a dual column loading frame that can apply a vertical compressive load up to $600\ kN$. The UTS machine consists of a hydraulic table equipped with a built-in load cell and can move up/down at a displacement-controlled rate to vertically load/unload the specimen against a fixed cylindrical top loading piston that has a diameter of 49 mm. The specimens were loaded in confined uniaxial compression at a displacement loading rate of 0.05 mm/min including an unloading cycle at the end of each test ($\varepsilon_1 = 25\%$). Figure 2-14 shows the evolution of e versus σ_1 for the 12 oedometer tests in which e was calculated based on the height of solids (H_s) as:

$$e = \frac{H_0(1-\varepsilon_1) - H_s}{H_s}, \qquad H_s = \frac{w_s}{(\pi D^2/_4)(\gamma_w G_s)} \tag{2-8}$$

Critical State (CS) Assessment

The compression curves depicted in Figure 2-14 show an initial elastic behavior followed by stiff yielding, which is marked by the gray semi-transparent lines. As proposed by the CS theory, the gray lines in Figure 2-14 represent the K_0-NCL that extends along the yield locus of tested materials as it grows with uniaxial compression. Assuming K_o compression conditions (zero lateral expansion of the sand specimen), p' can be calculated as:

$$p' = \frac{\sigma'_1 + 2(1-\sin\phi_{cs})\,\sigma'_1}{3} \tag{2-9}$$

where ϕ_{cs} is the CS angle of internal friction, which is expressed as:

$$\sin\phi_{cs} = \frac{3M}{6+M} \tag{2-10}$$

where M is the slope of the CSL in the stress plane that was determined earlier in Figure 2-3 using the results of the CTC experiments. Figure 2-15 displays the relationship between the CSL and K_0-NCL in the stress plane, which can be expressed by the yield locus Equation. Table 2-6 summarizes the models presented in Figure 2-15 that have been proposed in the literature to fit a yield locus in the stress plane for granular materials. The MIT-S1 model (Pestana and Whittle, 1999) was adopted:

$$\frac{(q-\beta p')^2}{p'^2} = (m^2+\beta^2-2\beta\eta)^2\left[1-\left(\frac{p'}{p'_0}\right)^n\right] \tag{2-11}$$

Where $\eta = q/p'$ denotes the stress ratio (e.g., $\eta = M = \frac{6\sin\phi_{cs}}{3-\sin\phi_{cs}}$ for the CSL and $\eta = \eta_{K_o} = \frac{3\sin\phi_{cs}}{3-2\sin\phi_{cs}}$ for the K_o-NCL). n and m are fitting parameters that; respectively, control the slenderness and aperture of the yield locus (e.g., $n = 0.7$ and $m = 1.55$ in Figure 2-15), while the orientation of yield locus is controlled by the dimensionless stress ratio type parameter β. The size of the yield locus is determined by the stress type parameter p_o', which is analogous to p' along the isotropic-NCL in the modified cam clay (MCC) model. However, the MIT-S1 model assumes a unique lateral earth pressure coefficient (K_o) for specimens loaded in 1D compression (Figure 2-14), for which $p' = p_o'$ and $\eta = \beta$. Accordingly, the data points along the yielding portion of the compression curves in Figure 2-14 (gray lines) were mapped from the K_o-NCL (medium gray line in Figure 2-15) to CSL (black line in Figure 2-15) using Equation 1-11 (red curve in Figure 2-15), and the CSL in the compression plane was established for each material as shown in Figure 2-16. The MIT-S1 model was selected since it alleviates concerns associated with the limited ellipsoidal shapes assumed by the MCC and MIT-E3 models (see Figure 2-15) as well as it significantly enhances the postulation of yield locus for sand, particularly in the super-critical region $(\eta > M)$ (Pestana and Whittle, 1994, Whittle et al., 1994, Pestana and Whittle, 1999).

Discussion

The linear regression models in Figure 2-16 have established the CSL in the compression plane very well (R-squared~1, p-value < 0.05 for the F-statistics, and narrow 95% confidence limits for the estimates Γ and λ). A trend can still be seen in Figure 2-16a-c in which data points of tested sands show a higher slope (λ) for the loose, medium dense, and dense experiments, respectively. Again, this trend supports the transitional behavior of sand because of particle breakage, the effect of the specimen's initial D_r, fabric, etc. However, the linear models in Figure 2-16 do not produce a diffused CS zone like the case in the CTC results (Figure 2-4) due to the lack of shear band development in oedometer tests.

To compare the oedometer with CTC results, the CSL in the compression plane was fitted with a linear model in Figure 2-17 using the CS data points of the CTC experiments that were conducted on each initial D_r state separately (dense, medium dense, and loose). Results of the linear fit among the CS data points of loose specimens in Figure 2-17a closely agree with Γ and λ determined by the oedometer tests (Table 2-7). This agreement supports the earlier conclusion of loose specimens providing more accurate CS assessment in the compression plane when tested in CTC conditions due to the slight bulging failure mode, which produced less discrepancy between e_{global} and e_{local} throughout the compression of the F35_MD_15_SMT specimen (Figure 2-13).

Summary and Conclusions

This chapter seeks to accurately measure the CSL and yield locus for poorly-graded spherical glass beads and three types of silica sands with different particle morphologies. The CSL was quantified in the stress plane based on the results of CTC experiments that were conducted on specimens with different initial densities and multiple levels of σ_3's. However, the CTC results revealed a diffused CS zone in the compression plane that was clearly dependent on the applied σ_3 and initial density of the specimen. Potential causes for the CS zone in the compression plane were investigated by analyzing high-resolution 3D images of in-situ SMT scans collected for CTC experiments on the same tested materials. The SMT scans provided excellent 3D images that offered interesting insights into the discrepancy in measuring the evolution of e within sand specimens subjected to CTC conditions. Processed 3D images affirmed a non-uniform distribution of e within the scanned specimens as they approached the CS due to shear strain localization. e_{local} measured at the center of the specimen exhibited significantly different evolution with ε_1 in comparison to e_{global}, particularly when a single shear band developed within the specimen at the CS. As proposed by the CS theory, scanned specimens with initial medium dense and dense states attained equal e_{local} at the CS when tested at the same σ_3. Therefore, the CS zone in the compression plane was attributed to the reliance on measurements of global change in volume provided by the conventional triaxial apparatus to calculate the evolution of e toward the CS. Alternatively, the CSL was quantified in the compression plane using the results of oedometer tests on specimens composed of the same granular materials. The oedometer specimens inhibit the development of internal shear bands, which leads to accurate quantification of the CS parameters in the compression plane compared to the CTC results. Accordingly, yield locus and the CSL in $p' - q - e$ space were established in Figure 2-18 for the four granular material by synthesizing the results of the CTC and oedometer experiments. Namely, the CS parameter M was measured using the CTC results while Γ and λ were determined based on the oedometer tests as summarized in Table 2-8.

Acknowledgments

This material was partially funded by the US National Science Foundation (NSF) under Grant No. CMMI-1266230. Any opinions, findings, conclusions, and recommendations expressed in this chapter are those of the authors and do not necessarily reflect the views of the NSF. The SMT scans presented in this chapter were collected using the x-ray Operations and Research Beamline Station 13-BMD of the Advanced Photon Source (APS), a U.S. Department of Energy (DOE) Office of Science User Facility operated by the Argonne National Laboratory (ANL) under Contract No. DE-AC02-06CH11357. We acknowledge the support of GeoSoilEnviroCARS (Sector 13), which is funded by the NSF Earth Sciences (EAR-1128799), and the DOE Geosciences (DE-FG02-94ER14466). We thank Dr. Mark Rivers for his guidance at APS.

References

Roscoe, K. H., Schofield, A. & Wroth, C. (1958) On the yielding of soils. *Geotechnique* **8(1)**:22-53.

Poorooshasb, H., Holubec, I. & Sherbourne, A. (1966) Yielding and flow of sand in triaxial compression: Part I. *Canadian Geotechnical Journal* **3(4)**:179-190.

Roscoe, K. H. & Burland, J. (1968) On the generalized stress-strain behavior of wet clay.

Schofield, A. & Wroth, P. (1968) Critical state soil mechanics.

Vesic, A. S. & Clough, G. W. (1968) Behavior of granular materials under high stresses. *Journal of Soil Mechanics & Foundations Div*.

Marschi, N. D., Chan, C. K. & Seed, H. B. (1972) Evaluation of properties of rockfill materials. *Journal of the Soil Mechanics and Foundations Division* **98(1)**:95-114.

Been, K. & Jefferies, M. G. (1985) A state parameter for sands. *Geotechnique* **35(2)**:99-112.

Coop, M. (1990) The mechanics of uncemented carbonate sands. *Geotechnique* **40(4)**:607-626.

Wood, D. M. (1990) *Soil behavior and critical state soil mechanics.* New York, NY 10011, USA, Press Syndicate of the University of Cambridge the Pitt Building.

Coop, M. & Lee, I. (1993) The behavior of granular soils at elevated stresses. *Predictive soil mechanics*:186-198.

Pestana, J. & Whittle, A. (1994) Model Prediction of Anisotropic Clay Behavior due to Consolidation Stress History. In *Proc. 8th Int. Conf. Comp. Meth. and Advances in Geomechanics*.).

Whittle, A. J., Degroot, D. J., Ladd, C. C. & Seah, T.-H. (1994) Model prediction of anisotropic behavior of Boston blue clay. *Journal of Geotechnical Engineering* **120(1)**:199-224.

Whittle, A. J. & Kavvadas, M. J. (1994) Formulation of MIT-E3 constitutive model for overconsolidated clays. *Journal of Geotechnical Engineering* **120(1)**:173-198.

Harris, W. W., Viggiani, G., Mooney, M. A. & Finno, R. J. (1995) Use of stereophotogrammetry to analyze the development of shear bands in sand. *Geotechnical Testing Journal* **18(4)**:405-420.

Garga, V. K. & Zhang, H. (1997) Volume changes in undrained triaxial tests on sands. *Canadian Geotechnical Journal* **34(5)**:762-772.

Iwashita, K. & Oda, M. (1998) Rolling resistance at contacts in simulation of shear band development by DEM. *Journal of Engineering Mechanics* **124(3)**:285-292.

Li, X. S. & Wang, Y. (1998) Linear Representation of Steady State Line for Sand. *Journal of Geotechnical and Environmental Engineering* **124(12)**:1215-1217.

Mcdowell, G. & Bolton, M. (1998) On the micromechanics of crushable aggregates. *Geotechnique* **48(5)**:667-679.
Mooney, M. A., Finno, R. J. & Viggiani, M. G. (1998) A Unique Critical State for Sand? *Journal of Geotechnical and Geoenvironmental Engineering* **124(11)**:1100-1108.
Pestana, J. M. & Whittle, A. J. (1999) Formulation of a unified constitutive model for clays and sands. *International Journal for Numerical and Analytical Methods in Geomechanics* **23(12)**:1215-1243.
Frost, J. D. & Jang, D.-J. (2000) Evolution of sand microstructure during shear. *Journal of Geotechnical and Geoenvironmental Engineering* **126(2)**:116-130.
Iwashita, K. & Oda, M. (2000) Micro-deformation mechanism of shear banding process based on modified distinct element method. *Powder Technology* **109(1-3)**:192-205.
Jefferies, M. & Been, K. (2000) Implications for critical state theory from isotropic compression of sand. *Geotechnique* **50(4)**:419-429.
Martins, F. B., Bressani, L. A., Coop, M. R. & Bica, A. V. D. (2001) Some aspects of the compressibility behavior of a clayey sand. *Canadian Geotechnical Journal* **38(6)**:1177-1186.
Alshibli, K. A., Batiste, S. N. & Sture, S. (2003) Strain localization in sand: plane strain versus triaxial compression. *Journal of Geotechnical and Geoenvironmental Engineering* **129(6)**:483-494.
Finno, R. J. & Rechenmacher, A. L. (2003) Effects of consolidation history on critical state of sand. *Journal of Geotechnical and Geoenvironmental Engineering* **129(4)**:350-360.
Dafalias, Y. F. & Manzari, M. T. (2004) Simple plasticity sand model accounting for fabric change effects. *Journal of Engineering Mechanics* **130(6)**:622-634.
Desrues, J. & Viggiani, G. (2004) Strain localization in sand: an overview of the experimental results obtained in Grenoble using stereophotogrammetry. *International Journal for Numerical and Analytical Methods in Geomechanics* **28(4)**:279-321.
Santamarina, J. & Cho, G.-C. (2004) Soil behavior: The role of particle shape. In *Advances in geotechnical engineering: The skempton conference*.) Citeseer, vol. 1, pp. 604-617.
Alshibli, K. & Roussel, L. (2006) Experimental investigation of slip□stick behavior in granular materials. *International Journal for Numerical and Analytical Methods in Geomechanics* **30(14)**:1391-1407.
Ferreira, P. & Bica, A. (2006) Problems in identifying the effects of structure and critical state in a soil with a transitional behavior. *Geotechnique* **56(7)**:445-454.
Nocilla, A., Coop, M. & Colleselli, F. (2006) The mechanics of an Italian silt: an example of 'transitional'behavior. *Geotechnique* **56(4)**:261-271.

Alshibli, K. & Hasan, A. (2008) Spatial variation of void ratio and shear band thickness in sand using x-ray computed tomography. *Geotechnique* **58(4)**:249-257.
Altuhafi, F., Baudet, B. A. & Sammonds, P. (2010) The mechanics of subglacial sediment: an example of new “transitional” behavior. *Canadian Geotechnical Journal* **47(7)**:775-790.
Evans, T. M. & Frost, J. D. (2010) Multiscale investigation of shear bands in sand: physical and numerical experiments. *International Journal for Numerical and Analytical Methods in Geomechanics* **34(15)**:1634-1650.
Lu, Y. & Frost, D. (2010) Three-dimensional DEM modeling of triaxial compression of sands. In *Soil Behavior and Geo-Micromechanics*.), pp. 220-226.
Altuhafi, F. & Coop, M. R. (2011) Changes to particle characteristics associated with the compression of sands. *Geotechnique* **61(6)**:459-471.
Fu, P. & Dafalias, Y. F. (2011) Fabric evolution within shear bands of granular materials and its relation to critical state theory. *International Journal for Numerical and Analytical Methods in Geomechanics* **35(18)**:1918-1948.
Jiang, M., Yan, H., Zhu, H. & Utili, S. (2011) Modeling shear behavior and strain localization in cemented sands by two-dimensional distinct element method analyses. *Computers and Geotechnics* **38(1)**:14-29.
Tagliaferri, F., Waller, J., Andò, E., Hall, S. A., Viggiani, G., Bésuelle, P. & Dejong, J. T. (2011) Observing strain localisation processes in bio-cemented sand using x-ray imaging. *Granular Matter* **13(3)**:247-250.
Hasan, A. & Alshibli, K. (2012) Three dimensional fabric evolution of sheared sand. *Granular Matter* **14**:469.
Shipton, B. & Coop, M. R. (2012) On the compression behavior of reconstituted soils. *Soils and Foundations* **52(4)**:668-681.
Alshibli, K. A., Druckrey, A. M., Al-Raoush, R. I., Weiskittel, T. & Lavrik, N. V. (2014) Quantifying morphology of sands using 3D imaging. *Journal of Materials in Civil Engineering* **27(10)**:04014275.
Druckrey, A. & Alshibli, K. (2014) 3D Behavior of Sand Particles Using x-ray Synchrotron Micro-Tomography. In *Geo-Congress 2014 Technical Papers*.), pp. 2814-2821.
Gao, Z., Zhao, J., Li, X. S. & Dafalias, Y. F. (2014) A critical state sand plasticity model accounting for fabric evolution. *International Journal for Numerical and Analytical Methods in Geomechanics* **38(4)**:370-390.
Gu, X., Huang, M. & Qian, J. (2014) Discrete element modeling of shear band in granular materials. *Theoretical and Applied Fracture Mechanics* **72**:37-49.
Coop, M. (2015) Limitations of a Critical State framework applied to the behavior of natural and “transitional” soils. In *Proceedings of 6th International Symposium on Deformation Characteristics of Geomaterials, IS-Buenos Aires*.), pp. 115-155.
Shipton, B. & Coop, M. R. (2015) Transitional behavior in sands with plastic and non-plastic fines. *Soils and Foundations* **55(1)**:1-16.

Xiao, Y., Liu, H., Ding, X., Chen, Y., Jiang, J. & Zhang, W. (2015) Influence of particle breakage on critical state line of rockfill material. *International Journal of Geomechanics* **16(1)**:04015031.
Yang, J. & Luo, X. (2015) Exploring the relationship between critical state and particle shape for granular materials. *Journal of the Mechanics and Physics of Solids* **84**:196-213.
Zuo, L. & Baudet, B. A. (2015) Determination of the transitional fines content of sand-non plastic fines mixtures. *Soils and Foundations* **55(1)**:213-219.
Alshibli, K. A., Jarrar, M. F., Druckrey, A. M. & Al-Raoush, R. I. (2016) Influence of Particle Morphology on 3D Kinematic Behavior and Strain Localization of Sheared Sand. *Journal of Geotechnical and Geoenvironmental Engineering* **143(2)**:04016097.
Druckrey, A. M., Alshibli, K. A. & Al-Raoush, R. I. (2016) 3D characterization of sand particle-to-particle contact and morphology. *Computers and Geotechnics* **74**:26-35.
Kwa, K. & Airey, D. (2016) Critical state interpretation of effects of fines in silty sands. *Géotechnique Letters* **6(1)**:100-105.
Theocharis, A. I., Vairaktaris, E., Dafalias, Y. F. & Papadimitriou, A. G. (2016) Proof of Incompleteness of Critical State Theory in Granular Mechanics and Its Remedy. *Journal of Engineering Mechanics*:04016117.
Xiao, Y., Coop, M., Liu, H., Liu, H. & Jiang, J. (2016) Transitional behaviors in well-graded coarse granular soils. *Journal of Geotechnical and Geoenvironmental Engineering* **142(12)**:06016018.
Alshibli, K. & Cil, M. (2017) Influence of Particle Morphology on the Friction and Dilatancy of Sand. *Journal of Geotechnical and Geoenvironmental Engineering*.
Andò, E., Salvatore, E., Desrues, J., Charrier, P., Toni, J.-B., Modoni, G. & Viggiani, G. (2017) Strain Localisation in Sand in Cycles of Triaxial Compression and Extension: Continuum and Grain-Scale Analysis. In *International Workshop on Bifurcation and Degradation in Geomaterials*.) Springer, pp. 489-497.
Druckrey, A., Alshibli, K. & Al-Raoush, R. (2017) Discrete particle translation gradient concept to expose strain localisation in sheared granular materials using 3D experimental kinematic measurements. *Geotechnique*:1-9.
Imseeh, W. H., Druckrey, A. M. & Alshibli, K. A. (2017) 3D Experimental Quantification of Fabric and Fabric Evolution of Sheared Granular Materials Using Synchrotron Micro-Computed Tomography. *Granular Matter*. 20(2), 24. https://doi.org/10.1007/s10035-018-0798-x
Kandasami, R. K. & Murthy, T. G. (2017) Manifestation of particle morphology on the mechanical behavior of granular ensembles. *Granular Matter* **19(2)**:21.
Ponzoni, E., Nocilla, A. & Coop, M. (2017) The behavior of a gap graded sand with mixed mineralogy. *Soils and Foundations* **57(6)**:1030-1044.

Salvatore, E., Modoni, G., Andò, E., Albano, M. & Viggiani, G. (2017) Determination of the critical state of granular materials with triaxial tests. *Soils and Foundations* **57(5)**:733-744.
Wang, R., Fu, P., Zhang, J.-M. & Dafalias, Y. F. (2017) Evolution of Various Fabric Tensors for Granular Media toward the Critical State. *Journal of Engineering Mechanics* **143(10)**:04017117.
Xu, L. & Coop, M. (2017) The mechanics of a saturated silty loess with a transitional mode. *Geotechnique* **67(7)**:581-596.
Todisco, M., Coop, M. & Pereira, J.-M. (2018) Fabric characterisation in transitional soils. *Granular Matter* **20(2)**:20.
Petalas, A. L., Dafalias, Y. F. & Papadimitriou, A. G. (2019) SANISAND□FN: An evolving fabric□based sand model accounting for stress principal axes rotation. *International Journal for Numerical and Analytical Methods in Geomechanics* **43(1)**:97-123.
Amirrahmat, S., Druckrey, A., Alshibli, K. & Al-Raoush, R. (2019) Micro shear bands: Precursor for strain localization in sheared granular materials. Journal of Geotechnical and Geoenvironmental Engineering **145(2):**04018104.

Appendices

Appendix A: Tables

Table 2-1. Properties of tested granular material (Alshibli et al., 2014b).

Material	Soda Lime Glass Beads	F-35 Ottawa Sand	#1 Dry Glass Sand	GS#40 Columbia Grout Sand
Label	GB	F35	DG	GS40
Specific Gravity, G_s	2.55	2.65	2.65	2.65
Min. void ratio, e_{min} [+]	0.554	0.490	0.626	0.643
Max. void ratio, e_{max}	0.800	0.763	0.947	0.946
Roundness Index, I_R	0.965	0.959	0.937	0.924
Sphericity Index, I_{sph}	1.096	1.872	1.704	1.674
Surface Texture Index, R_q (μm)	0.381	2.084	1.990	1.923
Grain Sizes	Size fraction between US sieves #40 (0.420 mm) and #50 (0.297 mm)			

[+]Alshibli and Cil (2017)

Table 2-2. Summary of the 50 CTC experiments reported by (Alshibli and Cil, 2017).

Tested Material[+]	Experiment Label	Confining Stress, σ_3 (kPa)	Initial Void Ratio, e_o	Visual Observation on the Specimen Surface at Failure
F35	F35_L_15	15	0.735	Slight Bulge, no Apparent Shear Band
	F35_L_50	50	0.731	Slight Bulge, no Apparent Shear Band
	F35_L_100	100	0.726	Slight Bulge, no Apparent Shear Band
	F35_L_400	400	0.738	Slight Bulge, no Apparent Shear Band
	F35_MD_15	15	0.617	Moderate Bulge, no Apparent Shear Band
	F35_MD_50	50	0.612	Moderate Bulge, Possible Internal Shear Band
	F35_MD_100	100	0.611	Shear Band at 61°
	F35_MD_400	400	0.615	Shear Band at 45.5°, Possible Second Shear Band
	F35_D_15	15	0.491	Shear Band at 57°
	F35_D_50	50	0.496	NA
	F35_D_100	100	0.498	Significant Bulge, Possible Internal Shear Band
	F35_D_400	400	0.491	Two Shear Bands at 49° and 58°
DG	DG_L_15	15	0.935	Slight Bulge, no Apparent Shear Bands
	DG_L_50	50	0.916	Slight Bulge, no Apparent Shear Bands
	DG_L_100	100	0.935	Slight Bulge, no Apparent Shear Bands
	DG_L_400	400	0.925	Slight Bulge, no Apparent Shear Bands
	DG_MD_15	15	0.777	Significant Bulge, Possible Internal Shear Band
	DG_MD_50	50	0.786	Moderate Bulge, Possible Internal Shear Band
	DG_MD_100	100	0.774	Two Shear Bands at 63.5° and 66°
	DG_MD_400	400	0.775	Moderate Bulge, Possible Internal Shear Band
	DG_D_15	15	0.635	NA
	DG_D_25	25	0.645	Two Shear Bands at 77° and 63°
	DG_MD_50	50	0.639	Significant Bulge, Possible Internal Shear Band
	DG_MD_100	100	0.645	NA
	DG_MD_400	400	0.631	Shear Band at 56°
GS40	GS40_L_15	15	0.921	Slight Bulge, no Apparent Shear Bands
	GS40_L_50	50	0.916	Slight Bulge, no Apparent Shear Bands
	GS40_L_100	100	0.933	Slight Bulge, no Apparent Shear Bands
	GS40_L_400	400	0.915	Slight Bulge, no Apparent Shear Bands
	GS40_MD_15	15	0.764	Moderate Bulge, Possible Internal Shear Band
	GS40_MD_50	50	0.762	Moderate Bulge, Possible Internal Shear Band
	GS40_MD_100	100	0.758	Moderate Bulge, Possible Internal Shear Band
	GS40_MD_400	400	0.762	Moderate Bulge, Possible Internal Shear Band
	GS40_D_15	15	0.638	NA
	GS40_D_25	25	0.640	NA
	GS40_MD_50	50	0.648	NA
	GS40_MD_100	100	0.635	NA
	GS40_MD_400	400	0.634	Shear Band at 55.5°
GB	GB_L_15	15	0.788	Slight Bulge, no Apparent Shear Bands
	GB_L_50	50	0.795	Slight Bulge, no Apparent Shear Bands
	GB_L_100	100	0.792	Slight Bulge, no Apparent Shear Bands
	GB_L_400	400	0.780	Slight Bulge, no Apparent Shear Bands
	GB_MD_15	15	0.707	Moderate Bulge, Possible Internal Shear Band
	GB_MD_50	50	0.706	Moderate Bulge, Possible Internal Shear Band
	GB_MD_100	100	0.721	NA
	GB_MD_400	400	0.701	Moderate Bulge, Possible Internal Shear Band
	GB_D_15	15	0.624	Significant Bulge, Possible Internal Shear Band
	GB_D_50	50	0.622	Significant Bulge, Possible Internal Shear Band
	GB_D_100	100	0.612	Significant Bulge, Possible Internal Shear Band
	GB_D_400	400	0.621	Apparent Shear Band at 62°

[+]See Table 2-1 for a detailed description of tested materials

Table 2-3. Summary of the regression model results fitted in Figure 2-4. Values in parentheses denote the 95% confidence limits of the parameter.

		Regression Equation $e = \Gamma - \lambda(p'/p_a)^{\alpha}$	
Regression Plot	Tested Material[+]	Γ	λ
Figure 1-4a	F35	0.694 (0.648,0.739)	0.0064 (0.0317, -0.0188)
Figure 1-4b	DG	0.866 (0.809,0.923)	0.0085 (0.0401, -0.0231)
Figure 1-4c	GS40	0.862 (0.808, 0.916)	0.0073 (0.037, -0.0228)
Figure 1-4d	GB	0.786 (0.749. 0.822)	0.0171 (0.0388, -0.0047)

[+]See Table 2-1 for a detailed description of tested materials

Table 2-4. Summary of the SMT scans that were acquired during the CTC experiments on specimens of the tested granular materials.

Tested Material[+]	**Experiment Label**	**Confining Stress, σ_3 (kPa)**	**Initial Void Ratio, e_o**	**Axial Strain at which SMT Scans were Acquired, ε_1 (%)**	**Resolution, $(\mu m/\text{pixel})$**
F35	F35_D_400_SMT	400	0.493	0, 1, 2, 3.4, 4.9, 6.9, 8.9, 11.8, 17.2	11.18
	F35_D_15_SMT	15	0.525	0, 1, 2, 3.5, 5, 6.9, 8.9, 11.9, 17.4, 22.3	11.14
	F35_MD_15_SMT	15	0.573	0, 1, 2, 3.6, 5.1, 7.1, 9.2, 12.2 15.8, 19.9, 22.9	8.16
DG	DG_D_400_SMT	400	0.689	0.0, 1.0, 2.0, 3.6, 5.1, 7.1, 9.2, 12.2, 17.8	11.18
	DG_D_15_SMT	15	0.688	0.0, 2.0, 3.5, 5.0, 7.0, 9.0, 11.9, 17.4	11.14
	DG_MD_15_SMT	15	0.737	0.0, 1.0, 2.0, 3.6, 5.1, 7.2, 9.2, 12.3, 15.8, 19.9	8.16
GS40	GS40_D_400_SMT	400	0.626	0.0, 1.0, 1.9, 3.3, 4.7, 6.7, 8.6, 11.4, 14.7	8.16
	GS40_D_15_SMT	15	0.675	0.0, 1.0, 2.0, 3.5, 5.0, 7.0, 9.0, 12.0, 17.5	11.14
GB	GB_D_400_SMT	400	0.547	0.0, 1.0, 2.1, 3.6, 5.2, 7.3, 9.3, 12.4, 18.1	11.18
	GB_D_15_SMT	15	0.525	0.0, 1.0, 2.0, 3.6, 5.1, 7.1, 9.1, 12.2	11.14

[+]See Table 2-1 for a detailed description of tested materials

Table 2-5. Summary of the oedometer tests.

Tested Material[+]	Experiment Label	Initial Void Ratio, e_o
F35	F35_L	0.757
	F35_MD	0.630
	F35_D	0.575
DG	DG_L	0.819
	DG_MD	0.926
	DG_D	0.716
GS40	GS40_L	0.930
	GS40_MD	0.778
	GS40_D	0.694
GB	GB_L	0.771
	GB_MD	0.721
	GB_D	0.690

[+]See Table 2-1 for a detailed description of tested materials

Table 2-6. Summary of common models used in the literature to describe the yield locus of sand in the stress plane $(q-p)$. Equations are plotted in Figure 2-15.

Model	Yield Locus Equation	Source
Modified Cam Clay (MCC)	$\frac{p'}{p'_o}=\frac{M^2}{M^2+\eta^2}$	Roscoe and Burland (1968)
MIT-E3	$\frac{(q-\beta p')^2}{p'p'_0}=N^2\left[1-\left(\frac{p'}{p'_0}\right)^n\right]^+$	Whittle and Kavvadas (1994)
MIT-S1	$\frac{(q-\beta p')^2}{p'^2}=(m^2+\beta^2-2\beta\eta)^2\left[1-\left(\frac{p'}{p'_0}\right)^n\right]^+$	Pestana and Whittle (1999)

[+]N, n, and m are fitting parameters

Table 2-7. Summary of the regression model results fitted in Figure 2-16. Values in parentheses denote the 95% confidence limits of the parameter.

		Regression Equation $e = \Gamma - \lambda(p'/p_a)^{\alpha}$	
Regression Plot	Tested Material[+]	Γ	λ
Figure 2-16a	F35	0.736 (0.727, 0.745)	0.0097 (0.0010, 0.0095)
Figure 2-16b	DG	0.931 (0.920, 0.943)	0.0165 (0.0170, 0.0160)
Figure 2-16c	GS40	0.940 (0.9289, 0.9518)	0.0180 (0.0185, 0.0175)
Figure 2-16d	GB	0.857 (0.841, 0.873)	0.0110 (0.0115, 0.0105)

[+]See Table 2-1 for a detailed description of tested materials

Table 2-8. Summary of the CS parameters for tested granular materials. Values in parentheses denote the 95% confidence limits of the parameter.

		CS Parameters		
Tested Material[+]	Yield Locus	M	Γ	λ
F35	Figure 2-18a	1.281 (1.310, 1.252)	0.736 (0.727, 0.745)	0.0097 (0.0010, 0.0095)
DG	Figure 2-18b	1.354 (1.392, 1.316)	0.931 (0.920, 0.943)	0.0165 (0.0170, 0.0160)
GS40	Figure 2-18c	1.361 (1.393, 1.329)	0.940 (0.9289, 0.9518)	0.0180 (0.0185, 0.0175)
GB	Figure 2-18d	1.064 (1.111, 1.018)	0.857 (0.841, 0.873)	0.0110 (0.0115, 0.0105)

[+]See Table 2-1 for a detailed description of tested materials

Appendix B: Figures

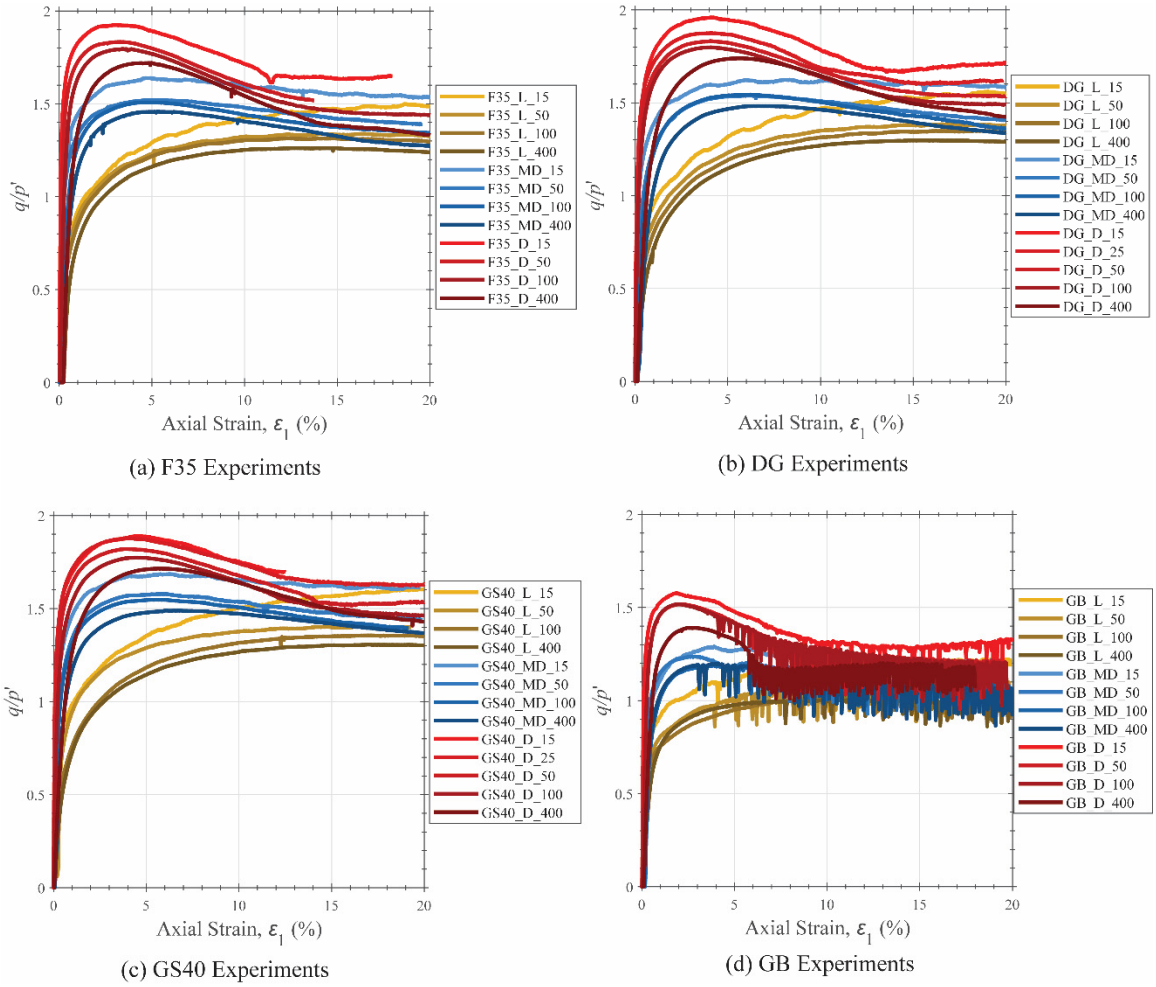


Figure 2-1. Evolution of q/p' versus ε_1 for the 50 CTC experiments listed in Table 1-2

, which were conducted on specimens of (a) F35, (b) DG, (c) GS40, and GB.

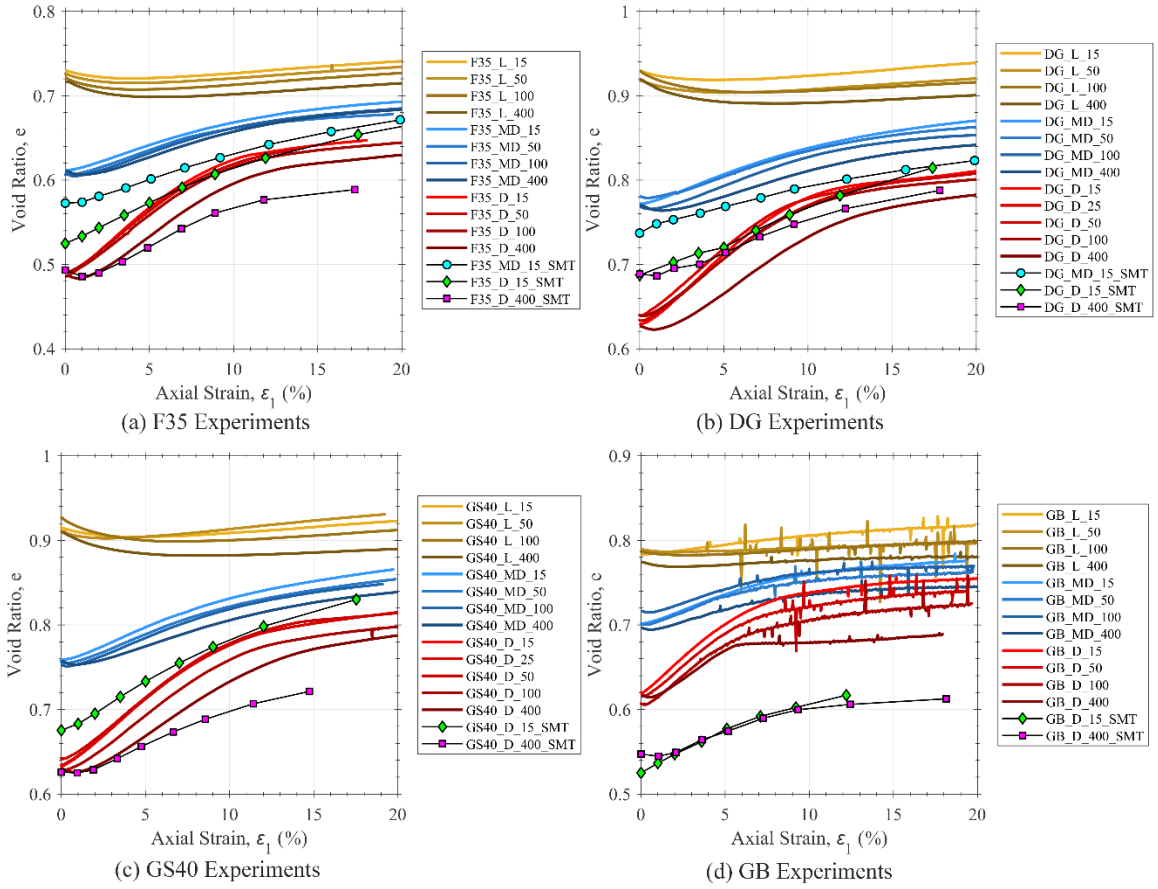


Figure 2-2. Evolution of e versus ε_1 for the 50 CTC experiments listed in Table 1-2

, which were conducted on specimens of (a) F35, (b) DG, (c) GS40, and GB.

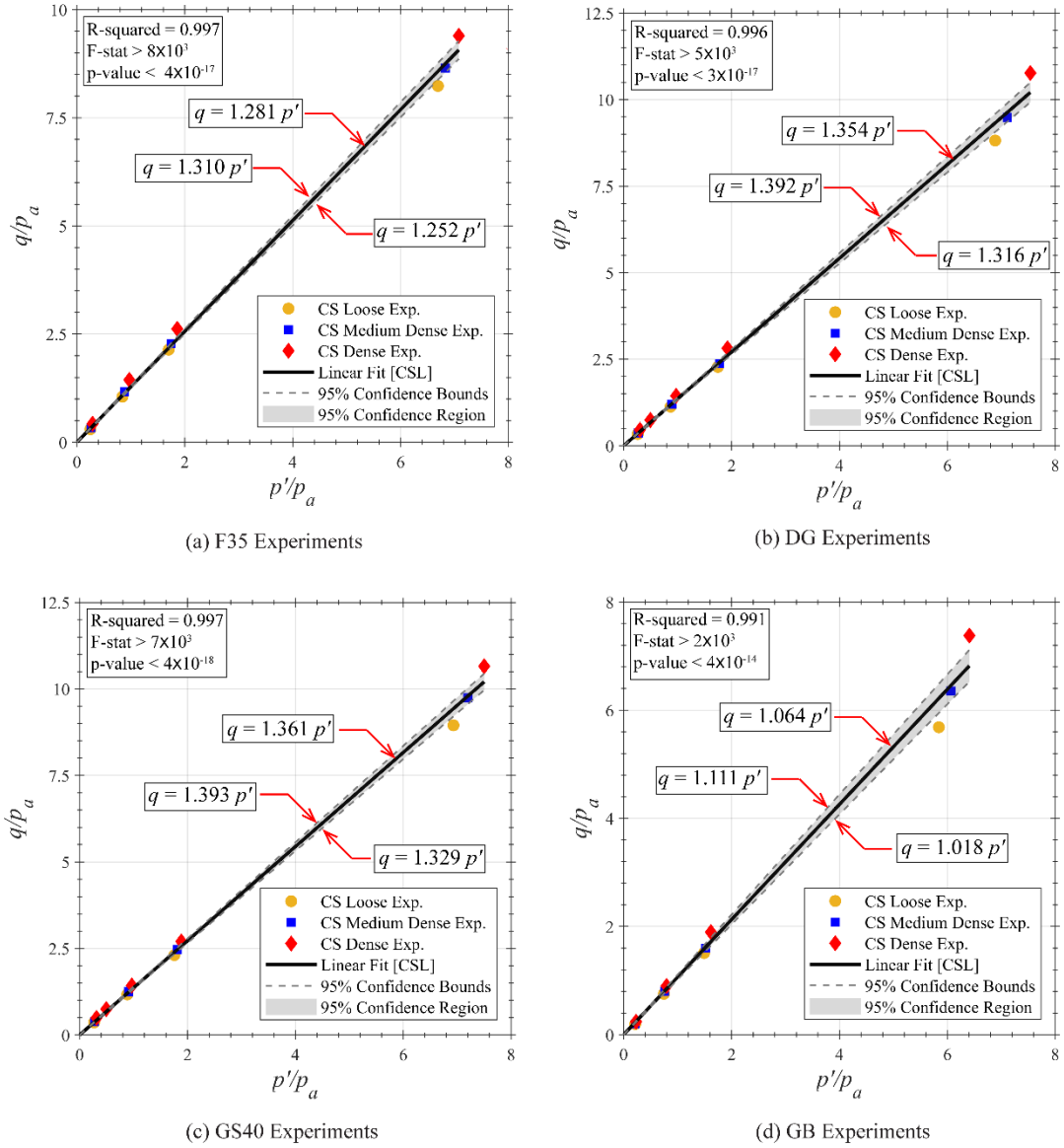


Figure 2-3. The CSL modeled in the stress plane $(q - p')$ using the 50 CTC experiments listed in Table 1-2, which were conducted on specimens of (a) F35, (b) DG, (c) GS40, and GB.

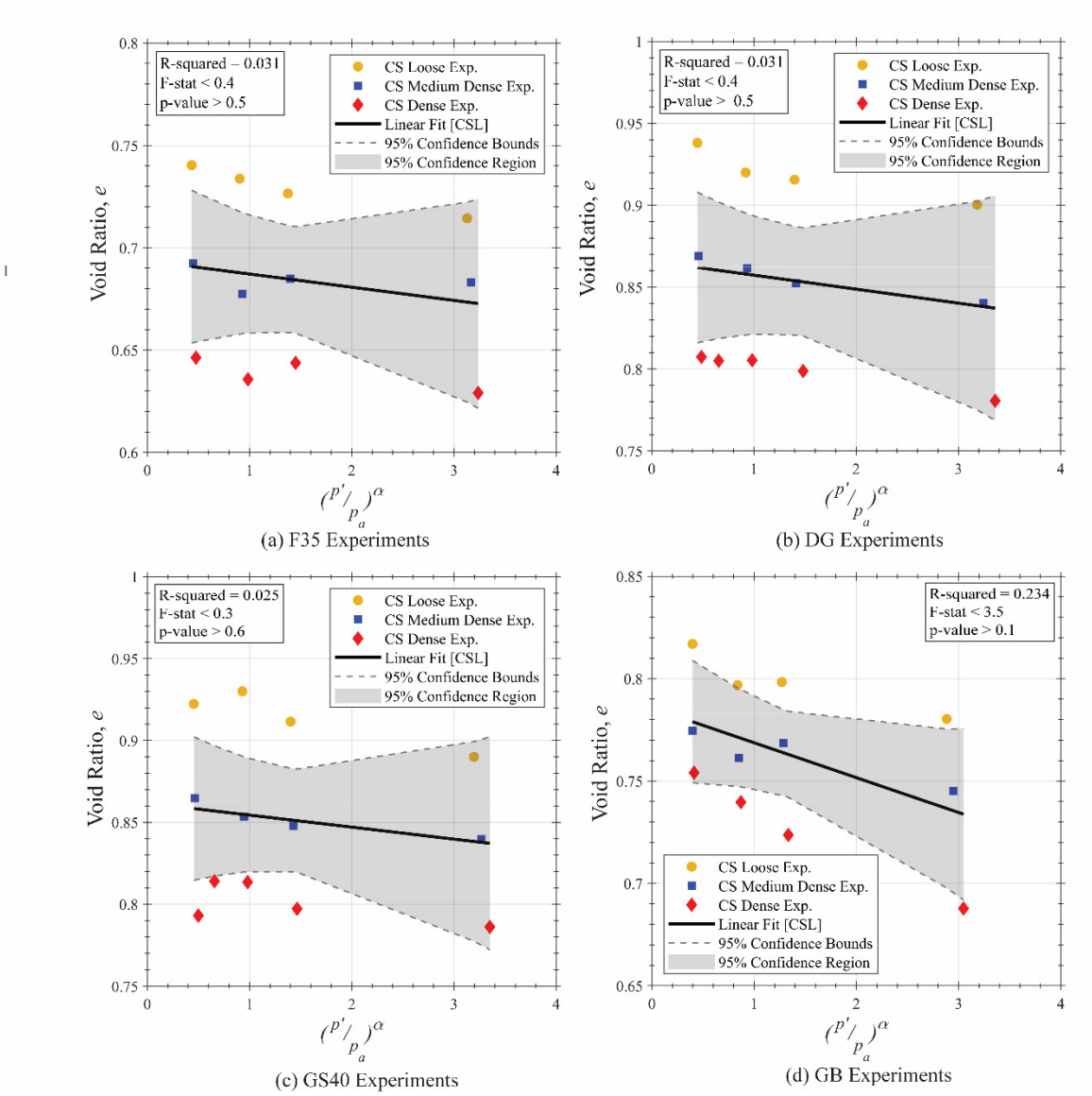


Figure 2-4. The CSL modeled in the compression plane $(e - p')$ using the 50 CTC experiments listed in Table 1-2, which were conducted on specimens of (a) F35, (b) DG, (c) GS40, and GB.

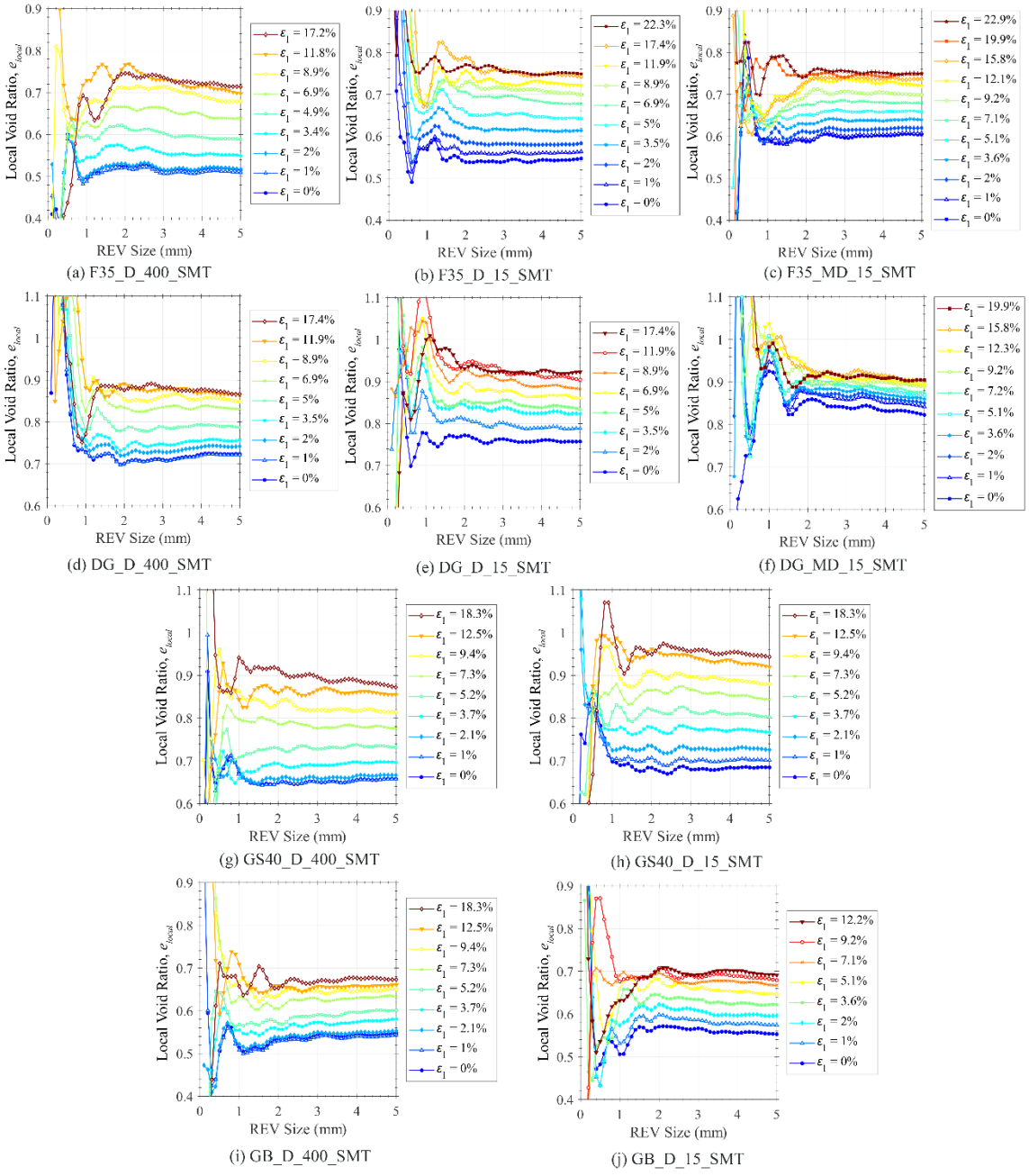


Figure 2-5. The change in e_{local} versus REV size for (a) F35_D_400_SMT; (b) F35_D_15_SMT; (c) F35_MD_15_SMT; (d) DG_D_400_SMT; (e) DG_D_15_SMT; (f) DG_MD_15_SMT; (g) GS40_D_400_SMT; (h) GS40_D_15_SMT; (i) GB_D_400_SMT; and (j) GB_D_15_SMT experiments. Refer to Table 1-4 for labels of experiments.

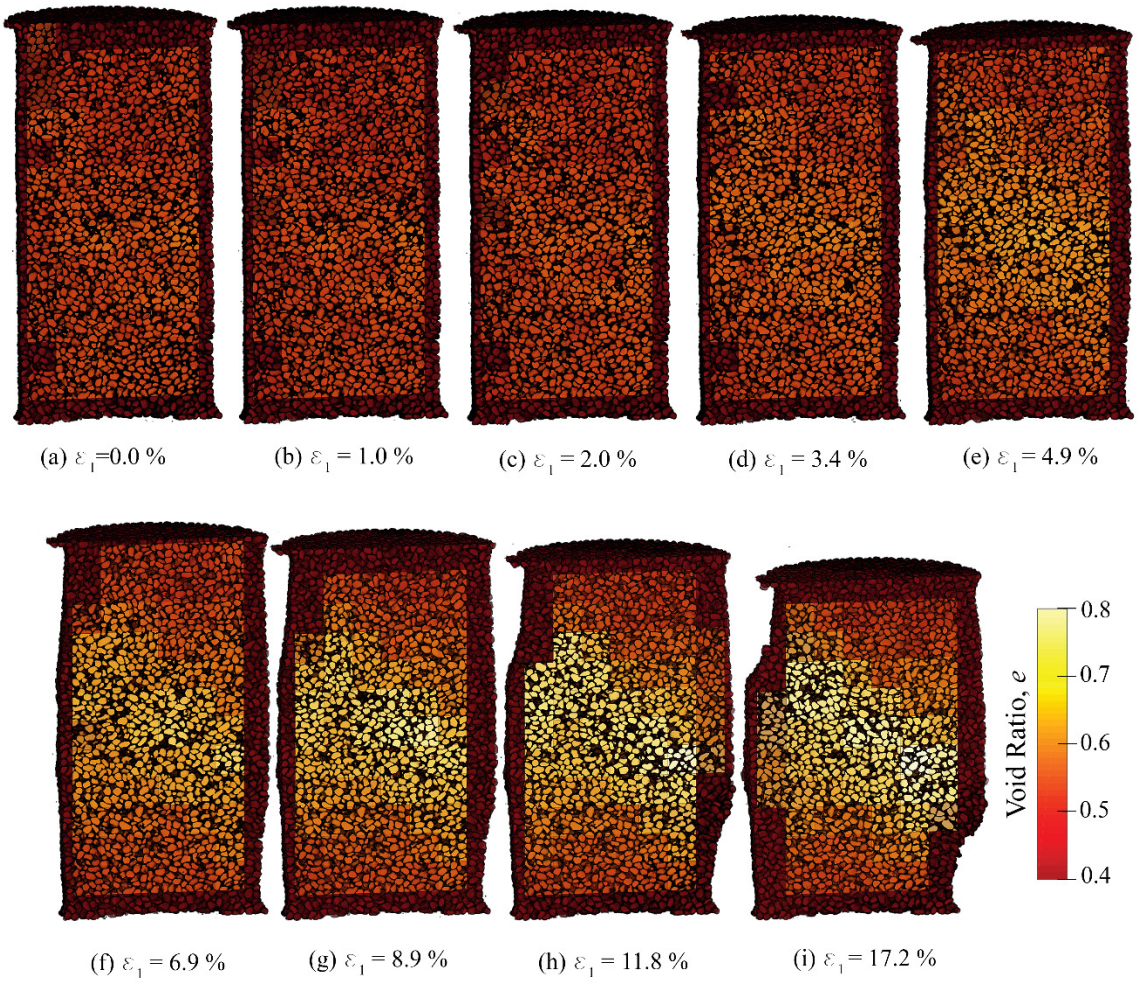


Figure 2-6. Distribution fields of e versus ε_1 at central Y-Z cuts across the SMT scans collected during the F35_D_400_SMT experiment. Refer to Table 1-4 for labels of experiments.

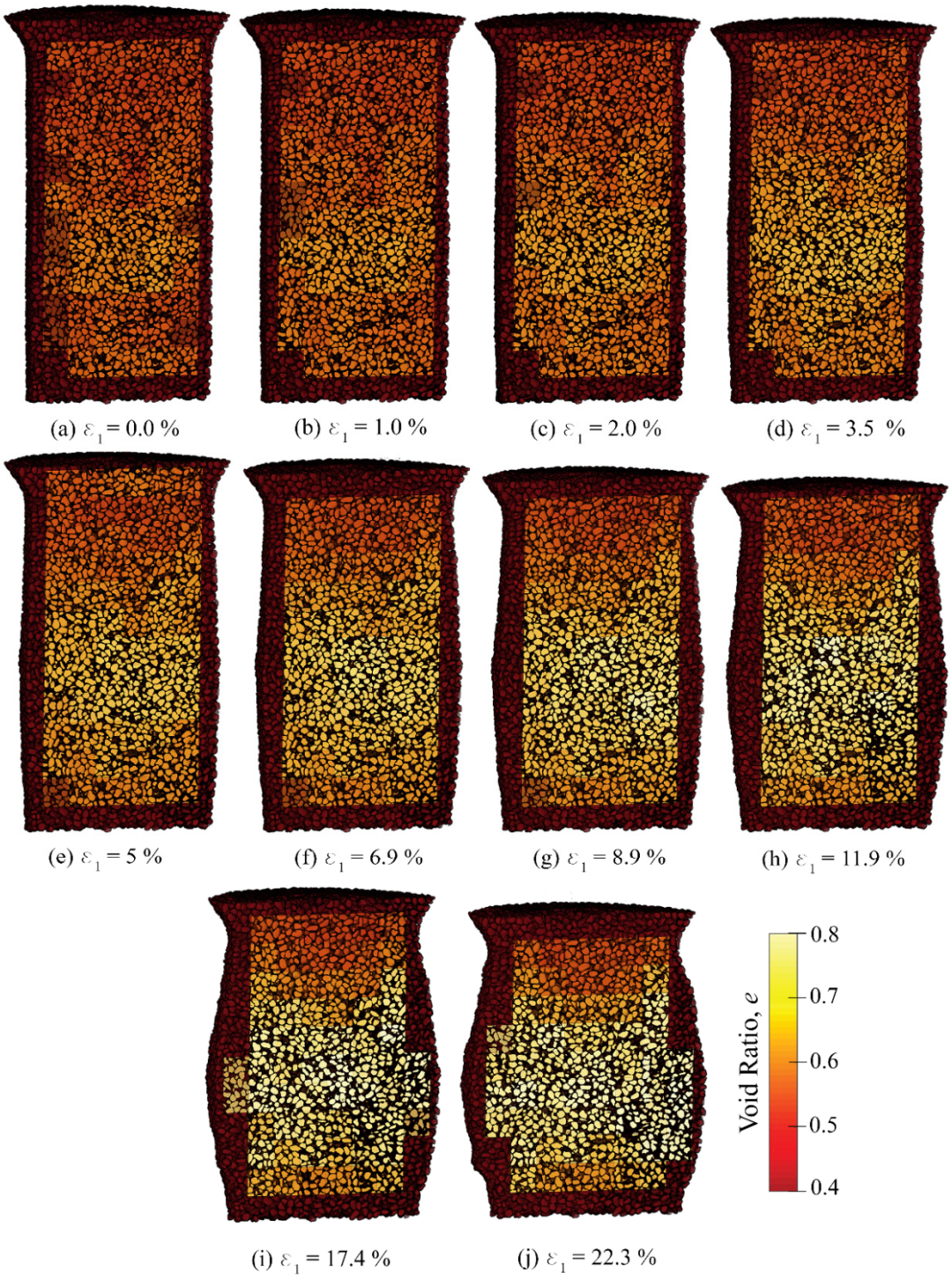


Figure 2-7. Distribution fields of e versus ε_1 at central Y-Z cuts across the SMT scans collected during the F35_D_15_SMT experiment. Refer to Table 1-4 for labels of experiments.

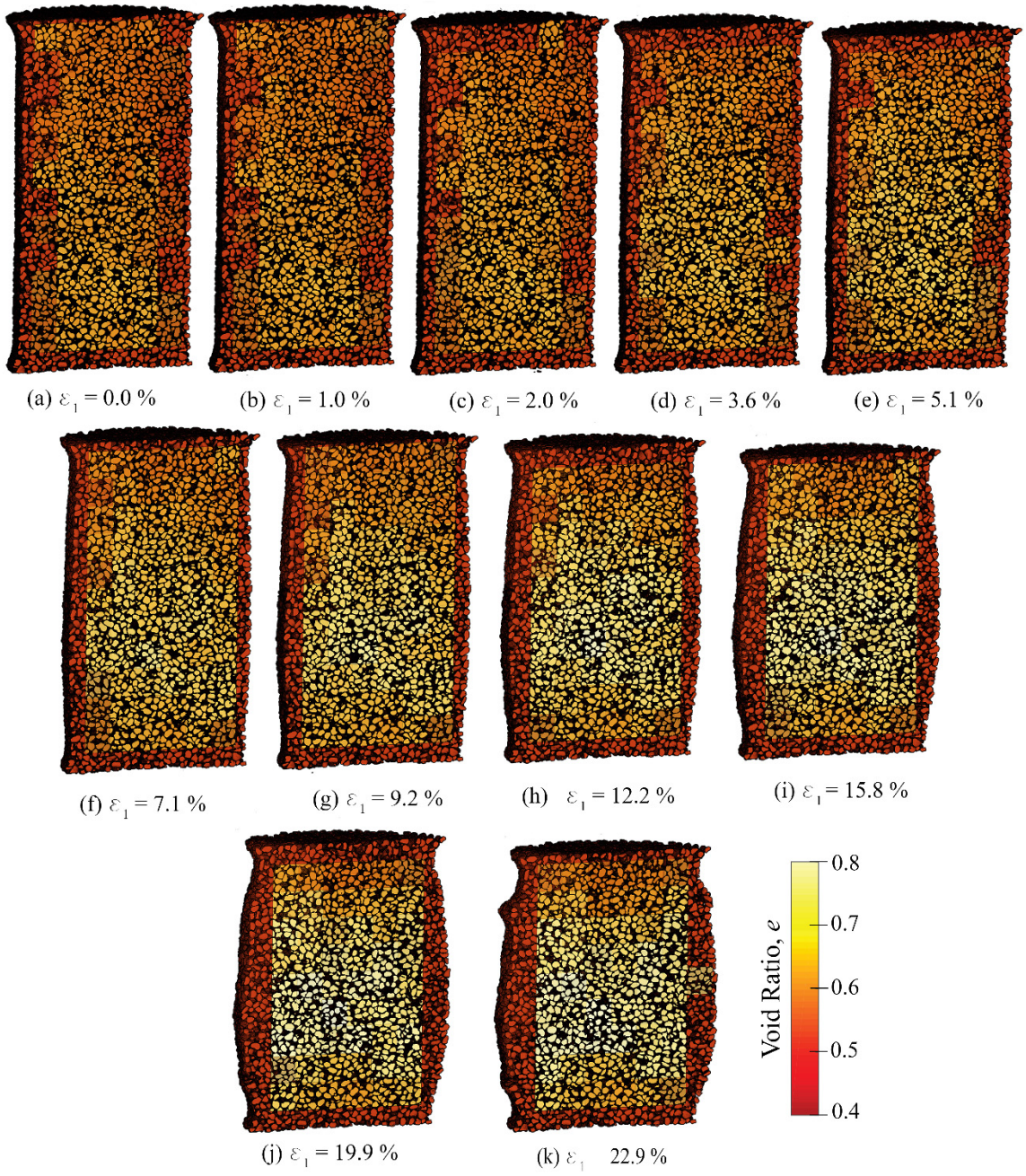


Figure 2-8. Distribution fields of e versus ε_1 at central Y-Z cuts across the SMT scans collected during the F35_MD_15_SMT experiment. Refer to Table 1-4 for labels of experiments.

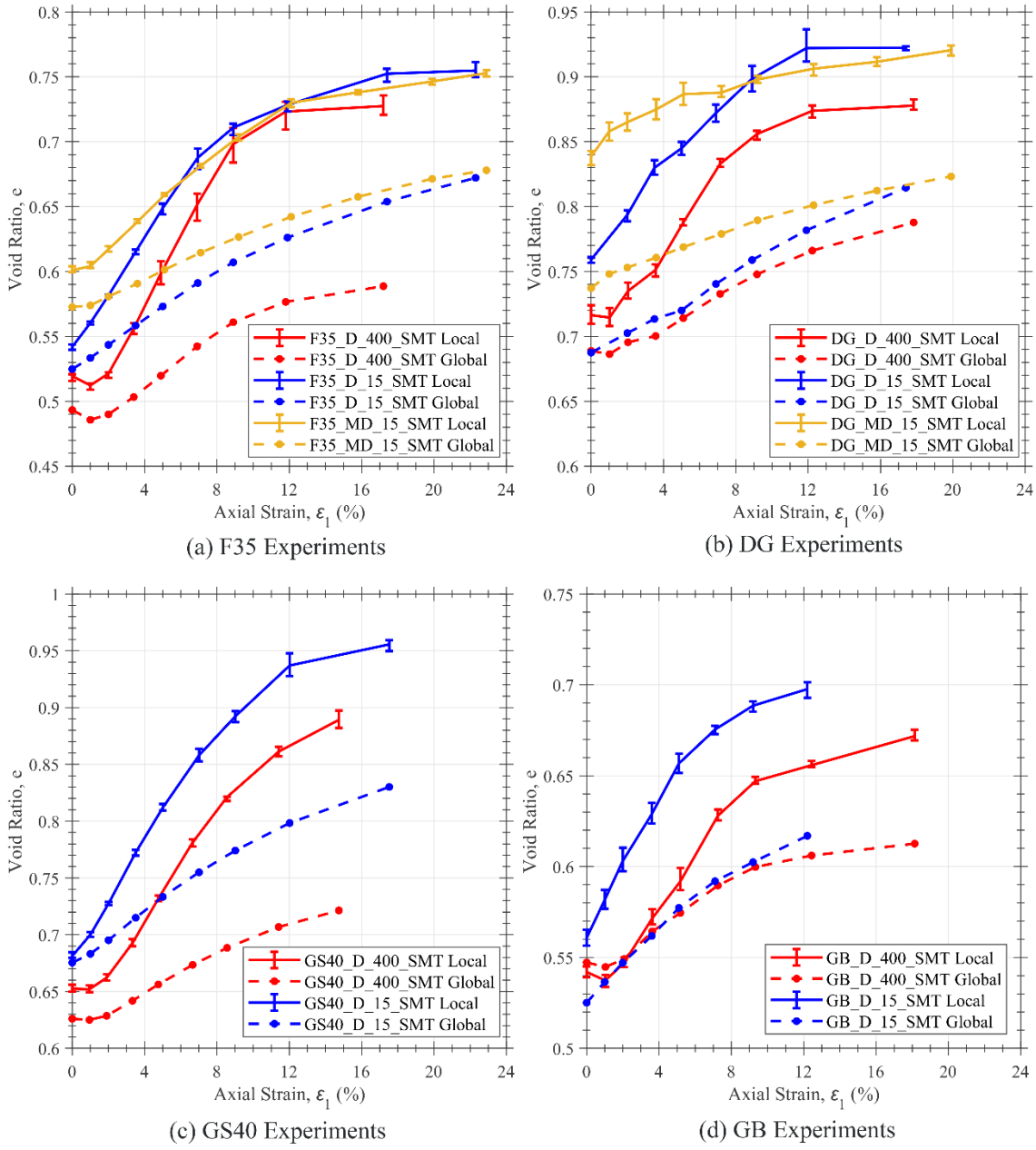


Figure 2-9. Comparison between the evolution of e_{global} and e_{local} versus ε_1 for (a) F35; (b) DG, (c) GS40; and (d) GB experiments. Refer to Table 1-4 for labels of experiments.

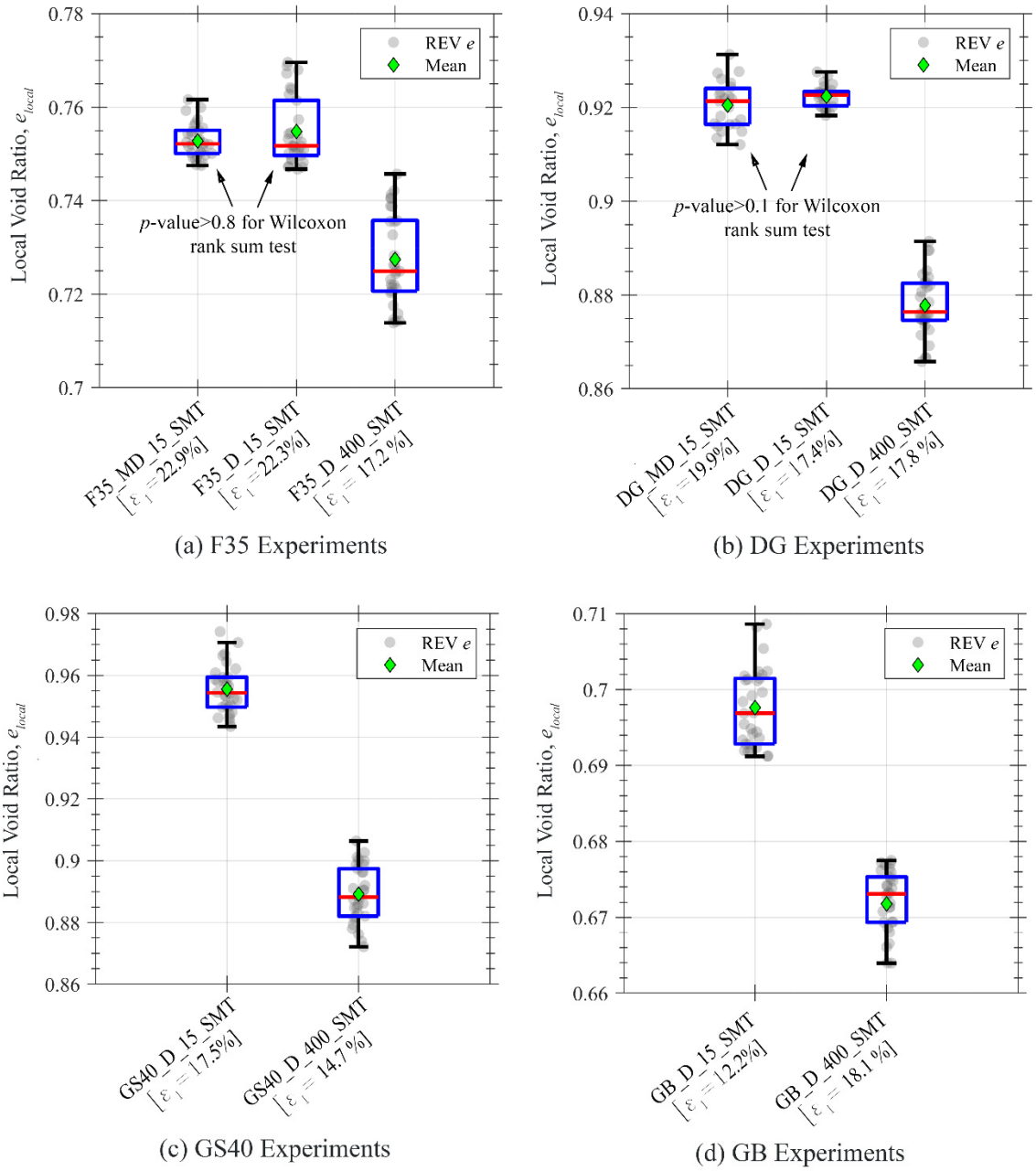


Figure 2-10. Boxplots of e_{local} at the last loading step for the (a) F35; (b) DG; (c) GS40; and (d) GB experiments. Refer to Table 1-4 for labels of experiments.

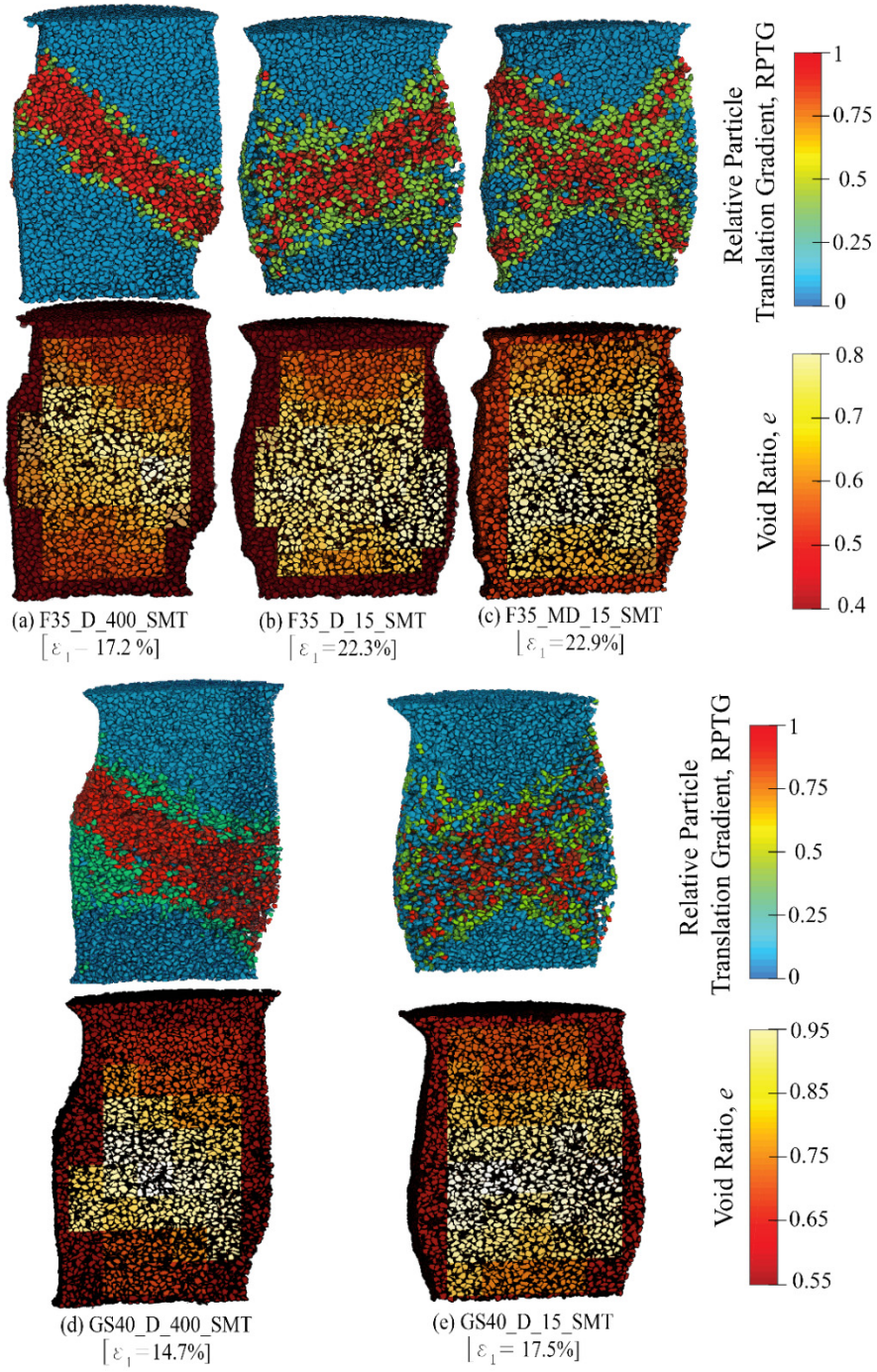


Figure 2-11. Distribution fields of RPTG and e_{local} calculated using the processed SMT images that were collected at the last loading steps for (a) F35_D_400_SMT; (b) F35_D_15_SMT; (c) F35_MD_15_SMT; (d) GS40_D_400_SMT; (e) GS40_D_15_SMT. Refer to Table 1-4 for labels of experiments.

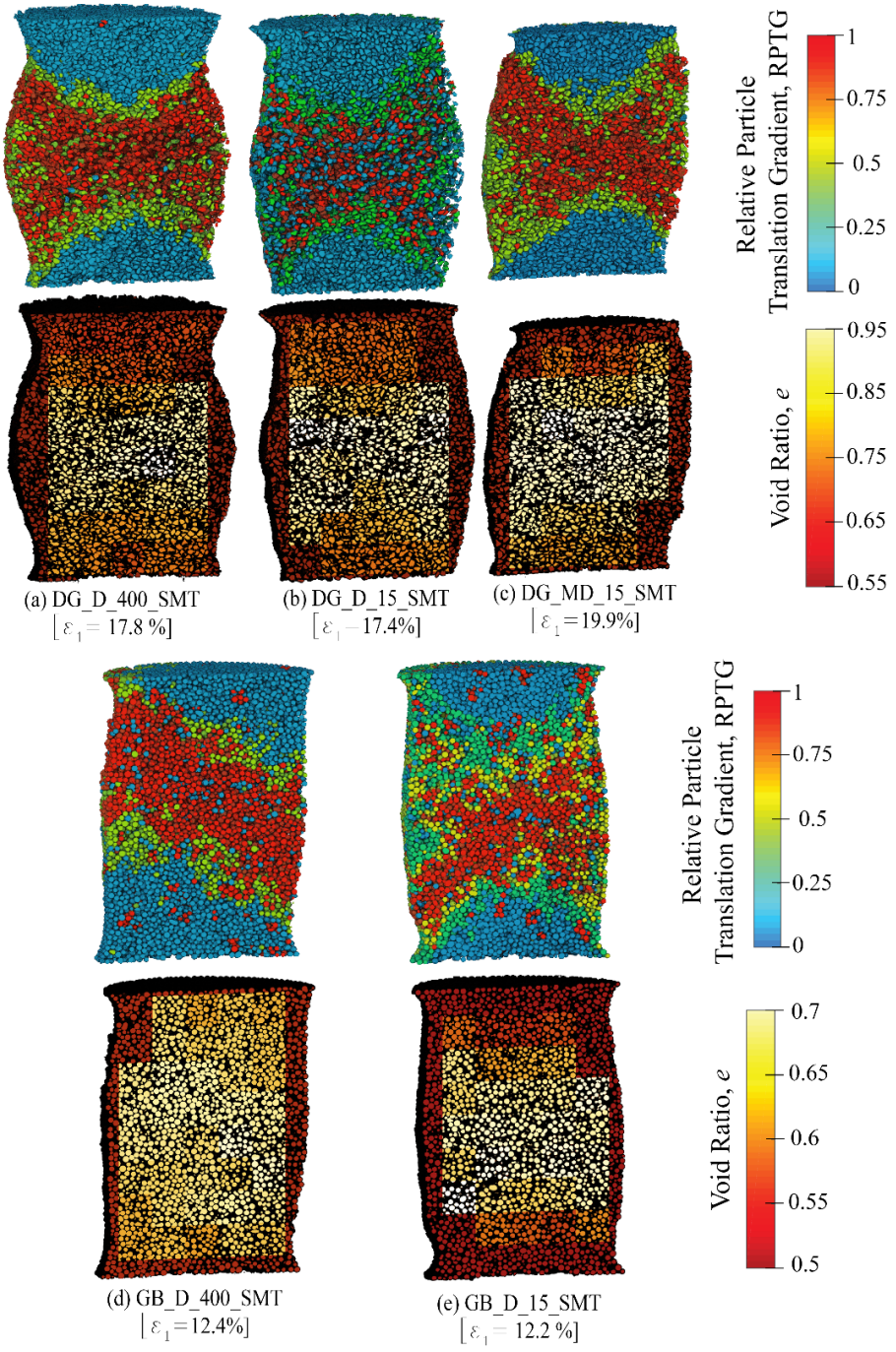


Figure 2-12. Distribution fields of RPTG and e_{local} calculated using the processed SMT images that were collected at the last loading steps for (a) DG_D_400_SMT; (b) DG_D_15_SMT; (c) DG_MD_15_SMT; (d) GB_D_400_SMT; (e) GB_D_15_SMT. Refer to Table 1-4 for labels of experiments.

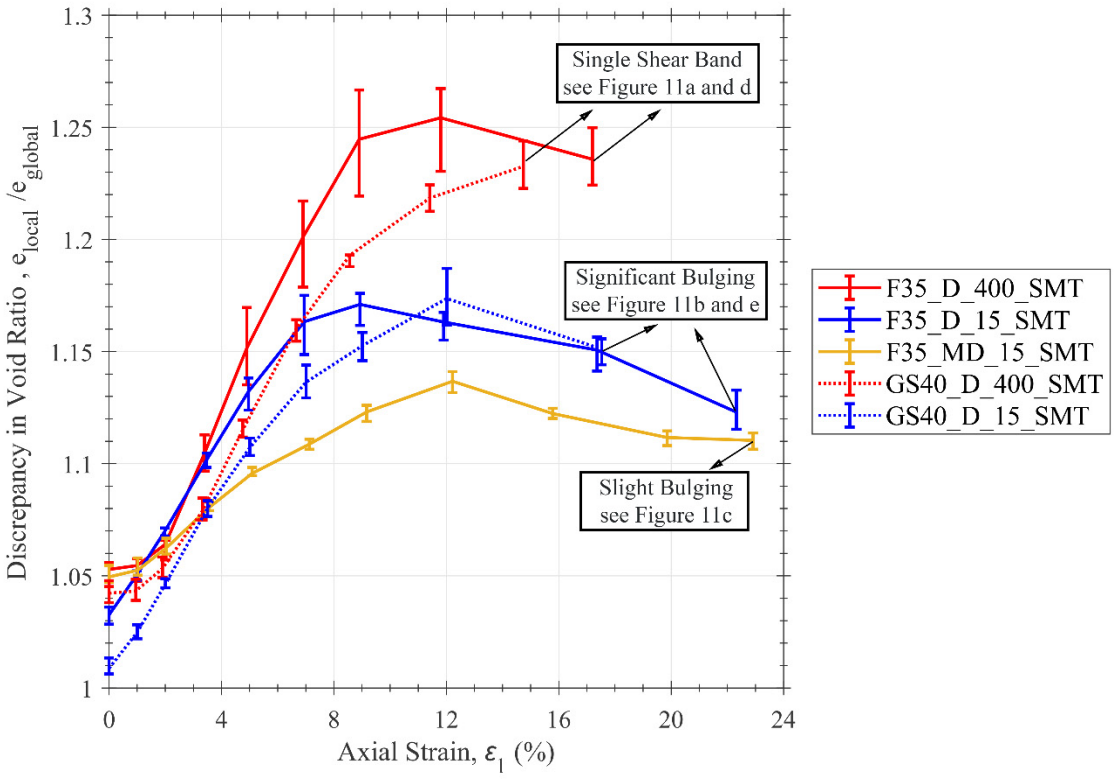


Figure 2-13. The discrepancy in the evolution of e toward the CS for the experiments presented in Figure 2-11 and conducted on F35 and GS40 sand.

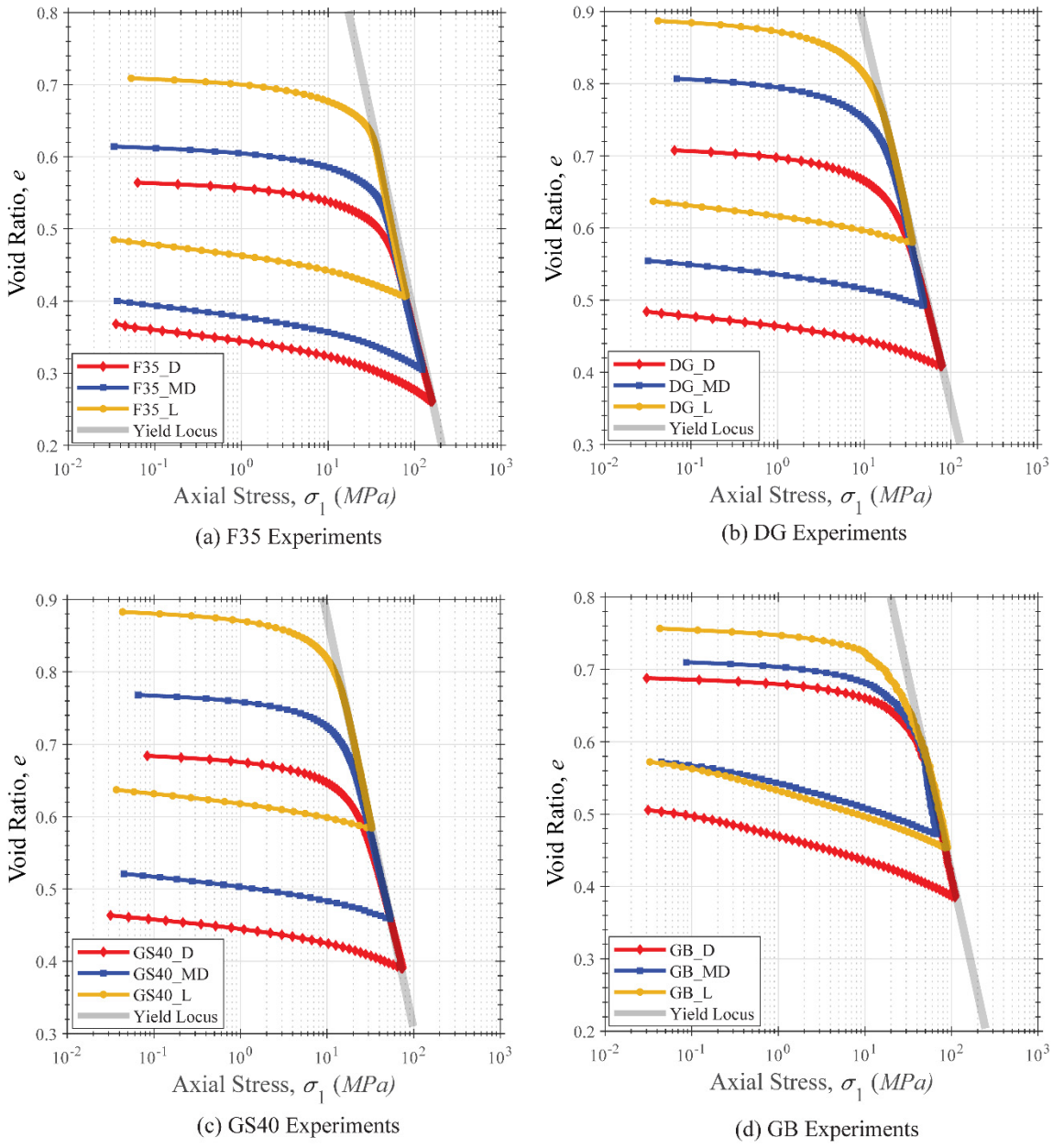


Figure 2-14. The evolution of e versus σ_1 for the 12 oedometer experiments listed in Table 1-5, which were conducted on specimens of (a) F35, (b) DG, (c) GS40, and GB.

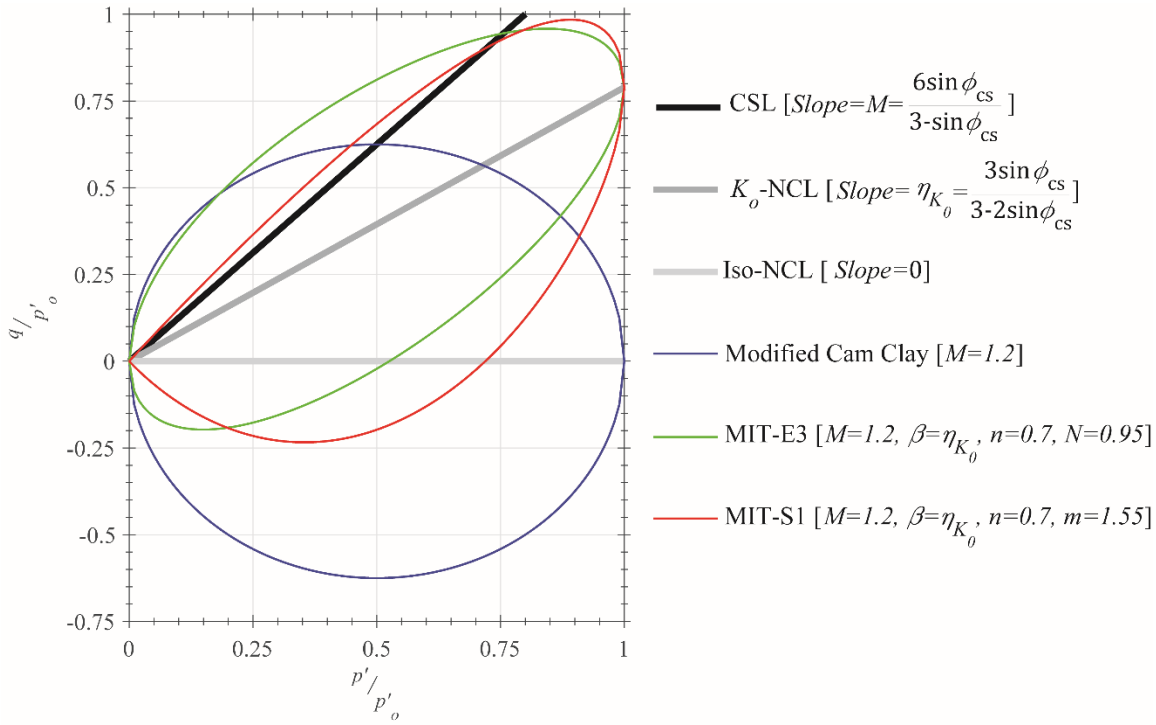


Figure 2-15. Illustration of common models used in the literature to fit a yield locus for sand in the stress plane $(q - p')$. Refer to Table 1-6 for more details on each model.

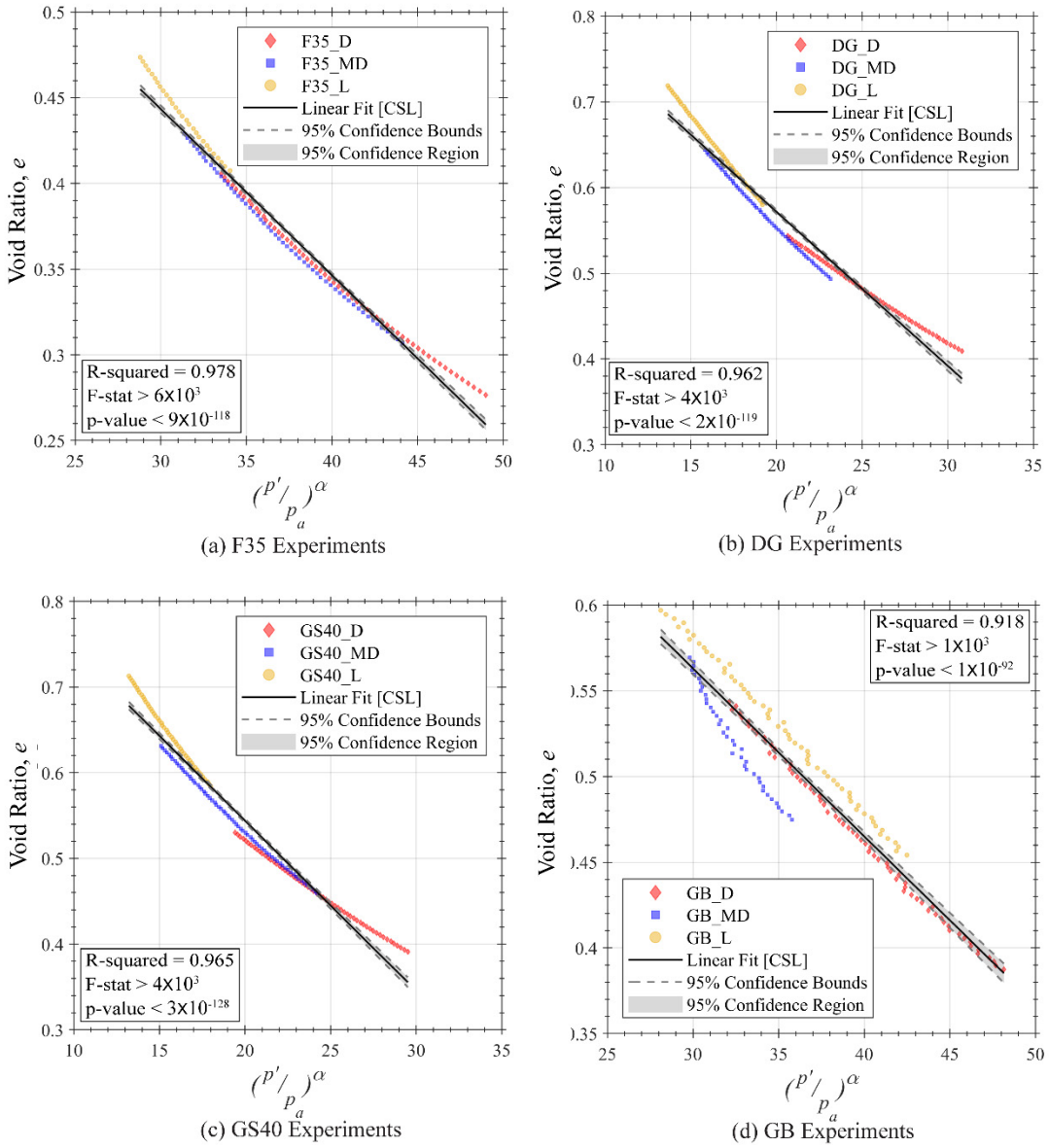


Figure 2-16. The CSL modeled in the compression plane $(e - p')$ using the 12 oedometer experiments listed in Table 1-5, which were conducted on specimens of (a) F35, (b) DG, (c) GS40, and GB.

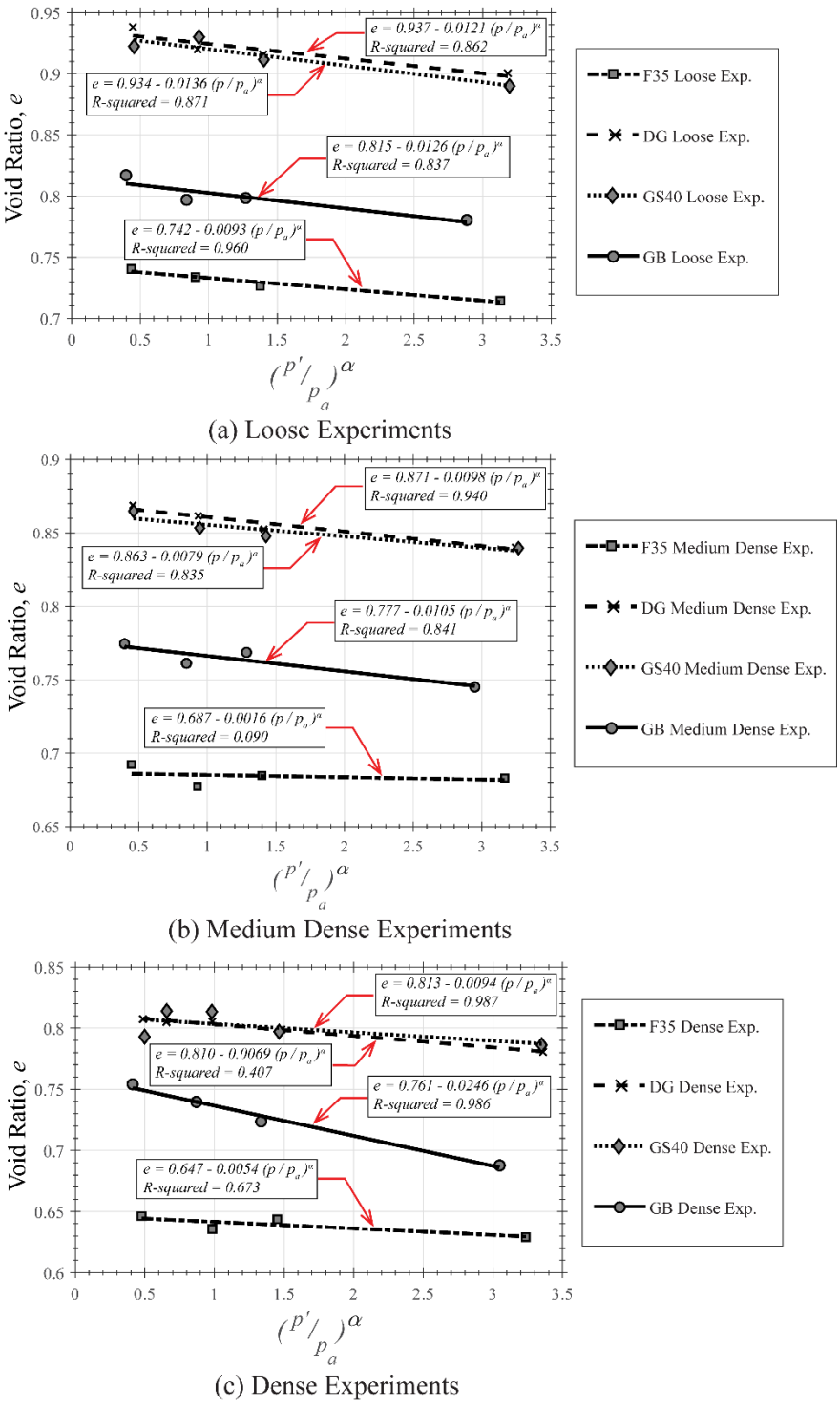


Figure 2-17. The CSL modeled in the compression plane $(e - p')$ using the 50 CTC experiments summarized in Table 1-2, which were conducted on (a) loose, (b) medium dense, and (c) dense specimens.

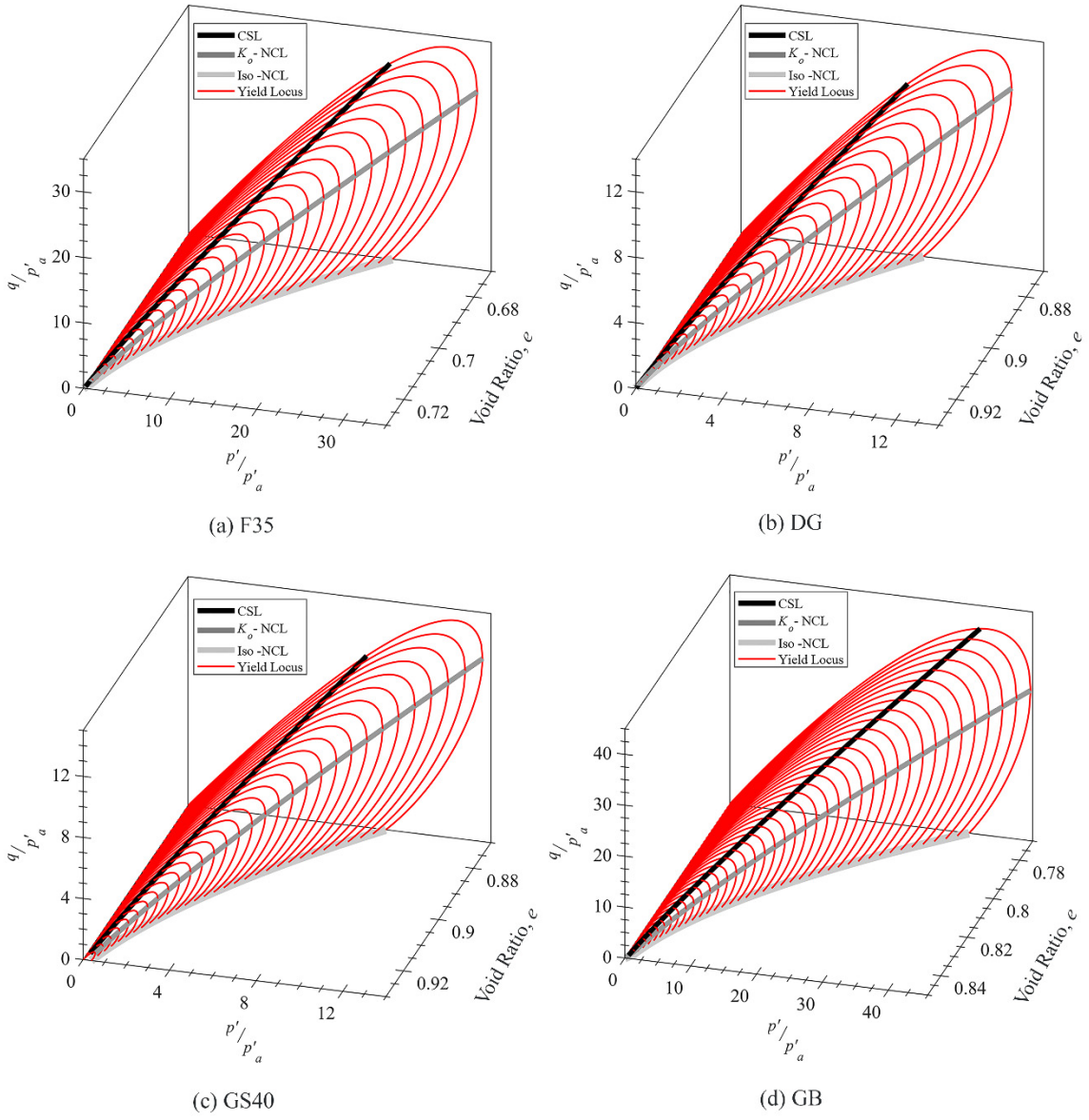


Figure 2-18. Yield locus for (a) F35, (b) DG, (c) GS40, and GB.

CHAPTER THREE

3D FINITE ELEMENT MODELING OF FORCE TRANSMISSION AND PARTICLE FRACTURE IN SAND

A version of this chapter was published as Imseeh, W. H. & Alshibli, K. A. (2017) "3D Finite Element Modelling of Force Transmission and Particle Fracture of sand". *Computers and Geotechnics*, 94, 184-195.
https://doi.org/10.1016/j.compgeo.2017.09.008

Abstract: Global compressive loading of granular media causes rearrangements of particles into a denser configuration. Under 1D compression, researchers observed that particles initially translate and rotate which lead to more contacts between particles and the development of force chains to resist applied loads. Particles within force chains resist most of the applied loads while neighbor particles provide lateral support to prevent particles within force chains from buckling. Several experimental and numerical models have been proposed in the literature to characterize force chains within granular materials. This chapter presents a 3D finite element (FE) model that simulates 1D compression experiment on F-75 Ottawa sand. The FE mesh of particles closely matched 3D physical shape of sand particles that were acquired using 3D synchrotron micro-computed tomography (SMT) technique. The chapter presents a quantitative assessment of the model, in which evolution of force chains, fracture modes, and stress-strain relationships showed an excellent agreement with experimental measurements reported by Cil et al. (2017).

Keywords: Force chains, fracture, sand, contact stresses

Introduction

Granular materials are composed of discrete solid particles that interact with each other in a complex fashion. Under 1D compression, it is well-known that particles within a granular media are held together and jammed into a complex network of mutual compressive forces. There are regions of high contact stresses transmitted through some of the particles to form what is known as force chains that resist global loads applied at boundaries. Conversely, other particles experience low contact stresses and provide support for particles within force chains against buckling. Force chains were visualized using photo-elastic materials (Dantu, 1957, Wakabayashi, 1957, Dantu, 1968, Jong and Verruijt, 1969, Behringer et al., 1999, Howell et al., 1999, Geng et al., 2003, Majmudar and Behringer, 2005, Clark et al., 2012). Besides photo-elasticity, many methods have been utilized in the last few decades to characterize and visualize force chains in granular material. To mention a few, Radjai et al. (1996) (1999) implemented contact dynamics simulations to study the statistical distribution of contact forces inside a confined packing of 2D circular rigid disks. Tordesillas (2007) quantitatively examined force chain buckling

and shear banding of 2D densely-packed cohesionless granular assembly subjected to quasi static biaxial compression using discrete element method (DEM). Similarly, Zhang et al. (2016) used DEM to investigate the role of force chains in granular materials under both quasi static biaxial loading and dynamic impact loading. Coppersmith et al. (1996) introduced the scaler q model to characterize force chains within a specimen composed of spherical beads in which the dominant physical mechanism leading to force chains was assumed to be the fluctuation in the force distribution that was attributed to variations in the contact angles and the constraints imposed by the force balance on each bead (Liu et al., 1995, Eloy and Clément, 1997, Socolar, 1998). Bouchaud et al. (1995) proposed phenomenological equations, also known as the oriented stress linearity model, to describe force propagation within a granular medium. Edwards and Grinev (2003) proposed a new approach that employs statistical-mechanical concepts to describe the probability of contact force distribution in granular material. In summary, most of recent studies reported in the literature on force network and force chains in granular assemblies were implemented on either 2D disks or 3D spherical particles (Andrade and Avila, 2012, Hurley et al., 2014, Brodu et al., 2015, Hall and Wright, 2015b, Hurley et al., 2016). However, there is a lack of studies that consider the exact 3D shape of natural sand grains in a granular assembly.

There are many 3D computational models to simulate laboratory experiments on granular material which can provide quantitative global stress-strain predictions that are difficult to verify experimentally at the particle scale (e.g., stress and strain tensor components for each particle). Most of these computational models were developed based on DEM or continuum theories. The DEM was first introduced by Cundall and Strack (1979) to numerically model the movement and interaction between discrete rigid particles in a granular assembly. Henceforth, DEM has been widely implemented in numerous numerical models to model the fracture of granular materials since it captures the discrete nature of particles. McDowell and Harireche (2002a) modeled soil particles in DEM as agglomerates of balls bonded togather to simulate fracture of individual soil particles, then succcesfully simulated oedometer tests on sand and showed that yielding coincides with the onset of bond breakage (McDowell and Harireche, 2002c). Ng (2004) introduced a new boundary condioton (i.e. hydrostatic boundary condition) in DEM to simulate the chamber fluid presure in a triaxial compression test on ellipsoidal shape particles. Cheung and O'Sullivan (2008) described algorithms to simulate the lateral boundary conditions imposed by the latex membrane used in physical triaxial tests in both 2D and 3D DEM simulations. Belheine et al. (2009) applied DEM to model compression triaxial test on 3D spherical packing of particles with a rolling resistance to account for surface roughness of particles. O'Sullivan and Cui (2009) simulated the response of specimens containing about 15,000 steel spheres subject to load–unload cycles in quasi-static triaxial tests to explore the particle-scale mechanics during the load reversals. Lu and Frost (2010) modeled triaxial compression tests on agglomerates of sand particles that were assembled as

unbreakable 2-circular clumps to achieve better interlocking between particles which yeilded more stable and efficient force chains. Hasan and Alshibli (2010) used clumped spheres to simulate the 3D axisymmetric triaxial compression experiment on JSC-1A lunar regolith at different densities and confining pressure in which a significant increase in peak and critical state friction angles was well predicted at near-zero confining pressure simulations. Yang et al. (2011) developed a discrete element and multiscale modeling methodology to represent granular media at their particle scale as they interact with solid deformable bodies, such as soil-tool, tire, penetrometer, pile, etc. Cil and Alshibli (2012) successfully modeled the fracture of individual silica sand particles in granular assemblies by adopting the bonded particle model concept within the framework of DEM. Kawamoto et al. (2016) outlined the level set discret element method (LS-DEM) which is a discrete element method version that is able to simulate systems of particles with arbitrary shape using level set functions as a geometric basis.

Alternatively, the continuum-based approach assumes an elasto-plastic material and applies constitutive relations to predict the overall stress-strain relationships. This method was originally implemented in numerical modeling of soil since the original work of Roscoe et al. (1958) and Drucker et al. (1957). Since then, it has been adopted in several constitutive models that can effectively predict stress-strain relations of granular material. Generally, both discrete and continuum models have successfully provided effective stress-strain predictions of behavior of granular materials. Nonetheless, continuum-based models still ignore the influence of the discrete natural of particles and assume a continuum material. On the other hand, DEM assumes rigid non-deformable particles and virtually calculates particle-level stress-strain estimations based on contact forces that are calculated with respect to a pre-defined numerical contact model. Thus, a combined approach that addresses both the continuum and discrete behavior of granular material has been established in recent years which is known as finite element-discrete element method (FEM-DEM). It adopts FEM to simulate the constitutive behavior of discrete particles, in which each discrete particle is meshed into deformable finite elements. Simultaneously, the conventional steps of DEM, including time integration, and contact detection are still applied to track the motion and interaction of individual particles. Mahabadi et al. (2009) implemented the FEM-DEM to simulate the behavior of a layered rock sample under standard laboratory Brazilian disk test. Mahabadi et al. (2010) used FEM-DEM to numerically simulate the behavior of Brazilian disc specimens as observed in laboratory during dynamic, high-strain rate, indirect tensile tests. Lisjak and Grasselli (2010) applied a new dissipative contact interaction algorithm in FEM-DEM framework to simulate the energy loss that is observed during rock fall impacts taking into account friction, fracturing, and non-conservative forces. Rougier et al. (2011) modeled Split Hopkinson Pressure Bar (SHPB) Brazilian experiments using an improved variant of FEM-DEM. Mahabadi et al. (2012) described a FEM-DEM numerical code for geomechanical applications. Recently, Druckrey and Alshibli (2016) successfully simulated the frature of individual silica

particles using the general concept of FEM-DEM within ABAQUS software framework. However, to the authors best knowledge, the FEM-DEM concept has not been adopted to model the 3D behavior of multi-particle granular assemblies. This chapter implements the concept of FEM-DEM to simulate 1D compression experiment on sand using ABAQUS FE code. 3D images of sand particles that were acquired using Synchrotron Micro-Computed Tomography (SMT) were used to create the 3D FE mesh. The implemented model captures the 3D physical shape of particles (morphology and particle-level characteristics) as discrete objects (discretization effect) that deform based on a FE framework (continuum behavior within each particle). A qualitative and quantitative assessment is presented by comparing the evolution of force chain, fracture modes, and stress-strain predictions with experimental results.

Experiment Description and Image Acquisition

Cil et al. (2017) conducted 1D compression experiment on a uniform natural silica sand known as F-75 Ottawa sand where only grain sizes between US sieve #40 (0.420 mm) and sieve #50 (0.297 mm) were used in the experiment. Sand particles were deposited inside a thick-walled acrylic mold with an inner diameter of 1 mm. The specimen had an initial height of about 2 mm. The experiment was conducted at beamline 1-ID of the Advance Photon Source (APS), Argonne National Laboratory (ANL), Illinois, USA. A special apparatus was used in which both 3D x-ray diffraction (3DXRD) and 3D SMT scans were acquired at different loading stages. The combination of 3DXRD and SMT techniques offers a unique approach to track individual particles and measure their lattice strains simultaneously. SMT scans were acquired using 70.5-keV x-ray energy while rotating the specimen at 0.2^o angular increments over 180^o at 0.65 second exposure time to construct a full 3D image with a spatial resolution of 1 μm/voxel. Similarly, 3DXRD scans were acquired at the same energy as the SMT scans while rotating the specimen at 1^o angular intervals over 180^o at a constant speed. Cil et al. (2017) reported experimental measurements of the averaged lattice strain within each sand particle based on 3DXRD data and then evaluated the lattice stress tensor for each particle. They also investigated the evolution and mode of fracture of sand particles using the high-resolution 3D SMT scans.

The initial SMT image of Cil et al. (2017) was used in this chapter to develop the FE model that captures the exact shape of sand particles. The initial SMT image was processed using AVIZO Fire 9.3 software in which 35 particles were identified as separate objects and numerical labels (1-35) were assigned to each particle. AVIZO Fire 9.3 software was then used to crop each particle individually and its surface mesh was then generated and saved as stereo-lithography (STL) file producing 35 STL files (one for each particle). A few smoothening and simplification cycles were applied on each surface image to generate a surface mesh with approximately 800 triangles per particle. Figure 3-1 shows an axial slice of the initial SMT scan and the surface meshes for all particles.

Finite Element (FE) Model Description

ABAQUS was implemented to perform the FE simulations. It provides two different solvers: Explicit and Implicit. Explicit ABAQUS solves for a state of dynamic equilibrium by constructing diagonal (lumped) element mass matrices to be used in computing nodal accelerations $(\ddot{u})$ at the beginning of each time increment as:

$$\ddot{u}_{(i)} = (M^{-1})(P_{(i)} - I_{(i)}) \quad (3\text{-}1)$$

Where M is the mass matrix, P is the applied load vector, I is the internal force vector, and subscript i refers to the time increment number in an explicit dynamic step. The explicit solver integrates nodal accelerations that were calculated at time t using the explicit central-difference integration algorithm to advance the velocity solution $(\dot{u})$ to time $t + \Delta t/2$ and the displacement solution (u) to time $t + \Delta t$ as:

$$\dot{u}_{(i+\frac{1}{2})} = \dot{u}_{(i-\frac{1}{2})} + \frac{\Delta t_{(i+1)} + \Delta t_{(i)}}{2} \ddot{u}_{(i)} \quad (3\text{-}2)$$

$$u_{(i+1)} = u_{(i)} + \Delta t_{(i+1)} \dot{u}_{(i+\frac{1}{2})} \quad (3\text{-}3)$$

Where u is a degree of freedom (displacement or rotation). The central-difference integration algorithm is explicit in a sense that kinematic state is advanced using the known values of $\dot{u}_{(i-\frac{1}{2})}$ and $\ddot{u}_{(i)}$ from the previous time step. The explicit solver can perform analysis on a large number of small inexpensive time increments to ensure that the central-difference integration rule is stable. However, if large increments are used then the solution becomes unstable and diverges rapidly. Alternatively, Implicit ABAQUS solves for a state of static equilibrium in which Newton-Raphson algorithm is implemented for each time increment i to satisfy equilibrium. In each time increment i, the implicit solver assumes an estimate of the solution at iteration n to be u_i^n (subscript refers to time increment number i and superscript refers to iteration number n). As a result, a Taylor series expansion about this estimate can be expressed as:

$$Kc = P - I \quad (3\text{-}4)$$

Where c is the correction factor and K is the system's tangent stiffness matrix which can be expressed as:

$$K = \frac{\partial I}{\partial u} - \frac{\partial P}{\partial u} \quad (3\text{-}5)$$

The implicit solver modifies the incremental displacement Δu_i after each iteration n using the following expression:

$$\Delta u_{(i)}^{n+1} = \Delta u_{(i)}^{n} + c_{(i)}^{n} \quad (3\text{-}6)$$

Iterations are repeated for each increment until the solution converges to equilibrium within a pre-defined tolerance. This implies that force and moment equilibrium are satisfied at each node. Lastly, as nodal displacements are calculated, then both the implicit and explicit solvers compute nodal forces based on classical FE approach using stiffness matrices (i.e. $f = ku$) and evaluate strain-stress values for each element.

Sand is as a granular material consists of discrete particles that interact with each other through contacts and undergo large deformations. The most challenging task

in such quasi-static FE simulation is the contact detection and possible mesh distortion. At first look, the implicit solver appears to be more appropriate for the quasi-static analysis reported in this chapter. However, iterating in each time increment to solve the system of non-linear differential equations (Equation (3-4) adds limitations on the capability of the implicit solver to detect, track, and modify location of contacts during each iteration step. Alternatively, the assumption of lumped masses in the explicit solver results in diagonal mass matrices that produce a system of linear differential equations that can be solved without iteration. This provides the explicit solver a powerful advantage to be implemented in such quasi-static problems with many contacts and large deformations. In other words, even though a given FE analysis on sand grains may require a large number of small time increments in the explicit package, the analysis can still be more computationally efficient in Explicit ABAQUS since large geometric changes due to contacts will require many iterations in each implicit ABAQUS time increment to achieve equilibrium. A common practice to speed up the explicit solver simulations in such rate-sensitive quasi-static problems is to apply a mass scaling factor that magnifies the mass of particles. An estimate of time increment size (Δt) in Explicit ABAQUS can be expressed as:

$$\Delta t = \sqrt{\frac{\rho}{E}} L^e \tag{3-7}$$

Where ρ is the material density, E is the modulus of elasticity, and L^e is the smallest element length. Therefore, an increase in mass (density) will increase the size of time increments that will result in reducing the total time scale of the simulation run. For example, an artificial increase in particles density by a factor f^2 will increase the size of time incrementation Δt by a factor of f. For the simulation reported in this chapter, a mass scaling factor of 10^6 was used to achieve a total simulation time of approximately one hour. In addition, ABAQUS takes advantage of parallel processing for the explicit solver that further speeds up the FE simulations. The kinetic energy of the deforming particles through the simulation was also checked to be less than 5% of the internal energy to ensure that the simulation yields an appropriate quasi-static response. Note that this limit was not fulfilled in the early stages of the simulation since deformable particles were moving freely until contacts were established to stabilize the granular system.

Meshed surface images (STL files) were imported into explicit ABAQUS through a plug-in tool. For each particle, the surface triangular elements were converted into 4-node tetrahedral elements producing solid filled particles. An isotropic elastic material model was assigned to elements of sand particles. Young's modulus of elasticity and Poisson's ratio of silica sand were assumed to be 91.1 GPa and 0.118, respectively (Heyliger et al., 2003). Then, particles were assembled (preserving the location of each particle to closely match the initial SMT image) into a discrete rigid mold and bounded by two discrete rigid end caps. A discrete rigid part represents a part that exhibits negligible deformation relative to the rest of the model and are ideally suited in ABAQUS to model tooling such as punch, mold, roller, cap, etc. The principal advantage of using discrete rigid parts over

deformable parts is the computational efficiency enhancement. Rigid parts in ABAQUS are associated with a node, called the rigid body reference point, in which its motion governs the motion of the entire rigid body. Therefore, the motion of a rigid part is completely determined by boundary conditions applied at the reference point rather than expensive element-level calculations. Rigid parts in ABAQUS have no element output variables due to the absence of element-level calculations. However, the only output from rigid elements is the motion of the nodes as well as nodal reaction forces. The mold and end caps diameters were assigned to be 1.04 mm and 1.02 mm, respectively, which is similar to the experimental setup based on measurements from the initial SMT scan.

Explicit ABAQUS General Contact Algorithm was adopted to define interaction properties between particles, particle-mold, and particle-end cap. The algorithm allows defining an inclusive surface that contains all exterior faces of deformable and rigid parts. In each configuration (i.e. time increment), the algorithm searches for slave node penetration including node-into-face and node-into-rigid surface penetration. For node-into-face contacts, forces which are a function of the penetration distance are applied to the slave nodes to oppose the penetration, while equal and opposite forces act on the master surface at the penetration point. Contact forces acting on the master surface are then distributed to the surface nodes. Similar formulation is implemented for node-into-rigid surface contacts with the equal and opposite contact forces always assigned to the rigid surface at the penetration point (i.e. reaction forces). Contact properties were assigned as part of contact interaction definition and were linked to the general contact domain. The chapter adopted the penalty contact formulation to simulate interactions between particles in which slippage is constrained by a tangential friction coefficient (μ) and hard normal behavior. The value of μ is attributed to the true angle of friction (ϕ_μ) that represents friction properties between mineral surfaces of the material (quartz for silica sand used in the experiments). ϕ_μ is assumed to be approximately 22° based on values reported in the literature for silica sand (Rowe, 1962) which yields a value of 0.4 for the friction coefficient μ (i.e. $\tan 22^0 \approx 0.4$). On the other hand, the normal behavior is attributed to the "spring" stiffness that relates the contact force to the penetration distance. For hard normal contact, a stiffness value is chosen automatically by Explicit ABAQUS such that the effect on time increments is minimal (i.e. allowed penetration is not significant in most of the analysis). Similar properties and formulation were estimated for particle-mold and particle-end cap interactions.

To mimic the experiment, the mold and bottom end cap were fixed with zero degrees of freedom while the top end cap was permitted to move in the vertical direction with one degree of freedom. The FE simulation was divided into two stages: seating and compression. In the seating stage, a seating load of 1 N was applied incrementally to the top cap in the vertical direction to introduce contacts between particles resulting in approximately 25 μm vertical displacement A 1 N load is a high seating value relative to the specimen dimensions. However, it is physically a very small measurement that was barely induced when contact occurs

between the loading plate and top end cap in the experiment. In FE simulations, a 1 N load was still barely enough to establish the contact between the top end cap and top particles. Furthermore, a seating load of 1 N was considered in the FE simulation to mimic the experiment. After seating the specimen in the FE simulations, the top end cap was programed to move in the vertical direction at a constant rate of 0.2 mm/min similar to the experimental loading rate.

Fracture of sand particles significantly affects the behavior of a granular assembly. The discrete nature of particles is a major factor that plays a significant role in understanding the mechanics of granular materials. This has already been proven by published research using DEM models. The discrete nature of particles can be characterized using several parameters such as sphericity, roundness, grain size distribution, etc. Each of these parameters is highly influenced by fracture of particles. In other words, fracture of particles in a loaded granular assembly completely change particles' sphericity, roundness, size, size distribution, etc. Accordingly, the mechanics of the granular assembly (e.g. global stress-strain response) is highly affected. A comprehensive understanding of sand response under loading cannot be fully understood without considering particle fracture phenomenon. A straight forward approach to simulate fracture of sand particles in Explicit ABAQUS is by applying the element deletion method based on a pre-defined damage criterion. The chapter adopted the brittle cracking model, which is a damage criterion where the material behavior is dominated by brittle tensile cracking. The brittle cracking model implements Rankine criterion to detect crack initiation where a crack forms when the maximum principal tensile stress exceeds a pre-defined maximum tensile strength limit (σ_{tu}^{I}). The crack surface is assumed to be normal to the direction of maximum principal tensile stress and the characteristic crack length is determined based on the considered element type and formulation (e.g. typically equal to the length of a line across an element for linear type mesh). This imposes mesh dependency on crack propagation while crack initiation is less sensitive to mesh refinement. The model aims to simulate behavior of particles under 1D compression which is more likely to be affected by crack initiation rather than crack propagation. Several trials were performed to calibrate the value of σ_{tu}^{I} based on comparison with experimental results (SMT scans), and calibration load-displacement curve of the top end cap. An optimum value of σ_{tu}^{I} was determined to be 750 MPa which yields the load-displacement calibration curve shown in Figure 3-2. The specimen behavior through the simulation is also depicted in Figure 3-3. It is important to emphasize that studies reported in literature suggest lower values for tensile strength of silica sand particles than the 750 MPa which was used in the FE simulations. For example, Cil and Alshibli (2012) constructed the Weibull Probability Distribution Function for tensile strength of silica sand grains according to experimental data and evaluated the 37% characteristic tensile strength of silica sand particles to be about 138 MPa. In the FE simulation conducted in this chapter, the 750 MPa is the maximum limit of principal tensile stress that elements can reach before deletion occurs. However, not all elements in the particle reached this limit when fracture occurs

(i.e. stress localization exists within the particle itself). On the other hand, the averaged maximum tensile stress of all elements in the particle was observed to be much less than $750\ MPa$.

Results

Force chains

Explicit ABAQUS provides contact forces at surface nodes for each particle. Initially, the surface of each particle was individually examined to determine surface nodal sets associated with each contact. Accordingly, contact forces of nodal sets forming each contact were summed up in which an equivalent contact force value was determined to act at the center of nodes. A weighted average of nodes' location with nodal contact forces as factor of importance was considered as the center of nodal sets associated with each contact (i.e. equivalent contact force location). Force equilibrium of each sand particle is fulfilled. In addition, pairs of contact forces were checked to be approximately equal in magnitude and opposite in direction. Location of contact pairs was also checked to match with minor differences (i.e. $\pm 0.5\ \mu m$). For further explanation on calculation of equivalent contact forces, Figure 3-4 shows an example of equivalent contact force calculation (magnitude, direction, and location) for contact C_{10-11} (contact between particle 10 and 11) at about 7% global axial strain.

As contact forces were quantified, transmission of forces was observed to occur through two main force chains. Force chains were detected based on maximum contact forces, particle assembly, stress concentrations, and quasi-linearity. The flow of major contact forces between the top and bottom end caps was tracked to identify force chains. For particles to be in a force chain, they must experience large stresses compared to other supporting particles. Since maximum principal stresses in the conducted simulations are mostly compressive stresses and ABAQUS code adopts a compression-negative sign convention, the maximum principal stress absolute ($\sigma_{abs.}$) was considered in stress level comparison between particles. In ABAQUS, $\sigma_{abs.}$ is defined as the largest value between the maximum and minimum principal stresses regardless of sign convention. In other words, particles associated with force chains must have $|\bar{\sigma}^{i}_{abs.}| > \frac{1}{R}\sum_{i=1}^{R}|\bar{\sigma}^{i}_{abs.}|$, where $\bar{\sigma}^{i}_{abs.}$ is the particle-level averaged maximum principal stress absolute of particle i and the summation runs over all particles in the assembly R. It is also important to emphasize on the quasi-linearity term in which the trajectories of $\bar{\sigma}_{abs.}$ for particles within a force chain must line up. A detailed description of the procedure followed in detection of force chains can be found in (Peters et al., 2005). The evolution of the two force chains is visualized in Figure 3-5 at different loading stages showing colored mesh contours of Von Mises Stress distribution through particles associated with force chains that were also experimentally identified in (Cil et al., 2017) based on particles with maximum averaged principal lattice strains. Figure 3-6 shows force chains based on 3DXRD experimental measurements versus FE model. It can be observed that force chains that were

identified by the FE model match within minor differences with force chains based on experiments, especially for the middle and bottom particles. Note that Cil et al. (2017) were unable to analyze the 3DXRD data for particle 31 due to possible crystal defects and the particle was only visualized in the SMT scans. Therefore, particle 31 may have caused the difference between the experiment and model quantified force chain II.

The two force chains were detected separately (i.e. no common particles) with approximately one particle separation distance (i.e. about 400 μm). Nonetheless, common supporting particles were observed to exist at certain vertical levels allowing interaction between the two detected force chains. For example, Figure 3-7 demonstrates parts of force chain I and II at about 7% global axial strain with particle 26 acting as a common supporting particle. Elemental trajectories of $\sigma_{abs.}$ are also plotted for each particle to illustrate stress flow within the two force chains. It can be observed from Figure 3-7 that particle 26 not only braces force chain I at particle 11 and force chain II at particle 34, but also provides a bridge that insures stress flow between both force chains which results in a preferential direction of $\sigma_{abs.}$ trajectories toward the horizontal plane.

A comparison between loading of particles associated with detected force chains versus other particles was assessed in Figure 3-8. Figure 3-8a isolates particle 11 with its surrounding particles (particles 12, 4, 26, and 10) and displays nodal contact forces at about 7% global axial strain. It is important to note that particles 12, 11, and 10 are associated with force chain I, while the other two particles (particles 4 and 26) are supporting particles. It can be observed from Figure 3-8a that contact forces between force chain particles are higher in value relative to contact forces with supporting particles. For further assessment, two particulate assemblies, each consists of 3 particles, were isolated in Figure 3-8b at about 7% global axial strain and plotted with $\sigma_{abs.}$ trajectory for each element. Note that both assemblies were selected at almost the same vertical level preserving their relative location as demonstrated in Figure 3-8b. Particles in the first assembly (i.e. particles 6, 12, and 11) were associated with force chain I, while particles in the second assembly (i.e. particles 17, 21, and 16) were not associated with any of the detected force chains. It can be noticed from Figure 3-8b that the assembly with force chain particles is subjected to higher stresses as well as a higher degree of line up of $\sigma_{abs.}$ trajectories in global compression direction (i.e. vertical direction). Again, this emphasizes on stress concentration and quasi-linearity terms that were adopted in detection of force chains.

Fracture Mode

Particles within force chains are more likely to fracture first as they experience higher contact stresses than other supporting particles. The FE simulation shows that Particle 6 in force chain I and particle 31 in force chain II are the first two particles to fracture. To assess the capabilities of the implemented fracture model, several particles (Particles 6, 31, 13, 27, and 28) with major fracture (fractured into two or more fragments) were tracked in the acquired SMT scans, isolated, and

compared with FE model predictions. Figure 3-9 visualizes experimental versus model fracture of selected particles where an excellent agreement was found between FE model prediction and experimental fracture modes.

For further assessment of fracture mode, particles 6 and 31 (first particles to fracture in force chains I and II) were isolated and visualized with surrounding particles before and after fracture as depicted in Figure 3-10. It can be observed that particles 6 and 31 fractured via two different failure modes. Referring to Figure 3-10(a), particle 6 fractured due to bending effect in which simple vertical supports were provided near edges by particles 12 and 5 while load was applied vertically at almost mid-length by particle 8, similar to a simply supported beam. As a result of bending effect, tensile stresses initiated in the bottom region of particle 6 which in turn caused the fracture. On the other hand, particle 31 was observed to be more confined between multiple particles in which load is transmitted vertically through the force chain by particles 32 and 1 while particles 27, 17, and 35 provided lateral supports against force chain buckling (Figure 3-10b). Particle 31 is supported by multiple particles that resulted in more even distribution of stresses through the whole particle elements which lead to particle fracture into several fragments (crushing) rather than breaking into just two major fragments as the case for particle 6. It can be observed from Figure 3-10b that fracture initiated from contact points between particle 31 and particles 1 and 32 which are all associated with force chain II.

Stress-Strain Relationships within Individual Particles

FE is considered as a powerful numerical modeling method since it provides quantitative estimations of stress and strain fields at each element. 3DXRD and SMT techniques have been successfully implemented to experimentally track and measure stress and strain within particles in a granular assembly (Cil et al., 2014, Hall and Wright, 2015b, Cil et al., 2017). However, such experimental particle-level measurements are still considered challenging since they require advanced and unique testing facilities. In this chapter, stress and strain components of elements constituting each particle were averaged based on elements' volumetric weights and an estimate of strain and stress tensor components per particle were computed as:

$$\bar{E} = \frac{\sum_{i=1}^{m} e_i V_i}{\sum_{i=1}^{m} V_i} \tag{3-8}$$

Where $\bar{E}$ is the particle-level averaged stress or strain tensor component, e is the stress or strain component of the individual element i, V is the volume of the considered element i, and the summation runs on all elements (m) forming the particle. Note that ABAQUS sets the volume of failed elements to 0 when the moment deletion occurs. Otherwise, volume of elements was exported in parallel with stress or strain components at each time step to compute the average estimate value. As estimates of particle-level averaged stress and strain tensors were evaluated, principal values and directions were then computed to be the tonsorial eigenvalues and eigenvectors, respectively. For example, Figure 3-11

shows the evolution of averaged principal stresses and strains of Particles 6 and 31 with respect to global axial strain. For particle 6, experimental measurements of principal stresses and strains that were reported in (Cil et al., 2017) are also plotted in Figure 3-11 which show a close match with the FE model predictions. Again, it is important to emphasize that particle 6 did not fracture at particle-level averaged maximum principal stress of $750\,MPa$ (i.e. value set for σ_{tu}^{I}) but at a much lower value around $70\,MPa$ versus experimental fracture around $90\,MPa$. This can be directly related to the localization of stresses within the particle itself. Beside particle-level averaged stress and strain estimates, FEM also provides the distribution of such estimates within the particle volume which can be used for further assessment of stress localization within the particle itself. For example, Figure 3-12 shows a histogram of maximum principal tensile stresses of particles 6 and 31 normalized by element numbers where a high percentage of elements within particle 6 are exposed to higher principal tensile stresses. Concurrently, elements exposed to low principal tensile stress are still more likely to exist within particle 6 than particle 31 (i.e. histogram steps of particle 31 levels more than particle 6). This can be explained by the two different fracture modes of particle 6 and 31. Particle 6 fractured as a result of tensile stress localization induced by bending effect due to bridging action. On the other hand, particle 31 fractured into multiple fragments by crushing due to higher confinement. Consequently, it is more likely to find more elements far from stress localization region within Particle 6 which are exposed to lower stresses. In other words, crushing action in particle 31 creates a better distribution of stresses between elements which levels down the histogram steps.

Summary and Conclusions

A FE approach that addresses the discrete nature of sand particles was adopted to simulate the 3D behavior of sand under 1D compression. The proposed approach captures 3D particles morphology and the effect of the discrete nature of sand in a continuum framework. 3D morphology of discrete particles was captured by extracting the exact shape of sand particles from the initial SMT scan images. Particles were individually meshed in AVIZO Fire 9.3 and were then used to generate the FE model in Explicit ABAQUS. A deformable isotropic linear elastic material model was used to investigate the behavior of sand particles. Transmission of vertical load was tracked to characterize force chains. The model captured the evolution of force chains to transmit the load between the top and bottom end caps while some of surrounding particles provided support against force chain buckling. The FE model gave an excellent prediction of force chains that compared well with experimental measurements based on 3DXRD data (Cil et al., 2017). Furthermore, fracture of sand particles was investigated in which an excellent agreement between experimental fracture and model fracture modes was observed. The fracture modes were also assessed using the powerful 3D visualization tool provided by ABAQUS software. Stress and strain field estimations were also calculated to better understand particles' fracture modes.

Two different fracture modes were observed to occur in two different particles (e.g. bending versus crushing). Fracture modes were found to be dependent on particle's boundary conditions that is induced by contacts with surrounding particles. Crushing failure mode was observed to occur under high boundary confinement while bending fracture mode occurs under less confinement and bridging action. Moreover, higher stress localization was observed to occur in bending fracture rather than crushing.

Acknowledgments

This material is based on work supported by the National Science Foundation under Grant No. CMMI- 1362510. Any opinions, findings, and conclusions or recommendations expressed in this material are those of the authors and do not necessarily reflect the views of the National Science Foundation. The SMT and 3DXRD images were collected using Beamline 1-ID at Argonne Photon Source (APS), Argonne National Laboratory. Use of the Advanced Photon Source, an Office of Science User Facility operated for the U.S. Department of Energy (DOE) Office of Science by Argonne National Laboratory, was supported by the U.S. DOE under Contract No. DE-AC02-06CH11357.

References

Dantu, P. (1957). In *The 4th international conference on soil mechanics and foundation engineering*.) Butterworths Scientific Publication, London, vol. vol 1, pp. p 133.

Drucker, D. C., Gibson, R. E. & Henkel, D. J. (1957) Soil mechanics and work hardening theories of plasticity. *Transactions of the American Society of Civil Engineers* **122**.

Wakabayashi, T. (1957) Photoelastic method for determination of stress in powdered mass. In *Japan National Congress for Appl. Mech.*), pp. p. 153.

Roscoe, K. H., Schofield, A. & Wroth, C. (1958) On the yielding of soils. *geotechnique* **8(1)**:22-53.

Rowe, P. W. (1962) The stress-dilatancy relation for static equilibrium of an assembly of particles in contact. In *Proceedings of the royal society of London a: mathematical, physical and engineering sciences*.) The Royal Society, vol. 269, pp. 500-527.

Dantu, P. (1968) Etude statistique des forces intergranulaires dans un milieu pulvérulent. *geotechnique* **18(1)**:50-55.

Jong, G. D. J. D. & Verruijt, A. (1969) étude photo-étlastique d'un empilement de disques. .

Cundall, P. A. & Strack, O. D. (1979) A discrete numerical model for granular assemblies. *geotechnique* **29(1)**:47-65.

Bouchaud, J.-P., Cates, M. & Claudin, P. (1995) Stress distribution in granular media and nonlinear wave equation. *Journal de Physique I* **5(6)**:639-656.

Liu, C., Nagel, S. R., Schecter, D., Coppersmith, S. & Majumdar, S. (1995) Force fluctuations in bead packs. *Science* **269(5223)**:513.

Coppersmith, S., Liu, C.-H., Majumdar, S., Narayan, O. & Witten, T. (1996) Model for force fluctuations in bead packs. *Physical review E* **53(5)**:4673.

Radjai, F., Jean, M., Moreau, J.-J. & Roux, S. (1996) Force distributions in dense two-dimensional granular systems. *Physical review letters* **77(2)**:274.

Eloy, C. & Clément, É. (1997) Stochastic aspects of the force network in a regular granular piling. *Journal de Physique I* **7(12)**:1541-1558.

Socolar, J. E. (1998) Average stresses and force fluctuations in noncohesive granular materials. *Physical review E* **57(3)**:3204.

Behringer, R., Howell, D., Kondic, L., Tennakoon, S. & Veje, C. (1999) Predictability and granular materials. *Physica D: Nonlinear Phenomena* **133(1)**:1-17.

Howell, D., Behringer, R. & Veje, C. (1999) Stress fluctuations in a 2D granular Couette experiment: a continuous transition. *Physical review letters* **82(26)**:5241.

Radjai, F., Roux, S. & Moreau, J. J. (1999) Contact forces in a granular packing. *Chaos: An Interdisciplinary Journal of Nonlinear Science* **9(3)**:544-550.

Mcdowell, G. & Harireche, O. (2002a) Discrete element modelling of soil particle fracture. *GEOTECHNIQUE-LONDON-* **52(2)**:131-136.

Mcdowell, G. & Harireche, O. (2002b) Discrete element modelling of yielding and normal compression of sand. *GEOTECHNIQUE-LONDON-* **52(4)**:299-304.
Edwards, S. & Grinev, D. (2003) Statistical mechanics of granular materials: stress propagation and distribution of contact forces. *Granular Matter* **4(4)**:147-153.
Geng, J., Reydellet, G., Clément, E. & Behringer, R. (2003) Green's function measurements of force transmission in 2D granular materials. *Physica D: Nonlinear Phenomena* **182(3)**:274-303.
Heyliger, P., Ledbetter, H. & Kim, S. (2003) Elastic constants of natural quartz. *The Journal of the Acoustical Society of America* **114(2)**:644-650.
Ng, T.-T. (2004) Triaxial test simulations with discrete element method and hydrostatic boundaries. *Journal of engineering mechanics* **130(10)**:1188-1194.
Majmudar, T. S. & Behringer, R. P. (2005) Contact force measurements and stress-induced anisotropy in granular materials. *Nature* **435(7045)**:1079.
Peters, J., Muthuswamy, M., Wibowo, J. & Tordesillas, A. (2005) Characterization of force chains in granular material. *Physical review E* **72(4)**:041307.
Tordesillas, A. (2007) Force chain buckling, unjamming transitions and shear banding in dense granular assemblies. *Philosophical Magazine* **87(32)**:4987-5016.
Cheung, G. & O'sullivan, C. (2008) Effective simulation of flexible lateral boundaries in two-and three-dimensional DEM simulations. *Particuology* **6(6)**:483-500.
Belheine, N., Plassiard, J.-P., Donzé, F.-V., Darve, F. & Seridi, A. (2009) Numerical simulation of drained triaxial test using 3D discrete element modeling. *Computers and Geotechnics* **36(1)**:320-331.
Mahabadi, O., Grasselli, G. & Munjiza, A. (2009) Numerical modelling of a Brazilian Disc test of layered rocks using the combined finite-discrete element method. In *RockEng09: 3rd Canada–US rock mechanics symposium, Toronto–Canada*.), vol. 9, pp. 2009.
O'sullivan, C. & Cui, L. (2009) Micromechanics of granular material response during load reversals: combined DEM and experimental study. *Powder Technology* **193(3)**:289-302.
Hasan, A. & Alshibli, K. A. (2010) Discrete element modeling of strength properties of Johnson Space Center (JSC-1A) lunar regolith simulant. *Journal of Aerospace Engineering* **23(3)**:157-165.
Lisjak, A. & Grasselli, G. (2010) Rock impact modeling using FEM/DEM. In *Discrete element methods: 5th international conference on discrete element methods. London–UK*.), pp. 25-26.
Lu, Y. & Frost, D. (2010) Three-dimensional DEM modeling of triaxial compression of sands. In *Soil Behavior and Geo-Micromechanics*.), pp. 220-226.
Mahabadi, O., Cottrell, B. & Grasselli, G. (2010) An example of realistic modelling of rock dynamics problems: FEM/DEM simulation of dynamic Brazilian test on Barre granite. *Rock mechanics and rock engineering* **43(6)**:707-716.

Rougier, E., Knight, E., Sussman, A., Swift, R., Bradley, C., Munjiza, A. & Broome, S. (2011) The combined finite-discrete element method applied to the study of rock fracturing behavior in 3D. In *45th US Rock Mechanics/Geomechanics Symposium*.) American Rock Mechanics Association.

Yang, G., Yu, T. & Hanlong, L. (2011) Numerical simulation of undrained triaxial test using 3D discrete element modeling. In *Instrumentation, Testing, and Modeling of Soil and Rock Behavior*.), pp. 99-106.

Andrade, J. E. & Avila, C. F. (2012) Granular element method (GEM): linking inter-particle forces with macroscopic loading. *Granular Matter* **14(1)**:51-61.

Cil, M. & Alshibli, K. (2012) 3D assessment of fracture of sand particles using discrete element method. *Géotechnique Lett* **2(3)**:161-166.

Clark, A. H., Kondic, L. & Behringer, R. P. (2012) Particle scale dynamics in granular impact. *Physical review letters* **109(23)**:238302.

Mahabadi, O., Lisjak, A., Munjiza, A. & Grasselli, G. (2012) Y-Geo: new combined finite-discrete element numerical code for geomechanical applications. *International Journal of Geomechanics* **12(6)**:676-688.

Cil, M. B., Alshibli, K., Kenesei, P. & Lienert, U. (2014) Combined high-energy synchrotron x-ray diffraction and computed tomography to characterize constitutive behavior of silica sand. *Nuclear Instruments and Methods in Physics Research Section B: Beam Interactions with Materials and Atoms* **324**:11-16.

Hurley, R., Marteau, E., Ravichandran, G. & Andrade, J. E. (2014) Extracting inter-particle forces in opaque granular materials: beyond photoelasticity. *Journal of the Mechanics and Physics of Solids* **63**:154-166.

Brodu, N., Dijksman, J. A. & Behringer, R. P. (2015) Spanning the scales of granular materials through microscopic force imaging. *Nature communications* **6**.

Hall, S. A. & Wright, J. (2015) Three-dimensional experimental granular mechanics. *Geotech. Lett.* **5**:236.

Druckrey, A. M. & Alshibli, K. A. (2016) 3D finite element modeling of sand particle fracture based on in situ x-ray synchrotron imaging. *Int. J. Numer. Anal. Methods Geomech.* **40**:105.

Hurley, R., Hall, S., Andrade, J. & Wright, J. (2016) Quantifying interparticle forces and heterogeneity in 3D granular materials. *Physical review letters* **117(9)**:098005.

Kawamoto, R., Andò, E., Viggiani, G. & Andrade, J. E. (2016) Level set discrete element method for three-dimensional computations with triaxial case study. *Journal of the Mechanics and Physics of Solids* **91**:1-13.

Zhang, L., Nguyen, N. G. H., Lambert, S., Nicot, F., Prunier, F. & Djeran-Maigre, I. (2016) The role of force chains in granular materials: from statics to dynamics. *European Journal of Environmental and Civil Engineering*:1-22.

Cil, M. B., Alshibli, K. A. & Kenesei, P. (2017) 3D Experimental Measurement of Lattice Strain and Fracture Behavior of Sand Particles Using Synchrotron

x-ray Diffraction and Tomography. *Journal of Geotechnical and Geoenvironmental Engineering* **143(9)**.

Appendix

Appendix A: Figures

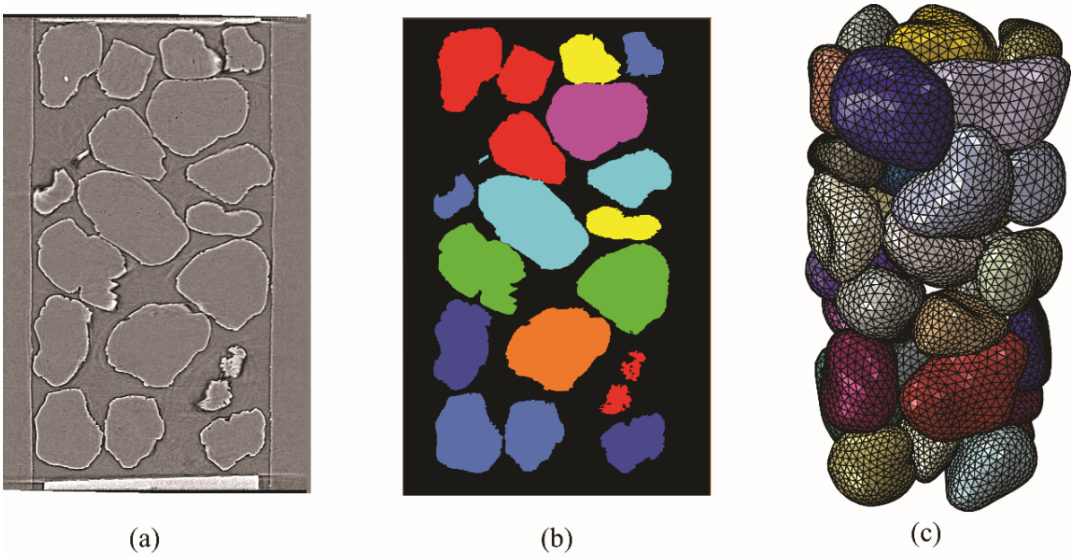


Figure 3-1. Axial slice through the initial SMT scan: (a) grayscale image; (b) labeled image; and (c) 3D view of the generated surface mesh.

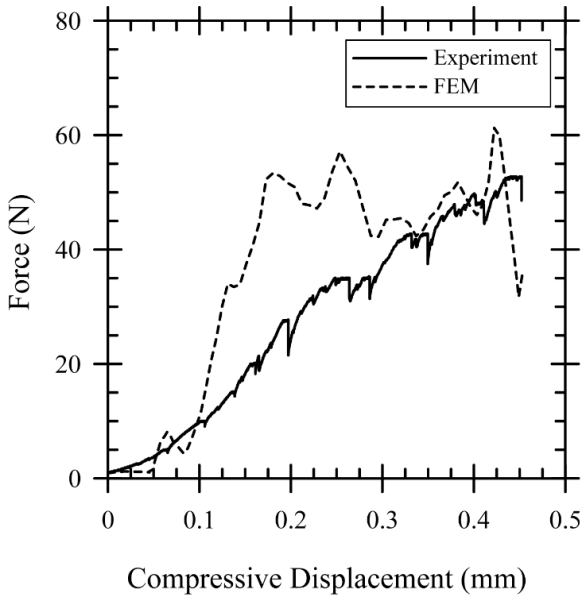


Figure 3-2. Global compressive displacement versus force calibration curve of the top end cap.

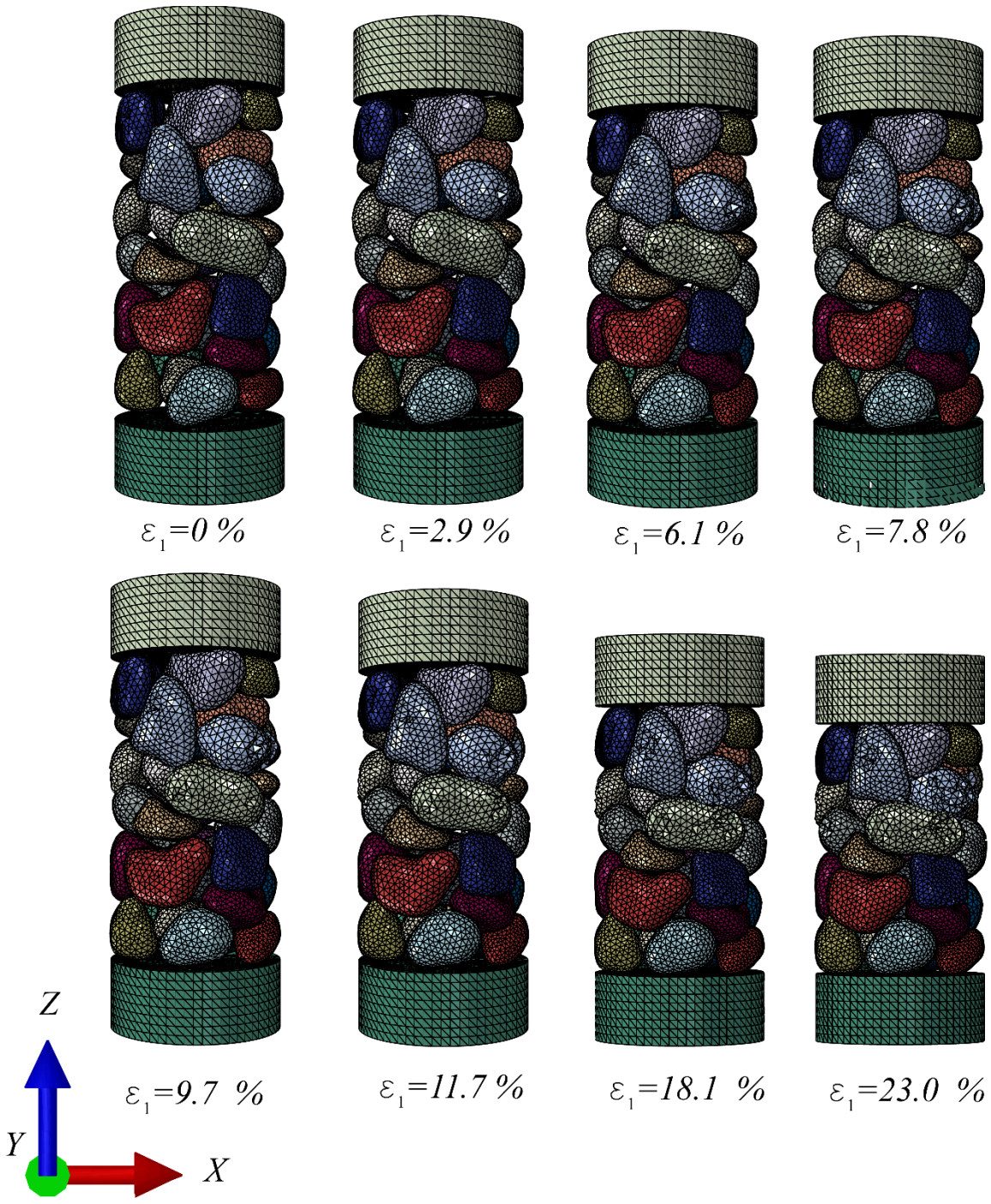
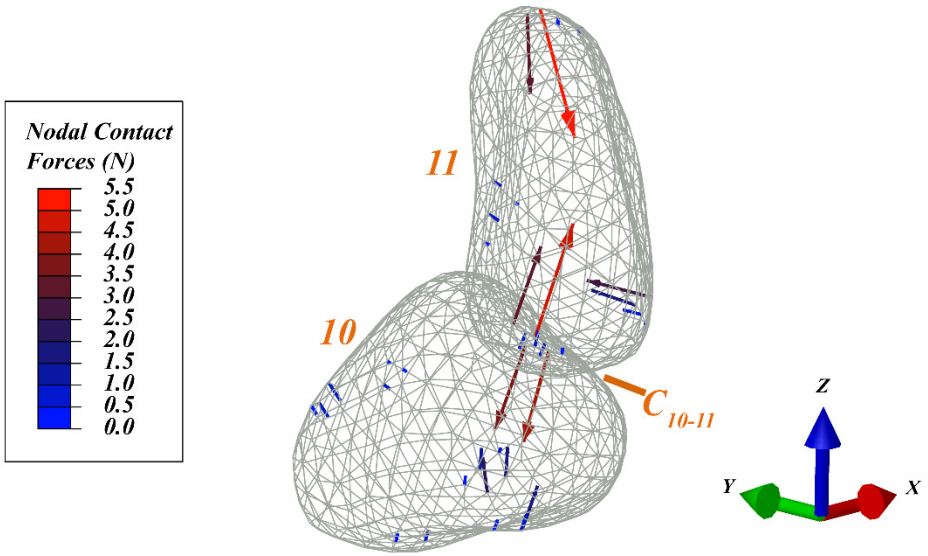


Figure 3-3. Specimen behavior using FE simulation in which surrounding mold is hidden for better visualization (ε_1 refers to the global axial strain).

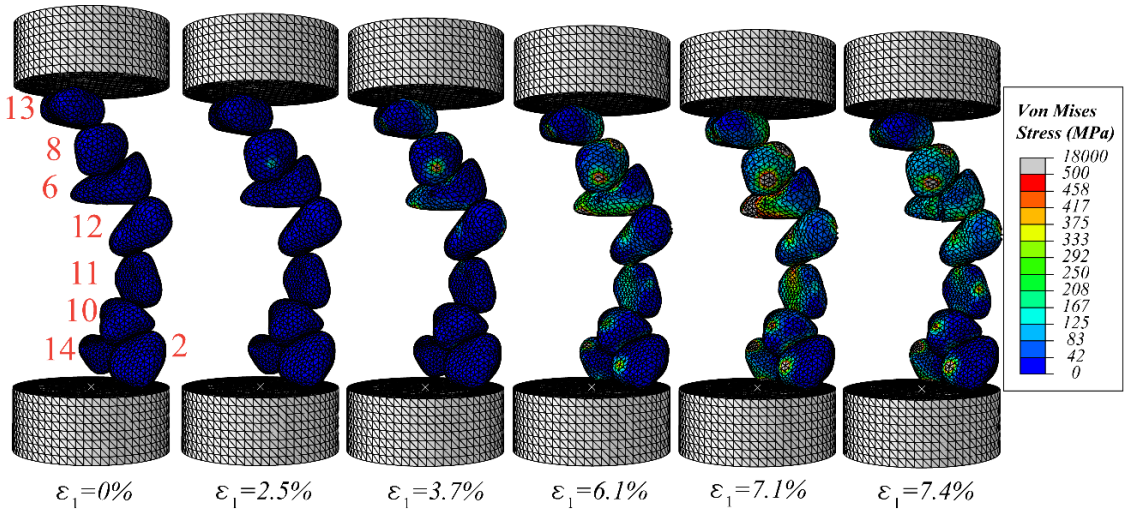


Equivalent Force Calculation Example of Contact $C_{10\text{-}11}$

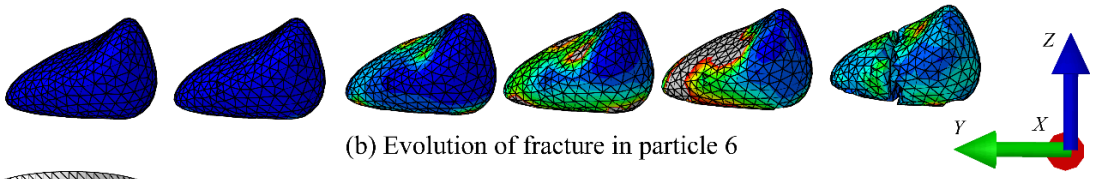
Particle Number	Node ID	Contact Force F_x (N)	Contact Force F_y (N)	Contact Force F_z (N)	Coordinate X (μm)	Coordinate Y (μm)	Coordinate Z (μm)
10	1868	-0.119	0.206	-0.620	278.948	-280.932	437.130
10	2036	-0.134	0.231	-0.695	252.582	-274.651	457.485
10	1801	-0.220	1.058	-4.063	257.032	-300.733	440.399
10	1990	-0.713	0.884	-3.508	227.279	-292.498	456.856
		-1.186	***2.380***	***-8.885***	***240.859***	***-293.424***	***448.005***
		Equivalent Contact Force (Summation over nodes)			*Coordinates of Equivalent Contact Force (Weighted average over nodes with forces as factor of importance)*		

Particle Number	Node ID	Contact Force F_x (N)	Contact Force F_y (N)	Contact Force F_z (N)	Coordinate X (μm)	Coordinate Y (μm)	Coordinate Z (μm)
11	105	0.024	-0.148	0.674	235.188	-317.093	438.723
11	243	0.646	-0.801	3.178	225.856	-290.508	458.559
11	129	0.535	-1.369	4.729	260.428	-290.989	443.366
11	17	-0.018	-0.062	0.307	269.278	-324.703	428.429
		1.186	***-2.380***	***8.888***	***240.951***	***-293.321***	***447.931***
		Equivalent Contact Force (Summation over nodes)			*Coordinates of Equivalent Contact Force (Weighted average over nodes with forces as factor of importance)*		

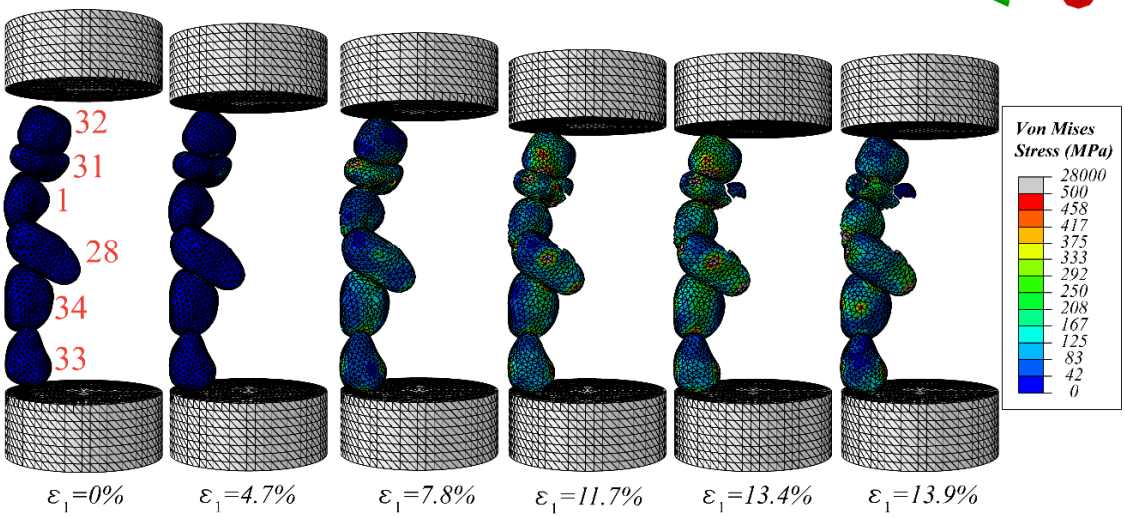
Figure 3-4. Illustrative example of equivalent contact force calculations between particle 10 and 11 at about 7% global axial strain.



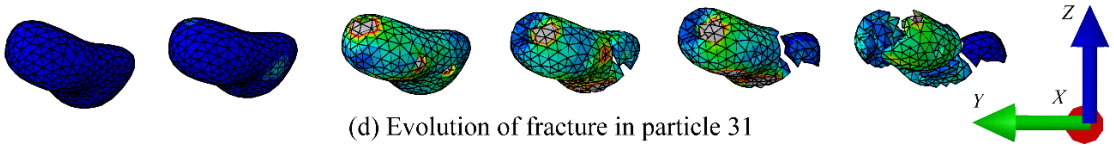
(a) Evolution of force chain I



(b) Evolution of fracture in particle 6



(c) Evolution of force chain II



(d) Evolution of fracture in particle 31

Figure 3-5. Evolution of (a) force chain I; (b) fracture in particle 6; (c) force chain II; and (d) fracture in particle 31. Surrounding mold is hidden for better visualization (ε_1 refers to the global axial strain).

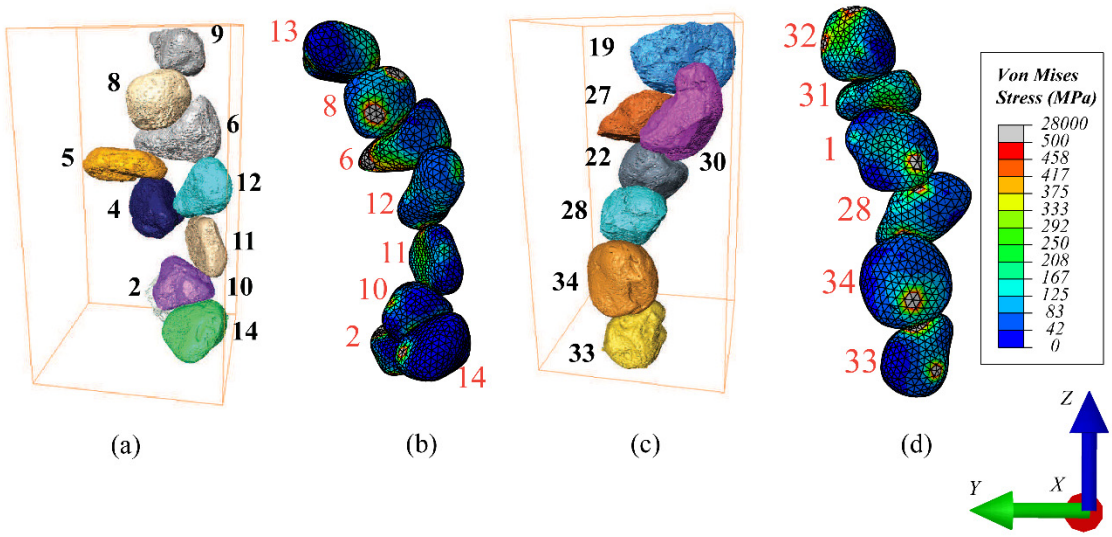


Figure 3-6. Comparison between (a) experimental force chain I; (b) model force chain I; (c) experimental force chain II; and (d) model force chain II.

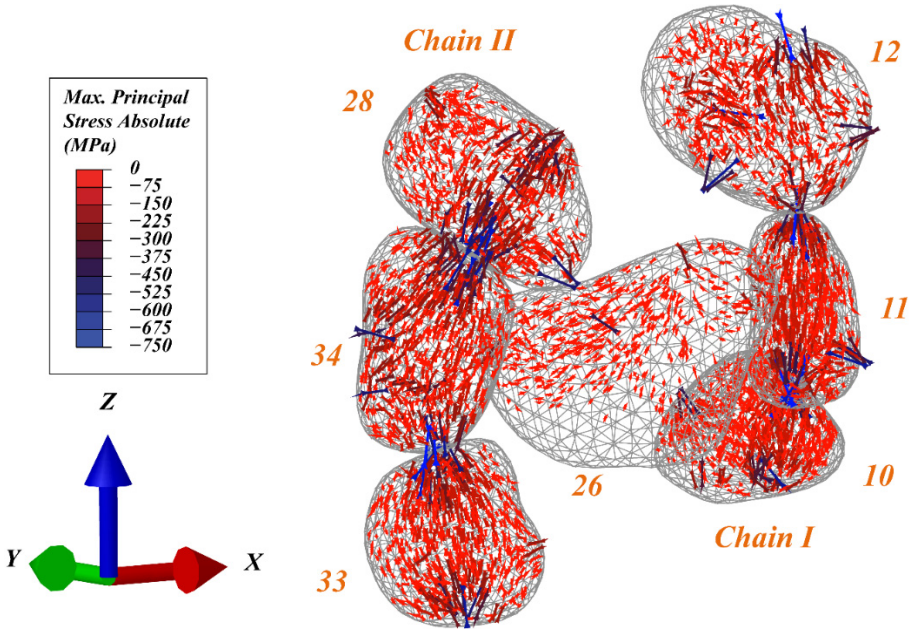


Figure 3-7. Visualization of interaction between force chain I and II through a common supporting particle #26 at about 7% global axial strain.

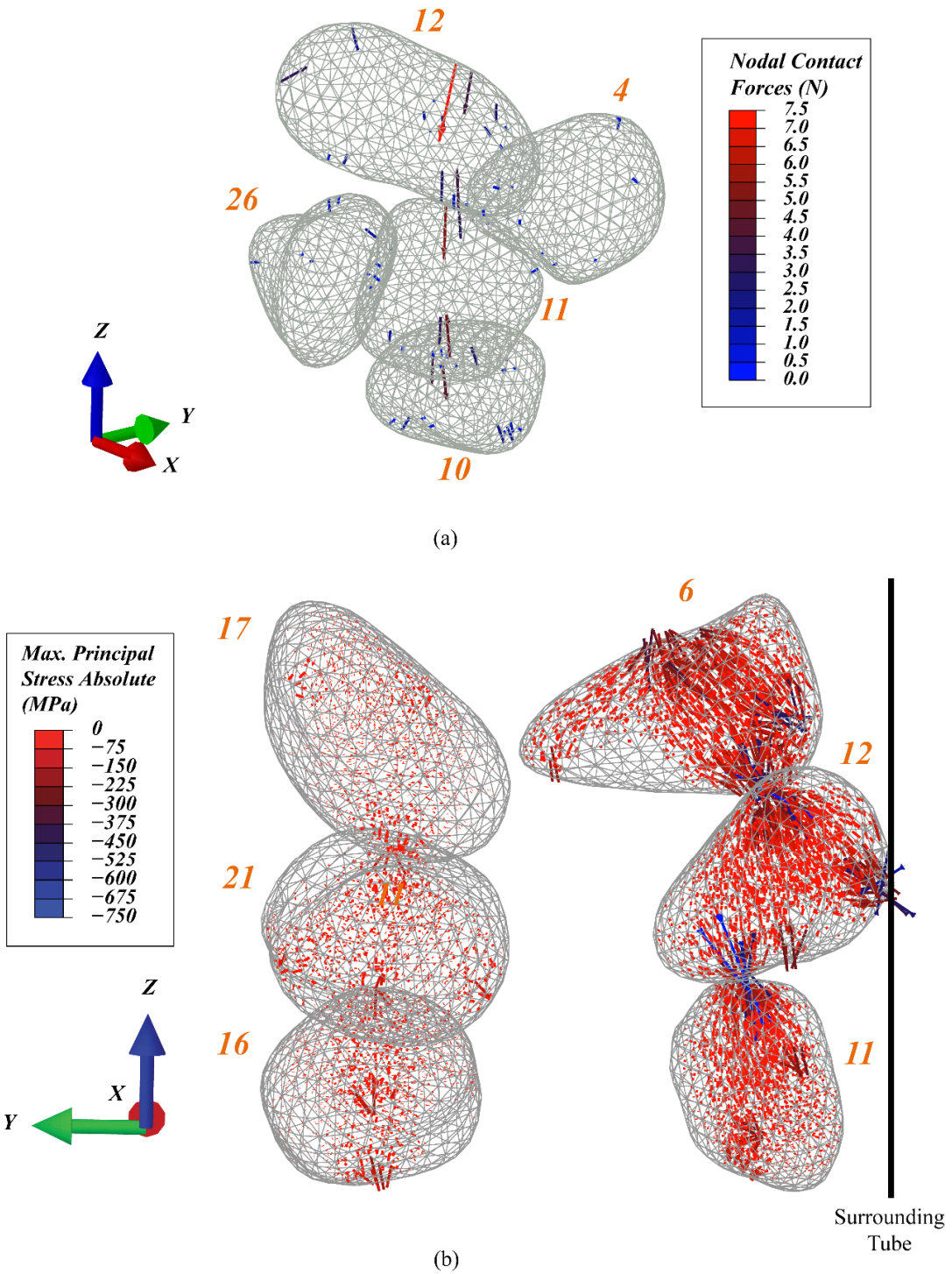
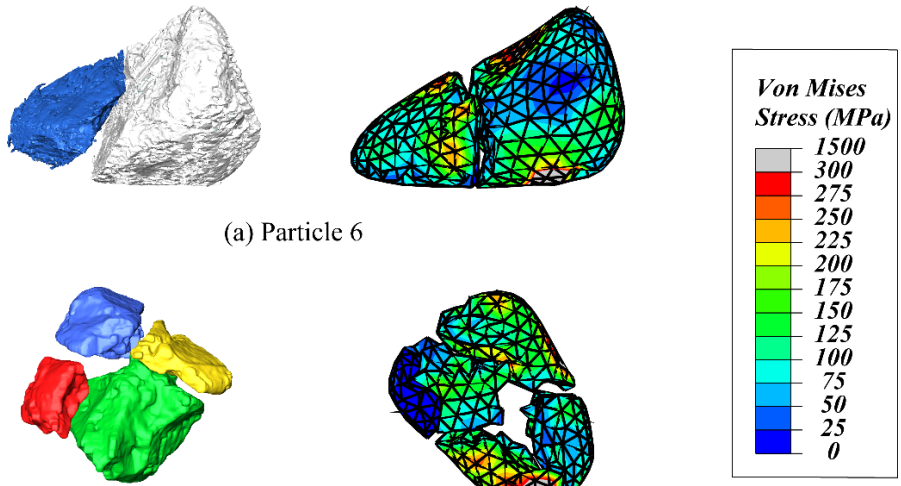


Figure 3-8. (a) Nodal contact forces between particle 11 and its surrounding particles and (b) stress flow in an assembly associated with force chain I and another assembly not associated with any of the detected force chains at about 7% global axial strain.



(a) Particle 6

(b) Particle 31

(c) Particle 13

(d) Particle 27

(e) Particle 28

Figure 3-9. Visualization and comparison between experimental versus model fracture of (a) Particle 6; (b) Particle 31; (c) Particle 13; (d) Particle 27; and (e) Particle 28.

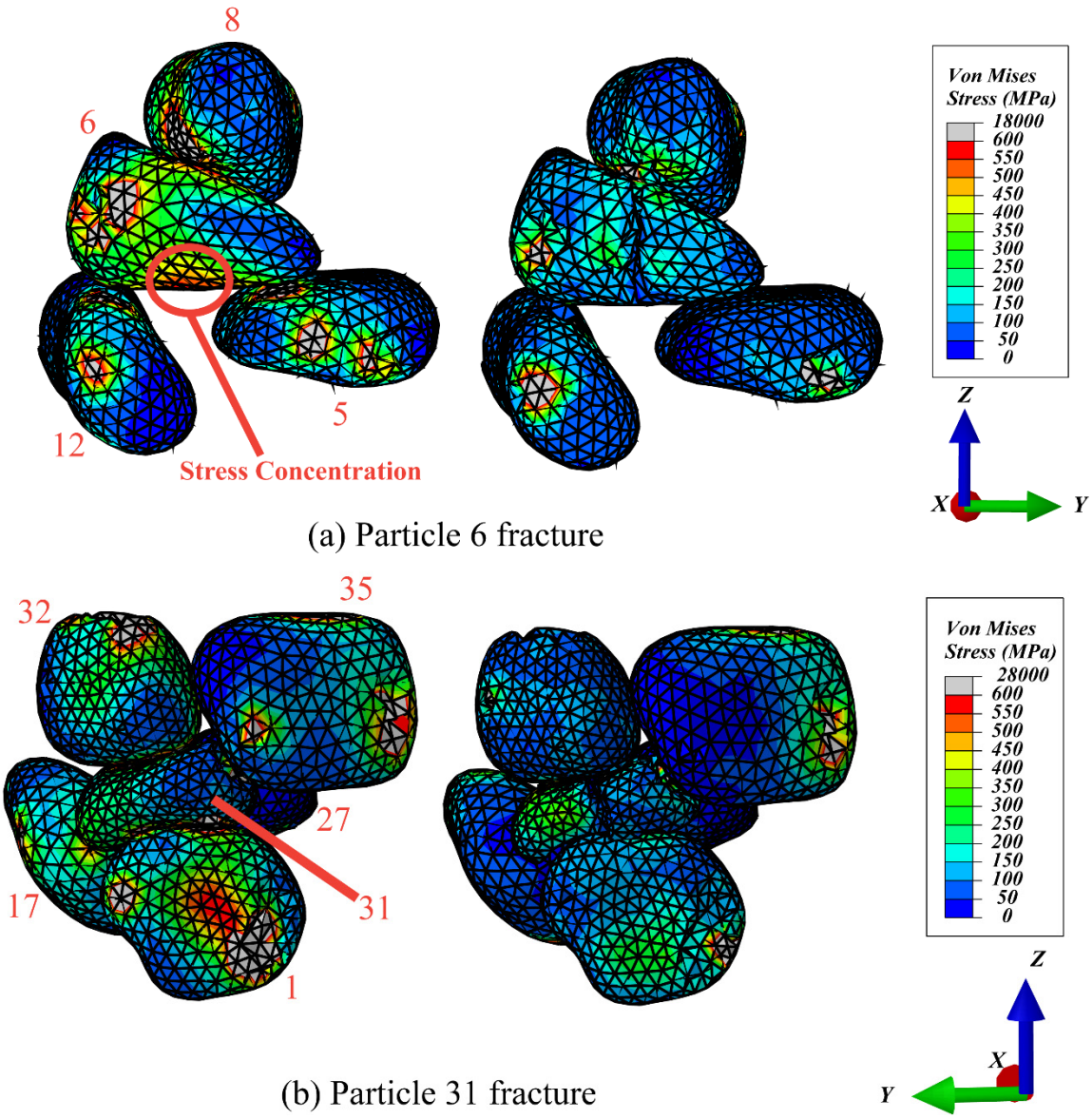


Figure 3-10. FE model fracture assessment for (a) Particle 6 (b) Particle 31.

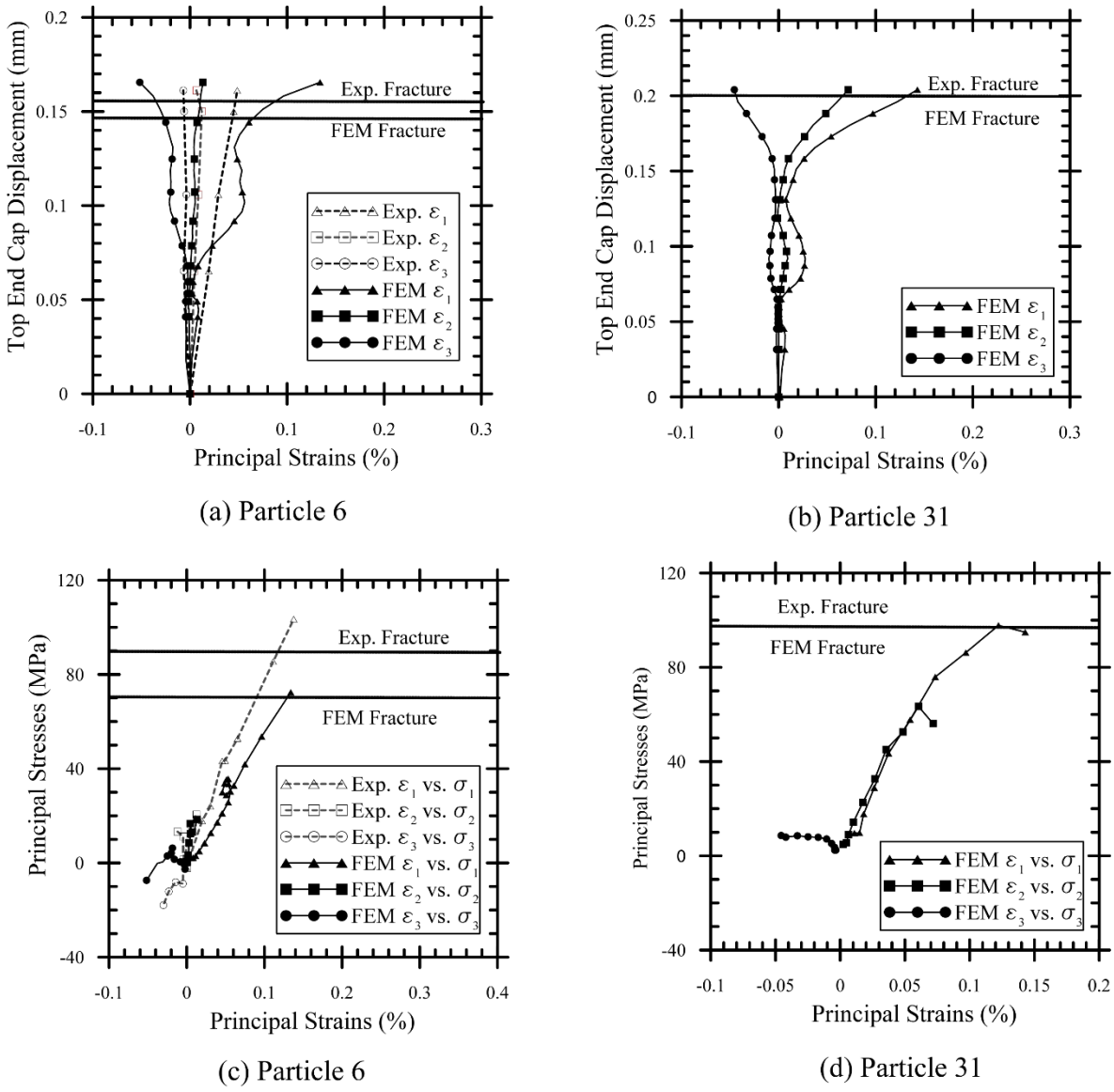


Figure 3-11. Evolution of principal stresses and strains within Particles 6 and 31.

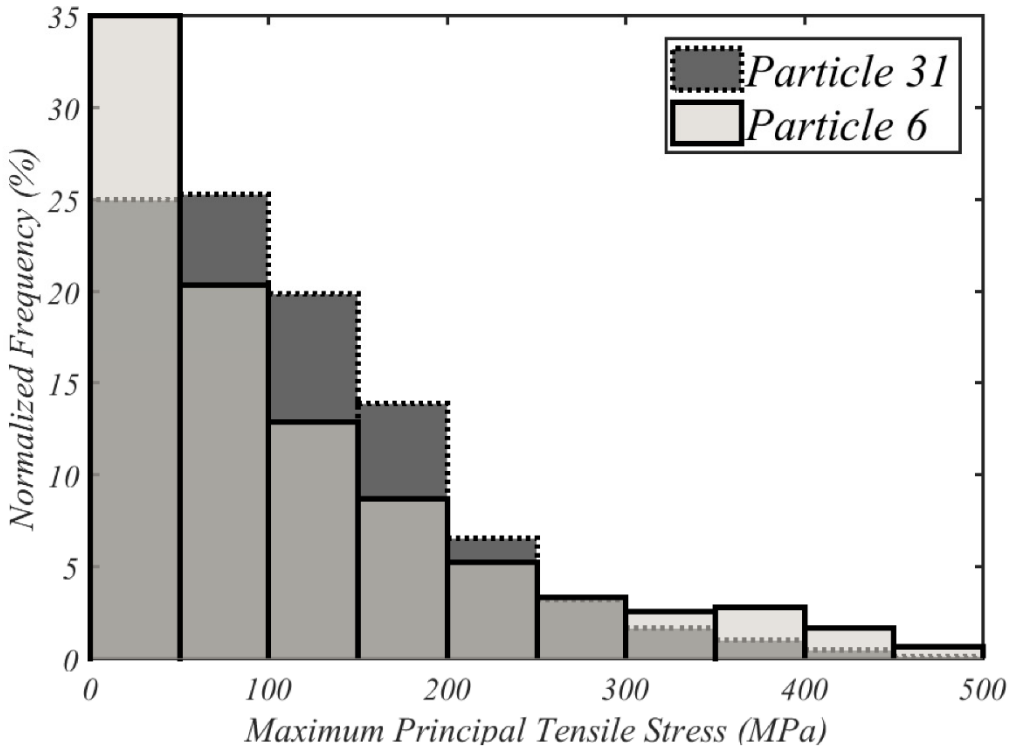


Figure 3-12. Histogram of maximum tensile principal stress distribution of particles 6 and 31.

CHAPTER FOUR

INFLUENCE OF SAND MORPHOLOGY ON INTER-PARTICLE FORCE AND STRESS TRANSMISSION USING 3D DISCRETE AND FINITE ELEMENT METHODS

A version of this chapter is currently under review as Imseeh, W. H., Jarrar, Z. A. & Alshibli, K. A. “Influence of Sand Morphology on Inter-Particle Force and Stress Transmission Using Three-Dimensional Discrete and Finite Element Methods". *Geotehcnique.* In this chapter, all the data analysis and figures/sub-figures related to the Discrete Element Method were originally generated by my research colleague Zaher A. Jarrar.

Abstract: In the last two decades, particle morphology has emerged as an essential and critical property for proper evaluation of the constitutive behavior of granular materials. When a mass of sand is loaded in a confined compression, a complex network of force chains develops and evolves to resist the applied stresses. Force chains have been extensively studied in the literature using the discrete element method (DEM) and to a lesser extent using the finite element method (FEM). This chapter investigates the influence of three-dimensional (3D) sand morphology on the onset and evolution of force chains within sand using both 3D DEM and FEM simulations. In-situ synchrotron micro-computed tomography (SMT) technique was utilized to acquire multiple 3D scans of a specimen composed of natural silica sand that was loaded under one-dimensional (1D) confined uniaxial compression. The SMT scans were processed and used to calibrate the model parameters for both DEM and FEM simulations, where particle sizes and shapes closely matched the natural morphology and fabric of sand particles within the tested specimen. In another virtual specimen, individual sand particles were substituted with equivalent spherical particles that have the same volume and center of mass. FEM and DEM simulations were then executed on the virtual specimen using the same model parameters that were calibrated by the tested sand specimen. A comparison between the simulated results of the virtual and tested specimens revealed a stiffer boundary response of reaction load versus displacement at the top loading platen of the specimen composed of particles with sand-like shapes. On the contrary, a micro-scale assessment showed higher particle stresses and inter-particle contact forces between the spherical particles than the sand-like particles under the same specimen boundary load at the top loading platen. The results of the chapter advocate for the importance of modeling the actual sand morphology in search of an accurate numerical prediction of inter-particle contact forces, particle stresses, and development of force chains in sands.

Keywords: Force chains, sand morphology, inter-particle contact forces, particle stresses, discrete element method, and finite element method.

Introduction

Sand consists of discrete particles that have complex morphology and particle-to-particle interaction. Compressive loads applied on the boundary of a sand specimen are internally resisted by a skeleton of particles forming complex networks of mutual compressive forces. There are networks of high contact stresses transmitted through some interaction between particles to form what is commonly known as force chains. In the published literature, force chains were investigated experimentally using two common techniques; namely photoelastic granular materials (Dantu, 1957, Wakabayashi, 1957, Jong and Verruijt, 1969, Behringer et al., 1999, Howell et al., 1999, Geng et al., 2003, Majmudar and Behringer, 2005, Daniels and Hayman, 2008, Clark et al., 2012, Zhang et al., 2014, Mahabadi and Jang, 2017, Zadeh et al., 2019) and propagation of sonic waves (Liu, 1994, Coste et al., 1997, Jia et al., 1999, Daraio et al., 2005, Sen et al., 2008, Owens and Daniels, 2011, Bassett et al., 2012). Most of the studies mentioned earlier reported a dual force network with strongly and weakly loaded particles. However, these studies utilized granular assemblies of synthetic particles (photoelastic material, steel, and Teflon) with simple geometry [two-dimensional (2D) discs or three-dimensional (3D) spherical particles], which differ from natural sand particles.

Recently, 3D x-ray diffraction (3DXRD) and synchrotron micro-computed tomography (SMT) techniques were used to characterize force chains for 3D granular assemblies composed of synthetic silica spherical particles (Hurley et al., 2016) as well as natural sand particles (Cil et al., 2017, Amirrahmat et al., 2020). 3DXRD enabled measuring the lattice strains within the particles subjected to a confined uniaxial compressive loading. Converting lattice strains to stresses identified highly stressed particles that resisted the majority of the applied boundary loads. Inter-particle contact forces were also calculated from the lattice stress of individual particles using basic newton mechanics and the balance of linear momentum (Andrade and Avila, 2012, Hurley et al., 2014). Under one-dimensional (1D) confined uniaxial compression, the distribution of inter-particle contact forces between synthetic silica spherical (Hurley et al., 2017) as well as angular particles (Hurley et al., 2018b) was assessed to follow an exponential decay with an increase in homogeneity while loading and a dramatic decrease in homogeneity with unloading.

In addition to experimental characterization of the force chains, many numerical models have been reported in the literature to investigate the rheology of granular materials such as the q scaler model (Coppersmith et al., 1996), phenomenological models (Bouchaud et al., 1995), and contact/molecular dynamic simulations (Radjai et al., 1996, Radjai et al., 1999). The discrete element method (DEM) (Cundall and Strack, 1979) has emerged a powerful numerical approach to quantify the properties of force chains within granular materials. Radjai et al. (1998) used DEM to analyze a 2D pack of rigid discs under biaxial compression. They reported that the contact force network was unambiguously decomposed into two complementary sub-networks called weak and strong. The weak sub-network

included the majority of discs and exhibited contact forces less than the average of the whole population of contact forces within the assembly. On the other hand, fewer discs formed the strong sub-network that carried contact forces above the average of the whole population. Peters et al. (2005) proposed a procedure that quantified force chains in DEM using the major principal stress of 2D discs that were subjected to indentation by a rigid flat punch. O'Sullivan and Cui (2009) utilized DEM to model the response of spherical steel particles exposed to cycles of loading-unloading in a conventional triaxial compression (CTC). They reported that the cyclic response of the spherical particles involved a substantial redistribution in the inter-particle contact forces. Guo (2012) used DEM to model the buckling of a single chain composed of mono-sized ellipsoidal particles, and they reported a critical buckling length of the chain. In summary, most of the studies published in the literature relied on 2D discs or 3D spherical/ellipsoidal particles to characterize the force chains in sands. Yet, there is little knowledge about the difference in the behavior of spherical versus complex shape particles like natural sands.

Published literature widely acknowledged the influence of sand morphology on particle friction (Yousuff and Page, 1993, Santamarina and Cho, 2004, Vangla and Latha, 2015, Vangla and Gali, 2016), rearrangement (Pena et al., 2007, Shin and Santamarina, 2012, Kandasami and Murthy, 2017), interlocking (Guo and Su, 2007, Azéma et al., 2013), and fracture (Nakata et al., 2001, Cavarretta and O'sullivan, 2012, Wang and Coop, 2016). Recognizing the importance of sand morphology motivated many researchers to enhance the resemblance of sand particles in DEM with their actual shape. These efforts included numerical formulation of particle kinematics for ellipsoids (Yan et al., 2010) and poly-ellipsoids (Zhang et al., 2018), filling surface meshes that closely match the morphology of sand particle with agglomerates of bonded spheres (Cil and Alshibli, 2015, Fu et al., 2017), and clumping of sub-spheres into unbreakable 2D (Lu and Frost, 2010) as well as 3D particles (Ferellec and McDowell, 2010, Gao et al., 2012, Li and McDowell, 2018). Level-set functions were also used to map the complex surface of sand particles (Kawamoto et al., 2016) and were successfully implemented in DEM to predict shear bands for simulations of CTC experiments (Kawamoto et al., 2018). In addition to the DEM, the finite element method (FEM) has been recently utilized to model the interaction between 3D deformable meshes that closely matches the shape of natural sand particles (Imseeh and Alshibli, 2017). The main advantage of the FEM simulation emerged from its ability to accurately capture the complex 3D morphology and particle-to-particle interaction in sand specimens as well as the potential of modeling particle breakage in sand from a fracture mechanics perspective (Druckrey and Alshibli, 2016, Turner et al., 2016, Zhou et al., 2020).

This chapter examines the influence of 3D sand morphology on the onset and evolution of force chains within sand using both 3D DEM and FEM. The chapter demonstrates how DEM and FEM can simulate sand particles that closely match the actual 3D morphology of sand acquired from in-situ SMT imaging. Numerically

simulated results emphasize the significant role of particle morphology in determining the constitutive behavior of sand from a micro-scale point of view.

Experiment and In-Situ SMT Scans

A specimen composed of natural silica sand, known as Ottawa ASTM 20-30, was tested and scanned in this chapter. Ottawa ASTM 20-30 is classified as a poorly graded sand (uniform) with rounded particles ranging in size between US sieve #20 (0.841 mm) and #30 (0.595 mm). The sand particles were deposited inside a cylindrical confining mold that is made of aluminum and measuring 4.5 mm in diameter. The confined specimen was vertically (axially) loaded using a special test cell under quasi-static loading rate of 0.2 mm/minute. The test cell was mounted on the stage of beamline 13BMD of the Advanced Photon Source (APS), Argonne National Laboratory (ANL), Illinois, USA. The experiment was paused at prescribed vertical loads of 0, 200, 400, and $500\,N$ to collect 900 radiograph images at rotational increments of 0.2°. The radiographs were then reconstructed into 3D slice-structured images with a spatial resolution of $7.11\,\mu m$ per pixel. Figure 4-1a depicts a schematic sketch of the experimental setup, and Figure 3-1b shows the vertical load versus displacement relationship that was recorded by the test cell at the top loading platen. The diamond-shaped markers in Figure 3-1b denote the load steps at which the experiment was paused to acquire the SMT scans.

The SMT scans were processed using AVIZO Thermo Fisher Scientific, commercial computer software for high-performance 3D image visualization and analyses. The procedure of image processing is outlined in Druckrey et al. (2016) and included several modules such as anisotropic diffusion filtering, interactive thresholding, watershed segmentation, and particle labeling. Briefly, sand particles within the scanned specimen were separated from one another, and a unique numerical label was assigned to each particle. The processed images represented a confined sand specimen with an initial height of 7 mm and containing 236 particles. Figure 3-1c shows 3D volume rendering images of the scanned specimen at different loading steps. The fracture onset of 4 sand particles was observed in the last scan that was collected at a vertical compressive load of 500 N.

The morphology of sand particles was characterized using the aspect ratio (the ratio between 3D length to width). Sand particles in the initial-state image (0 N) were individually projected on 2D planes by a certain angle, and the distance between the outermost tangents of projections was calculated to represent the 3D Feret diameter of that angle. Multiple 3D Feret diameters were computed with a sampling of 31 angles regularly spread in 3D space around the upper part of a unit sphere. The 3D length and width were determined as the longest and shortest of the 3D Feret diameters, respectively. Figure 3-2a presents the grain size distribution (GSD) curves of the scanned specimen that were plotted using the particles' 3D width, length, and equivalent diameter. The equivalent diameter was computed as the diameter of a sphere with an equal volume to the sand particle. The particle sizes claimed by the sand supplier company (between US sieve #20

and #30) were in agreement with the GSD curves that were plotted using the particles' 3D width as well as the equivalent diameter. Figure 3-2b displays a histogram distribution of the aspect ratio of the sand particles within the scanned specimen, which ranged between 1.2 and 2. Figure 3-2c presents 3D volume rendering of a few representative sand particles along with their equivalent diameter spheres.

3D DEM and FEM Simulations

The main objective of this section is to describe the FEM and DEM numerical models that were used to simulate the uniaxial compression experiment. The analyses focus on assessing micro-scale measurements that are difficult to experimentally acquire for sand specimens such as the distribution of inter-particle contact forces, particle stresses, and development of force chains. The experimental evaluation of these micro-scale measurements requires expensive techniques such as 3DXRD with a few assumptions such as homogeneous material mineralogy, ideal crystal structure of the sand particles, and no defects in the particles. The state-of-the-art numerical simulations are cost-effective, provide insights into such micro-scale measurements of sand specimens, and overcome the problem with material and experimental imperfections that might lead to misleading results. Moreover, several micro-scale properties of sand are fully adjustable by the numerical simulations, whereas it is impractical to experimentally control the morphology of individual particles in a sand specimen. Particle Flow Code (PFC3D) was used to conduct the DEM simulations, while the FEM simulations were developed using ABAQUS/CAE software. Both methods implemented different procedures for modeling the discrete nature of sand at the particle-level calculations of stresses and forces. The following sub-sections describe the procedures and assumptions adopted in each of the two numerical methods.

For each particle in the scanned specimen (Figure 3-3a), special meshing modules in AVIZO were utilized to generate stereolithography (STL) surfaces that closely match the 3D morphology (aspect ratio) of the natural sand particles. The STL surfaces were constructed using the marching cube algorithm and meshes of equilateral triangles measuring ~50 μm in side length. For the FEM simulations (Figure 3-3b), the STL surfaces were imported to ABAQUS/CAE software and converted to solid 3D meshes composed of ~4,500 tetrahedral elements per particle. For the DEM simulations (Figure 3-3c), PFC3D used the STL surfaces to generate rigid clumps that closely match the morphology of each sand particle in the scanned specimen. Each clump consisted of ~300 overlapping pebbles that are joint together to form a rigid sand particle. Note that the morphology of sand is modeled more accurately with a higher resolution of 3D particle meshes in the FEM simulations or by increasing the number of pebbles per particle in the DEM simulations. The mesh resolution and the number of pebbles were selected to strike a balance between the computational runtime and closely matching the actual morphology of the sand particles (Figures 3-3a, b, and c). The vertical load-

displacement curve measured during the experimental (solid black line in Figure 3-1b) was used to calibrate the model parameters in both FEM and DEM simulations. Additionally, a virtual specimen was prepared where each sand particle from the scanned specimen was replaced by a spherical particle with an equivalent diameter and located at the centroid of the sand particle (Figures 3-3d and e). The purpose here is to investigate the influence of sand morphology on particle stress and force transmission while eliminating the contribution of other factors such as the grain sizes, particle mineralogy, specimen density, and boundary conditions. The specimen composed of spherical particles was virtually prepared with the help of special modules in PFC3D. Some neighboring spherical particles in the virtual specimen were noticed to overlap, even though the authors intentionally tested rounded sand particles to accommodate their substitution with spherical particles that have equal volume (diameter). The contact points between spherical particles were fixed in PFC3D by moving apart the overlapping particles and allowing up to 90% reduction in their diameters for critical cases when a sphere replaces an elongated sand particle (aspect ratio > 1.5). The numerical specimens (sand and spherical particles) were also dropped by gravity to initiate the contact interfaces between particles. Overall, the preparation procedure of the numerical specimens produced small differences (<70 μm) between the center location of the sand particles relative to their counter spherical particles. The uniaxial compression experiment was simulated by moving the top loading platen to compress the specimen in the vertical Z direction, whereas the confining mold and bottom loading platen were fixed in place.

Finite Element Method (FEM)

10-noded tetrahedral elements with isotropic linear elastic behavior were used to model the constitutive behavior of the sand and spherical particles. The elastic modulus and Poisson's ratio were set $= 99.45\ GPa$ and 0.06, respectively, which are typical values reported in the literature for particles composed of silica mineral (Heyliger et al., 2003). The 10-noded tetrahedrons are also known as quadratic tetrahedrons and represent the second complete-polynomial member of the isoperimetric tetrahedron family. The main motive behind using 10-noded tetrahedrons was to perform the element-level calculations at four Gaussian integration points using quadratic shape functions as opposed to one integration point and linear shape functions in conventional 4-noded tetrahedrons. Despite the extra computational cost (four integration points versus one), 10-noded tetrahedrons are known to behave significantly better in stress calculations when compared to the 4-noded tetrahedrons that suffer from volumetric locking deficiencies. The loading platens and confining mold were modeled using rigid elements of 2D triangles. Rigid elements in ABAQUS/CAE experience no deformation and are associated with a reference node such that the element kinematics are entirely determined by the boundary conditions imposed at the reference point rather than the expensive element-level calculations.

The general contact module in ABAQUS/CAE was adopted to model the particle-particle, particle-mold, and particle-platen interactions. Surface elements of individual particles, loading platens, and confining mold were extracted into element sets and included in the domain of the general contact module. When elements of the general contact module domain are in contact, shear and normal forces are transmitted across the contact interface to resist node-into-face, node-into-rigid surface, and edge-into-edge penetration. The default hard contact model of ABAQUS/CAE was used to relate the normal contact forces to penetration distances. Briefly, the normal to contact force was calculated using the bulk element stiffness at the contact interface such that the effect of contact deformation on the time increment is minimal (e.g., allowed nodal penetration was insignificant during the simulation). The Coulomb frictional model was utilized to simulate the transmission of tangential forces at the particle contact interfaces with a friction coefficient of 0.38, which is a typical value for the true angle of friction of silica mineral surface ($\tan 21^o = 0.38$).

The explicit dynamic solver was employed in ABAQUS/CAE to execute the FEM calculations in this chapter. The primary computational challenge was the numerous contact interfaces ($\sim 1200 - 1500$ particle-to-particle, particle-to-mold, and particle-to-platen contact interfaces in one assembly). In the explicit dynamic procedure, the assumption of nodal lumped masses produced a diagonal mass matrix (M) that was used to balance the equation of motion. The explicit central-difference time integration rule was then used to advance the nodal kinematic state (nodal displacement, velocity, and acceleration) over time. The key advantage of this procedure comes from the fast inversion of M versus the Newton-Raphson procedure that is executed in every time increment of the static implicit solver to iterated equilibrium. Although the explicit dynamic solver was originally designated for problems with impact loading (i.e., high strain rate), the use of uniform mass scaling limited the speed of stress wave propagation, allowing us to utilize the explicit dynamic solver for quasi-static analysis. Moreover, the mass scaling offered the advantage of dramatically reducing the simulation runtime by increasing the size of the minimum stable time increment.

Discrete Element Method (DEM)

This sub-suction is quoted since it is originally written by my research colleague Zaher A. Jarrar

“A unique clump template was generated for each sand particle using the Bubble Pack algorithm (Taghavi, 2011) in PFC3D. The algorithm first refines the triangulated surface mesh of each particle to provide optimum facet size. The medial axis was then approximated as the locations of centroids of the spheres that are nearly tangent to the surface. Prospective pebbles were selected as the spheres whose closest distance from the pebble center to the surface was greater than the pebble radius divided by 1.05. The remaining pebbles were filtered using two user-defined parameters: the ratio of the smallest to largest pebble in the clump (ρ), and the maximum sphere-to-sphere intersection angle (ϕ). The sphere-

to-sphere intersection angle is defined as the angle between the tangents of the two spheres at the intersection point. Higher values of ϕ lead to a higher number of pebbles and smoother clumps. In this study, ρ and ϕ values were selected to be 0.25 and 160°, respectively. These values were examined to resemble the morphology of tested sand particle accurately.

Loading platens and confining mold were modeled as rigid walls, and the loading rate was chosen to be slow enough to ensure a quasi-static loading condition. The linear contact model was adopted for clump-clump, clump-wall, sphere-sphere, and sphere-wall contacts. The linear model provides a linear elastic frictional behavior via linear springs with constant normal and shear stiffness, k_n, and k_s. Slip was introduced in the linear elastic interface by imposing a Coulomb limit on the shear force using a friction coefficient, μ. In this chapter, effective modulus (E^*) and normal to shear stiffness ratio (κ) were used to set the values of k_n and k_s as:

$$k_n = \frac{AE^*}{R_1+R_2} \quad (4\text{-}1)$$

$$k_s = \frac{k_n}{\kappa} \quad (4\text{-}2)$$

where R_1 and R_2 are the radii of the pebbles or spheres in contact, A is defined as:

$$A = \pi \times \min(R_1, R_2) \quad (4\text{-}3)$$

DEM contact model parameters were calibrated to closely match the load-displacement behavior observed in the experiment at the top loading platen, with values of E^*, κ, and μ selected to be 70 GPa, 2.7, and 0.38, respectively."

Results and Discussion

Boundary Load-Displacement and Averaged Coordination Number

Figure 3-4 presents the evolution of uniaxial compression in the FEM and DEM simulations at multiple steps of the global vertical compressive load (100, 200, 300, 400, and 500 N). Hereafter, the simulations of the specimen composed of particles with shapes like actual sand are referred to as "FEM-Sand" and "DEM-Sand", while the terms "FEM-Spheres" and "DEM-Spheres" denote the simulations of the virtual specimens composed of spherical particles. The vertical load steps represented the summation of reaction forces acting against the top loading platen in the FEM and DEM simulations. Figure 3-1b plots the load-displacement curves obtained from FEM and DEM simulations, where a significant difference can be seen between modeling the actual morphology of the sand particles versus spherical particles. The curves of DEM-Sand and DEM-Spheres simulations in Figure 3-1b manifest slightly stiffer boundary response compared to the FEM-Sand and FEM-Spheres, respectively, which is attributed to the rigid particles nature in DEM as opposed to the deformable particles in FEM. Furthermore, the curves of FEM-Sand and DEM-Sand simulations exhibited a stiffer response than the FEM-Spheres and DEM-Spheres simulations. Recall that the constitutive behavior of natural sand and spherical particles was simulated using the same model parameters in FEM and DEM. In addition, the specimens of actual-shape sand and spherical particles had the same initial density, dimensions, boundary conditions, number of particles,

and particle sizes (equivalent diameter). Therefore, the stiffer boundary response of the FEM-Sand and DEM-Sand simulations was fundamentally caused by the 3D morphology of the sand particles compared to the simple geometry of the spherical particles in FEM-Spheres and DEM-Spheres simulations. This observation comes in contrast to Cho et al. (2006), who reported a decrease in the compressibility of sand particles with fewer irregularities in shape. However, the conclusion by Cho et al. (2006) was based on oedometer experiments conducted on sand specimens with angular sand particles that might have influenced other properties such as the specimen density, packing, and instability of contact interfaces between angular sand particles. Namely, angular sand particles with more shape irregularities can produce less stable contact interfaces as well as pack in a looser density state that form regions with large voids within the specimen and thus be more compressible.

The complex morphology of sand enhanced the accommodation of each particle with respect to its neighboring. This enhancement can be noticed implicitly in Figure 3-5 from the evolution of the averaged coordination number (CN) versus the global vertical compressive load of the assemblies. The averaged CN was calculated as the total number of contact interfaces between the particles divided by 236, which is the total number of particles in the assemblies. Throughout the uniaxial compression, the averaged CN curves in Figure 3-5 showed that the particles in FEM-Sand and DEM-Sand simulations exhibited almost one additional contact interface compared to FEM-Spheres and DEM-Spheres simulations. These additional contact interfaces in the FEM-Sand and DEM-Sand simulations improved the embracement between the particles, introduced more restriction to the movement of particles, and resulted in the stiffer boundary response compared to the FEM-Spheres and DEM-Spheres simulations. As uniaxial compression begins (between 0 and 100 N vertical load), the DEM-Sand curve (green dashed) in Figure 3-5 displayed a faster increase in CN than the FEM-Sand (solid red) or the experimental (solid black) responses. This latter observation was examined to be a result of the artificial surface aliasing created by the ~300 surface pebbles in the DEM clumps to match the natural morphology of the sand particles, while the FEM detected the contact interfaces between particles at a smother surface and smaller scale-level (~1500 surface nodes per particle). The evolution of averaged CN during the experiment (solid black curve) was quantified via digital image post-processing of the in-situ SMT scans in Figure 3-1c (Druckrey et al., 2016).

Distribution of Inter-Particle Contact Forces and Stresses within Particles

It is particularly challenging to accurately measure and compare inter-particle contact forces and particle stresses experimentally when testing specimens composed of granular materials with complex particle morphologies such as natural sand. The simulated results in this chapter offered excellent estimates of these measurements for comparison and assessment with high fidelity since the same contact model and material parameters were used in both FEM-Sand and FEM-Spheres simulations, as well as DEM-Sand and DEM-Spheres simulations.

The FEM simulations calculated contact forces at the penetrating nodes between touching particles. For every two particles in contact (sand or spherical particles), the nodal contact forces were summed into a mutual inter-particle contact force acting at the center of the penetrating nodes, as illustrated in Figure 3-6a and b. The magnitude of each nodal force was used as the weight of importance in computing the center location of the inter-particle contact force. Furthermore, components of the Cauchy stress tensor (σ_{ij}) were calculated at four integration points within each element. These four estimates were averaged into an element-level stress tensor, and then into a particle-level using the element volume as a weighting factor of importance.

An analogous procedure was also adopted in calculating the inter-particle contact forces for the DEM-Sand simulations (Figures 3-6b) through substituting the nodal contact forces in FEM with pebble contact forces in DEM. For the DEM-Spheres simulations, inter-particle contact forces were directly computed by PFC3D since the interaction between two rigid spheres occurs at a single contact point (one mutual contact force). σ_{ij} of each DEM particle (clump or sphere) was then computed using the following analytical model (Oron and Herrmann, 1998, Oda and Iwashita, 2000, Potyondy and Cundall, 2004):

$$\sigma_{ij} = \frac{1}{V}\sum_{c=1}^{N_c} f_i^c r_j^c \qquad (4\text{-}4)$$

where f is the pebble-to-pebble or sphere-to-sphere contact force, r is the vector extending from the center of the particle to the contact location, V is the volume of the particle, and the summation runs over all contact points surrounding the particle ($c = 1$ to $Nc =$ number of contacts per particle). The subscripts i and j in Equation 3-4 denote the dimensional components (1, 2, and 3 $\stackrel{\text{def}}{=}$ X, Y, and Z), and the multiplication of f and r components is expressed in the Einstein summation convention.

As σ_{ij} was determined per particle in the DEM and FEM simulations, the eigenvalues of σ_{ij} were calculated to represent the particles' major (σ_1), intermediate (σ_2), and minor (σ_3) principal stresses that were mostly negative in values (compressive). The dominance of negative principal stresses has also been reported in DEM simulations for assemblies of 2D discs (Peters et al., 2005) and was attributed to the major compressive loading mechanism acting at the contact interfaces between particles as well as the confinement imposed by the mold in the lateral direction. Figure 3-7 presents the distribution of the inter-particle contact forces and σ_1 in the four simulations using the empirical cumulative distribution function (CDF) at 200 and 500 N global vertical compressive load of the assembly. The corresponding dashed curves in Figure 3-7 represent a Weibull fit of the data distribution:

$$CDF = 1 - e^{-\left(\frac{x}{\lambda}\right)^{\kappa}} \qquad (4\text{-}5)$$

where x denotes the data of interest (inter-particle contact forces or σ_1), λ and κ are scalar and shape fit parameters of the Weibull fit, respectively. Several studies in the literature reported that the inter-particle contact forces between 2D discs and

3D spheres followed an exponential distribution ($CDF = 1 - e^{-\frac{x}{\lambda}}$), whether using simulations of contact dynamics (Radjai et al., 1996, Radjai et al., 1999) or experimental observations (Majmudar and Behringer, 2005). In this chapter, Weibull distribution (Equation 3-5) is a generalized form of the exponential distribution with an additional shape parameter (κ) that has significantly improved the data fit. The goodness of distribution fits in Figure 3-7 was assessed using the Kolmogorov–Smirnov statistical test. Tables 3-1 and 3-2 list the probability value (p-value) for the Kolmogorov–Smirnov goodness of fit test. The p-values were larger than the significance limit of 0.05, which indicated a significant Weibull fit for the distribution of inter-particle contact forces and σ_1. Figure 3-8 depicts the evolution of the Weibull fitting parameters λ and κ with the global compressive load of the assemblies. λ increased linearly with the global vertical compressive load, while κ exhibited values between 0.95 and 1.25 with no clear trend.

Two clear trends can be seen in Figure 3-7 that were also observed at other steps of the assembly vertical compressive load but were not reported here to avoid prolonging the chapter. The DEM simulations (green and black curves) implied higher inter-particle contact forces and σ_1 when compared to the FEM simulations (red and blue curves). Recall that rigid particles were assumed by the DEM simulations versus deformable particles in the FEM. The deformability of particles in the FEM appeared to alleviate inter-particle contact forces and σ_1 relative to the DEM. The second observation was a shift to the left in the red and green curves in Figure 3-7 with respect to the blue and black curves, respectively. In other words, FEM-Sand and DEM-Sand simulations interestingly resulted in lower inter-particle contact forces and σ_1 than the FEM-Spheres and DEM-Spheres simulations, respectively, in contradiction to the stiffer boundary response of the FEM-Sand and DEM-Sand simulations (Figure 3-1b). This shift fundamentally arises from the influence of sand morphology on the micro-scale behavior of the assembly, such as the difference in the evolution of the averaged CN in Figure 3-5. The additional CN per particle in the FEM-Sand and DEM-Sand simulations allowed the transmission of stresses through a larger number of contact interfaces (paths), and thus produced the lower inter-particle contact forces and σ_1 in comparison to the simulations of FEM-Spheres and DEM-Spheres.

Correlation between the Inter-Particle Contact Forces and Coordination Number (CN)

It appears from Figure 3-5 that particle morphology influenced the evolution of the averaged CN when comparing the simulations of FEM-Sand and DEM-Sand to FEM-Spheres and DEM-Spheres. Amirrahmat et al. (2020) experimentally measured the lattice strain of 2705 sand particles that were loaded in 1D confined uniaxial compression using in-situ SMT and 3DXRD scanning techniques. They reported that highly stressed particles within the force chains have higher CN than particles outside the force chains. In this sub-section, we explore a potential correlation between the inter-particle contact forces and CN for the highly stressed particles. In the DEM and FEM simulations, the highly stressed particles were

selected to have σ_1 greater than the upper quartile of the whole population of particles within the specimen. The magnitudes of inter-particle contact forces acting on these particles were averaged and plotted in Figure 3-9 versus the particle CN at 400 N and 500 N global vertical compressive loads of the assemblies.

For the highly stressed particles, Figure 3-9 shows an inverse trend such that particles with higher CN exhibited a lower mean of the inter-particle contact forces. This inverse trend was supported by the hypothesis that particles with higher CN allowed the compressive stresses to transmit between particles through additional contact interfaces (paths). The transmission of compressive stresses through additional paths appeared to reduce the mean value of the inter-particle contact forces acting on the highly stressed particles. Note that the CN of the highly stressed particles fundamentally depends on particle morphology and the accommodation of these particles within their neighboring. This statement advocates for the importance of modeling sand morphology in a quest for an accurate prediction of the force and stress transmission in granular assemblies.

Development of Force Chains

Force chains are internal structures that develop and evolve to resist and transmit the majority of applied boundary stresses in sand from a micro-scale point of view. Figure 3-10 visualizes the force chains that developed in the FEM-Sand, DEM-Sand, FEM-Spheres, and DEM-Spheres simulations at 500 N global vertical compressive load of the assemblies. Particles in Figure 3-10 are colored according to their σ_1 value, which is a common measurement used in the literature as an indicator of the force chains in granular assemblies of 2D discs (Peters et al., 2005). The σ_1 color bar in Figure 3-10 incorporated a transparency value such that particles with a high σ_1 are opaque whereas particles with low σ_1 appeared semi-transparent. Furthermore, the inter-particle contact forces were superimposed in Figure 3-10 using the same procedure for transparency and the blue color bar.

The first explicit observation from Figure 3-10 is that the force chains developed utterly different when comparing between the simulations of actual-shape sand versus spherical particles. In the FEM-Sand simulations (Figure 3-10a), particles developed three major force chains that started from the sides of the top loading platen. The force chains then evolved toward the center of the specimen and diverted back toward the sides at the bottom loading platen. The force chains in the FEM-Spheres simulations (Figure 3-10b) were different in a way that a cluster of highly stressed particles occurred near the top loading platen, while two major chains of spherical particles were braced by the confining mold and transmitted most of the vertical load toward the bottom loading platen. Sand morphology fundamentally caused these differences in the onset and evolution of the force chains. Namely, the morphology of sand improved the interlocking between particles and thus pushed the force chains toward the center of the specimen in FEM-Sand simulations. However, the spherical particles in FEM-Spheres

simulations lacked this interlocking phenomenon, and the confining mold mostly braced the force chains. The force chains in DEM (Figure 3-10c and d) developed in a similar manner to the FEM; however, they were less discerning when plotted using σ_1 since the DEM postulate an analytical σ_1 and particles experience no actual deformation. Figure 3-10 also supported the previous conclusion of higher inter-particle contact forces in the DEM than FEM simulations. In summary, the morphology of sand particles must be modeled for an accurate prediction and investigation of the force chains in sands.

Lastly, the authors would like to discuss their preferences between using FEM or DEM simulations to model the micro-scale behavior of granular materials. The FEM simulations have the primary advantage of executing a material subroutine at the element-level that numerically models the constitutive behavior within an individual particle. This material subroutine can quantify stress concentrations within each particle and have the potential to implement a constitutive damage criterion that models particle breakage using continuum fracture mechanics (Imseeh and Alshibli, 2018, Turner et al., 2019, Wei et al., 2019). However, DEM lacks the application of fracture mechanics, and particle breakage is instead introduced by substituting clumps or spheres that attain a pre-defined failure criterion with a group of smaller particles (Lobo-Guerrero and Vallejo, 2005a, McDowell and de Bono, 2013, Zhou et al., 2016). DEM has also developed other numerical models to simulate particle breakage in sands such as filling individual particles with agglomerates of bonded small spheres (Potyondy and Cundall, 2004, Hanley et al., 2011, Cil and Alshibli, 2014a) or rigid blocks (Nicksiar and Martin, 2014, Jarrar et al., 2020), and the split of particles along fractured surfaces defined by level set functions (Harmon et al., 2020). The runtime of the simulations is another factor of concern in which the element-level calculations in FEM are expensive computationally relative to the assumption of rigid spheres or pebbles in DEM. For an accurate comparison, the simulations in this chapter were performed via parallel computing using a workstation that has dual central processing units (Intel Xeon CPU E5-2670 v2 @ 2.5 GHz) with 10 hyper-threaded cores in each unit (total of 40 logical cores). The runtime of the simulations was ~24 hours for FEM-Sand and FEM-Spheres compared to ~5 hours for DEM-Sand and ~9 minutes for DEM-Spheres. Note that ~4,500 elements and ~6,500 nodes were modeled per particle, whether in the simulations of FEM-Sand or FEM-Spheres, and thus there is no difference between the runtime of both simulations. On the other hand, the simulations of DEM-Sand modeled ~300 pebbles per particle compared to a single sphere per particle in DEM-Spheres, which made the DEM-Spheres simulations superfast.

Conclusions

The chapter investigated the influence of 3D morphology on sand micro-scale mechanics, including inter-particle contact forces, particle stresses, CN, and force chains. DEM and FEM simulations were developed for a 1D confined uniaxial compression experiment that was conducted on a specimen composed of natural

silica sand particles. In-situ SMT scans were acquired for the experiment and processed to produce numerical simulations with particles that closely match the morphology and fabric of individual sand particles within the tested specimen. The tested sand has rounded particles that allowed replacing each particle within the specimen by a spherical particle with an equivalent diameter, and then executing analogous DEM and FEM simulations of the 1D compression experiment. The following conclusions are drawn from this chapter:

1. The use of particles with shapes that match the sand morphology in the experiment led to an enhanced accommodation and particle-to-particles association (fabric) within the specimen. In the course of uniaxial compression, the evolution of the averaged CN showed about one additional contact interface per particle for the specimen composed of actual-shape sand particles compared to the specimen containing spherical particles.
2. Specimens composed of actual-shape sand particles exhibit a stiffer boundary response compared to specimens consisting of spherical particles. The stiffer boundary response can be related to the sand morphology that improved the embracement between particles through additional contact interfaces and restricted the movement of the particles during uniaxial compression.
3. Weibull distribution offers an excellent statistical fit for the distribution of inter-particle contact forces and particle stresses for both DEM and FEM simulations of specimens composed of particles with sand-like shapes as well as spherical particles. Additionally, DEM simulations exhibited higher inter-particle contact forces and particle stresses than FEM due to the inherent assumption of rigid particles in DEM versus deformable particles in FEM.
4. Highly stressed particles within granular assemblies have an inverse trend between the inter-particle contact forces and CN. Namely, particles with σ_1 greater than the upper quantile of the whole particles in the assembly exhibited lower mean inter-particle contact forces with a higher CN. The inverse trend was related to the transmission of forces and stresses through a larger number of contact interfaces (paths) between particles that reduced the inter-particle contact forces.
5. Particle morphology has a significant influence on the onset and evolution of force chains in granular materials. Under 1D confined uniaxial compression, specimens composed of particles with shapes like natural sand increase the chance of interlocking between particles, and thus force chains evolve toward the center of the specimen. However, specimens composed of spherical particles exhibit a cluster of highly stressed particles near the top loading platen, and the confining mold braced the force chains toward the bottom of the specimen.

Acknowledgments

This material was partially funded by the US National Science Foundation (NSF) under Grant No. CMMI-1362510. Any opinions, findings, conclusions, and recommendations expressed in this chapter are those of the authors and do not necessarily reflect the views of the NSF. The SMT scans presented in this chapter were collected using the x-ray Operations and Research Beamline Station 13-BMD of the Advanced Photon Source (APS), a US Department of Energy (DOE) Office of Science User Facility operated by the Argonne National Laboratory (ANL) under Contract No. DE-AC02-06CH11357. We acknowledge the support of GeoSoilEnviroCARS (Sector 13), which is funded by the NSF Earth Sciences (EAR-1128799), and the DOE Geosciences (DE-FG02-94ER14466). We thank Dr. Mark Rivers for his guidance at APS.

References

Dantu, P. (1957). In *The 4th international conference on soil mechanics and foundation engineering*.) Butterworths Scientific Publication, London, vol. vol 1, pp. p 133.

Wakabayashi, T. (1957) Photoelastic method for determination of stress in powdered mass. In *Japan National Congress for Appl. Mech.*), pp. p. 153.

Jong, G. D. J. D. & Verruijt, A. (1969) étude photo-étlastique d'un empilement de disques. .

Cundall, P. A. & Strack, O. D. (1979) A discrete numerical model for granular assemblies. *Geotechnique* **29(1)**:47-65.

Yousuff, M. & Page, N. (1993) Particle material, morphology and load effects on internal friction in powders. *Powder Technology* **76(2)**:155-164.

Liu, C.-H. (1994) Spatial patterns of sound propagation in sand. *Physical Review B* **50(2)**:782.

Bouchaud, J.-P., Cates, M. & Claudin, P. (1995) Stress distribution in granular media and nonlinear wave equation. *Journal de Physique I* **5(6)**:639-656.

Coppersmith, S., Liu, C.-H., Majumdar, S., Narayan, O. & Witten, T. (1996) Model for force fluctuations in bead packs. *Physical Review E* **53(5)**:4673.

Radjai, F., Jean, M., Moreau, J.-J. & Roux, S. (1996) Force distributions in dense two-dimensional granular systems. *Physical Review Letters* **77(2)**:274.

Coste, C., Falcon, E. & Fauve, S. (1997) Solitary waves in a chain of beads under Hertz contact. *Physical Review E* **56(5)**:6104.

Oron, G. & Herrmann, H. (1998) Exact calculation of force networks in granular piles. *Physical Review E* **58(2)**:2079.

Radjai, F., Wolf, D. E., Jean, M. & Moreau, J.-J. (1998) Bimodal character of stress transmission in granular packings. *Physical review letters* **80(1)**:61.

Behringer, R., Howell, D., Kondic, L., Tennakoon, S. & Veje, C. (1999) Predictability and granular materials. *Physica D: Nonlinear Phenomena* **133(1)**:1-17.

Howell, D., Behringer, R. & Veje, C. (1999) Stress fluctuations in a 2D granular Couette experiment: a continuous transition. *Physical Review Letters* **82(26)**:5241.

Jia, X., Caroli, C. & Velicky, B. (1999) Ultrasound propagation in externally stressed granular media. *Physical Review Letters* **82(9)**:1863.

Radjai, F., Roux, S. & Moreau, J. J. (1999) Contact forces in a granular packing. *Chaos: An Interdisciplinary Journal of Nonlinear Science* **9(3)**:544-550.

Oda, M. & Iwashita, K. (2000) Study on couple stress and shear band development in granular media based on numerical simulation analyses. *International Journal of Engineering Science* **38(15)**:1713-1740.

Nakata, Y., Kato, Y., Hyodo, M., Hyde, A. F. & Murata, H. (2001) One-dimensional compression behavior of uniformly graded sand related to single particle crushing strength. *Soils and Foundations* **41(2)**:39-51.

Geng, J., Reydellet, G., Clément, E. & Behringer, R. (2003) Green's function measurements of force transmission in 2D granular materials. *Physica D: Nonlinear Phenomena* **182(3)**:274-303.
Heyliger, P., Ledbetter, H. & Kim, S. (2003) Elastic constants of natural quartz. *The Journal of the Acoustical Society of America* **114(2)**:644-650.
Potyondy, D. O. & Cundall, P. (2004) A bonded-particle model for rock. *International journal of rock mechanics and mining sciences* **41(8)**:1329-1364.
Santamarina, J. & Cho, G.-C. (2004) Soil behavior: The role of particle shape. In *Advances in geotechnical engineering: The skempton conference*.) Citeseer, vol. 1, pp. 604-617.
Daraio, C., Nesterenko, V., Herbold, E. & Jin, S. (2005) Strongly nonlinear waves in a chain of Teflon beads. *Physical Review E* **72(1)**:016603.
Lobo-Guerrero, S. & Vallejo, L. E. (2005) Analysis of crushing of granular material under isotropic and biaxial stress conditions. *Soils and Foundations* **45(4)**:79-87.
Majmudar, T. S. & Behringer, R. P. (2005) Contact force measurements and stress-induced anisotropy in granular materials. *Nature* **435(7045)**:1079.
Peters, J., Muthuswamy, M., Wibowo, J. & Tordesillas, A. (2005) Characterization of force chains in granular material. *Physical Review E* **72(4)**:041307.
Cho, G.-C., Dodds, J. & Santamarina, J. C. (2006) Particle shape effects on packing density, stiffness, and strength: natural and crushed sands. *Journal of Geotechnical and Geoenvironmental Engineering* **132(5)**:591-602.
Guo, P. & Su, X. (2007) Shear strength, interparticle locking, and dilatancy of granular materials. *Canadian Geotechnical Journal* **44(5)**:579-591.
Pena, A., Garcia-Rojo, R. & Herrmann, H. J. (2007) Influence of particle shape on sheared dense granular media. *Granular Matter* **9(3-4)**:279-291.
Daniels, K. E. & Hayman, N. W. (2008) Force chains in seismogenic faults visualized with photoelastic granular shear experiments. *Journal of Geophysical Research: Solid Earth* **113(B11)**.
Sen, S., Hong, J., Bang, J., Avalos, E. & Doney, R. (2008) Solitary waves in the granular chain. *Physics Reports* **462(2)**:21-66.
O'sullivan, C. & Cui, L. (2009) Micromechanics of granular material response during load reversals: combined DEM and experimental study. *Powder Technology* **193(3)**:289-302.
Ferellec, J.-F. & Mcdowell, G. R. (2010) A method to model realistic particle shape and inertia in DEM. *Granular Matter* **12(5)**:459-467.
Lu, Y. & Frost, D. (2010) Three-dimensional DEM modeling of triaxial compression of sands. In *Soil Behavior and Geo-Micromechanics*.), pp. 220-226.
Yan, B., Regueiro, R. A. & Sture, S. (2010) Three-dimensional ellipsoidal discrete element modeling of granular materials and its coupling with finite element facets. *Engineering Computations* **27(4)**:519-550.

Hanley, K. J., O'sullivan, C., Oliveira, J. C., Cronin, K. & Byrne, E. P. (2011) Application of Taguchi methods to DEM calibration of bonded agglomerates. *Powder Technology* **210(3)**:230-240.
Owens, E. T. & Daniels, K. E. (2011) Sound propagation and force chains in granular materials. *EPL (Europhysics Letters)* **94(5)**:54005.
Taghavi, R. (2011) Automatic clump generation based on mid-surface. In *2nd International FLAC/DEM Symposium*.), Melbourne, pp. 791-797.
Andrade, J. E. & Avila, C. F. (2012) Granular element method (GEM): linking inter-particle forces with macroscopic loading. *Granular Matter* **14(1)**:51-61.
Bassett, D. S., Owens, E. T., Daniels, K. E. & Porter, M. A. (2012) Influence of network topology on sound propagation in granular materials. *Physical Review E* **86(4)**:041306.
Cavarretta, I. & O'sullivan, C. (2012) The mechanics of rigid irregular particles subject to uniaxial compression. *Geotechnique* **62(8)**:681-692.
Clark, A. H., Kondic, L. & Behringer, R. P. (2012) Particle scale dynamics in granular impact. *Physical Review Letters* **109(23)**:238302.
Gao, R., Du, X., Zeng, Y., Li, Y. & Yan, J. (2012) A new method to simulate irregular particles by discrete element method. *Journal of Rock Mechanics and Geotechnical Engineering* **4(3)**:276-281.
Guo, P. (2012) Critical length of force chains and shear band thickness in dense granular materials. *Acta Geotechnica* **7(1)**:41-55.
Shin, H. & Santamarina, J. (2012) Role of particle angularity on the mechanical behavior of granular mixtures. *Journal of Geotechnical and Geoenvironmental Engineering* **139(2)**:353-355.
Azéma, E., Radjai, F., Saint-Cyr, B., Delenne, J.-Y. & Sornay, P. (2013) Rheology of three-dimensional packings of aggregates: Microstructure and effects of nonconvexity. *Physical Review E* **87(5)**:052205.
Mcdowell, G. R. & De Bono, J. P. (2013) On the micro mechanics of one-dimensional normal compression. *Geotechnique* **63(11)**:895-908.
Cil, M. & Alshibli, K. (2014) 3D evolution of sand fracture under 1D compression. *Geotechnique* **64(5)**:351-364.
Hurley, R., Marteau, E., Ravichandran, G. & Andrade, J. E. (2014) Extracting inter-particle forces in opaque granular materials: beyond photoelasticity. *Journal of the Mechanics and Physics of Solids* **63**:154-166.
Nicksiar, M. & Martin, C. (2014) Factors affecting crack initiation in low porosity crystalline rocks. *Rock mechanics and rock engineering* **47(4)**:1165-1181.
Zhang, L., Cai, S., Hu, Z. & Zhang, J. (2014) A comparison between bridges and force-chains in photoelastic disk packing. *Soft Matter* **10(1)**:109-114.
Cil, M. B. & Alshibli, K. A. (2015) Modeling the influence of particle morphology on the fracture behavior of silica sand using a 3D discrete element method. *Comptes Rendus Mécanique* **343(2)**:133-142.
Vangla, P. & Latha, G. M. (2015) Influence of particle size on the friction and interfacial shear strength of sands of similar morphology. *International Journal of Geosynthetics and Ground Engineering* **1(1)**:6.

Druckrey, A. M. & Alshibli, K. A. (2016) 3D finite element modeling of sand particle fracture based on in situ x-ray synchrotron imaging. *Int. J. Numer. Anal. Methods Geomech.* **40**:105.

Druckrey, A. M., Alshibli, K. A. & Al-Raoush, R. I. (2016) 3D characterization of sand particle-to-particle contact and morphology. *Computers and Geotechnics* **74**:26-35.

Hurley, R., Hall, S., Andrade, J. & Wright, J. (2016) Quantifying interparticle forces and heterogeneity in 3D granular materials. *Physical Review Letters* **117(9)**:098005.

Kawamoto, R., Andò, E., Viggiani, G. & Andrade, J. E. (2016) Level set discrete element method for three-dimensional computations with triaxial case study. *Journal of the Mechanics and Physics of Solids* **91**:1-13.

Turner, A. K., Kim, F. H., Penumadu, D. & Herbold, E. B. (2016) Meso-scale framework for modeling granular material using computed tomography. *Computers and Geotechnics* **76**:140-146.

Vangla, P. & Gali, M. L. (2016) Effect of particle size of sand and surface asperities of reinforcement on their interface shear behavior. *Geotextiles and Geomembranes* **44(3)**:254-268.

Wang, W. & Coop, M. (2016) An investigation of breakage behavior of single sand particles using a high-speed microscope camera. *Geotechnique* **66(12)**:984-998.

Zhou, W., Yang, L., Ma, G., Chang, X., Lai, Z. & Xu, K. (2016) DEM analysis of the size effects on the behavior of crushable granular materials. *Granular Matter* **18(3)**:64.

Cil, M. B., Alshibli, K. A. & Kenesei, P. (2017) 3D Experimental Measurement of Lattice Strain and Fracture Behavior of Sand Particles Using Synchrotron x-ray Diffraction and Tomography. *Journal of Geotechnical and Geoenvironmental Engineering* **143(9)**.

Fu, R., Hu, X. & Zhou, B. (2017) Discrete element modeling of crushable sands considering realistic particle shape effect. *Computers and Geotechnics* **91**:179-191.

Hurley, R., Hall, S. & Wright, J. (2017) Multi-scale mechanics of granular solids from grain-resolved x-ray measurements. *Proceedings of the Royal Society A: Mathematical, Physical and Engineering Sciences* **473(2207)**:20170491.

Imseeh, W. H. & Alshibli, K. A. (2017) 3D Analysis of Force Chains in Sand Using Finite Element Method In *Proceedings of 3rd International Conference on Tomography of Materials and Structures Lund*.

Kandasami, R. K. & Murthy, T. G. (2017) Manifestation of particle morphology on the mechanical behavior of granular ensembles. *Granular Matter* **19(2)**:21.

Mahabadi, N. & Jang, J. (2017) The impact of fluid flow on force chains in granular media. *Applied Physics Letters* **110(4)**:041907.

Hurley, R. C., Herbold, E. B. & Pagan, D. C. (2018) Characterization of the crystal structure, kinematics, stresses and rotations in angular granular quartz during compaction. *Journal of Applied Crystallography* **51(4)**:1021-1034.

Imseeh, W. H. & Alshibli, K. A. (2018) 3D Finite Element Modelling of Force Transmission and Particle Fracture of Sand. *Computers and Geotechnics* **94**:184-195.

Kawamoto, R., Andò, E., Viggiani, G. & Andrade, J. E. (2018) All you need is shape: Predicting shear banding in sand with LS-DEM. *Journal of the Mechanics and Physics of Solids* **111**:375-392.

Li, H. & Mcdowell, G. R. (2018) Discrete element modelling of under sleeper pads using a box test. *Granular Matter* **20(2)**:26.

Zhang, B., Regueiro, R., Druckrey, A. & Alshibli, K. (2018) Construction of poly-ellipsoidal grain shapes from SMT imaging on sand, and the development of a new DEM contact detection algorithm. *Engineering Computations* **35(2)**:733-771.

Turner, A. K., Sharma, A., Penumadu, D. & Herbold, E. B. (2019) Finite element analyses of single particle crushing tests incorporating computed tomography imaging and damage mechanics. *Computers and Geotechnics* **115**:103158.

Wei, D., Zhao, B., Dias-Da-Costa, D. & Gan, Y. (2019) An FDEM study of particle breakage under rotational point loading. *Engineering fracture mechanics* **212**:221-237.

Zadeh, A. A., Barés, J., Brzinski, T. A., Daniels, K. E., Dijksman, J., Docquier, N., Everitt, H. O., Kollmer, J. E., Lantsoght, O. & Wang, D. (2019) Enlightening force chains: a review of photoelasticimetry in granular matter. *Granular Matter* **21(4)**:83.

Amirrahmat, S., Imseeh, W. H., Alshibli, K. A., Kenesei, P., Jarrar, Z. A. & Sharma, H. (2020) 3D Experimental Measurements of Evolution of Force Chains in Natural Silica Sand. *Journal of Geotechnical and Geoenvironmental Engineering* **146(5)**:04020027.

Harmon, J. M., Arthur, D. & Andrade, J. E. (2020) Level set splitting in DEM for modeling breakage mechanics. *Computer Methods in Applied Mechanics and Engineering* **365**:112961.

Jarrar, Z. A., Alshibli, K. A. & Al-Raoush, R. I. (2020) Three-Dimensional Evaluation of Sand Particle Fracture Using Discrete-Element Method and Synchrotron Microcomputed Tomography Images. *Journal of Geotechnical and Geoenvironmental Engineering* **146(7)**:06020007.

Zhou, B., Wei, D., Ku, Q., Wang, J. & Zhang, A. (2020) Study on the effect of particle morphology on single particle breakage using a combined finite-discrete element method. *Computers and Geotechnics* **122**:103532.

Appendices

Appendix A: Tables

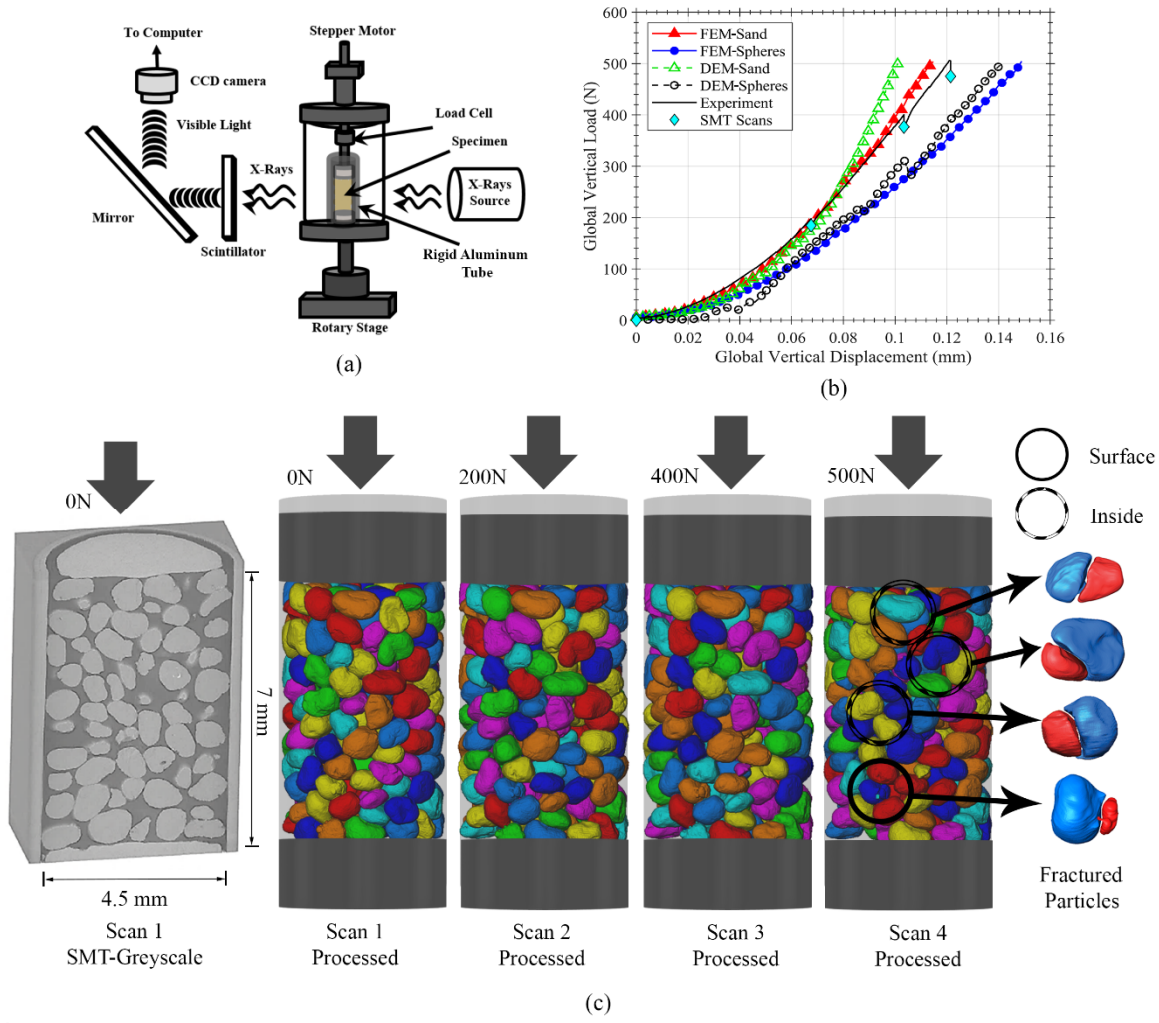
Table 4-1. *P*-values for Kolmogorov-Smirnov goodness of fit test for the inter-particle contact forces.

Vertical Load: N	FEM-Sand	FEM-Spheres	DEM-Sand	DEM-Spheres
100	> 0.1	> 0.5	> 0.4	> 0.4
200	> 0.1	> 0.2	> 0.3	> 0.1
300	> 0.1	> 0.4	> 0.5	> 0.2
400	> 0.2	> 0.5	> 0.2	> 0.5
500	> 0.4	> 0.5	> 0.6	> 0.4

Table 4-2. *P*-value for Kolmogorov-Smirnov goodness of fit test for the major principal stress of particles (σ_1).

Vertical Load : N	FEM-Sand	FEM-Spheres	DEM-Sand	DEM-Spheres
100	> 0.4	> 0.7	> 0.6	> 0.2
200	> 0.2	> 0.6	> 0.7	> 0.2
300	> 0.3	> 0.5	> 0.8	> 0.2
400	> 0.2	> 0.6	> 0.3	> 0.2
500	> 0.2	> 0.4	> 0.6	> 0.2

Appendix B: Figures



,

Figure 4-1. (a) Schematic sketch of the experimental setup; (b) displacement versus vertical load relationship at the top loading platen; and (c) 3D volume rendering of the processed SMT images showing the onset of particle breakage within the specimen.

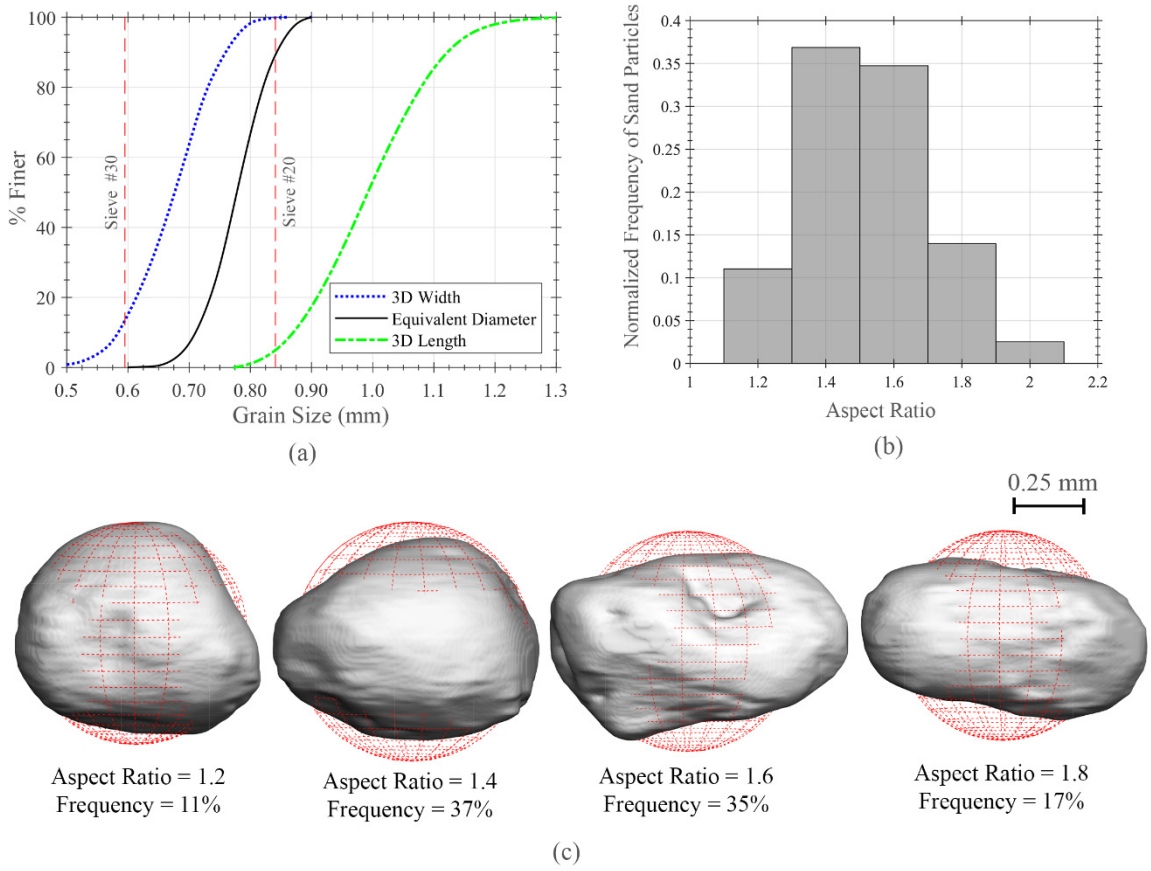


Figure 4-2. (a) Grain size distribution of the scanned sand specimen; (b) histogram plot of the aspect ratio of the sand particles in the scanned specimen; and (c) 3D volume rendering of a few representative sand particles with different aspect ratio along with their equivalent diameter spheres.(The wired-meshes disappear when they overlap with the sand particles).

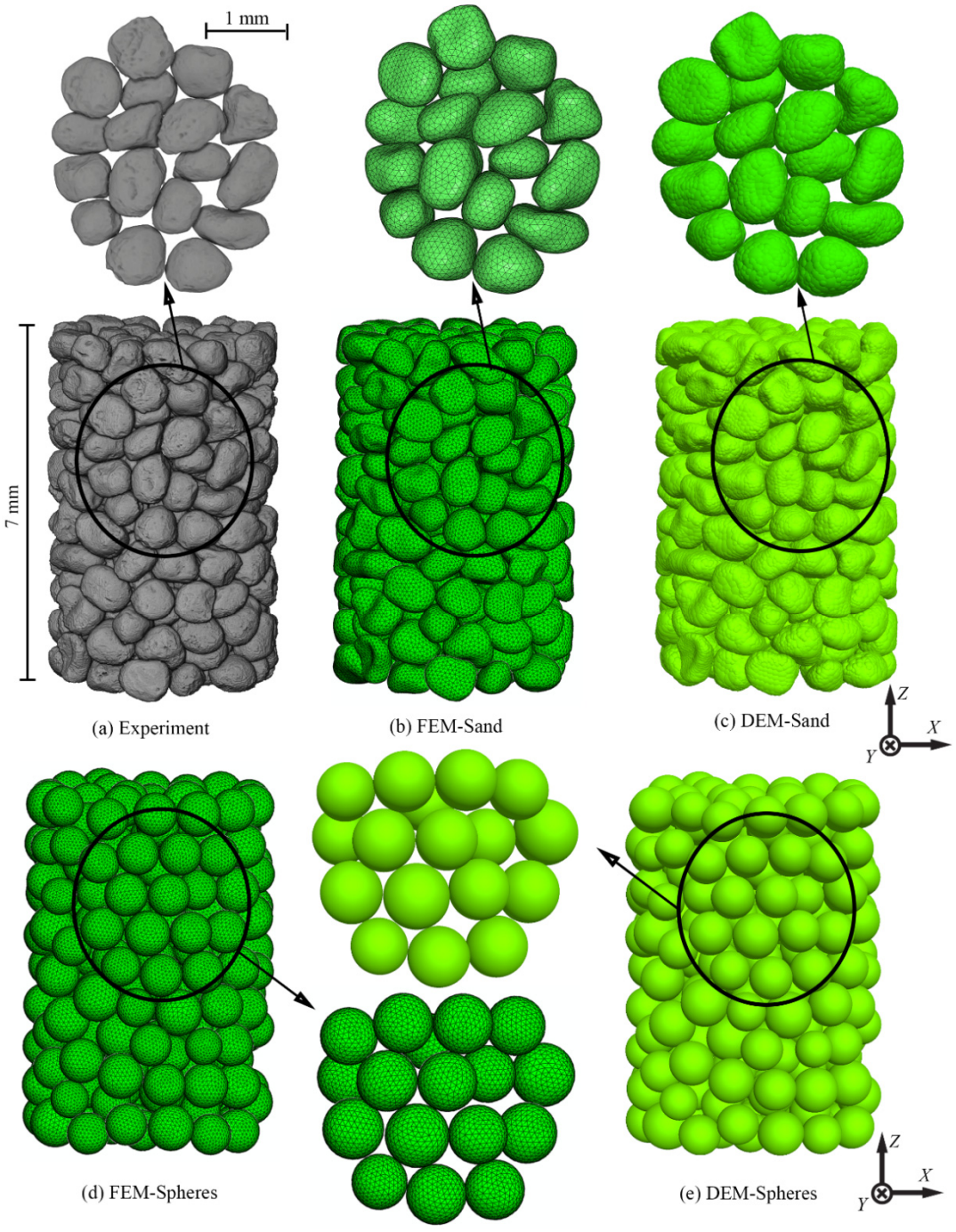


Figure 4-3. (a) 3D volume rendering of the scanned sand specimen; (b) 3D particle meshes used in FEM-Sand simulations; (c) 3D particle clumps used in DEM-Sand simulations; (d) 3D particle meshes used in FEM-Sphere simulations; and (e) spherical particles used in DEM-Sphere simulations.

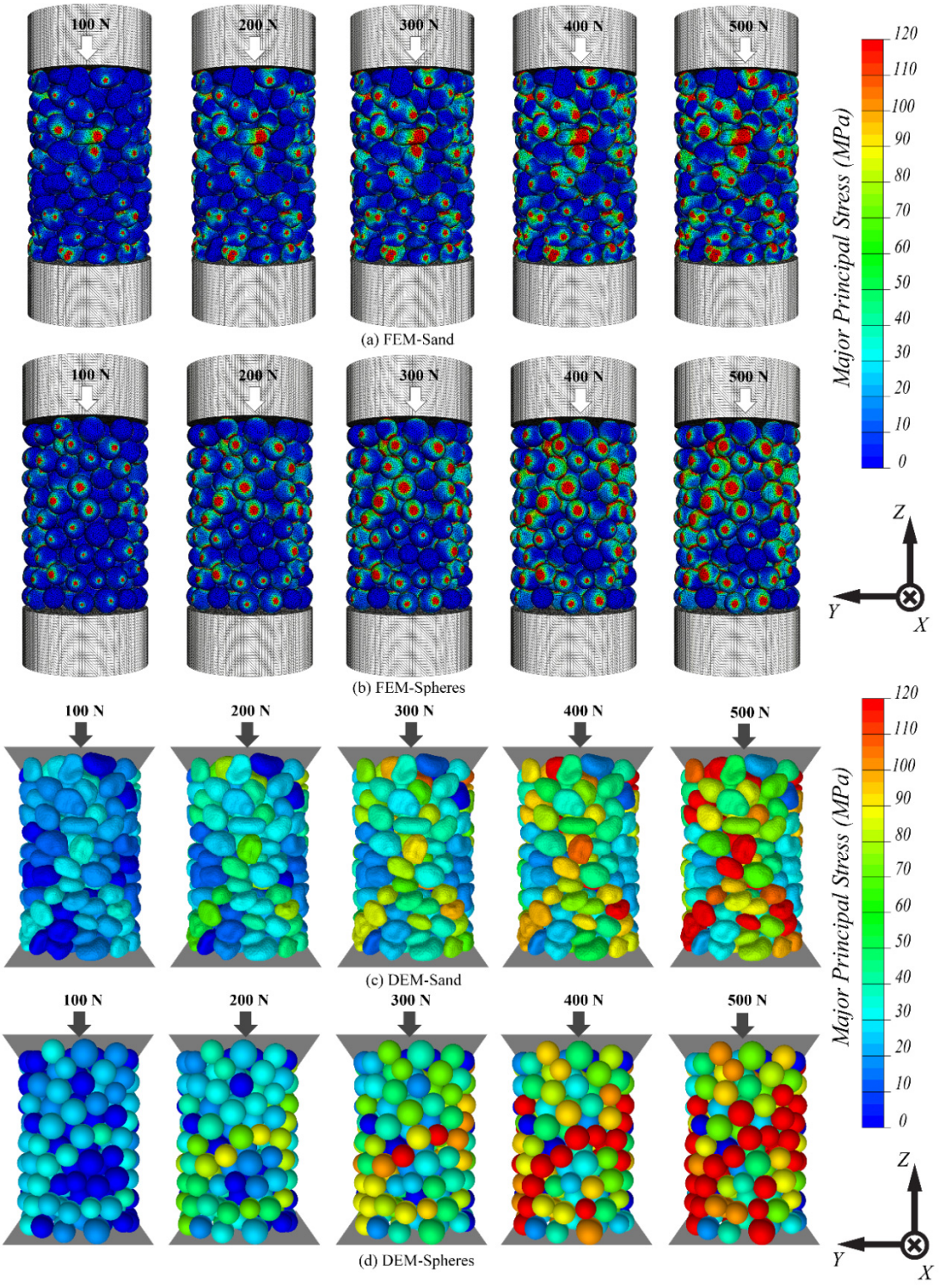


Figure 4-4. The 3D numerical simulations of the uniaxial compression experiment (a) FEM-Sand; (b) FEM-Spheres; (c) DEM-Sand; and (d) DEM-Spheres.

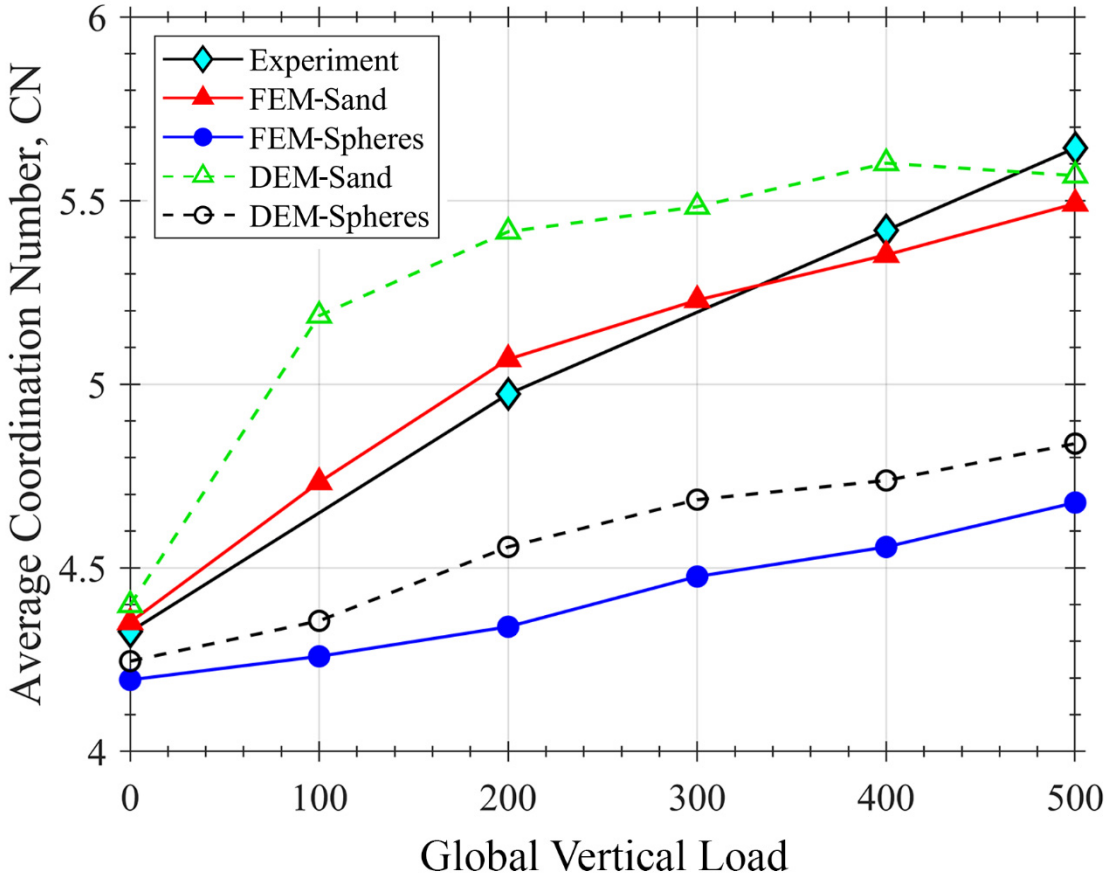


Figure 4-5. Evolution of the averaged coordination number (CN) with the global vertical compressive load.

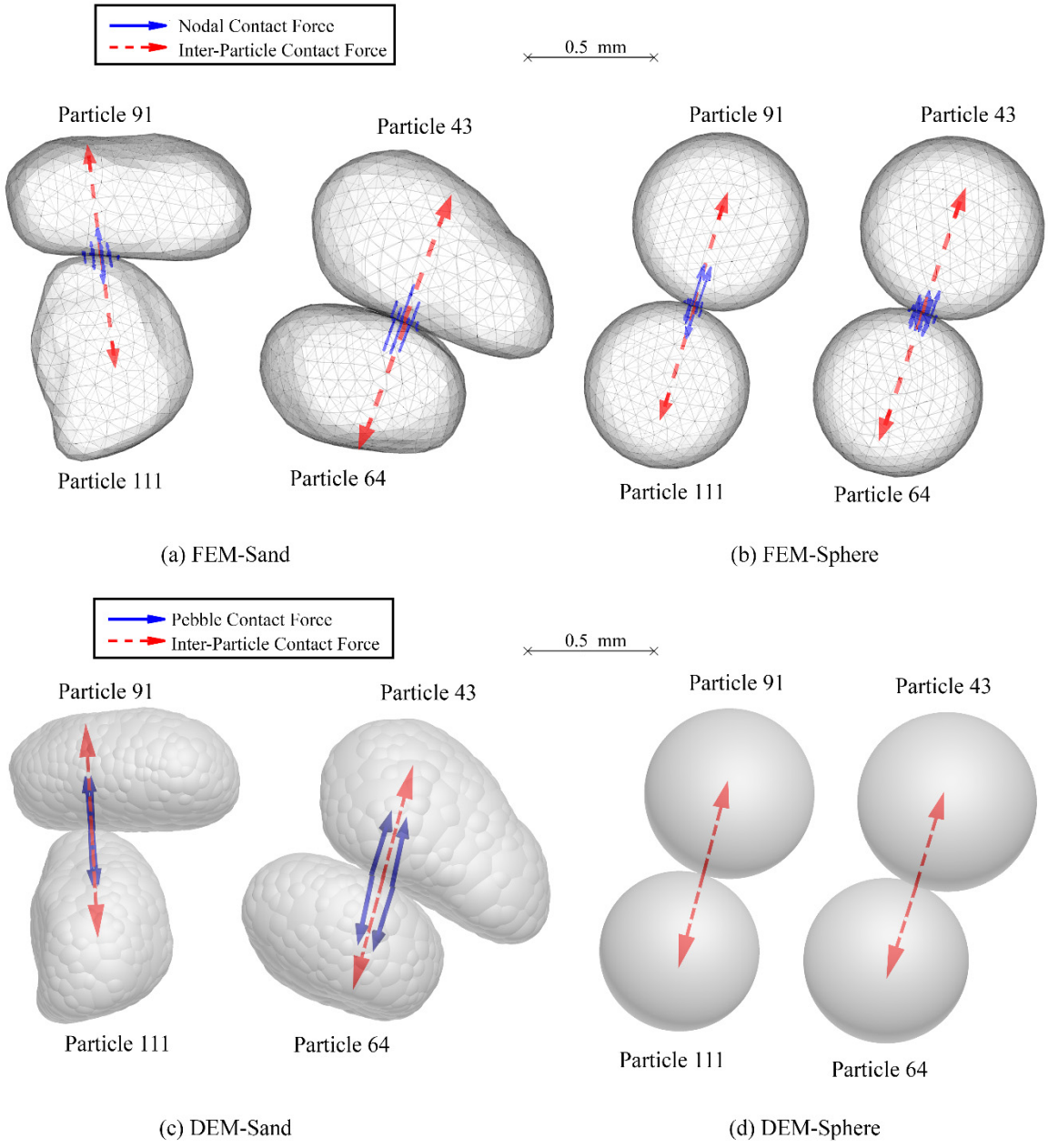


Figure 4-6. Illustration of the procedure used to calculate inter-particle contact forces for simulations of (a) FEM-Sand; (b) FEM-Spheres; (c) DEM-Sand; (e) and DEM-Spheres.

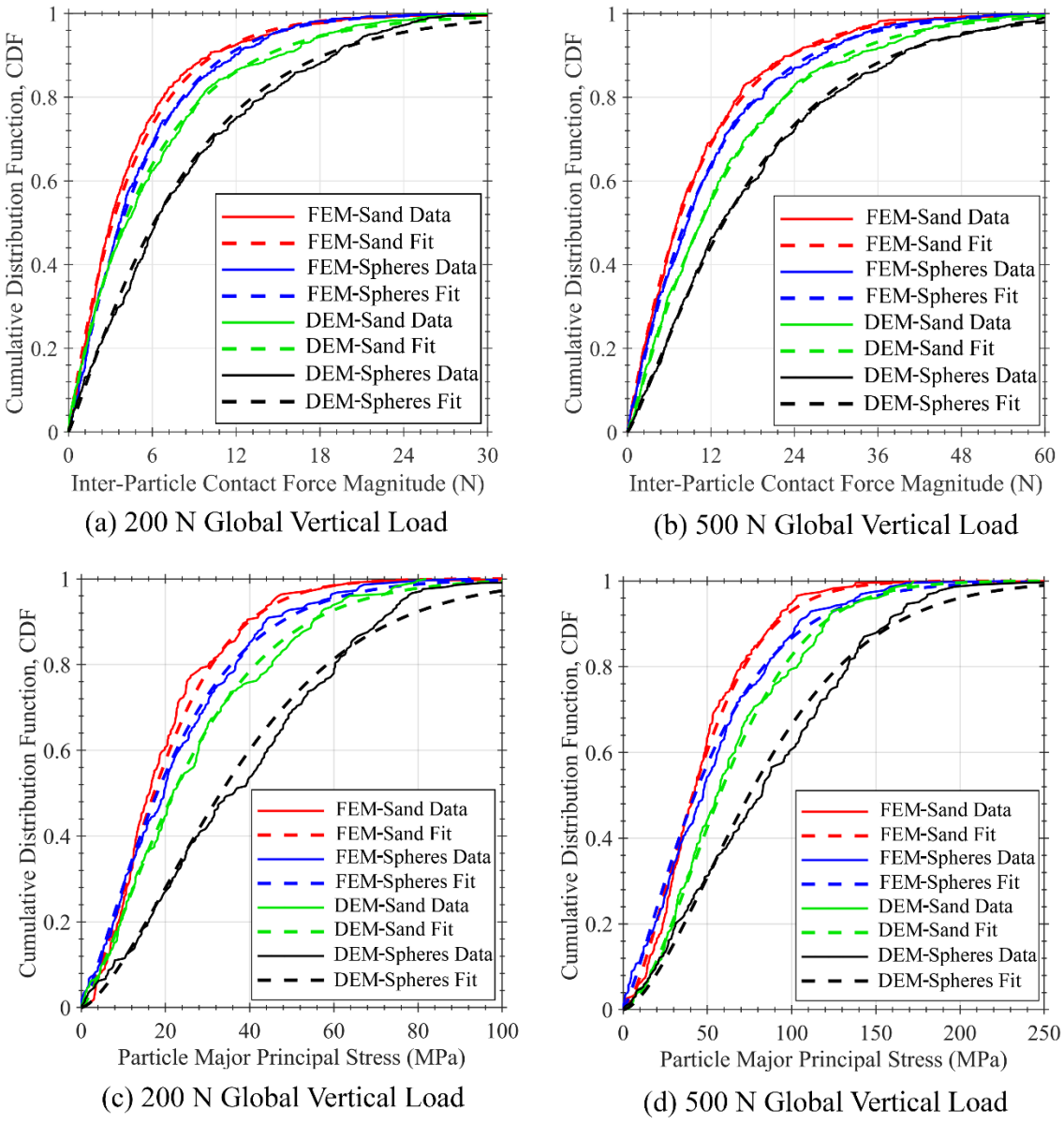
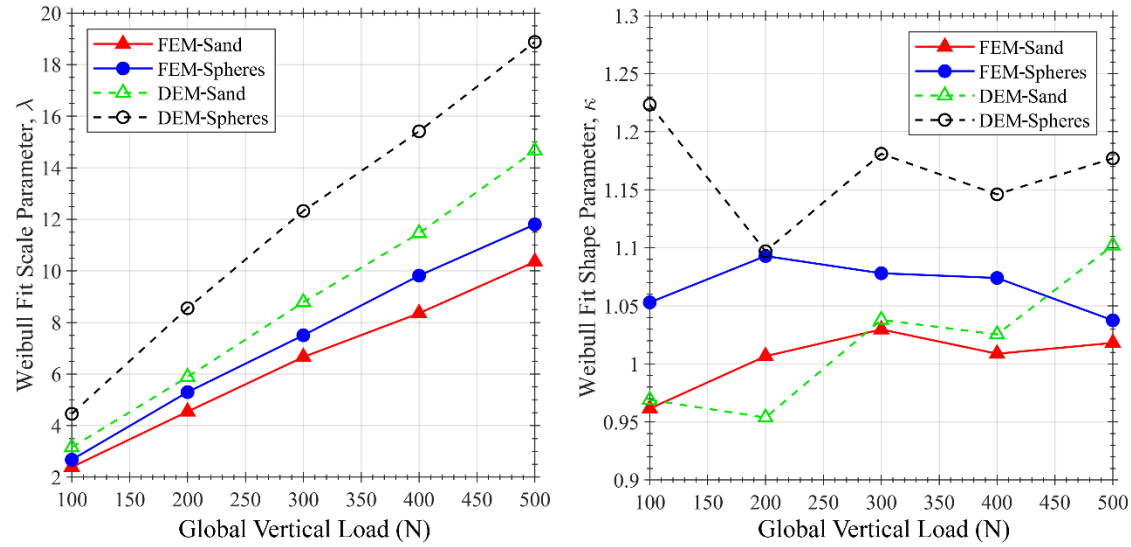
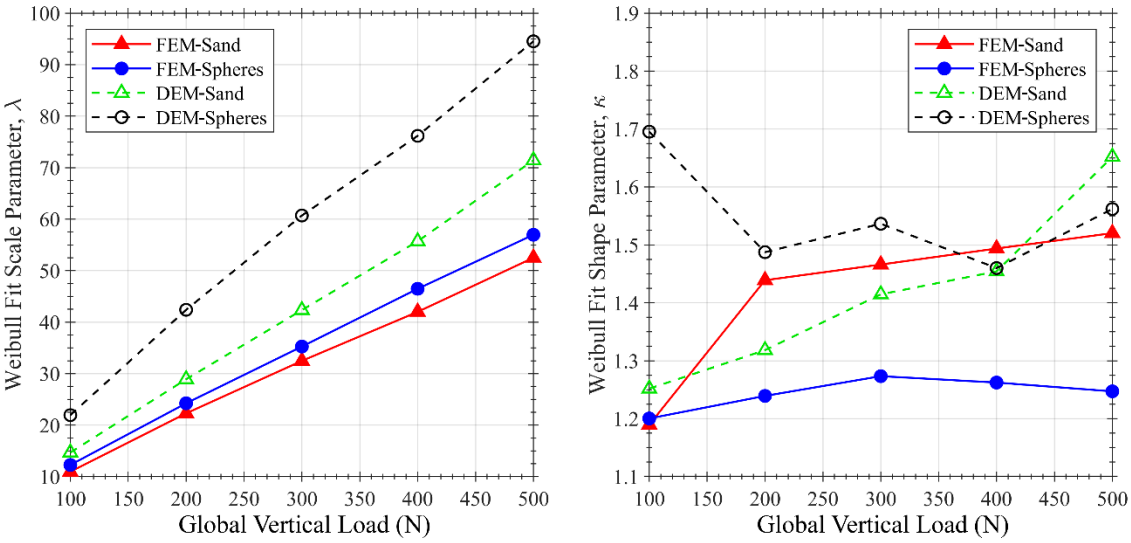


Figure 4-7. The distribution of inter-particle contact forces within the simulated specimens at global vertical compressive loads of 200 and 500 N.



(a) Inter-Particle Contact Forces



(b) Particles' Major Principal Stress, σ_1

Figure 4-8. Weibull fit parameters for the distribution of (a) inter-particle contact forces; and (b) particles' major principal stress (σ_1) within the specimen at multiple steps of the global vertical compressive load.

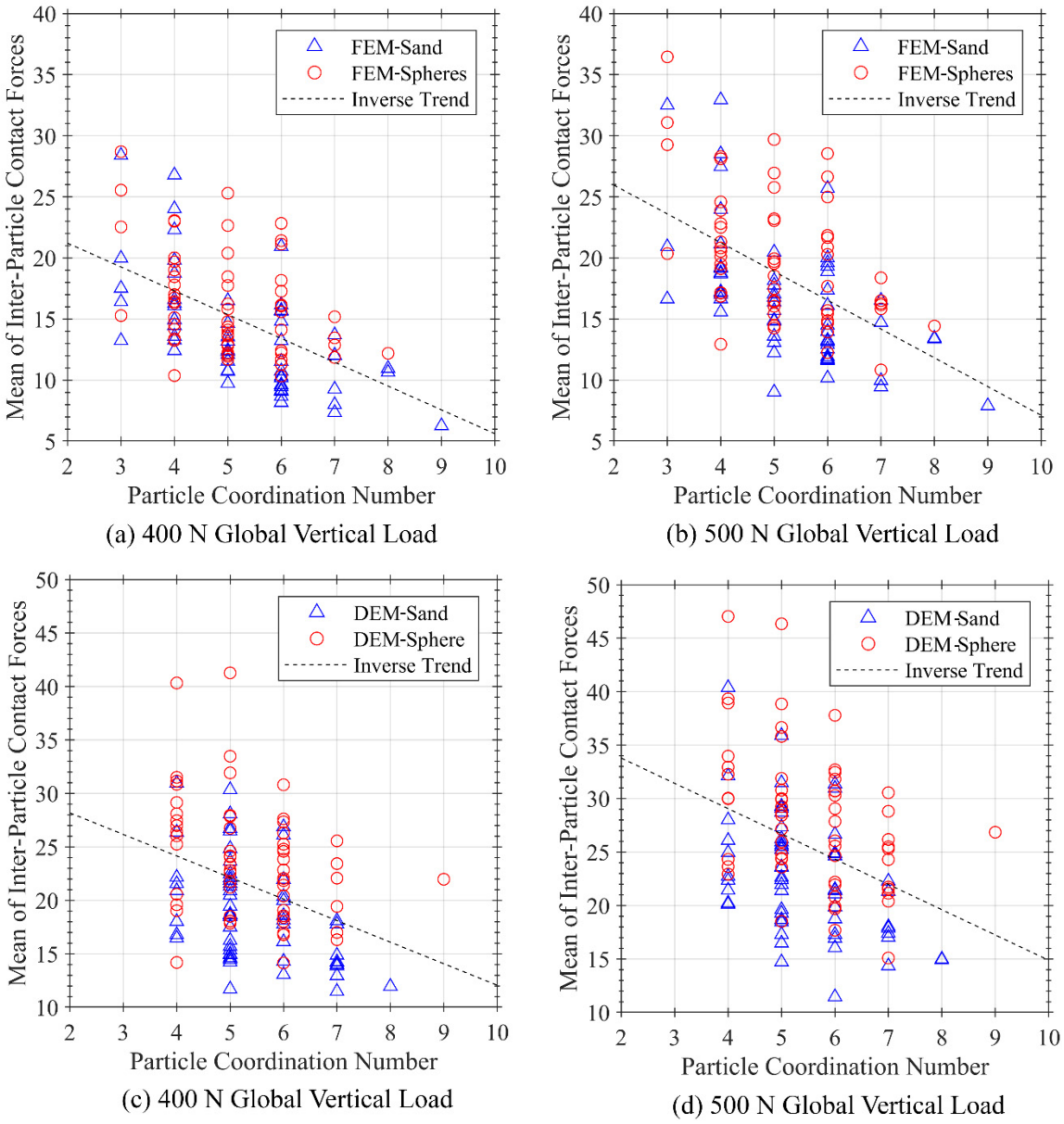


Figure 4-9. Inverse trend between the mean of inter-particle contact forces acting on highly stresses particles and the associated coordination number.

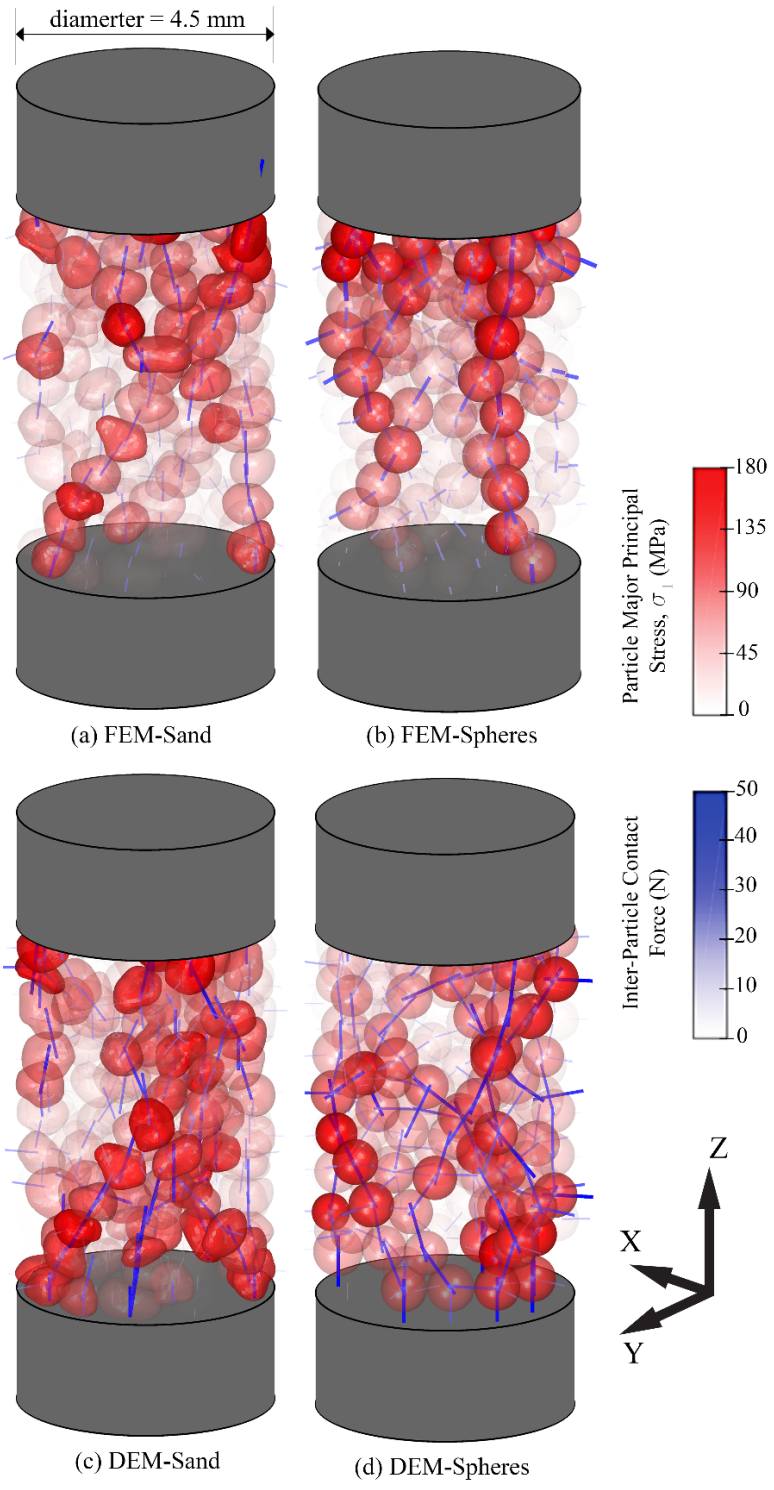


Figure 4-10. Influence of particle morphology on the development of force chains: DEM versus FEM.

CHAPTER FIVE

INFLUENCE OF CRYSTAL STRUCTURE ON CONSTITUTIVE ANISOTROPY OF SILICA SAND AT PARTICLE-SCALE

A version of this chapter is published as Imseeh, W. H., Alshibli, K. A., Moslehy, A., Kenesei, P. & Sharma, H. “Influence of Crystal Structure on Constitutive Anisotropy in Silica Sand at Particle Scale”. *Computers and Geotechnics*, 127, 103718. https://doi.org/10.1016/j.compgeo.2020.103718

Abstract: In spite of recent advanced geotechnical research regarding the influence of particle-scale morphology and fabric on the constitutive behavior of silica sands, there is still no published literature that investigated the influence of crystal structure of sand particles on their constitutive behavior. The main constituent of silica sand particles is quartz mineral, which has a trigonal crystal system and hexagonal lattice. This chapter investigates the influence of quartz crystal structure on the constitutive response of silica sand particles using 3D x-ray diffraction (3DXRD), synchrotron micro-computed tomography (SMT), and 3D finite element (FE) analysis. Unconfined uniaxial compression experiments on single particles of synthetic silica cubes exposed the notion of constitutive anisotropy caused by the crystal structure of quartz. Since the silica cubes have simple regular geometry $(1\ \mathrm{mm})^3$, they were loaded in different directions with respect to their crystal local planes. The crystal structure was also identified for a natural silica sand specimen composed of 2705 particles and loaded in confined uniaxial compression. Physical limitations of the experimental measurements made a strong case for the use of 3D FE analysis to study how the change in crystal local orientation of individual sand particles can fundamentally produce anisotropy in the constitutive response of natural sand specimens. The 3D FE analysis was validated to accurately model the crystal-based constitutive anisotropy in silica particles using the results of the silica cube experiments. The analysis was then executed on 3D FE meshes that closely matched the physical shape and fabric of the 2705 particles in the natural sand specimen. Both the experiments and 3D FE analysis showed that the crystal structure of quartz essentially causes a directional anisotropy in the constitutive behavior of silica particles.

Key Words: **Silica sand, crystal quartz, constitutive anisotropy, x-ray diffraction, x-ray tomography, finite element analysis.**

Introduction

A comprehensive understanding of sand constitutive behavior is fundamentally challenged by the complex contribution of properties that exist at multi-scale levels. Critical state (CS) soil mechanics (Roscoe et al., 1958, Schofield and Wroth, 1968) offered a theoretical solution for sand constitutive modeling by measuring stresses and strains at specimen boundaries (global-scale). However, the CS for sand is still questioned when one considers particle breakage (Altuhafi and Coop, 2011, Shipton and Coop, 2012, Xiao et al., 2015), grain size distribution (Nocilla et al., 2006, Shipton and Coop, 2014, Zuo and Baudet, 2015), particle morphology (Santamarina and Cho, 2004,

Yang and Luo, 2015, Kandasami and Murthy, 2017), and fabric evolution (Li and Dafalias, 2011, Coop, 2015, Dafalias, 2016, Imseeh et al., 2017, Todisco et al., 2018). The complexity in understanding the contribution of particle-scale properties has triggered the development of the Distinct Element Method (DEM) as a powerful numerical computer simulation that effectively predicts the mechanical response of sand and granular material under specific loading conditions (Ting et al., 1993, Fortin et al., 2005, Kruggel-Emden et al., 2007, O'Sullivan, 2014, Yan and Regueiro, 2018a). Advances in x-ray computed tomography (CT) have also provided experimental calibration/validation for DEM models (Kawamoto et al., 2016, Fu et al., 2017, Dosta et al., 2018). DEM and x-ray CT/SMT have substantially enhanced our understanding of sand mechanics from a particle-scale point of view. For instances, DEM (Iwashita and Oda, 2000, Jiang et al., 2011, Zhou et al., 2017, Kawamoto et al., 2018, Tang et al., 2019) as well as in-situ x-ray CT/SMT (Hall et al., 2010, Charalampidou et al., 2011, Desrues et al., 2018, Amirrahmat et al., 2019) provided excellent 3D measurements of shear strain localization in sheared sand specimens. x-ray CT and direct numerical simulations enhanced our understanding of multiphase flow in complex 3D pore networks of round and angular sands (Mohsin Thakur et al., 2020). In-situ x-ray CT/SMT was also coupled with 3DXRD to experimentally measure the lattice strains for synthetic (Hall and Wright, 2015a) and natural (Cil et al., 2017) silica sand particles. The lattice strains exposed skeletons of highly stressed particulate chains that evolved within sand specimens when tested in confined uniaxial compression (Hurley et al., 2017). Yet, DEM fundamentally fails to model lattice strains due to its principle assumption of rigid particles.

DEM has incorporated numerical fracture models to simulate particle breakage in sand such as the parallel-particle bonding model (Robertson and Bolton, 2001, McDowell and Harireche, 2002b, Cheng et al., 2003), particle replacement method (Tsoungui et al., 1999, Lobo-Guerrero and Vallejo, 2005b), and Hoek-Brown fracture criterion (Hoek and Martin, 2014, Zhang et al., 2015). However, these models fundamentally lack the principal concepts of fracture mechanics in brittle crystalline material such as sand particles. Breakage of a sand particle is primarily caused by the successive fracture of intermolecular bonds along preferred crystallographic planes, commonly known as slip planes or slip systems (Callister, 2007, Quintana-Alonso and Fleck, 2009). In recent years, discrete sand particles have been meshed into deformable 3D finite elements (Druckrey and Alshibli, 2016, Turner et al., 2016, Imseeh and Alshibli, 2018) in a quest for modeling particle breakage in sand using crystal-based fracture framework, which has not been accomplished yet. Theretofore, these FE models need to address the constitutive anisotropy in sand particles due to their crystal structure.

Sand is a granular material composed of finely weathered rock and mineral particles. The mineralogy of sand particles is mainly inherited from the parent rock sources and weathering conditions (Pettijohn et al., 1972). Quartz is the most common mineral in sand since it has the lowest potential for weathering in the Goldich dissolution series (Goldich, 1938). In general, minerals have unique physical (e.g., hardness), chemical (e.g., reaction to acids), and mechanical (i.e., constitutive response) properties that are fundamentally governed by their crystal structure (Reynolds et al., 2016). Molecules in a crystal are arranged in a periodic manner (lattice) that defines the symmetry properties (Hahn et al., 1983) and determines the isotropy/anisotropy of the material's constitutive behavior (Roters et al., 2010). A crystalline material is called anisotropic when it behaves differently

depending on the direction of external loads with respect to the crystal orientation. The building block (unit cell) of crystal quartz is silicon oxide tetrahedra (SiO_4) with each oxygen atom shared between two tetrahedra. This composition gives quartz an overall chemical formula of silicon dioxide (SiO_2), commonly known as silica. In crystallography, crystal quartz is known to possess a hexagonal lattice system, trigonal crystal system, and rhombohedral unit cell (Dušek et al., 2001, Nikitin et al., 2007). A thorough description of quartz crystal structure can be found in (Akhavan, 2013). As demonstrated in Figure 5-1, there are two types of crystal quartz: right-handed and left-handed. The trigonal crystal system of quartz, whether right- or left-handed, is spanned by a local coordinate system of four axes: a_1,a_2, a_3, and c. The three a axes correspond to a and b lattice parameters that have equal length, span the hexagonal lattice plane, intersect at 60^o angles, and are commonly referred to as the a-axis for simplification. The c-axis runs perpendicular to the lattice hexagonal plane and corresponds to the c lattice parameter, which is 1.1 times the length of a or b. This non-trivial crystal structure of quartz has given it special attention in material science research and certainly produced constitutive anisotropy (Bechmann, 1958, Gregoryanz et al., 2000, Ogi et al., 2006, Cady, 2018). This chapter will refer to the crystal local orientations using the Miller-Bravais four-index system $(a_1\ a_2\ a_3\ c)$, in which parentheses and brackets respectively describe the crystal local planes and axes. For example, $[0\ 0\ 0\ 1]$ represents the c-axis in the crystal diagrams of Figure 5-1, while $(0\ 0\ 0\ 1)$ refers to the crystal plane perpendicular to the c-axis.

Crystal quartz is well-known in material science for forming different types of penetration and contact twins such as Dauphiné, Brazil, and Japan (Gault, 1949). Crystal twins occur when two or more separate sub-domain crystals share some of the lattice points. This results in an inter-grown structure of the sub-domain crystals in specific configurations known as twin laws (Tilley, 1961). In contact twins, the sub-domain crystals share a single composition surface that is often manifested in electron crystal microscopy as mirror distortion across the boundary between the sub-domain crystals (Sunagawa and Yasuda, 1983). Penetration twins occur when two or more sub-domain crystals interpenetrate each other with the surface between the sub-domains being indefinable and irregular. For instance, Dauphiné is a type of penetration twins that occurs when sub-domain crystals of either right- or left-handed quartz are combined in the same structure. The sub-domain crystals share the same c-axis and are rotated about the common c-axis by 60° relative to one another (Eder et al., 2015). Dauphiné twins are recognized to influence stress concentrations and the onset of lattice fracture near crystal boundaries (Lloyd, 2000, Barton and Wenk, 2007). Recently, Hurley et al. (2018c) reported on the notion of Dauphiné twins in synthetic silica particles that were scanned using in-situ x-ray CT and 3DXRD. Yet, little is known about crystal twins in geotechnical research.

Recent geotechnical research has investigated the constitutive behavior of sand at the scale of an individual or multi-particle fracture (Bolton et al., 2008, Zhao et al., 2015, Jarrar et al., 2020) and a single contact interface (Cole and Hopkins, 2016, Nardelli and Coop, 2018, Sandeep et al., 2018). However, the stress-strain response of silica sand particles is fundamentally governed by their crystal constitutive behavior (Alshibli et al., 2013). Although recent 3DXRD measurements of lattice strain have recognized the crystal structure of silica sand particles (Cil et al., 2017, Hurley et al., 2017, Hurley et al., 2018c), much is still unknown about the contribution of crystalline-scale properties. This chapter experimentally measures lattice strains for a synthetic silica cube subjected to unconfined

uniaxial compression and compares the evolution of lattice strain versus compression when the cube is loaded in different directions with respect to its crystal planes. The simple geometry of the cube eliminates the effect of particle-scale morphology and isolates the influence of crystalline-scale properties on the constitutive behavior of silica particles. The stress-strain response of the silica cube permits us to assess the agreement among the experimental constitutive behavior, calculated closed-form solution, and simulated 3D FE analysis. Outcomes of this chapter will also lay the groundwork for the near future application of crystal-based fracture mechanics to simulate particle breakage in sand.

Experiments and Modeling of Synthetic Silica Cubes

This section seeks to experimentally calibrate the constitutive behavior of silica sand particles. Cil et al. (2013) examined the tensile strength of 87 silica sand particles using a special single-particle compression apparatus. Surprisingly, the 87 particles manifested a wide variation in the tensile fracture stress with a mean value of $118.43\ MPa$ and a standard deviation of $37.89\ MPa$. Less variation in the tensile fracture stress was expected since Cil et al. (2013) tested particles of ASTM 20-30 Ottawa sand; a standard type of sand widely used in geotechnical testing and known for having 99% silica constituent as well as uniform grain sizes (between US sieve $\#20$ and $\#30$). The special single-particle compression apparatus was mounted on the SMT scanner stage to acquire in-situ 3D images that would help explain the unexpected wide variation in tensile strength. At a μm level resolution, 3D images revealed complex particle morphologies of the ASTM 20-30 sand that essentially imposed different particle-to-loading platens interactions resulting in the wide variation of fracture tensile stress. Cil et al. (2013) used DEM to further investigate the influence of sand morphology on single-particle fracture. DEM postulated the same constitutive response for two sand particles if both have identical morphology and particle-platen interactions. This section will experimentally challenge the aforementioned DEM postulate by testing identical $1 \times 1 \times 1\ mm$ synthetic silica cubes, which will eliminate the influence of particle morphology. The silica cubes were manufactured from synthetic α-quartz crystals by MaTeck, a leading company in producing innovative research materials located in Juelich, Germany. The cubes were precisely cut in a highly controlled environment using special laser technology to ensure identical physical and crystalline properties.

Powder and Laue x-ray Diffraction

My Research Colleague Amirsalar Moslehy contributed to writing some parts of this subsection

The crystal structure of the synthetic silica cubes was identified using powder x-ray diffraction at the Joint Institute for Advanced Materials (JIAM), University of Tennessee-Knoxville (UTK). Multiple cubes were ground into powder to a size passing US sieve $\#200$ ($75\ \mu m$), and a powder sample was scanned by a PANalytical Empyrean Bragg-Brentano instrument with copper tubing using k_{α_1} x-ray beam. The diffracted x-ray beam was collected on a Pixel 3D detector, and the diffraction pattern was analyzed via HighScore software (Degen et al., 2014) to identify the material phase, which was found to be pure α – quartz. A full Rietveld refinement was executed on the diffraction pattern using GSAS II software (Toby and Von Dreele, 2013) and the standard input for α –

quartz crystal structure (Jorgensen, 1978) to measure the lattice parameters, volume, and density of the powder sample (Table 4-1). Results of the x-ray powder diffraction experiment provided the initial phase identification and baseline crystal information required for further x-ray diffraction scanning procedures. The experimental measurements in Table 4-1 have an excellent agreement with MaTeck crystal specifications by means of lattice parameters, unit cell dimensions, and density.

The crystal lattice parameters reported in Table 4-1 were used as input data to conduct Laue x-ray diffraction at the JIAM facility on several intact cubes. A single cube was mounted on a Huber x-ray diffraction instrument, and it was scanned twice against two orthogonal faces. The diffracted x-ray beam was collected on Polaroid film, and the diffraction pattern was analyzed using OrientExpress software (Laugier and Bochu, 2004) to identify the orientation of crystal planes with respect to the scanned face of the cube. Analysis of the Laue x-ray diffraction patterns confirmed MaTeck's claim that the cube faces are perfectly aligned with (2 -1 -1 0), (0 1 -1 0), and (0 0 0 1) crystal local planes. Cube faces aligned with the (2 -1 -1 0) and (0 0 0 1) crystal local planes (a-axis and c-axis; respectively) were colored differently with sharpie markers. The cubes were later subjected to unconfined uniaxial compression against the differently colored faces while collecting in-situ SMT and 3DXRD scans.

Combined In-Situ SMT and 3DXRD

The single-particle compression apparatus described in Druckrey and Alshibli (2016) was used to test the silica cubes under unconfined uniaxial compression conditions. Briefly, the apparatus can apply quasi-static uniaxial compression via two concentric cylindrical steel loading platens measuring $4\ \mathrm{mm}$ in diameter. The bottom loading platen was attached to a load cell and fixed to the apparatus base plate. The top loading platen was connected to a stepper motor and supported by the apparatus top plate. A cylindrical acrylic jacket assembled the apparatus top and base plates by bolted connections. The stepper motor axially drives the top loading platen at a displacement-controlled mode. The load cell and stepper motor provide continuous measurements of uniaxial force and displacement via a data acquisition system with a computer Labview interface.

The apparatus was mounted on the stage of the x-ray beamline 1-ID, the advanced photon source (APS), Argonne National Laboratory (ANL), Illinois, USA. Two experiments were conducted on two cubes that were loaded against differently marked faces corresponding to the (2 -1 -1 0) and (0 0 0 1) crystal planes while acquiring in-situ SMT and 3DXRD scans. Uniaxial compression was paused at pre-determined uniaxial load steps of $0,\ 300, 600, 900,$ and $1200\ N$ to acquire SMT scans followed by 3DXRD. SMT scans were acquired using a $1.6\ \mathrm{mm}$ (width) $\times$ $1.2\ \mathrm{mm}$ (height) beam while rotating the apparatus over 360^0 at 0.2^o angular increments and 0.5 second exposure time. This procedure produced 1800 radiographs per scan that were reconstructed into 3D slice-structured images with an excellent spatial resolution of $0.98\ \mu m$/pixel. 3DXRD scans were collected using a $1.6\ \mathrm{mm}$ (width) $\times$ $0.2\ \mathrm{mm}$ (height) beam during another 360^0 rotation of the apparatus at 0.2^oangular increments and 0.3 second exposure time. The height of the 3DXRD beam was intentionally reduced to $0.2\ \mathrm{mm}$ to improve the accuracy of the measurements and to scan the entire cube by five vertically-stacked layers. This scanning procedure provided measurements of the cube's lattice strain at multiple vertical sections in a quest for a potential stain gradient with respect to the cube's vertical height.

SMT scans offered visualization of the cube's microstructure to check for potential initial defects and the absence of crack evolution during compression since the scope of the cube experiments is to experimentally evaluate the elastic constitutive behavior of silica particles. 3DXRD scans were analyzed using Microstructural Imaging Diffraction Analysis Software (MIDAS) that was developed by APS staff (Sharma et al., 2012b, Sharma et al., 2012a, Park et al., 2015). The x-ray diffraction data recorded on a flat-panel detector was input in MIDAS to produce a 3D mapping of individual crystal lattices within the scanned specimen (e.g., cube). Hereafter, the term "3DXRD measurements" refers to the final output of MIDAS, which includes:

1. Unit cell parameters: lengths and angles between a, b, and c lattice parameters.
2. Positioning: (x, y, z) coordinates of the crystal lattice center with respect to a global right-handed Cartesian coordinate system located at a fixed reference point on the scanner stage of the APS beamline station. The global $X - axis$ is aligned with the direction of the incident x-ray beam, and the global $Z -$ axis runs in the direction of the global uniaxial compression applied by the single-particle compression apparatus.
3. *Orientations*: rotational matrix $(\boldsymbol{R})$ that transforms the crystal local axes into the global coordinate system:
$$\boldsymbol{R} = \begin{bmatrix} x_1 & x_2 & x_3 \\ y_1 & y_2 & y_3 \\ z_1 & z_2 & z_3 \end{bmatrix} \quad (5\text{-}1)$$
Where (x_1, y_1, z_1), (x_2, y_2, z_2), and (x_3, y_3, z_3) are unit vectors expressed in the global coordinate system and span the [2 -1 -1 0], [0 1 -1 0], and [0 0 0 1] crystal local axes; respectively. In terms of algebraic notation, bold symbols in this chapter refer to tensors/vectors, whereas regular text symbols denote scaler quantities.
4. Strains: lattice strains in the form of a symmetric second-order tenor $(\boldsymbol{\epsilon})$ expressed in the global coordinate system and positive sign convention represents compression:
$$\boldsymbol{\epsilon} = \begin{bmatrix} \epsilon_{xx} & \epsilon_{xy} & \epsilon_{xz} \\ \epsilon_{yx} & \epsilon_{yy} & \epsilon_{yz} \\ \epsilon_{zx} & \epsilon_{zy} & \epsilon_{zz} \end{bmatrix} \quad (5\text{-}2)$$

Figure 5-2a displays the relationships between the global uniaxial compressive load versus displacement as recorded by the data acquisition system of the single-particle compression apparatus. Diamond shape markers in Figure 5-2a represent the load steps at which compression was paused to acquire in-situ SMT and 3DXRD scans. The evolution of uniaxial compression is displayed in Figures 2b&c using central vertical slices across the SMT scans for the two cubes where the superimposed color represents the major principal strain in the cube's crystal lattice as quantified by 3DXRD measurements. At the same global uniaxial compressive load, the cube loaded against (2 -1 -1 0) crystal plane (Figure 5-2c) exhibited a significantly higher major principal lattice strain than the cube loaded against (0 0 0 1) crystal plane (Figure 5-2b). Hereinafter, the terms "weak cube" (less stiff) and "strong cube" (stiffer) refer to the cube loaded against (2 -1 -1 0) and (0 0 0 1) crystal plane, respectively. Later in this section, the term "isotropic cube" will also be introduced to describe 3D FE analysis for an isotropic approximation of the silica cube constitutive behavior.

Table 5-2 reports the variation of lattice strains within the vertical height of the silica cubes. Recall that five vertically-stacked 3DXRD scans were collected for the silica cubes at each

load step. This stacking procedure offered five measurements of the lattice major principal strain per load step per cube. Layers 1 to 5 in Table 5-2 sequentially refer to the vertical one-fifth portions of the cube in which layer 1 corresponds to the portion that is in contact with the top loading platen, whereas layer 5 of the cube is in contact with the bottom loading platen. The mean value of the major principal strains are also reported in Table 5-2 with the coefficient of variation for the five measurements. The coefficient of variation exhibited values $< 2\%$ at most of the load steps, which indicates a fairly uniform distribution of the lattice strain along the cube's height. In fact, this finding advocate for the reliability of the experimental measurements and MIDAS analyses. Further, Table 5-2 shows no definitive gradient of the major principal strain with the cube's height such as consistent higher values toward the top loading platen (layer 1) nor the cube center (layers 2 to 4).

3D FE Analysis of the Silica Cube Experiments

Uniaxial load-displacement curves in Figure 5-2a postulate a typical constitutive behavior of crystal quartz within the framework of the anisotropic linear elasticity theory. Crystal quartz possesses trigonal symmetry (point group 32) and six independent elastic constants $(C_{11}, C_{12}, C_{13}, C_{14}, C_{33}, C_{44})$:

$$[\boldsymbol{\sigma}] = [\boldsymbol{C}][\boldsymbol{\varepsilon}] \tag{5-3}$$

$$\begin{bmatrix}\sigma_1\\ \sigma_2\\ \sigma_3\\ \sigma_4\\ \sigma_5\\ \sigma_6\end{bmatrix} = \begin{bmatrix} C_{11} & C_{12} & C_{13} & C_{14} & 0 & 0 \\ C_{12} & C_{11} & C_{13} & -C_{14} & 0 & 0 \\ C_{13} & C_{13} & C_{33} & 0 & 0 & 0 \\ C_{14} & -C_{14} & 0 & C_{44} & 0 & 0 \\ 0 & 0 & 0 & 0 & C_{44} & C_{14} \\ 0 & 0 & 0 & 0 & C_{14} & \frac{1}{2}(C_{11}-C_{12}) \end{bmatrix} \begin{bmatrix}\varepsilon_1\\ \varepsilon_2\\ \varepsilon_3\\ \varepsilon_4\\ \varepsilon_5\\ \varepsilon_6\end{bmatrix} \tag{5-4}$$

where $[\boldsymbol{\sigma}]$,$[\boldsymbol{\varepsilon}]$, and $[\boldsymbol{C}]$ denote the stress, strain, and elastic-stiffness tensors; respectively, expressed in conventional Voigt notation. Table 5-3 lists the values of quartz elastic constants reported in Heyliger et al. (2003) based on experimental measurements using resonance-ultrasound spectroscopy (RSU). The constitutive relationship defined by Equation 4-3 was scripted into a FORTRAN user-subroutine to numerically model silica material in ABAQUS FE code. Equation 4-3 principally works in the local coordinate system spanned by the orthogonal matrix $\boldsymbol{R}$ described in Equation 4-1. Accordingly, the user-subroutine included rotational transformations of strain/stress tensors between the global and local coordinate systems. 3DXRD measurements provided initial $\boldsymbol{R}$ matrices that were assigned to the finite element meshing the cube. At the beginning of the user-subroutine, $\boldsymbol{R}$ was updated to account for the element's rigid rotation, which was calculated from the polar decomposition of the element deformation gradient.

In another user-subroutine, $[\boldsymbol{C}]$ in Equation 4-3 was replaced by the isotropic approximation $[\boldsymbol{C}]_{iso}$ to compare the isotropic with the anisotropic behavior:

$$[\boldsymbol{C}]_{iso} = \frac{E}{(1+v)(1-2v)}\begin{bmatrix} 1-v & v & v & 0 & 0 & 0 \\ v & 1-v & v & 0 & 0 & 0 \\ v & v & 1-v & 0 & 0 & 0 \\ 0 & 0 & 0 & \frac{1-2v}{2} & 0 & 0 \\ 0 & 0 & 0 & 0 & \frac{1-2v}{2} & 0 \\ 0 & 0 & 0 & 0 & 0 & \frac{1-2v}{2} \end{bmatrix} \quad (5\text{-}5)$$

where $E = 99.45\ GPa$ and $v = 0.06$ are the modulus of elasticity and Poisson's ratio calculated by Voigt-Reuss-Hill averaging (Heyliger et al., 2003). Since the latter material model is isotropic, $[\boldsymbol{C}]_{iso}$ is invariant for all orthogonal coordinate systems. Therefore, the rotational stress/strain transformations are redundant and were eliminated from the user-subroutine algorithm.

The material user-subroutines were executed in ABAQUS to model the constitutive response of the silica cube under unconfined uniaxial compression. The silica cube was modeled by a 20-noded hexahedral element that performed the stress-strain FE calculations (call the material user-subroutine) at 27 integration points using quadratic shape functions. As illustrated in Figure 5-3, the hexahedral element measured $0.5\ mm$ in side length and plane symmetry boundary conditions were appropriately assigned for the nodes across the X-Z, Y-Z, and X-Y faces. The FE calculations were conducted via the static implicit solver in ABAQUS, which simulated the uniaxial compression using 1×10^{-4} mm load increments assigned to the nodes across the top face of the hexahedral element (see Figure 5-3). The incremental uniaxial displacement was halved and doubled in preliminary trials and its effect on the FE analysis was found to be negligible. Three trial simulations were conducted on the hexahedral element with the same boundary conditions. Two of the trials modeled the strong (Figure 5-3a) and weak (Figure 5-3b) silica cubes using the anisotropic material user-subroutine with $\boldsymbol{R}$ initialized at each integration point as:

$$R = \begin{bmatrix} 1 & 0 & 0 \\ 0 & 1 & 0 \\ 0 & 0 & 1 \end{bmatrix} \rightarrow \text{strong cube simulations} \quad (5\text{-}6)$$

$$R = \begin{bmatrix} 0 & -1 & 0 \\ 0 & 0 & -1 \\ 1 & 0 & 0 \end{bmatrix} \rightarrow \text{weak cube simulations} \quad (5\text{-}7)$$

The third trial (Figure 5-3c) modeled the constitutive behavior of the silica cube elements using the isotropic user-subroutine Equation (5-5. For the three trials, Figure 5-3d displays the relationship between the major principal stress versus strain averaged over the 27 integration points of the hexahedral element. The constitutive response of the strong cube in Figure 5-3d is stiffer (slope $=103.1\times10^3$) than the weak cube (slope $=79.9\times10^3$), which is in agreement with the experimental observations in Figure 5-2a. The red line (slope $=79.9\times10^3$) in Figure 5-3d represents the simulation that executed the isotopic user-subroutine and has a closer response to the strong cube line than weak.

Discussion of Results

The main objective of testing and simulating the silica cubes is to compare the results with the closed-form solution. The regular geometry of the cube made the closed-form solution computable using the theory of linear elasticity as demonstrated in Figure 5-4.

The cube Cauchy strain tensor was calculated using $[\boldsymbol{C}]^{-1}$ and assuming $\boldsymbol{R}$ matrices as shown in Figures 4-5a and b for the strong and weak cube, respectively; and $[\boldsymbol{C}]_{iso}^{-1}$ for the isotopic cube in Figure 5-4c. Table 5-4 compares among the experimental (3DXRD), simulated (3D FE), and calculated (closed-form) major principal strain of the cube at multiple steps of the global uniaxial compression. The experimental strains represent the major principal lattice strain averaged over the five vertically-stacked layers of the silica cube (mean values from Table 5-2), while the simulated strains were averaged over the 27 integration points (see Figure 5-3). The slope row in Table 5-4 denotes a measurement of stiffness: the change rate of the global uniaxial compressive stress (MPa) with respect to the major principal strain (mm/mm) of the cubes. Figure 5-5 plots the data reported in Table 5-4 for the relationship between the uniaxial compressive load and the major principal strain of the cube using solid lines for experimental data, dotted lines for simulated data, and dashed lines for calculated data. The simulated responses were earlier presented in Figure 5-3d, which evidently overlay their corresponding dotted lines (closed-form solution) in Figure 5-5 with a difference in slope < 1%. The experimental responses in Figure 5-5 include filled-circle markers that represent the cube's global uniaxial compressive load versus major principal strains of the crystal lattice per 3DXRD measurements (Table 5-2). At each load step, multiple filled-circle markers appear because of the vertical stacking procedure in 3DXRD scanning that provided five lattice strain measurements per load step. Solid lines in Figure 5-5 represent the uniaxial load (N) versus displacement (mm) relationships as recorded by the data acquisition system of the compression apparatus (Figure 5-2a). Recall that the solid lines in Figure 5-5 also represent the cube's global uniaxial stress (MPa) versus strain (mm) since the cube side length is 1 mm. Referring to Figure 5-5, the red color denotes the data (e.g., points, lines, and curves) related to the isotopic cube, while the black and grey colors represent the strong and weak cube's data, respectively.

A close agreement can be seen between the solid lines and filled-circle markers in Figure 5-5 ($<$4% difference in slope), which confirms the capability of MIDAS to analyze and measure lattice strains of the scanned cubes under 3DXRD. This agreement fundamentally demonstrates that the crystal lattice strain of the cube has accurately manifested the global uniaxial strain measured at its top face. Overall, Figure 5-5 shows an excellent agreement among the experimental (solid line, and circular points), 3D FE (dashed line), and closed-form (dotted line) constitutive behavior for the strong (black) as well as the weak cube (grey). Since the solid black and grey curves in Figure 5-5 divert more from one another than the dashed/dotted lines, it can be concluded that the experimental response manifests a bit higher degree of constitutive anisotropy than what is captured by the 3D FE simulations and strong-form solutions. Finally, the red lines in Figure 5-5 represent the isotropic approximation of crystal quartz constitutive behavior, which appears to over-estimate the stiffness since the red lines are closer to the black lines (strong cube) than grey (weak cube).

Experiments, simulations, and closed-form analysis of the silica cube under uniaxial compression have clearly demonstrated constitutive anisotropy in the behavior of silica particles due to quartz crystalline-scale characteristics. Natural silica sand particles are also expected to exhibit similar behavior, but they are much complex to assess experimentally or theoretically. Unlike the simple cube geometry, natural sand particles have complex morphologies that make it very difficult to establish a closed-form solution

or experimentally control the loading direction of a sand particle with respect to its crystal planes. In order to assess the constitutive anisotropy of natural silica sand particles, the authors have upgraded their 3D FE simulation capabilities via coding development in ABAQUS in order to model natural sand specimens with thousands of particles. The new simulations seek to model sand specimens using 3D FE meshes that closely match the natural sand morphology and particle-scale fabric. Subsequently, element strains of the 3D FE meshes are converted to stresses via the isotropic or anisotropic material user-subroutine that was developed in Section 2.2. A numerical contact model also simulates the transmission of stresses at contact interactions between the 3D FE meshes (sand particles). An example of the upgraded 3D FE simulations is presented in Section 3.2 for a uniaxial compression experiment on a natural sand specimen composed of 2705 silica particles. Beforehand, the new 3D FE simulations were calibrated using the rich 3D experimental data collected for the silica cubes as depicted in Figure 5-6 that have some major enhancements compared to the simulations presented earlier in Figure 5-3. Namely, the silica cube was meshed into 10-noded tetrahedral finite elements (i.e., four integration points per element) measuring 100 μm in size since tetrahedral elements are widely acknowledged to effectively mesh 3D complex geometries like natural sand particles. Furthermore, uniaxial compression was simulated by two compressing loading platens using ABAQUS 2D rigid elements. Rigid elements in ABAQUS experience no deformation and are associated with a reference node in which the element kinematics are completely determined by boundary conditions imposed at the reference point rather than the computationally-expensive element-level calculations. In Figure 5-6, meshed parts were assembled together to resemble the experimental setup of a single cube compression. The cube was accurately placed between the two loading platens and the nodes of the bottom loading platen were fully restrained (zero degrees of freedom), while uniaxial displacement (one degree of freedom) was assigned to the top loading platen at a rate of $0.015\ \mathrm{mm/min}$ similar to the experiment. The cube-platen contact was simulated using a frictional contact model and the dynamic explicit solver. An urgent need for the dynamic explicit solver has emerged in a quest for simulating thousands of 3D FE contacts between particles in a sand specimen. Appendix A compares the static implicit and dynamic explicit solvers. It explains the fundamental reason for choosing the dynamic explicit solver to conduct the 3D FE simulations, and supplements details about the numerical contact model that was used to simulate the transmission of stresses at contact interfaces between meshes (e.g., particles, platens, etc.).

Experiments and Modelling of Natural Silica Sand Particles

This section exploits the unique experimental measurements of the combined SMT and 3DXRD scanning technique as well as the numerical 3D FE analysis to assess the directional anisotropy in the constitutive behavior of a specimen composed of natural silica sand particles from a crystalline-scale point of view. Scanning and simulations were conducted using particles with grain sizes between U.S. sieve $\#100\ (150\ \mu m)$ and $\#140\ (106\ \mu m)$ that were sieved from F-75 Ottawa sand; a natural silica sand mined from Ottawa, Illinois and supplied by U.S. Silica Company, Frederick, MD, USA. For initial crystal phase identification of the sand particles, powder sample (passing US sieve #200) was prepared by grinding several sand particles, and then scanning the sample at the JIAM facility using powder x-ray diffraction. The crystal information of the sand particles

identified by powder x-ray diffraction was similar to the synthetic silica cubes as summarized in Table 5-1. Furthermore, eight intact particles were randomly selected from the sand and were scanned using Laue x-ray diffraction at JIAM. Out of the eight sand particles, three possessed single crystal structure, while the other five surprisingly manifested complex Laue x-ray diffraction patterns that were suspected to describe either twins or poly crystals. Tested sand particles were expected to have a single crystal structure, since 35 particles of the same sand source (F-75 Ottawa) but different size portion (U.S. Sieve $\#40$ and $\#50$) were earlier scanned by Cil et al. (2017) using the combined 3DXRD and SMT technique in which all the 35 particles exhibited single crystal structure.

Amirrahmat et al. (2020) acquired combined in-situ SMT and 3DXRD scans for a sand specimen composed of the F-75 Ottawa with grain size between U.S. Sieve $\#100$ and $\#140$ and loaded under confined uniaxial compression. The experiment was conducted at beamline 1-ID of APS using a modified version of the single-particle compression apparatus. The cylindrical concentric loading platens were replaced by $1.55\ \mathrm{mm}$ tungsten carbide platens that uniaxially compressed sand particles confined by a cylindrical nylon tube and housed inside another thick-wall acrylic tube. Uniaxial compression was paused at certain load steps, and the apparatus was rotated twice over 360^0 to collect in-situ SMT and 3DXRD scans using a $1\ \mathrm{mm}$ high beam over four vertically stacked layers to cover the entire height of the sand specimen. Likewise the analysis of the silica cubes, 3DXRD scans were processed in MIDAS to measure the center, orientation, and strain for individual crystal lattices of the sand particles within the scanned specimen. Furthermore, individual particles from the SMT scans (spatial resolution equal to 1.17 μm) were accurately segmented and labeled using AVIZO 9.7.0, a commercial computer software developed by Thermo Fisher Scientific for high-performance 3D image visualization and processing. Figure 5-7 displays the scans collected at the initial unloaded state including a central Y-Z vertical slice in the greyscale SMT scan, 3D volume rendering processed by AVIZO, and centers of the crystal lattices for particles within the specimen as quantified by 3DXRD measurements. The AVIZO processed image (Figure 5-7b) represents a specimen measuring $1.6\ \mathrm{mm}$ in diameter $\times\ 3.7\ \mathrm{mm}$ in height and contained 2705 sand particles, while MIDAS quantified 5027 3DXRD measurements (Figure 5-7c). The abundance of 3DXRD measurements relative to the total number of sand particles was directly linked to the surprising twins and poly crystals manifested by Laue x-ray patterns for some particles of the same sand as well as the stitching procedure of the 3DXRD scans in which edge particles between two adjacent layers were scanned twice. Amirrahmat et al. (2020) developed post-processing algorithms that accurately identified the 3DXRD measurements belonging to individual sand particles in the AVIZO processed images. Out of the 5027 3DXRD measurements, they quantified 4511 centers of the crystal lattices contained inside the 3D bodies of the 2705 sand particles. The rest of the crystal lattices (~10%) were found to be within the void space of the specimen and these measurements were matched with the nearest surrounding sand particle. This chapter will use the SMT and 3DXRD data processed by Amirrahmat et al. (2020) at the initial unloaded state (Figure 5-7) to examine the crystal structure of the individual sand particles, then build 3D FE simulations of the confined uniaxial compression experiment. For the 3D FE simulations, AVIZO was used to generate surface meshes that closely matched the natural morphology of the 2705 sand particles. The surface of each particle

was accurately traced by a closed 3D mesh composed of ~750 equilateral triangles measuring ~12 μm in size. Refer to Figures in Appendix B for examples of wire-frame surface meshes versus 3D volume rendering of the sand particles to visually evaluate the quality of meshes in resembling the 3D natural morphology of the sand.

Crystal Structure of Natural Silica Sand Particles

3DXRD measurements quantified a Cartesian right-handed coordinate system that spanned the crystal lattices within individual sand particles by means of $\boldsymbol{R}$ (Equation 4-1). Figure 5-8 shows an illustrative example of a single 3DXRD measurement quantified by MIDAS for sand particle No. 111 with the circular point representing the center of the particle's crystal lattice. Note that the particle label "111" in Figure 5-8 is according to the particle numbering in AVIZO labeled image. Local coordinate axes in Figure 5-8 span vectors of $\boldsymbol{R}$ column-basis with the blue, green, and red axes denoting the [0 0 0 1] (c-axis), [0 1 -1 0], and [2 -1 -1 0] (a-axis) crystal local axes, respectively. Hereafter, this convention of vector colors will be used to identify the crystal axes in plots of local orientations.

As illustrated in Figure 5-9, multiple 3DXRD measurements were quantified by MIDAS for 47% of sand particles. Preliminary examination of these particles revealed repeated patterns of crystal local orientations such as $0, 60^o, 90^o, 120^o$, and 180^o rotation about a common c-axis. These patterns are thoroughly assessed in Appendix B with illustrative examples for each case and fundamentally produced by the 3_2 rotational symmetry of crystal quartz, while essentially described the same crystal lattice or Dauphiné twins. Figure 5-10 shows a histogram that summarizes the crystal structure of sand particles. Namely, 1441 sand particles (53%) were found to compose of a single crystal structure, 1066 particles (40%) possess Dauphiné twins, and 198 particles (7%) have a poly-crystal structure.

3D FE Simulations of the Confined Uniaxial Compression Experiment

Single cube compression experiments confirmed the hypothesis of constitutive anisotropy in silica particles when loaded in different directions with respect to their crystal local orientation. This anisotropic behavior is also expected for the 2705 natural sand particles when loaded in the confined uniaxial compression experiment. However, natural sand exhibits complex morphology and particle-to-particle interaction unlike the regular shape of the cube that provided a baseline geometry. It is challenging to experimentally investigate the influence of crystal local orientations on the constitutive behavior of natural silica sand particles. The influence of particle-scale properties would be significant and may predominate the influence of crystal local orientations, and it is impossible to experimentally prepare identical sand specimens with the same particle morphology, fabric, etc. The 2705 sand particles in the confined uniaxial compression experiment were arbitrarily deposited inside the confining nylon tube during the specimen preparation stage with no experimental control on the crystal local orientations of individual sand particles. Furthermore, measuring crystal local orientations requires advanced instruments (e.g., SMT and 3DXRD) that are available only in special user facilities such as APS. As mentioned earlier DEM cannot model crystalline-scale characteristics of granular materials. Therefore, the 3D FE analysis that was calibrated using the silica cube

experiments has emerged as an invaluable tool to study how the crystal local orientations of individual sand particles affect their constitutive behavior.

Surface meshes of the 2705 natural sand particles were imported into ABAQUS and filled with 3D solid tetrahedral elements. On average, particles were filled into $\sim 12\ \mu\mathrm{m}$ size tetrahedrons that produced ~3,600–3,800 elements per particle depending on the volume of sand particles. Meshes of individual sand particles were assembled together in ABAQUS/CAE similar to the initial experimental setup including two loading platens and a confining tube. Analogous to the simulations of the cubes, sand particles were modeled using quadratic tetrahedrons, while loading platens and the confining tube were modeled using 2D rigid elements. Elements of the confining tube and bottom loading platen were fully restrained (zero degrees of freedom), whereas elements of the top loading platen were permitted to axially compress the meshed specimen at a loading rate of $0.02\ \mathrm{mm/min}$ similar to the experiment.

Four 3D FE simulations were performed on the same meshed specimen and boundary conditions; they are labeled as isotropic (Iso), strong, weak, and experimental (Exp). The isotropic simulations used the isotopic material user-subroutine (Equation (5-5) to numerically model the constitutive behavior of quadratic tetrahedrons meshing individual sand particles. At 3% global uniaxial strain, components of stress tensors at the integration points were arithmetically averaged into element-level stresses. Subsequently, components of element-level stress tensors were averaged into particle-level stresses with each element volume considered as a weighing factor. This averaging procedure yielded one stress tensor per particle and eigenvalues were computed for each particle to represent the major (σ_1), intermediate (σ_2), and minor (σ_3) principal stresses. Particle-level σ_1, σ_2, and σ_3 were mostly compressive due to the mutual loading mechanism imposed at the contact interfaces between particles. Eigenvectors for particle-level stress tensors were also calculated as $\boldsymbol{V_1}$, $\boldsymbol{V_2}$, and $\boldsymbol{V_3}$ unit vectors spanning the directions of σ_1, σ_2, and σ_3, respectively.

The strong, weak, and experimental simulations implemented the anisotropic material subroutine (Equation (5-4) to numerically model the constitutive behavior of the quadratic tetrahedrons. In weak simulations, element meshing individual particles were initially assigned to $\boldsymbol{R}$ (Equation 4-1) matrices as $[\boldsymbol{V_1}\ \boldsymbol{V_2}\ \boldsymbol{V_3}]$; column stacking of particle-level σ_1, σ_2, and σ_3 directions, respectively. Conversely, $\boldsymbol{R}$ matrices in strong simulations were initialized as $[\boldsymbol{V_3}\ \boldsymbol{V_2}\ \boldsymbol{V_1}]$; column stacking of particle-level σ_3, σ_2, and σ_1 directions, respectively. This idea of $\boldsymbol{R}$ pre-assignment seeks to compare the constitutive response of the sand specimen when the crystal [0 0 0 1] axes (stiffer) of individual particles are aligned with the direction of the σ_1 (strong simulations) versus the opposite case of the [2 -1 -1 0] (less stiff) aligned with the direction of σ_1 (weak simulations). The experimental simulations attempted to match the crystal local orientations of individual particles as quantified by 3DXRD measurements. Assessment of 3DXRD crystal local orientations presented in Appendix B revealed 53% of the particles are composed of single crystal structure that is spanned by one $\boldsymbol{R}$ matrix. However, 3DXRD measurements provided multiple crystal local orientations for particles with Dauphiné twins (40%) and poly crystals (7%). For these particles, $\boldsymbol{R}$ matrices were initialized based on a random selection among the multiple 3DXRD measurements matched with the particle. The 3D FE simulations presented in this chapter have the capability to implement material user-subroutines that can numerically model the constitutive behavior of Dauphiné twins and

poly crystals (Barton and Wenk, 2007). However, the development of such user-subroutines is beyond the scope of this chapter, which is mainly to study how the crystal local orientation of sand particles influence their constitutive behavior. After all, the percentage of particles with poly crystals was low and particles possessing Dauphiné twins shared the same c-axis, which is the direction with the major difference in stiffness. The configurations of crystal local orientations are depicted in Figure 5-11 as assigned to individual particles in strong, weak, and experimental simulations. Although one crystal's local coordinate system was plotted in Figure 5-11 at the centroid of each particle, the local coordinate systems were assigned to all the elements meshing the particle. In the strong simulations (Figure 5-11a), the local blue axes (c-axis) for the particles clearly shows a preferred orientation toward the direction of the global uniaxial compression. Conversely, the local red axes (a-axis) in weak simulations (Figure 5-11b) tends to point toward the direction of the global uniaxial compression. As expected, local coordinate systems in Figure 5-11c were randomly distributed since particles were arbitrarily deposited inside the confining tube during the experiment preparation stage. The idea of aligning the crystal local orientation of individual sand particles in preferred directions for the weak and strong simulations was originally inspired by the studies reporting on the effect of preferred contact fabric (e.g., normal to contact vectors between particles) on the constitutive behavior of sand specimens. However, the preferred orientations in this chapter describe properties at the crystalline-scale rather than the particle-scale in contact fabric studies. To further clarify the preferred crystal orientations, Figure 5-12 visualizes the distribution of the crystal c-axis (blue axes in Figure 5-11) in strong, weak, and experimental simulations on a unit radius semi-sphere with respect to the global coordinate system. Scatter points in Figure 5-12 represent the (x, y, z) coordinates of the crystal local c-axis that was assigned to the 2705 sand particles of the meshed specimen. Crystal local c-axes with negative global Z coordinate were substituted in the scatter plots by the equivalent two-fold symmetrical axes. 3D scatter plots clearly exposed the preferred orientations in the crystal local c-axis of sand particles toward the direction of the global uniaxial compression in strong simulations versus the horizontal plane in weak simulations. The experimental simulations in Figure 5-12c exhibited a random scatter, which supports the intended arbitrary distribution of the experimental crystal local orientations for individual sand particles within the specimen.

Discussion of FE Simulation Results

The evolution of the global uniaxial stress versus strain is depicted in Figure 5-13 for the four FE simulations. The uniaxial stress was calculated as the summation of reaction forces against the top loading platen divided by the specimen cross-sectional area. The uniaxial strain was computed as the displacement of the top loading platen normalized with respect to the specimen's initial height. Note that the specimen's diameter and initial height are the same for the four simulations since the simulations were repeated on the same meshed specimen. The difference between the curves in Figure 5-13 is directly caused by the differently assigned crystal local orientation to individual sand particles. The strong curve in Figure 5-13 clearly exhibits the stiffest constitutive response, while the weak curve shows the least stiff behavior. This aforementioned finding is in agreement with the experimental and FE simulation results for the silica cubes (Figure 5-5) but on the scale of a multi-particle specimen. The experimental and isotropic curves are between

the weak and strong as expected for an arbitrary distribution of crystal orientations in the experimental simulations and isotropic estimation of crystal quartz elastic constitutive behavior in the isotropic simulations. Yet, the isotropic curve in Figure 5-13 exhibited stiffer evolution than the experimental curve and closer to the strong curve, which is comparable to the findings on the isotropic cube simulations in Figure 5-5.

Particle-level σ_1 was compared at 3% global uniaxial strain using histograms displayed in Figure 5-14 for isotropic versus experimental and strong versus weak simulations. Experimental and isotropic histograms match well in Figure 5-14a, but the isotropic histogram still shows a minor over-estimated stress (more highly stressed particles). The weak histogram in Figure 5-14b clearly displays a setback compared to the strong. This setback postulates that at the same global uniaxial strain, particles experience higher stresses when their crystal local c-axis is aligned with the direction of their σ_1 which supports the previous finding of stiffer behavior for the strong cube (Figure 5-5) as well as strong FE simulations (Figure 5-14).

Figure 5-15 displays fringe plots for element-level σ_1 in the isotropic simulations at 3% global uniaxial strain. Six particles were selected from representative regions within the specimen in which they exhibited high stresses (binned the 75% quantile of the isotropic histogram in Figure 5-14a). Selected particles were used as stress gauges to compare among the four FE simulations by means of the assigned crystal local orientations, the direction of particle-level σ_1, and fringe plots of element-level σ_1 at a Y-Z cut across particles' centroids. Figure 5-15 clearly shows how the crystal c-axis in strong particles and the a-axis in weak particles spanned the direction of the particle-level σ_1 in isotropic particles. In fact, the direction of the particle-level σ_1 is almost the same in all FE simulations. Morphology and particle-to-particle interaction are identical in the four simulations. This identicalness essentially imposed the same loading mechanism at contacts between sand particles, which produced similar directions of particle-level σ_1 in the four simulations. However, differences in the value of element-level σ_1 among the four simulations can be evidently seen in the fringe plots for the selected particles at their central Y-Z cut.

The evolution of particle-level σ_1 versus major principal strain is plotted in Figure 5-16 for the six selected particles to compare particle-scale stiffness among the four FE simulations. The strong curves in Figure 5-16 showed stiffer behavior when compared to the isotropic and weak with the isotropic curves laying between the strong and weak, but closer to the strong than weak (isotropic curves exhibit over-estimated stiffness). The experimental curves in Figure 5-16 have no definitive trend in which for some cases the experimental curves exhibited the lowest stiffness like the case of particle 2500, close to the weak as in particles 476 and 2266, between the weak and strong but still less than the isotropic for particle 675, close to the strong as in particle 1455, and stiffer than the strong for particle 828. This arbitrary trend advocates for the quest of modeling the actual crystal local orientations of the sand particles to accurately simulate the experimental constitutive response.

Conclusions

This chapter synthesizes basic knowledge from material science and crystallography with geotechnical research regarding the constitutive behavior of silica sand particles. The influence of quartz crystal structure on the constitutive response of natural and synthetic

silica particles was examined using rich 3D experimental measurements quantified by combined in-situ SMT and 3DXRD scanning as well as numerical 3D FE analysis. The following conclusions are drawn:

5. The crystal structure of quartz essentially produces directional anisotropy in the constitutive behavior of silica particles. On the scale of a single silica $(1\ \mathrm{mm})^3$ cube subjected to unconfined uniaxial compression, major principal lattice strain experimentally manifested ~ 1.3 stiffer response when the cube was loaded against the face aligned with (0 0 0 1) versus (2 -1 -1 0) crystal plane.
6. 3D FE analysis can numerically model the constitutive anisotropy in silica particles by implementing crystal-based material subroutines. 3D FE analysis accurately simulated the significant difference in the evolution of the major principal lattice strain for the silica cube when loaded against opposite crystal planes.
7. Natural silica sand particles possess a rather complex crystal structure compared to the synthetic silica cubes. Upon inspecting the crystals of 2705 natural silica sand particles, 53% of the particles were composed of single crystals, 40% possessed Dauphiné twins, and 7% with poly crystals.
8. The crystal structure of tested sand particles surprisingly manifested Dauphiné twins and poly crystals, while none was reported in likewise analysis on 35 particles of the same sand source (but with larger grain size range) in Cil et al. (2017). It is either that the 35 particles tested in Cil et al. (2017) were not representative of the sand source or that Dauphiné twins might have formed in the sand particles with smaller grain size range.
9. At the particle-scale, natural silica sand particles exhibit significant stiffer constitutive behavior when their major principal stress direction is aligned with the [0 0 0 1] crystal local axis compared to [2 -1 -1 0]. At the global-scale, this anisotropy in the constitutive behavior was also noticed at a less significant-level when the [0 0 0 1] crystal local axes of individual sand particles line up in preferred orientations toward their major principal stress direction. Crystal local orientations of sand particles are primarily determined by the geological weathering conditions. Residual sand particles may inherit preferential crystal local orientations from their parent bedrocks, which can influence their constitutive response.
10. Crystal local orientations of sand particles have minimal effect on the direction of the particles' major principal stress. In fact, the direction of the particles' major principal stress is determined by the loading mechanism imposed at contact interfaces among sand particles. The loading mechanism imposed on sand particles is essentially governed by particle-scale properties such as sand morphology and particle-to-particle interaction.
11. The isotropic elastic model of crystal quartz yields a stiffer estimation of the constitutive behavior of silica particles in which simulated results showed closer response to the case when the [0 0 0 1] crystal local axis of individual sand particles are aligned in preferred orientations toward the direction of the particles' major principal stress.
12. Although particle-scale properties (e.g., morphology, contact fabric, etc.) are widely recognized in geotechnical research to alter the constitutive behavior of sand specimens, particle stresses are fundamentally determined by the

constituent crystalline-scale properties, which a comprehensive constitutive framework modeling sand behavior cannot overlook or ignore.

Acknowledgments

The work in this chapter is funded by the National Science Foundation (NSF) Grant No. CMMI-1362510. Any opinions, findings, conclusions, and recommendations expressed in this chapter are those of the authors and do not necessarily reflect the views of NSF. This chapter has used resources of the Joint Institute for Advanced Materials (JIAM), x-ray diffraction facility located at the University of Tennessee, Knoxville, TN and the Advanced Photon Source (APS), a U.S. Department of Energy (DOE) Office of Science User Facility operated for the DOE Office of Science by Argonne National Laboratory (ANL) under Contract No. DE-AC02-06CH11357. I would also like to thank Zaher A. Jarrar and Andrew M. Druckrey of the University of Tennessee for contributing to the experimental work at APS, and Amirsalar Moslehy for leading the powder and Laue x-ray diffraction experiments at JIAM.

References

Goldich, S. S. (1938) A study in rock-weathering. *The journal of Geology* **46(1)**:17-58.

Gault, H. (1949) The frequency of twin types in quartz crystals. *American Mineralogist: Journal of Earth and Planetary Materials* **34(3-4)**:142-162.

Bechmann, R. (1958) Elastic and piezoelectric constants of alpha-quartz. *Physical Review* **110(5)**:1060.

Roscoe, K. H., Schofield, A. & Wroth, C. (1958) On the yielding of soils. *Geotechnique* **8(1)**:22-53.

Tilley, C. E. (1961) Leonard James Spencer, 1870-1959.) The Royal Society London.

Schofield, A. & Wroth, P. (1968) Critical state soil mechanics.

Pettijohn, F. J., Potter, P. E. & Siever, R. (1972) Introduction and Source Materials. In *Sand and Sandstone*.) Springer, pp. 1-23.

Jorgensen, J. (1978) Compression mechanisms in α-quartz structures—SiO2 and GeO2. *Journal of Applied Physics* **49(11)**:5473-5478.

Hahn, T., Shmueli, U. & Wilson, A. J. C. (1983) *International tables for crystallography.* Reidel Dordrecht.

Sunagawa, I. & Yasuda, T. (1983) Apparent re-entrant corner effect upon the morphologies of twinned crystals; A case study of quartz twinned according to Japanese twin law. *Journal of Crystal Growth* **65(1-3)**:43-49.

Ting, J. M., Khwaja, M., Meachum, L. R. & Rowell, J. D. (1993) An ellipse-based discrete element model for granular materials. *International Journal for Numerical and Analytical Methods in Geomechanics* **17(9)**:603-623.

Tsoungui, O., Vallet, D. & Charmet, J.-C. (1999) Numerical model of crushing of grains inside two-dimensional granular materials. *Powder Technology* **105(1-3)**:190-198.

Gregoryanz, E., Hemley, R. J., Mao, H.-K. & Gillet, P. (2000) High-pressure elasticity of α-quartz: instability and ferroelastic transition. *Physical Review Letters* **84(14)**:3117.

Iwashita, K. & Oda, M. (2000) Micro-deformation mechanism of shear banding process based on modified distinct element method. *Powder Technology* **109(1-3)**:192-205.

Lloyd, G. E. (2000) Grain boundary contact effects during faulting of quartzite: an SEM/EBSD analysis. *Journal of Structural Geology* **22(11-12)**:1675-1693.

Dušek, M., Petříček, V., Wunschel, M., Dinnebier, R. & Van Smaalen, S. (2001) Refinement of modulated structures against X-ray powder diffraction data with JANA2000. *Journal of Applied Crystallography* **34(3)**:398-404.

Robertson, D. & Bolton, M. (2001) DEM simulations of crushable grains and soils. *Powders and grains. Lisse. The Netherlands: Balkema*:623-6.

Mcdowell, G. & Harireche, O. (2002) Discrete element modelling of yielding and normal compression of sand. *Geotechnique* **52(4)**:299-304.

Cheng, Y., Nakata, Y. & Bolton, M. (2003) Discrete element simulation of crushable soil. *Geotechnique* **53(7)**:633-641.

Heyliger, P., Ledbetter, H. & Kim, S. (2003) Elastic constants of natural quartz. *J. Acoust. Soc. Am* **114**:644.

Laugier, J. & Bochu, B. (2004) LMGP-Suite of Programs for the Interpretation of x-ray Experiments. *ENSP/Laboratories des Materiaux et du Genie Physique, BP46* **38042**.

Santamarina, J. & Cho, G.-C. (2004) Soil behavior: The role of particle shape. In *Advances in geotechnical engineering: The skempton conference*.) Citeseer, vol. 1, pp. 604-617.

Fortin, J., Millet, O. & De Saxcé, G. (2005) Numerical simulation of granular materials by an improved discrete element method. *International Journal for Numerical Methods in Engineering* **62(5)**:639-663.

Lobo-Guerrero, S. & Vallejo, L. E. (2005) Discrete element method evaluation of granular crushing under direct shear test conditions. *Journal of Geotechnical and Geoenvironmental Engineering* **131(10)**:1295-1300.

Nocilla, A., Coop, M. & Colleselli, F. (2006) The mechanics of an Italian silt: an example of 'transitional'behavior. *Geotechnique* **56(4)**:261-271.

Ogi, H., Ohmori, T., Nakamura, N. & Hirao, M. (2006) Elastic, anelastic, and piezoelectric coefficients of α-quartz determined by resonance ultrasound spectroscopy. *Journal of Applied Physics* **100(5)**:053511.

Barton, N. R. & Wenk, H.-R. (2007) Dauphiné twinning in polycrystalline quartz. *Modelling and Simulation in Materials Science and Engineering* **15(3)**:369.

Callister, W. D. (2007) *Materials science and engineering-an introduction.* John wiley & sons.

Kruggel-Emden, H., Simsek, E., Rickelt, S., Wirtz, S. & Scherer, V. (2007) Review and extension of normal force models for the discrete element method. *Powder Technology* **171(3)**:157-173.

Nikitin, A., Markova, G., Balagurov, A., Vasin, R. & Alekseeva, O. (2007) Investigation of the structure and properties of quartz in the α-β transition range by neutron diffraction and mechanical spectroscopy. *Crystallography Reports* **52(3)**:428-435.

Bolton, M., Nakata, Y. & Cheng, Y. (2008) Micro-and macro-mechanical behavior of DEM crushable materials. *Geotechnique* **58(6)**:471-480.

Quintana-Alonso, I. & Fleck, N. A. (2009) Fracture of brittle lattice materials: A review. In *Major accomplishments in composite materials and sandwich structures*.) Springer, pp. 799-816.

Hall, S. A., Bornert, M., Desrues, J., Pannier, Y., Lenoir, N., Viggiani, G. & Bésuelle, P. (2010) Discrete and continuum analysis of localised deformation in sand using x-ray [mu] CT and volumetric digital image correlation. *Geotechnique* **60(5)**:315.

Roters, F., Eisenlohr, P., Hantcherli, L., Tjahjanto, D. D., Bieler, T. R. & Raabe, D. (2010) Overview of constitutive laws, kinematics, homogenization and multiscale methods in crystal plasticity finite-element modeling: Theory, experiments, applications. *Acta Materialia* **58(4)**:1152-1211.

Altuhafi, F. & Coop, M. R. (2011) Changes to particle characteristics associated with the compression of sands. *Geotechnique* **61(6)**:459-471.

Charalampidou, E.-M., Hall, S. A., Stanchits, S., Lewis, H. & Viggiani, G. (2011) Characterization of shear and compaction bands in a porous sandstone deformed under triaxial compression. *Tectonophysics* **503(1-2)**:8-17.

Jiang, M., Yan, H., Zhu, H. & Utili, S. (2011) Modeling shear behavior and strain localization in cemented sands by two-dimensional distinct element method analyses. *Computers and Geotechnics* **38(1)**:14-29.
Li, X. & Dafalias, Y. (2011) Anisotropic Critical State Theory: Role of Fabric. *Journal of Engineering Mechanics* **138(3)**:263-275.
Sharma, H., Huizenga, R. M. & Offerman, S. E. (2012a) A fast methodology to determine the characteristics of thousands of grains using three-dimensional X-ray diffraction. I. Overlapping diffraction peaks and parameters of the experimental setup. *Journal of Applied Crystallography* **45(4)**:693-704.
Sharma, H., Huizenga, R. M. & Offerman, S. E. (2012b) A fast methodology to determine the characteristics of thousands of grains using three-dimensional X-ray diffraction. II. Volume, centre-of-mass position, crystallographic orientation and strain state of grains. *Journal of Applied Crystallography* **45(4)**:705-718.
Shipton, B. & Coop, M. R. (2012) On the compression behavior of reconstituted soils. *Soils and Foundations* **52(4)**:668-681.
Akhavan, A. C. (2013) *The Page of Quartz*, See http://www.quartzpage.de/about.html (accessed Dec. 14 2018).
Alshibli, K., Cil, M., Kenesei, P. & Lienert, U. (2013) Strain tensor determination of compressed individual silica sand particles using high-energy synchrotron diffraction. *Granular Matter*:1-14.
Cil, M., Alshibli, K., Mcdowell, G. & Li, H. (2013) Discussion: 3D assessment of fracture of sand particles using discrete element method. *Géotech. Lett* **3(3)**:13-15.
Toby, B. H. & Von Dreele, R. B. (2013) GSAS-II: the genesis of a modern open-source all purpose crystallography software package. *Journal of Applied Crystallography* **46(2)**:544-549.
Abaqus, V. (2014) 6.14 Documentation. *Dassault Systemes Simulia Corporation*.
Degen, T., Sadki, M., Bron, E., König, U. & Nénert, G. (2014) The highscore suite. *Powder Diffraction* **29(S2)**:S13-S18.
Hoek, E. & Martin, C. (2014) Fracture initiation and propagation in intact rock–a review. *Journal of Rock Mechanics and Geotechnical Engineering* **6(4)**:287-300.
O'sullivan, C. (2014) *Particulate discrete element modelling: a geomechanics perspective.* CRC Press.
Shipton, B. & Coop, M. R. (2014) Transitional behavior in sands with plastic and non-plastic fines. *The japanese geotechnical society*.
Coop, M. (2015) Limitations of a Critical State framework applied to the behavior of natural and “transitional” soils. In *Proceedings of 6th International Symposium on Deformation Characteristics of Geomaterials, IS-Buenos Aires*.), pp. 115-155.
Eder, S. D., Fladischer, K., Yeandel, S., Lelarge, A., Parker, S. C., Søndergård, E. & Holst, B. (2015) A giant reconstruction of α-quartz (0001) interpreted as three domains of nano dauphine twins. *Scientific reports* **5**:14545.
Hall, S. & Wright, J. (2015) Three-dimensional experimental granular mechanics. *Géotechnique Letters* **5(4)**:236-242.
Park, J.-S., Zhang, X., Sharma, H., Kenesei, P., Hoelzer, D., Li, M. & Almer, J. (2015) High-energy synchrotron x-ray techniques for studying irradiated materials. *Journal of Materials Research* **30(9)**:1380-1391.

Xiao, Y., Liu, H., Ding, X., Chen, Y., Jiang, J. & Zhang, W. (2015) Influence of particle breakage on critical state line of rockfill material. *International Journal of Geomechanics* **16(1)**:04015031.
Yang, J. & Luo, X. (2015) Exploring the relationship between critical state and particle shape for granular materials. *Journal of the Mechanics and Physics of Solids* **84**:196-213.
Zhang, B., Herbold, E. B., Homel, M. & Regueiro, R. A. (2015) *DEM Particle Fracture Model*.
Zhao, B., Wang, J., Coop, M., Viggiani, G. & Jiang, M. (2015) An investigation of single sand particle fracture using x-ray micro-tomography. *Geotechnique* **65(8)**:625-641.
Zuo, L. & Baudet, B. A. (2015) Determination of the transitional fines content of sand-non plastic fines mixtures. *Soils and Foundations* **55(1)**:213-219.
Cole, D. M. & Hopkins, M. A. (2016) The contact properties of naturally occurring geologic materials: experimental observations. *Granular Matter* **18(3)**:62.
Dafalias, Y. F. (2016) Must critical state theory be revisited to include fabric effects? *Acta Geotechnica* **11(3)**:479-491.
Druckrey, A. M. & Alshibli, K. A. (2016) 3D finite element modeling of sand particle fracture based on in situ x-ray synchrotron imaging. *Int. J. Numer. Anal. Methods Geomech.* **40**:105.
Kawamoto, R., Andò, E., Viggiani, G. & Andrade, J. E. (2016) Level set discrete element method for three-dimensional computations with triaxial case study. *Journal of the Mechanics and Physics of Solids* **91**:1-13.
Reynolds, S. J., Johnson, J. K., Morin, P. J. & Carter, C. (2016) *Exploring geology.* McGraw-Hill Education.
Turner, A. K., Kim, F. H., Penumadu, D. & Herbold, E. B. (2016) Meso-scale framework for modeling granular material using computed tomography. *Computers and Geotechnics* **76**:140-146.
Cil, M. B., Alshibli, K. A. & Kenesei, P. (2017) 3D Experimental Measurement of Lattice Strain and Fracture Behavior of Sand Particles Using Synchrotron x-ray Diffraction and Tomography. *Journal of Geotechnical and Geoenvironmental Engineering* **143(9)**.
Fu, R., Hu, X. & Zhou, B. (2017) Discrete element modeling of crushable sands considering realistic particle shape effect. *Computers and Geotechnics* **91**:179-191.
Hurley, R., Hall, S. & Wright, J. (2017) Multi-scale mechanics of granular solids from grain-resolved x-ray measurements. *Proceedings of the Royal Society A: Mathematical, Physical and Engineering Sciences* **473(2207)**:20170491.
Imseeh, W. H., Druckrey, A. M. & Alshibli, K. A. (2017) 3D Experimental Quantification of Fabric and Fabric Evolution of Sheared Granular Materials Using Synchrotron Micro-Computed Tomography. *Granular Matter* **Under revision**.
Kandasami, R. K. & Murthy, T. G. (2017) Manifestation of particle morphology on the mechanical behavior of granular ensembles. *Granular Matter* **19(2)**:21.
Zhou, W., Yang, L., Ma, G., Xu, K., Lai, Z. & Chang, X. (2017) DEM modeling of shear bands in crushable and irregularly shaped granular materials. *Granular Matter* **19(2)**:25.
Cady, W. G. (2018) *Piezoelectricity: Volume Two.* Courier Dover Publications.

Desrues, J., Andò, E., Mevoli, F. A., Debove, L. & Viggiani, G. (2018) How does strain localise in standard triaxial tests on sand: Revisiting the mechanism 20 years on. *Mechanics Research Communications* **92**:142-146.

Dosta, M., Bröckel, U., Gilson, L., Kozhar, S., Auernhammer, G. K. & Heinrich, S. (2018) Application of micro computed tomography for adjustment of model parameters for discrete element method. *Chemical Engineering Research and Design*.

Hurley, R. C., Herbold, E. B. & Pagan, D. C. (2018) Characterization of the crystal structure, kinematics, stresses and rotations in angular granular quartz during compaction. *Journal of Applied Crystallography* **51(4)**.

Imseeh, W. H. & Alshibli, K. A. (2018) 3D Finite Element Modelling of Force Transmission and Particle Fracture of Sand. *Computers and Geotechnics* **94**:184-195.

Kawamoto, R., Andò, E., Viggiani, G. & Andrade, J. E. (2018) All you need is shape: Predicting shear banding in sand with LS-DEM. *Journal of the Mechanics and Physics of Solids* **111**:375-392.

Nardelli, V. & Coop, M. R. (2018) The experimental contact behavior of natural sands: normal and tangential loading. *Geotechnique*:1-15.

Sandeep, C., He, H. & Senetakis, K. (2018) An experimental micromechanical study of sand grain contacts behavior from different geological environments. *Engineering Geology* **246**:176-186.

Todisco, M., Coop, M. & Pereira, J.-M. (2018) Fabric characterisation in transitional soils. *Granular Matter* **20(2)**:20.

Yan, B. & Regueiro, R. (2018) Large-scale dynamic and static simulations of complex-shaped granular materials using parallel three-dimensional discrete element method (DEM) on DoD supercomputers. *Engineering Computations* **35(2)**:1049-1084.

Amirrahmat, S., Druckrey, A. M., Alshibli, K. A. & Al-Raoush, R. I. (2019) Micro Shear Bands: Precursor for Strain Localization in Sheared Granular Materials. *Journal of Geotechnical and Geoenvironmental Engineering* **145(2)**:04018104.

Tang, H., Dong, Y., Wang, T. & Dong, Y. (2019) Simulation of strain localization with discrete element-Cosserat continuum finite element two scale method for granular materials. *Journal of the Mechanics and Physics of Solids* **122**:450-471.

Amirrahmat, S., Imseeh, W., Alshibli, K., Kenesei, P., Jarrar, Z. & Sharma, H. (2020) 3D Experimental Measurements of Evolution of Force Chains in Natural Silica Sand. *ASCE's Journal of Geotechnical and Geoenvironmental Engineering* **146 (5),** 04020027.

Jarrar, Z., Alshibli, K. & Al-Raoush, R. (2020) 3D Evaluation of Sand Particle Fracture using Discrete Element Method and Synchrotron Micro-computed Tomography Images. *ASCE's Journal of Geotechnical and Geoenvironmental Engineering*.

Mohsin Thakur, M., Penumadu, D. & Bauer, C. (2020) Capillary Suction Measurements in Granular Materials and Direct Numerical Simulations Using x-ray Computed Tomography Microstructure. *Journal of Geotechnical and Geoenvironmental Engineering* **146(1)**:04019121.

Appendices

Appendix A: Description of the 3D Finite Element (FE) Simulations

This chapter developed 3D FE simulations in ABAQUS that numerically model the constitutive behavior of silica sand specimens by synthesizing the contribution of multiple properties at different scale levels. At the particle-scale, the simulations used tetrahedral 3D FE meshes that closely resemble the natural morphology and particle-to-particle interaction of sand specimens. At the crystalline-scale, the simulations executed a material user-subroutine that models the constitutive anisotropy in the linear elastic behavior of crystal quartz. The FE simulations employed a frictional contact model to determine the transmission of stresses between meshed particles that are in contact. The employment of a contact model made a strong need for the dynamic explicit solver to conduct the 3D FE calculations. This Appendix compares the static implicit and dynamic explicit solvers. It comments on the advantage and appropriateness of the dynamic explicit solver for our case. Furthermore, it provides details about the frictional contact model that was adopted in the FE simulations.

3D Finite Element (FE) Solver

ABAQUS offers two types of 3D FE solvers: static implicit and dynamic explicit. At first sight, the implicit solver appears to be a suitable choice since the 3D FE analysis in this chapter is quasi-static (strain rate $< 10^{-2}$/second). However, our 3D FE simulations contain a large number of node-to-element contacts between meshes of sand particles. The static implicit solver struggled to model the numerous number of contacts since in each time increment it runs Newton's iterative procedure to converge static equilibrium. This iterative procedure usually lacks the equilibrium convergence when modeling complex 3D contacts because it requires the contact information (e.g., nodes in contact, nodal contact forces, and displacement) to be updated after every Newton's iteration at every time increment (computationally expensive). Namely, the static implicit solver aborted the first time increment when executed on the 3D FE simulations of sand particles since it exceeded the maximum number of allowed iterations per increment that is typically set to 100 in ABAQUS. Alternatively, the authors have used the dynamic explicit solver to perform the FE calculations. The assumption of nodal-lumped masses ($\boldsymbol{M}$) in the dynamic explicit procedure produces diagonal mass matrices that are used to incrementally solve the equation of motion, then the explicit central-difference time integration rule advances the nodal kinematic state (nodal displacement, velocity, and acceleration) over time. The main advantage in this procedure is the explicit equilibrium equations that are efficiently solved by the fast inversion of $\boldsymbol{M}$ (diagonal matrix) compared to the iterative Newton-Raphson procedure in the static implicit solver.

The dynamic explicit solver is originally designated to simulate engineering problems with high-strain loading conditions by advancing the current nodal state kinematics over small time increments. However, mass scaling offers two major advantages: it significantly speeds up the simulation running time and appropriately produces quasi-static analysis. In dynamic simulations, the stable size time increment (Δt_s) is primarily controlled by the time required for stress wave to propagate through the smallest element in the model. The artificial increase in element mass reduces the propagation speed of stress and allows the solver to use larger Δt_s, which dramatically reduces the total running time of the simulations. The ratio between kinetic and total energy is also limited to 5% during

the simulations in order to ensure having quasi-static-like analysis. Figure 5-17 evaluates the difference between the explicit and implicit 3D FE solver when implemented on the silica cube simulations. It also presents a mesh sensitivity assessment by halving the mesh size of the cube and comparing results. The uniaxial compression in the implicit simulations (Figure 5-17c and d) was modeled using displacement boundary conditions in order to eliminate the contact problem and allow the solver to converge equilibrium in a fast manner. Figure 5-17e plots the major principal stress versus strain, averaged over the four integration points of each element, then over the entire elements meshing the cube with the volume of each element considered as a weighing factor. Furthermore, the results of the single hexahedral element simulations (Figure 5-3) and closed-form solution (Figure 5-4) are plotted in Figure 5-17e to compare and assess the results. Figure 5-17e clearly demonstrates a negligible influence for the selected mesh size and an excellent agreement between the dynamic explicit and static implicit solvers as well as with the closed-form solution and single element simulations.

Contact Model

ABAQUS general contact module is adopted to model the transmission of contact stresses between interacting meshes of separate parts (e.g., cube-to-platen, particle-to-particle, particle-to-platen, particle-to-wall). Surface elements of ABAQUS assembly parts are extracted into individual element-sets and included in the general contact module domain. Contacts are detected using a node-into-face penetration mechanism for the element-sets included in the domain of the general contact module. When elements are in contact, shear and normal forces are transmitted across the contact interface to resist node-into-face, node-into-rigid surface, and edge-into-edge penetration. ABAQUS default hard contact model is used to relate normal contact forces to penetration distance. Briefly, the element bulk stiffness is automatically scaled at the normal to contact interface in which the effect of contact deformation on the time increment is minimal (allowed penetration is neglected in most of the simulations). A frictional contact model is also adopted from ABAQUS to simulate the tangential force transmission at contact interfaces using a friction coefficient of 0.38, a typical value recommended for silica mineral.

The FE simulations reported in this chapter used an enhanced version of the 10-node tetrahedron to eliminate contact problems that exist in general quadratic finite elements. Contact forces acting on mid-edge nodes can essentially vary from corner nodes in a regular 10-node tetrahedron, which leads to solution convergence issues. The enhanced 10-noded tetrahedron is specially designed in ABAQUS to alleviate these shortcomings and produce uniform contact pressure. Refer to ABAQUS Analysis User's Guide section 28.1.1 for more information on the enhanced 10-noded tetrahedron

Appendix B: Assessment of Local Crystal Orientations for Sand Particles with Multiple 3DXRD Measurements

Upon examining the 3DXRD measurements for the sand specimen with 2705 silica particles, it was found that 56% of the particles have multiple 3DXRD measurements. For these particles, local crystal orientations of the multiple measurements were interestingly observed to follow certain patterns such as a 60^o rotation relative to one another about a common c-axis. The authors thoroughly investigated these patterns with illustrative examples to explain how we identified sand particles with Dauphiné twins and single crystal structure. Beforehand, a clear understanding of rotational symmetry in crystal quartz must be reviewed. As described earlier in Figure 5-1, there are two types of crystal quartz: right-handed versus left-handed. Both right- and left-handed crystal quartz exhibits 3_2 rotational symmetry: three-fold symmetry about the c-axis/[0 0 0 1] and two-fold symmetry about the a-axis/[2 -1 -1 0]. In other words, the crystal diagrams depicted in Figures 4-1a&b repeat themselves every 120^o rotation about the c-axis (three-fold symmetry) or 180^o rotation about the a-axis (two-fold symmetry). In summary, crystal local orientations provided by 3DXRD measurements can fundamentally be substituted by the equivalent two-fold or three-fold symmetrical orientation, and still describe the same crystal lattice.

Figure 5-18 presents a sample of particles that are matched with multiple 3DXRD measurements but indirectly possessed a single crystal lattice. Blue, red, and green axes in Figure 5-18 denote the crystal axis [0 0 0 1] (c-axis), [0 1 -1 0] , and [2 -1 -1 0] (a-axis), respectively, while different symbols (circle, and 'x') mark the lattice center of different 3DXRD measurements (crystal lattice). Next to each particle in Figure 5-18, crystal local orientations of the multiple 3DXRD measurements are plotted in the same graph where the arrowheads of crystal axes are substituted by the same symbols used to mark the 3DXRD measurement and the crystal axes are colored differently by blue, red, and green. Figure 5-18a displays two local orientations plotted from two 3DXRD measurements that matched with particle 941. Both local orientations are approximately the same with $< 0.01^0$ miss-orientation. Crystal local orientations measured for particle 1937 are illustrated in Figure 5-18b. By acknowledging the three-fold symmetry in crystal quartz, it can be concluded that both local orientations in Figure 5-18b are equivalent and describe the same lattice since they share the same c-axis but at 120^0 rotation relative to each other. Likewise, substituting one of the local orientations in Figure 5-18c by the equivalent two-fold symmetry (180^o rotation about the a-axis) aligns both local orientations measured for particle 666. A more complex case for particle 403 is presented in Figure 5-18d in which 180^o rotation about the a-axis (two-fold symmetry) followed by a 120^o rotation about the c-axis (three-fold symmetry) brings both sets of crystal local axes to the same orientation (single crystal). Figure 5-18 examples for multiple 3DXRD measurements describing the same crystal lattice can occur because of the stacking procedure in 3DXRD scanning to cover the full height of the specimen. In fact, the centers of 3DXRD measurements (crystal lattices) relative to the particles' body in Figure 5-18 supports the latter statement.

Quartz is well-known in material science to form Dauphiné twins in its crystal structure. In Dauphiné twins, sub-domains of either right- or left-handed quartz crystals are intergrown into one structure. The sub-domains share the same c-axis but are rotated about the common c-axis by 60^0 relative to one another. This pattern of relative rotation can be

seen in Figure 5-19a for the local orientations of the two 3DXRD measurements matched with particle 70. Due to the 3_2 rotational symmetry in quartz, more complex patterns of crystal local orientations are detected to describe Dauphiné twins. For instance, replacing one of the local orientations in Figure 5-19b by the equivalent three-fold symmetry (120^o rotation about the c-axis) brings both orientations of particle 9 to a case like particle 70. Likewise, replacing one of the local orientations of particle 198 in Figure 5-19c by the equivalent two-fold symmetry (180^0 rotation about the a-axis) produces a case similar to particle 70. Finally, substituting one of the local orientations in Figure 5-19d by the two-fold (180^o rotation about the a-axis) followed by three-fold symmetry (120^0 rotation about the c-axis) reveals Dauphiné twins in particle 189.

A general example is presented in Figure 5-20 for four 3DXRD measurements matched with particle 272. Crystal local orientations of the four 3DXRD measurements exhibit the same/opposite c-axis. The local crystal axes capped with diamond and 'x' symbols are the same in Figure 5-20b ($< 0.01^0$ miss-orientation), while the axes capped with pentagrams are rotated by 60^0 about the common c-axis (Dauphiné twins). Furthermore, substituting the axes capped with circles by the two-fold symmetry (180^o rotation about a-axis) aligns the c-axis direction for all 3DXRD measurements in Figure 5-20b, and makes the axes capped with circles rotated at 60^o relative to the axes capped with diamond or 'x' symbols (Dauphiné twins) and 120^0 relative to the axes capped with pentagrams (equivalent three-fold symmetry). Accordingly, the pentagram and circle crystal 3DXRD measurements of particle 272 are concluded to span the same lattice, while the diamond and 'x' represent Dauphiné twins. This example is very unlikely to be random since it is observed in several particles that are matched with two or more 3DXRD measurements, and it is very rare for these specific local orientations to share the same c-axis direction with two- or three-fold symmetrical properties. The procedure of assessing crystal orientation for particles with multiple 3DXRD measurements was automated in a MATLAB script to identify particles with single crystal, Dauphiné twins, and poly-crystals. Particles with poly-crystals are basically identified to possess multiple 3DXRD measurements that exhibit arbitrary patterns of crystal local orientations as depicted in Figure 5-21. The number of poly crystal particles is low (198 out of 2705 particles) and can be directly attributed to experimenting with a natural sand in which non-silica constituent could have existed.

Appendix C: Tables

Table 5-1. x-ray powder diffraction results on silica cubes. Values in parentheses are provided by MaTecK. Values in this table were obtained with the help of my research colleague Amirsalar Moslehy.

Property/Material	**Synthetic Silica Cubes**		**Natural silica particles of F-75 Ottawa sand**	
Chemical formula	SiO_2		SiO_2	
Crystal system	Trigonal		Trigonal	
Lattice system	Hexagonal		Hexagonal	
Space group #	154		154	
Space group name	$P\ 3_2\ 2\ 1\ (P\ 3_2\ 2\ 1)$		$P\ 3_2\ 2\ 1$	
Unit cell lattice parameters	a: 4.915 Å (4.914 Å) b: 4.915 Å (4.914 Å) c: 5.406 Å (5.405 Å)	α: 90° (90°) β: 90° (90°) γ: 120° (120°)	a: 4.914 Å b: 4.914 Å c: 5.405 Å	α: 90° β: 90° γ: 120°
Volume: $Å^3$	113.08		113.02	
Density: g/cm^3	2.647 (2.649)		2.648	

Table 5-2. Summary of the major principal strain measured for silica cubes using 3DXRD. Layers 1 to 5 denote sequential and equal vertical layers along the cube 1 mm height, in which layer 1 represents the top one-fifth portion of the cube that is in contact with the top loading platen.

Cube	Global Axial Load: N	Major principal lattice strain – compression: $10^{-3}mm/mm$						
		Layer 1	Layer 2	Layer 3	Layer 4	Layer 5	Mean	CV[+]
Strong Cube	300	2.71	2.69	2.65	2.60	2.65	2.66	1.61%
	600	5.38	5.32	5.27	5.25	5.27	5.30	0.99%
	900	7.84	8.06	7.98	7.88	8.04	7.96	1.20%
	1200	10.87	10.96	10.84	10.67	10.97	10.86	1.09%
Weak Cube	300	3.76	3.76	3.72	3.65	3.59	3.70	1.96%
	600	7.71	7.69	7.65	7.62	7.60	7.65	0.62%
	900	11.55	11.74	11.89	12.03	12.18	11.88	2.09%
	1200	15.47	15.64	15.95	15.92	16.11	15.82	1.62%

[+] $Coefficient\ of\ variation = \frac{Mean}{Standaed\ Deviation}$

Table 5-3. Elastic constants of crystal quartz (Heyliger et al., 2003)

Elastic constant	C_{11}	C_{12}	C_{13}	C_{14}	C_{33}	C_{44}
Value: GPa	87.26	6.57	11.95	-17.18	105.8	57.15

Table 5-4. Comparison between experimental (3DXRD), simulated (3D FE), and calculated (closed-form) major principal strain for the silica cubes.

Global uniaxial Load: N or stress: MPa	Global uniaxial Displacement: mm or strain: $10^{-3}\ mm/mm$	Major principal strain – compression: $10^{-3}mm/mm$		
		Experimental (3DXRD)	Simulated (3D FE)	Calculated (closed-form)
Strong cube				
300	2.79	2.66	2.91	2.92
600	5.59	5.30	5.82	5.84
900	8.38	7.96	8.73	8.76
1200	11.17	10.86	11.64	11.68
Slope: GPa	107.4 (fitted)	110.9 (fitted)	103.1	102.7
Weak cube				
300	3.92	3.70	3.76	3.78
600	7.84	7.65	7.51	7.56
900	11.76	11.88	11.26	11.33
1200	15.68	15.82	15.02	15.11
Slope: GPa	76.5 (fitted)	76.3 (fitted)	79.9	79.4
Isotropic cube				
300	-	-	3.01	3.02
600	-	-	6.02	6.03
900	-	-	9.04	9.05
1200	-	-	12.05	12.07
Slope: GPa	-	-	99.6	99.4

Appendix D: Figures

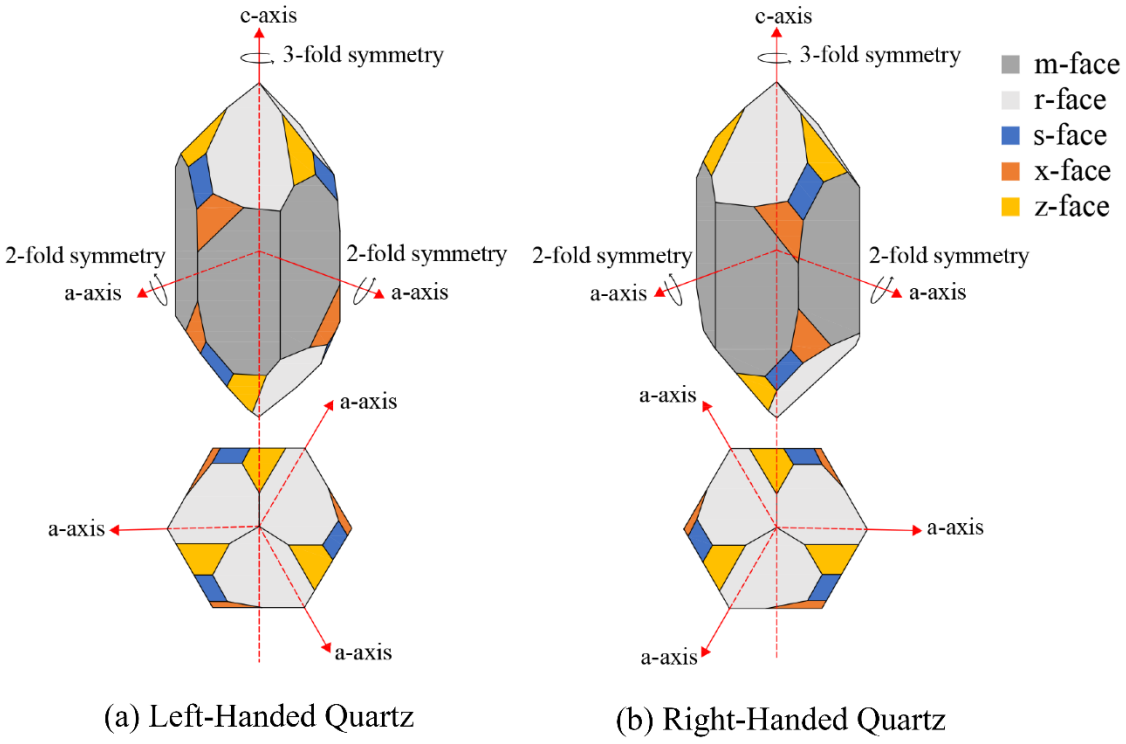


Figure 5-1. Illustrative diagrams of (a) left- and (b) right-handed crystal quartz. The crystal diagrams are a modified version of Figure 6 in Akhavan (2013).

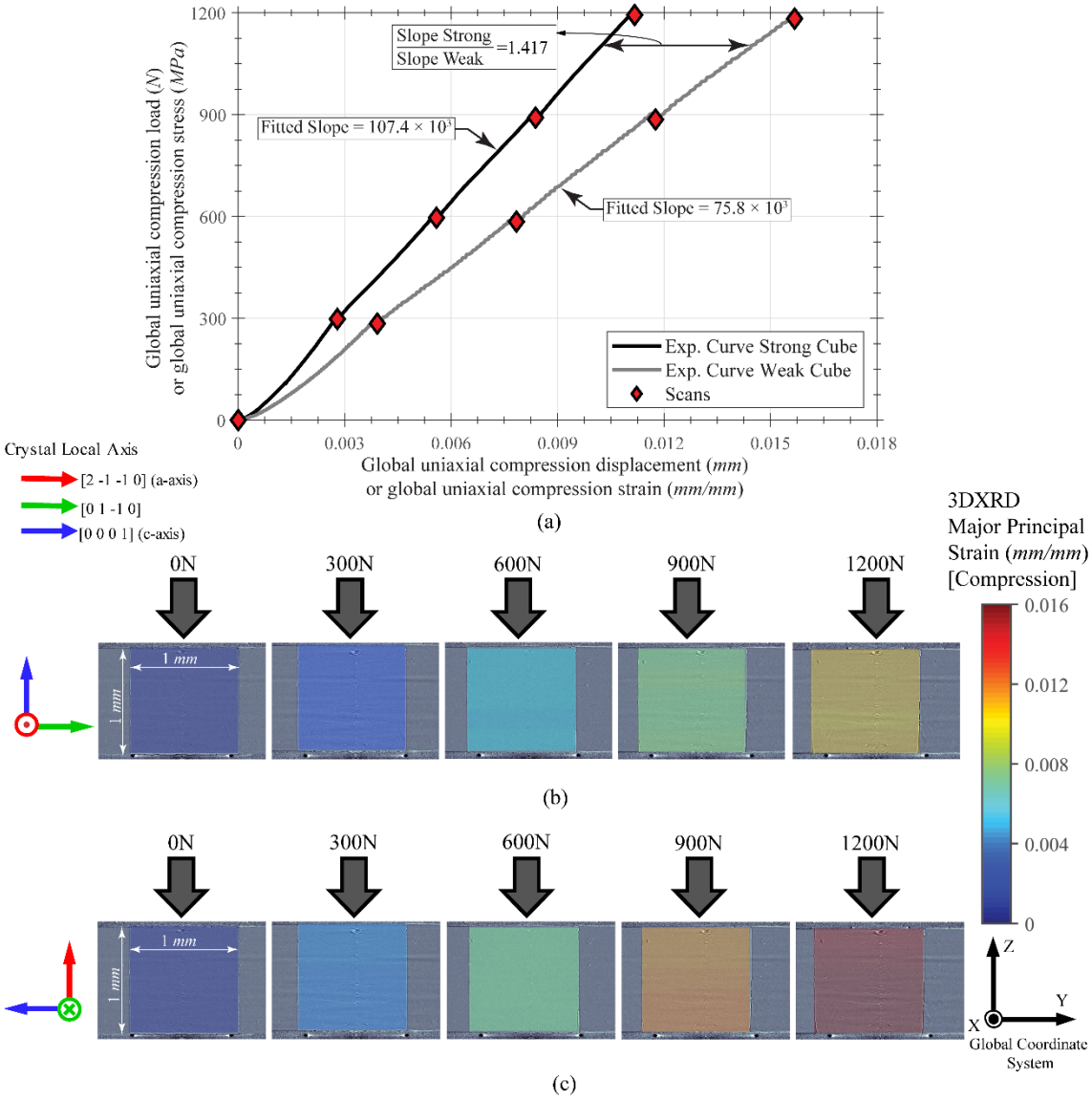


Figure 5-2. (a) Uniaxial global load versus displacement relationships for the weak and strong cube experiments as recorded by the testing sensors. Central vertical Y-Z slice in SMT scans visualizing the evolution of lattice strains versus compression as quantified from 3DXRD measurements for the (b) strong and (c) weak cube experiments.

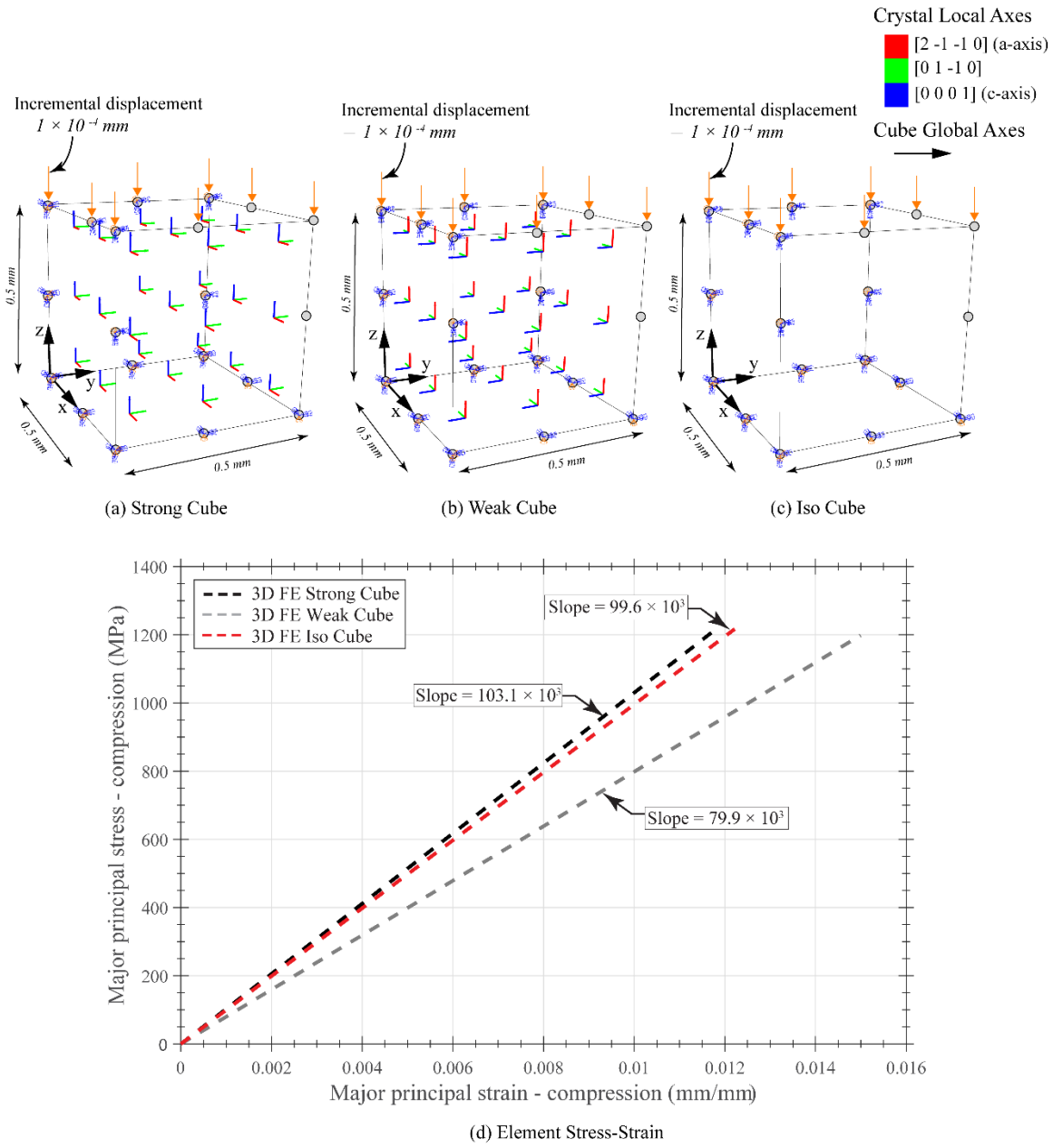


Figure 5-3. 3D FE modeling of the (a) strong; (b) weak; and (c) isotropic cubes using a single 20-noded hexahedral element. (d) Relationships between the major principal strains and the major principal stresses for the hexahedral element.

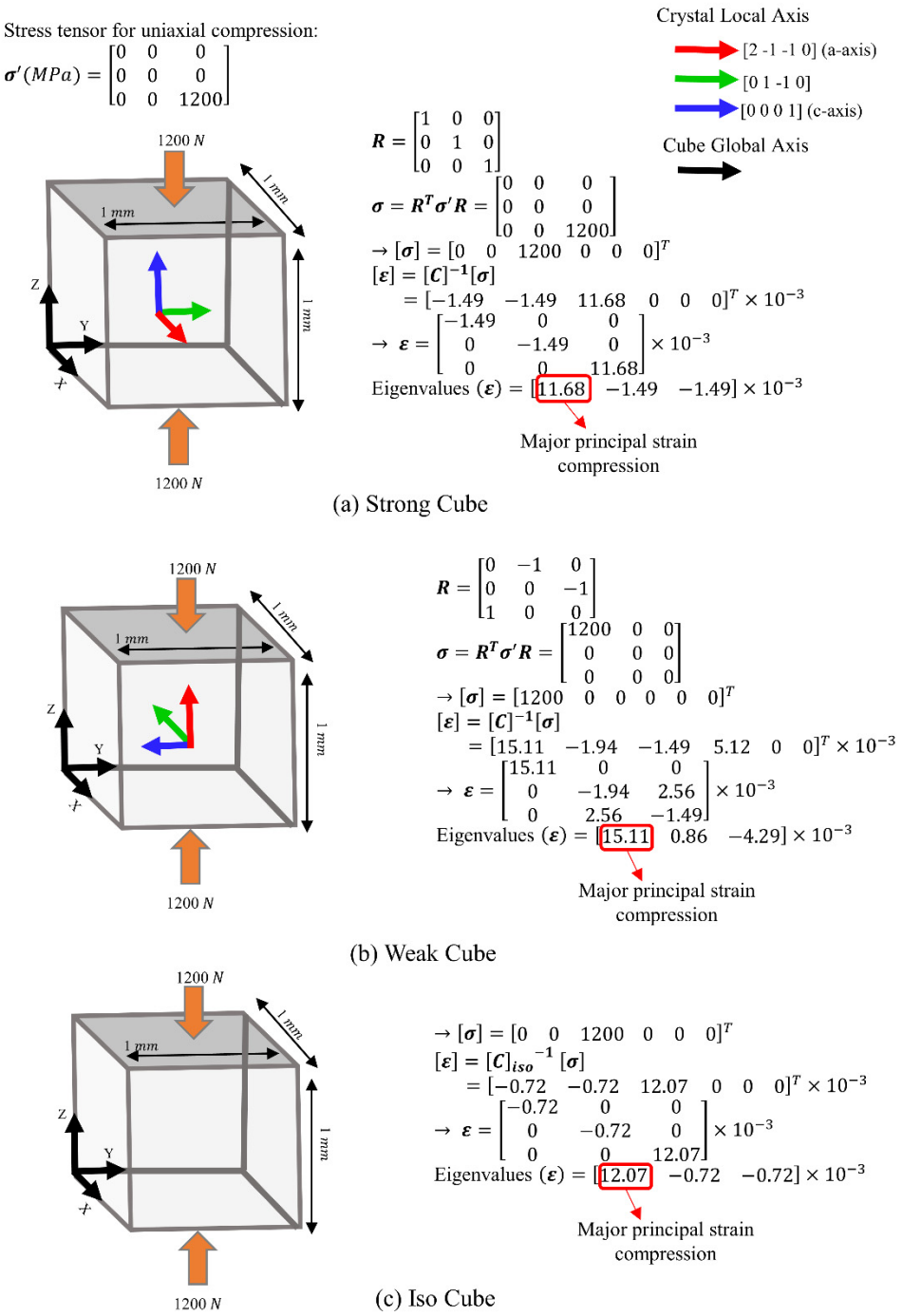


Figure 5-4. Demonstration of the closed-form solution for the (a) strong; (b) weak; and (c) isotropic cubes under uniaxial compression loading conditions.

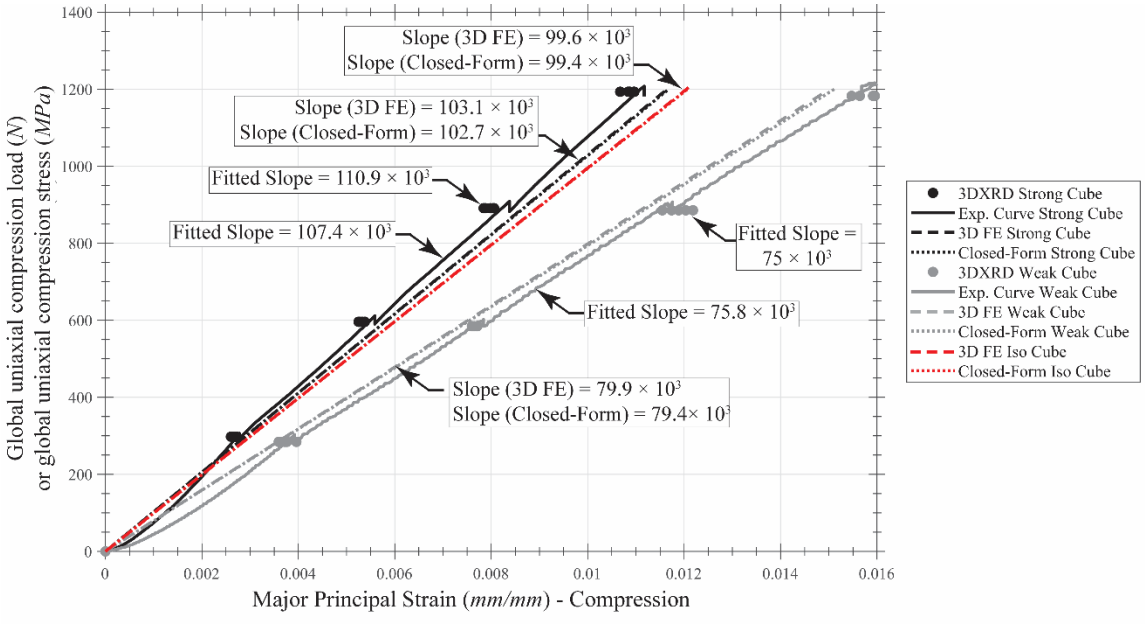


Figure 5-5. Synthesis of the experimental (3DXRD), simulated (3D FE), and calculated (closed-form) major principal strain for the cube under uniaxial compression conditions.

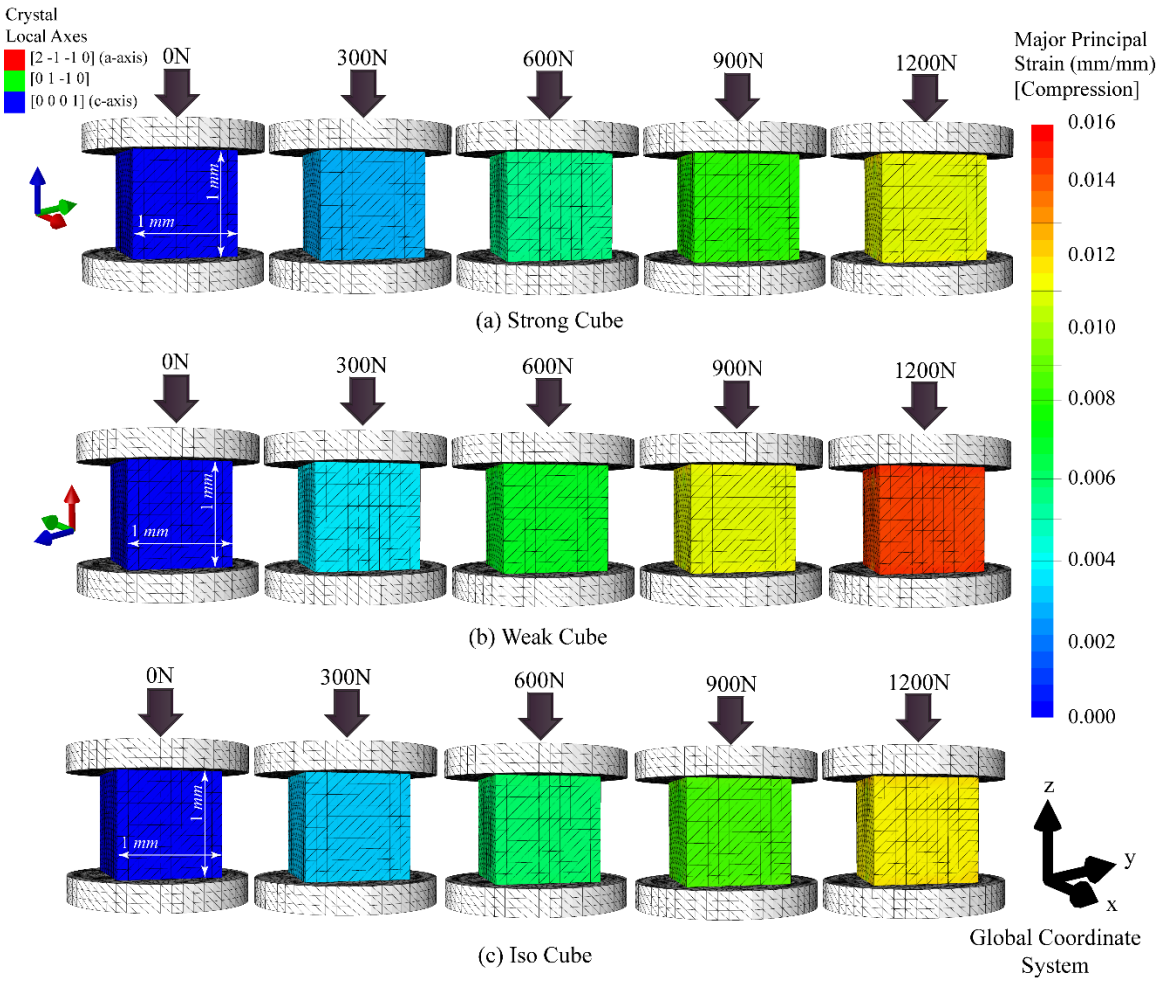


Figure 5-6. Evolution of the major principal strain versus compression in the 3D FE simulations of (a) strong; (b) weak; and (c) isotropic cube at load steps similar to the experiments.

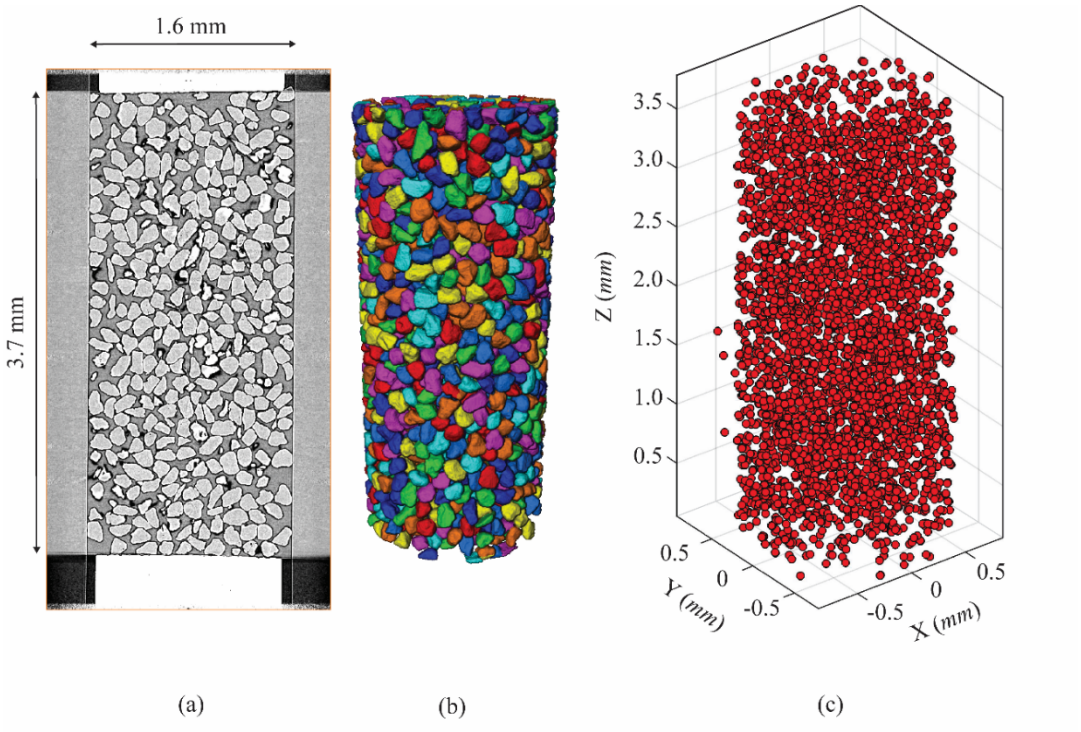


Figure 5-7. (a) Central vertical Y-Z slice in the SMT greyscale image; (b) 3D volume rendering of AVIZO processed image; and (c) centroids of crystal lattices from 3DXRD measurements for the natural sand specimen composed of 2705 silica particles.

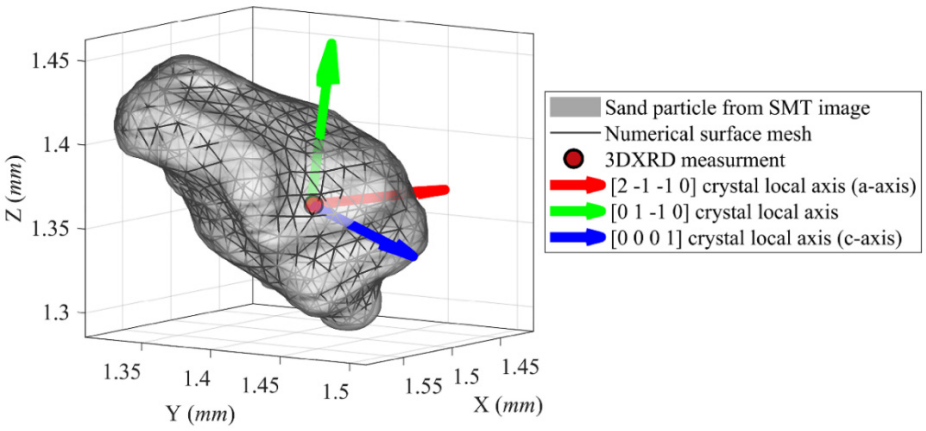


Figure 5-8. 3D volume rendering in greyscale SMT image for particle 111 showing the wire-frame mesh used in 3D FE analysis and the crystal local orientation as quantified from 3DXRD measurements.

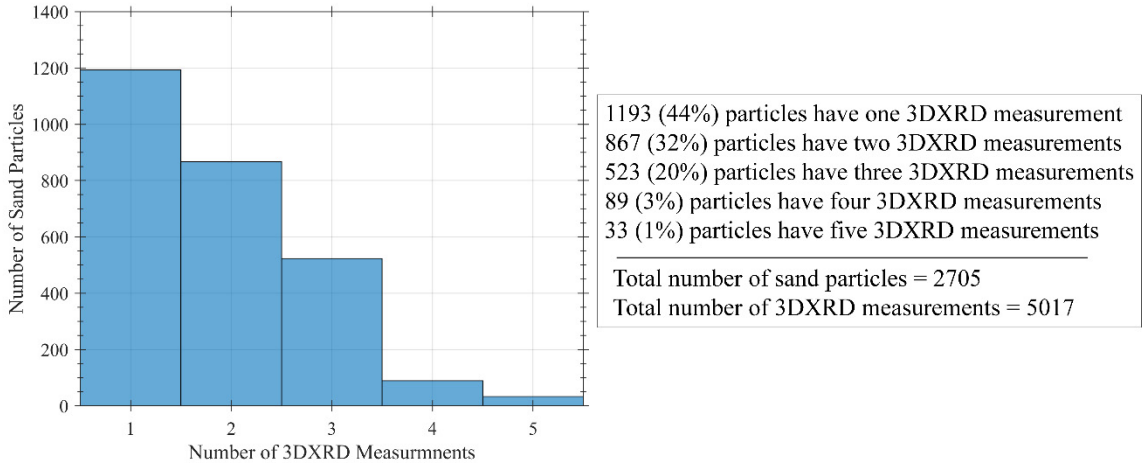


Figure 5-9. Histogram of the number of 3DXRD measurements matched to the SMT particles.

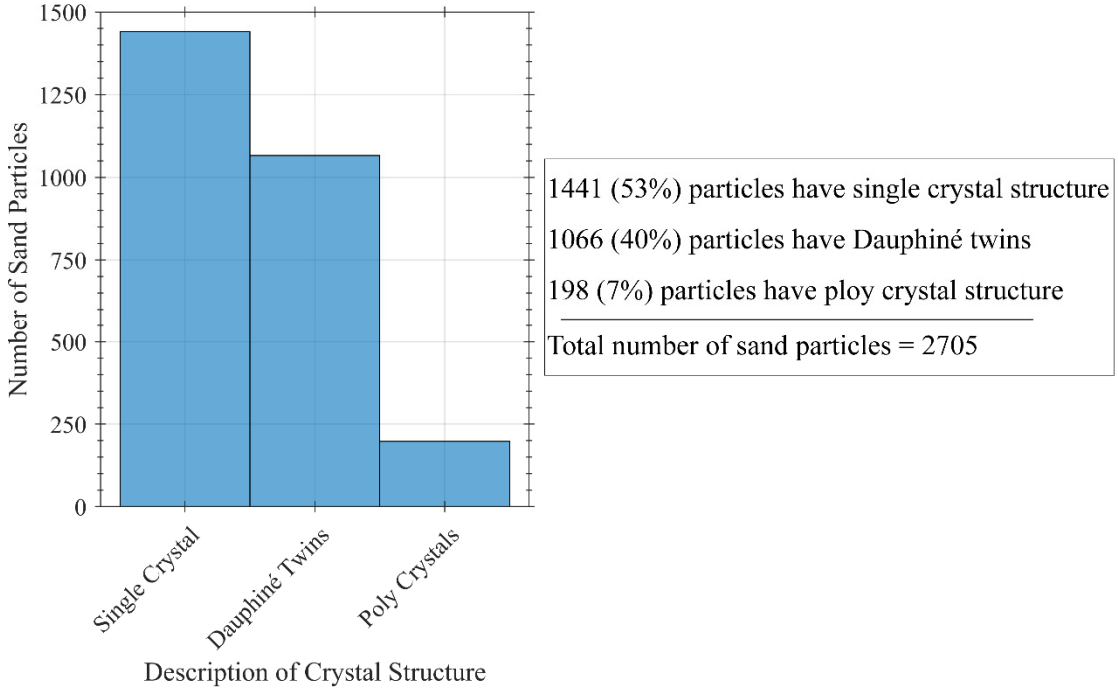


Figure 5-10. Histogram of the crystal structure of sand particles.

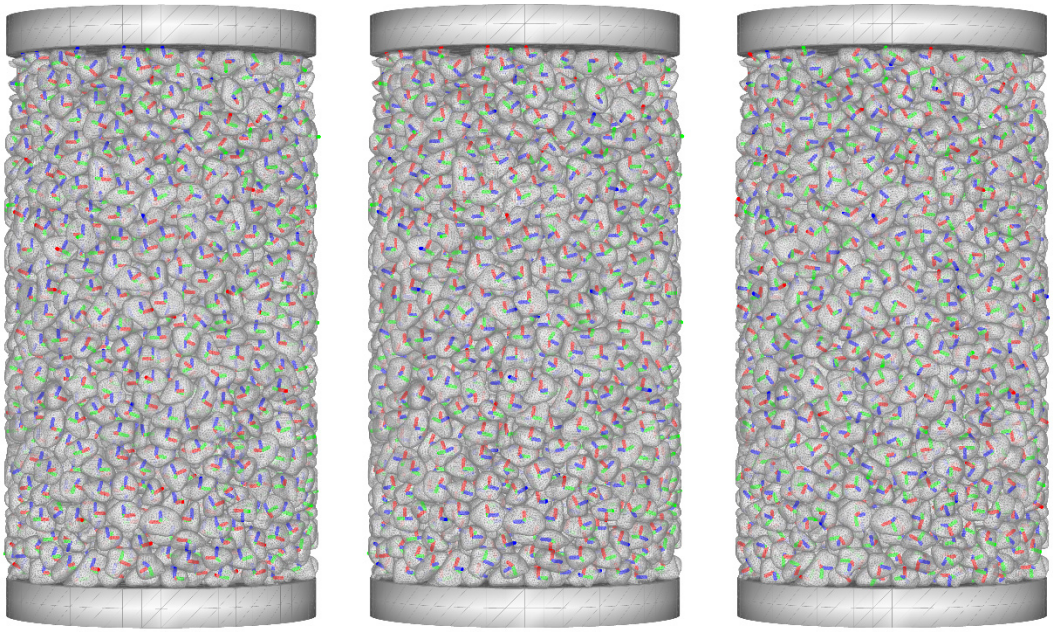


Figure 5-11. Configurations of crystal local orientations pre-assigned to individual particle meshes in (a) strong; (b) weak; and (c) experimental simulations. The blue, green, and red vectors, respectively, denote the [0 0 0 1] (c-axis), [0 1 -1 0], and [2 -1 -1 0] (a-axis) crystal local axes. Confining tube surrounding the specimen is hidden for better visualization of the specimen internal fabric.

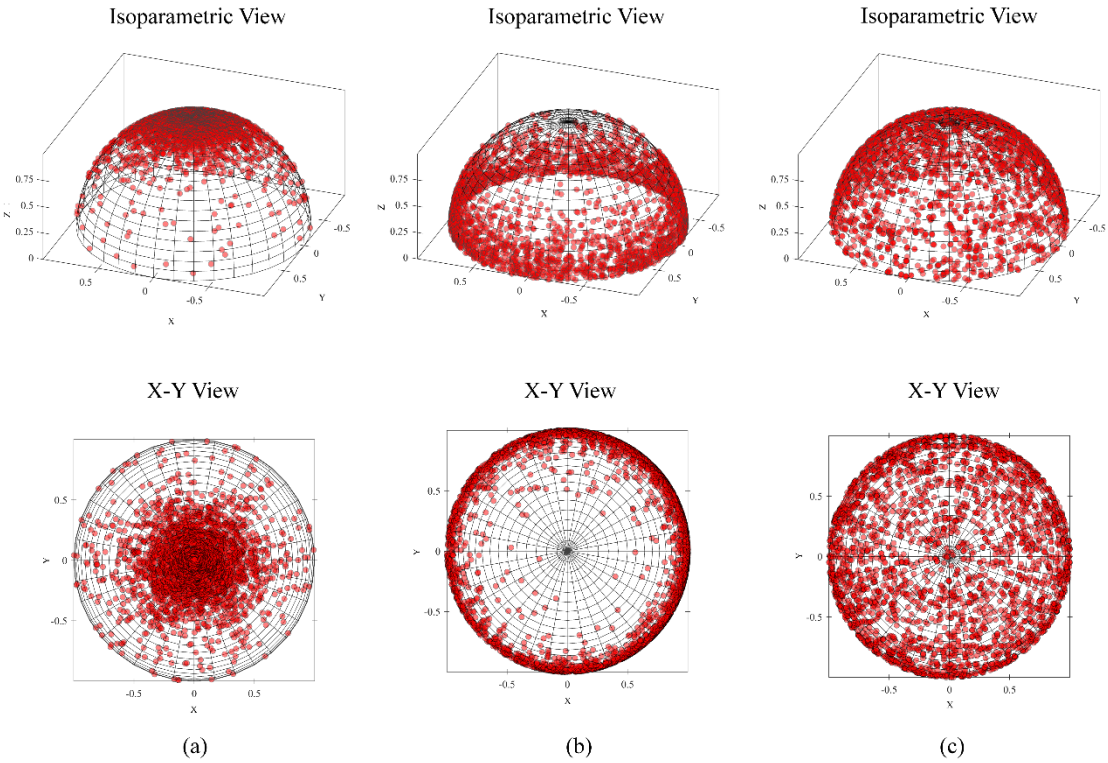


Figure 5-12. 3D spherical distribution on a unit radius semi-sphere of the pre-assigned [0 0 0 1] crystal local axis (c-axis) for the 2705 sand particles in the (a) strong; (b) weak; and (c) experimental simulations.

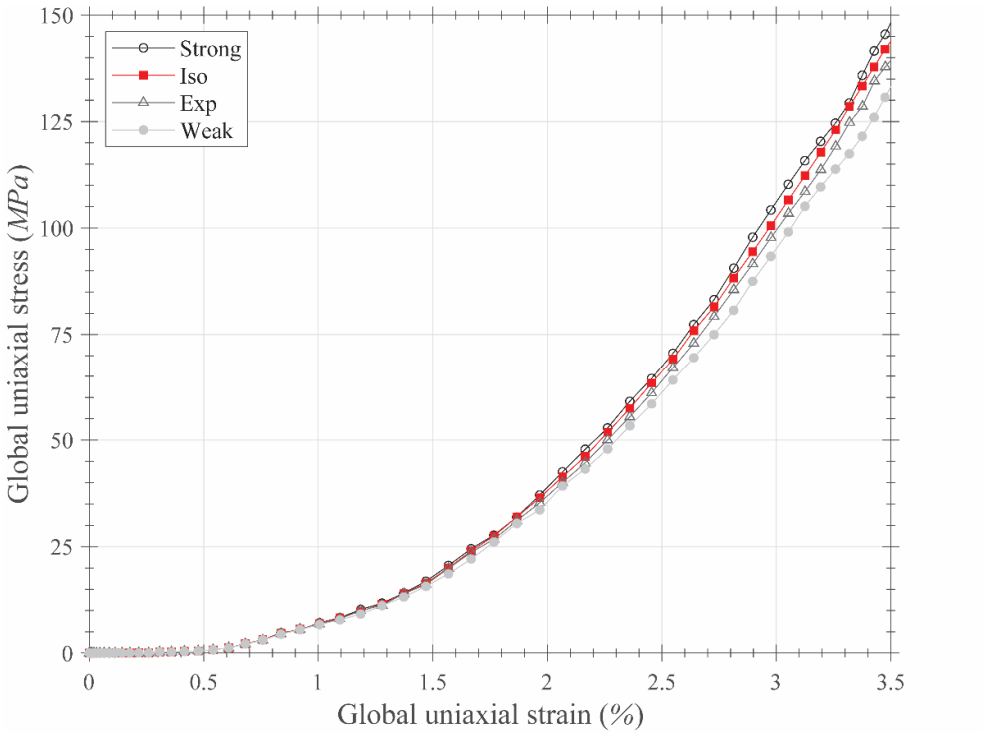


Figure 5-13. Evolution of global uniaxial strain versus global uniaxial stress for 3D FE simulations.

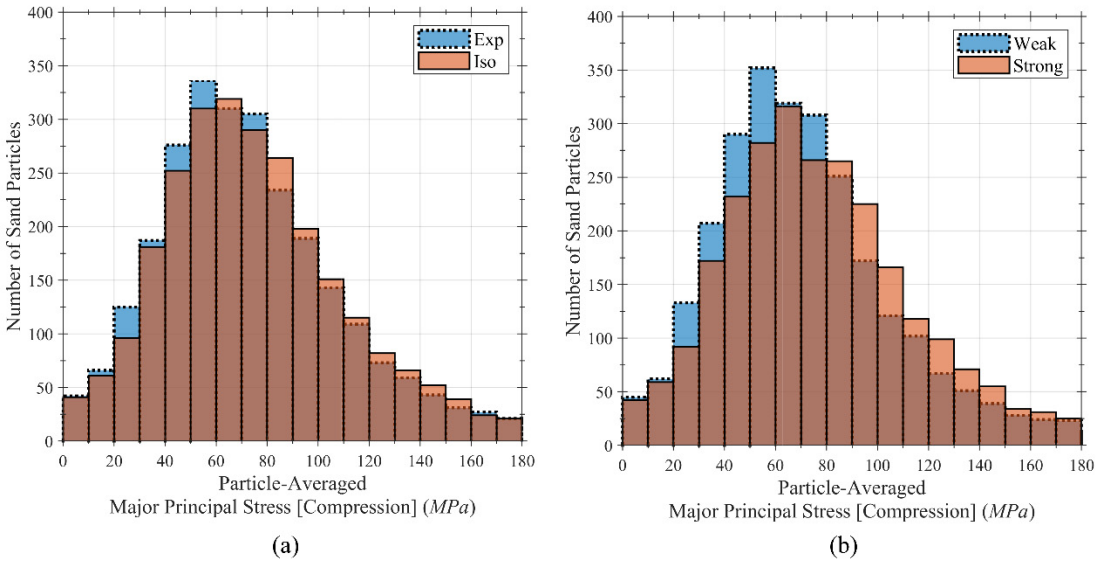


Figure 5-14. Histograms of major principal stress of sand particles in (a) experimental versus isotropic and (b) strong versus weak simulations at 3% global uniaxial strain.

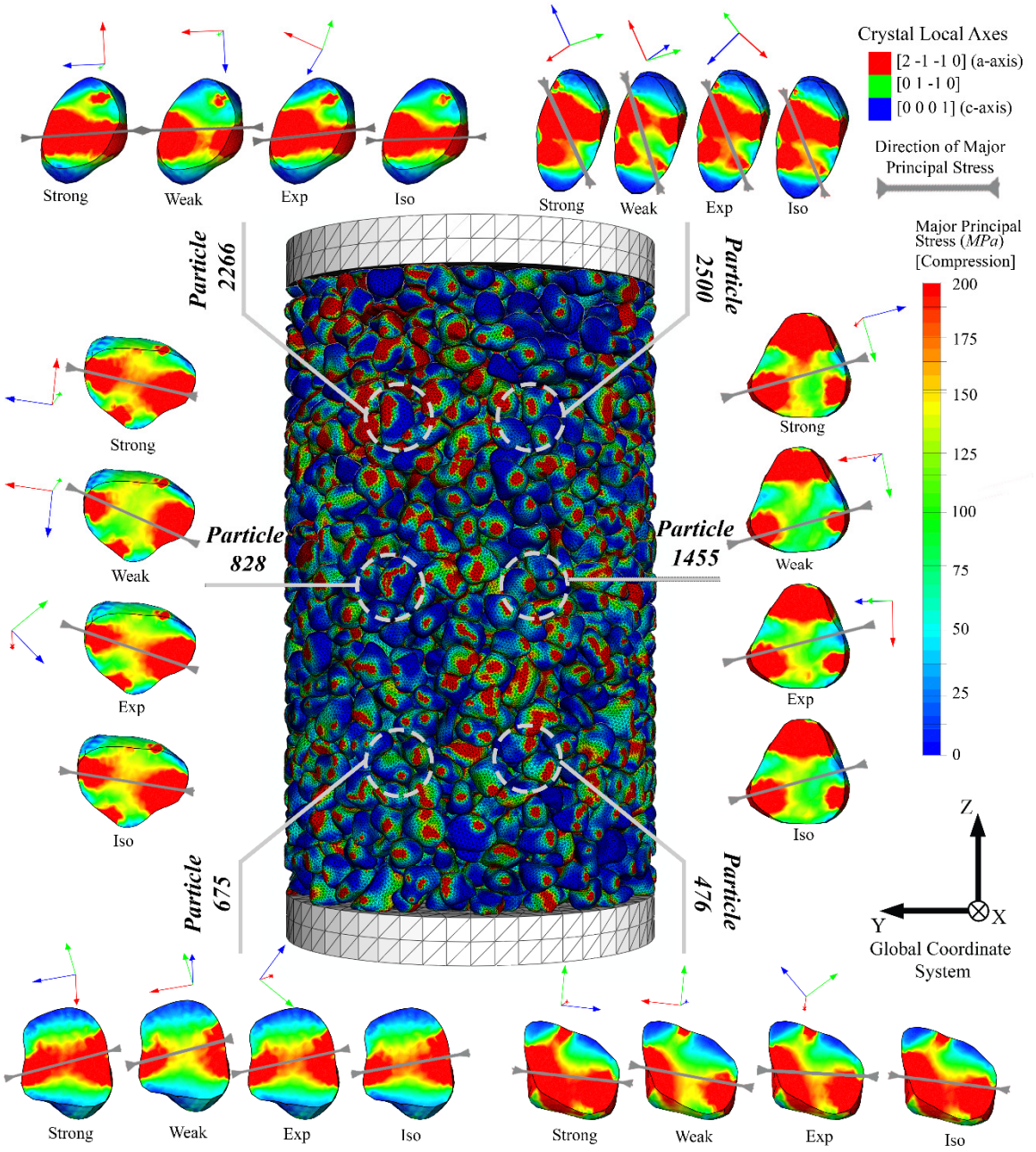


Figure 5-15. FE fringe plot for the major principal stress in the isotropic simulations at 3% global uniaxial strain. Side particles compare major principal stress and crystal local orientations among the four conducted 3D FE simulations (strong, weak, experimental, and isotropic).

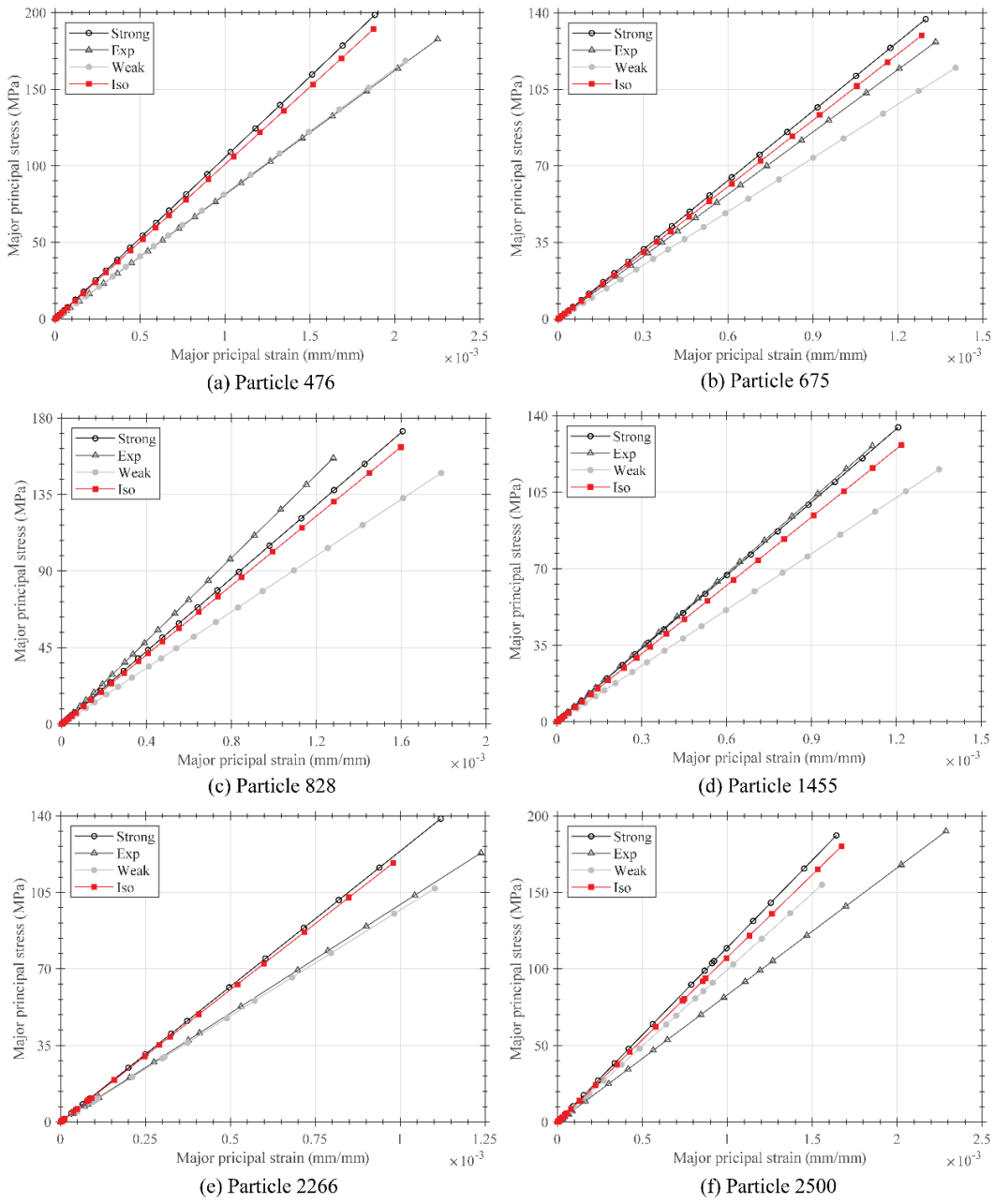


Figure 5-16. Evolution of major principal strain versus stress in the 3D FE simulations (strong, weak, experimental, and isotropic) for particles (a) 476; (b) 675; (c) 828; (d) 1445; (e) 2266, and (f) 2500.

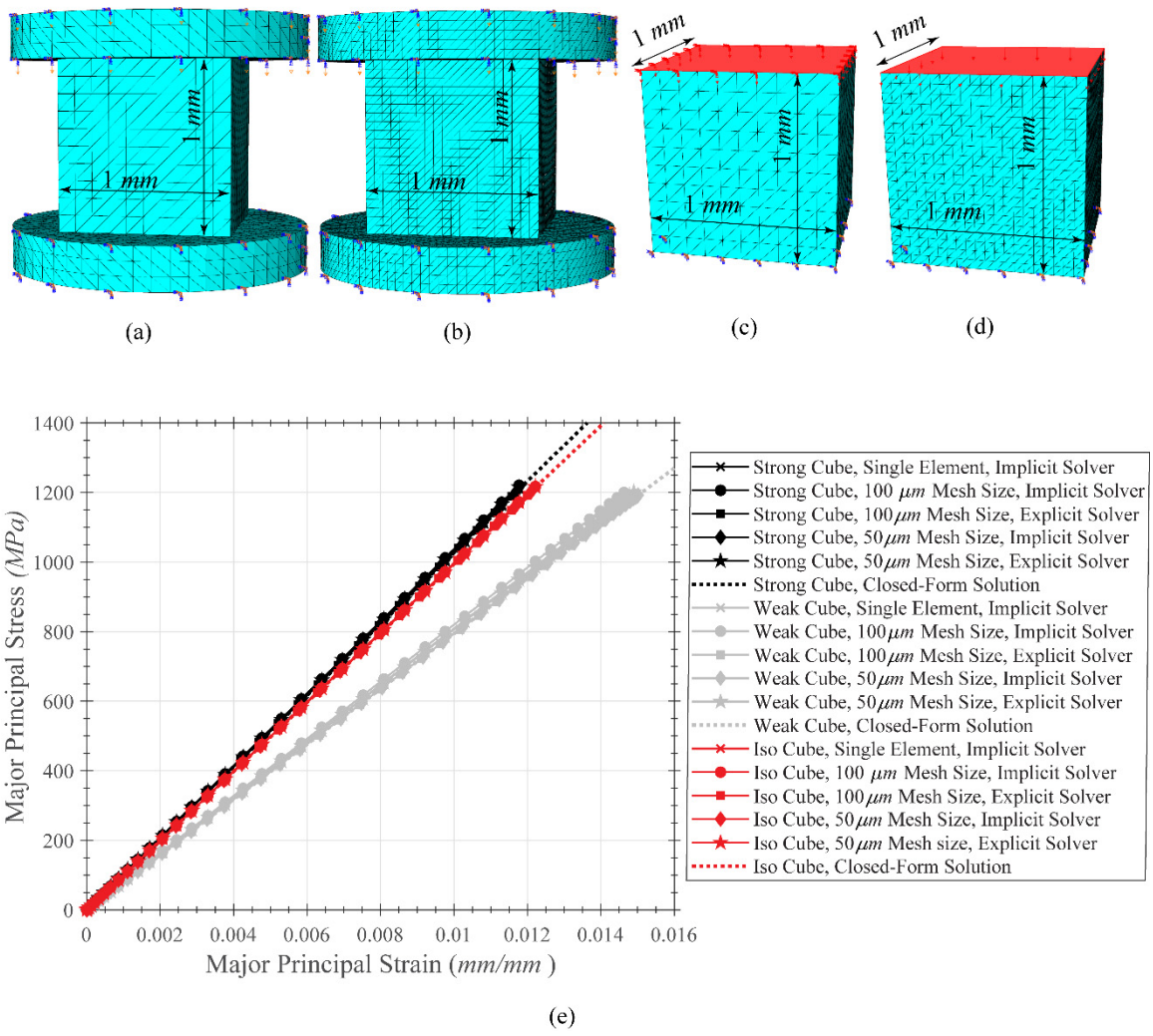


Figure 5-17. Dynamic explicit model of the cube experiments using (a) 100 μm, and (b) 50 μm mesh size. Static implicit model of the cube experiments using (c) 100 μm, and (d) 50 μm mesh size. (e) Assessment of mesh sensitivity and quasi-static response for (a)–(d) models.

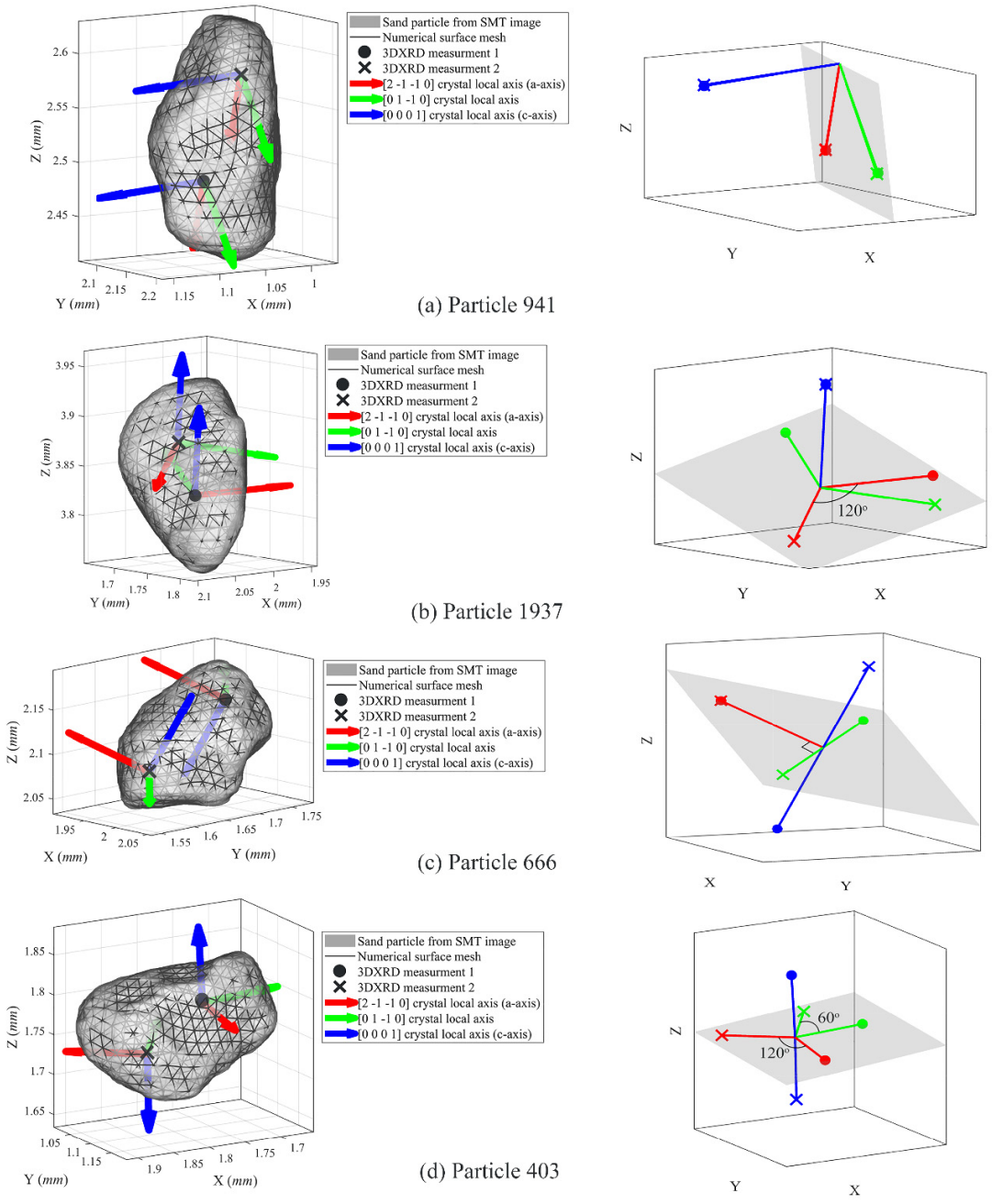


Figure 5-18. Illustrative examples of sand particles matched with multiple 3DXRD measurements but possessed a single crystal structure.

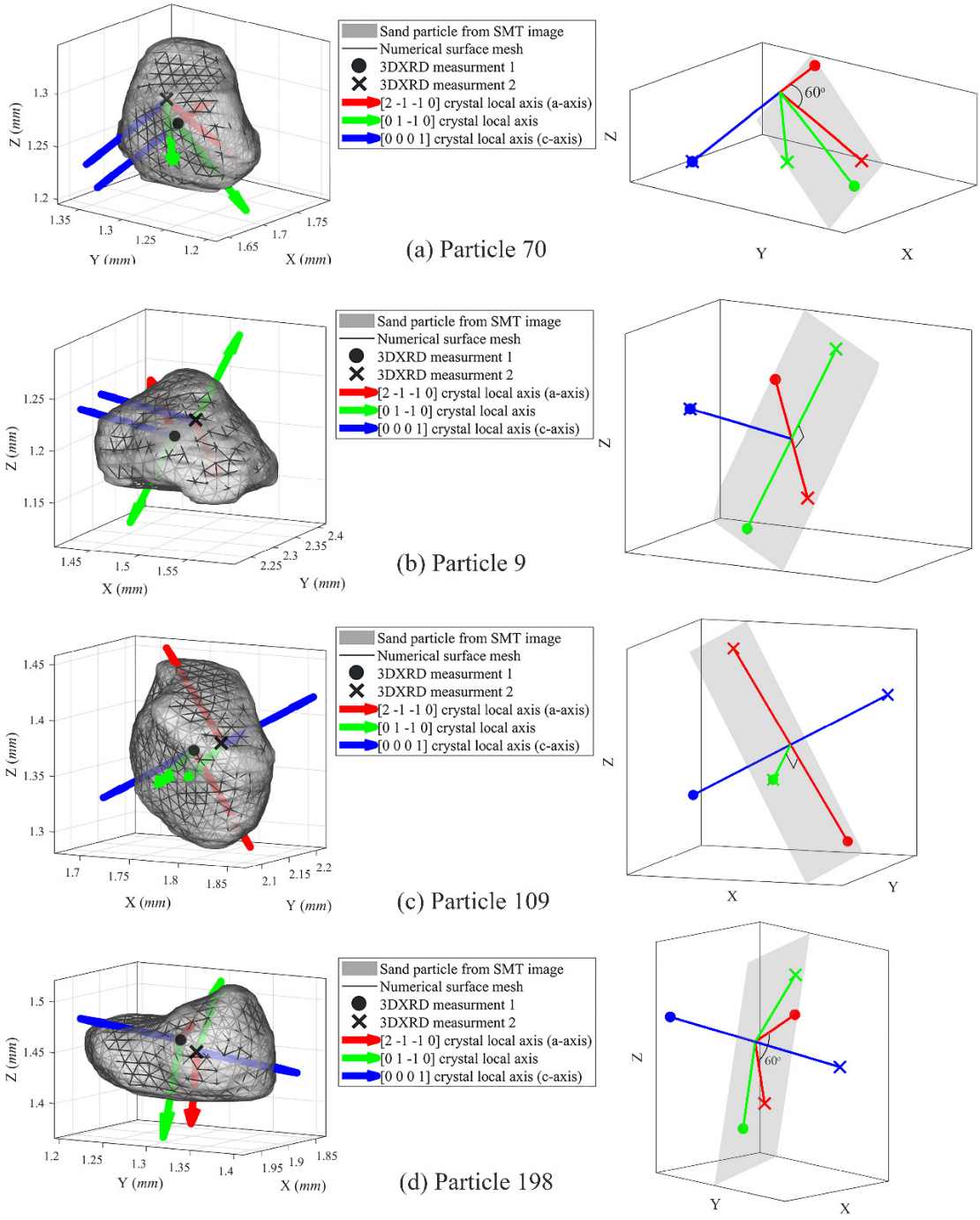


Figure 5-19. Illustrative examples of sand particles matched with multiple 3DXRD measurements and possessed Dauphiné twins.

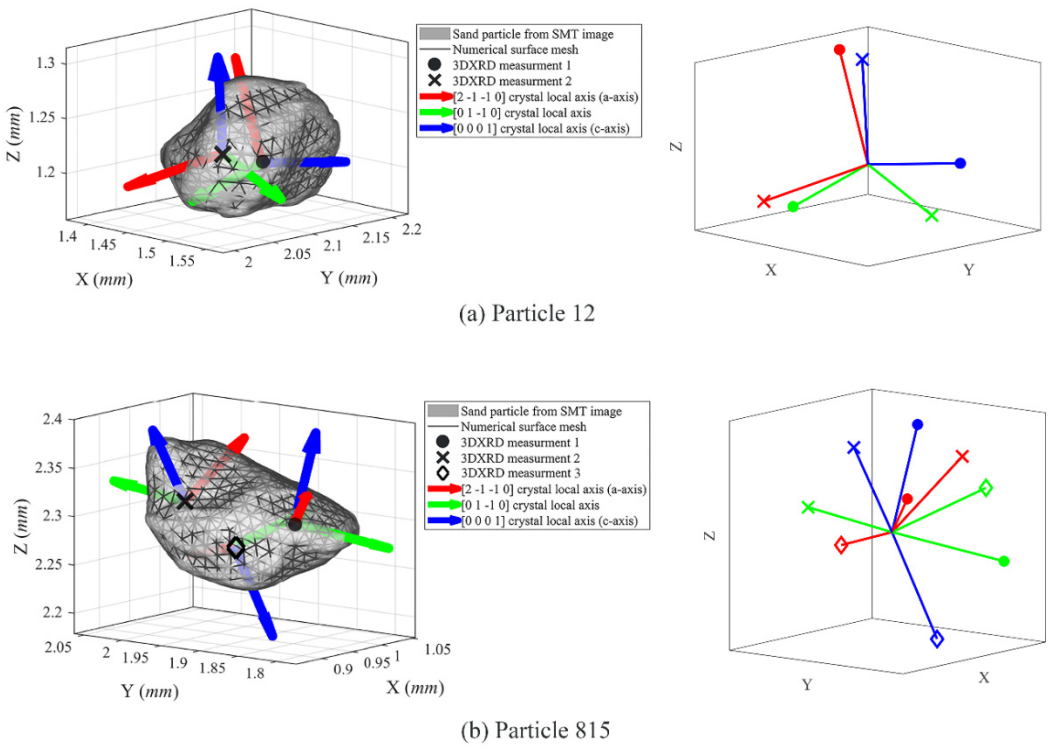


Figure 5-20. Illustrative example of particle 272 matched with four 3DXRD measurements and possessed Dauphiné twins.

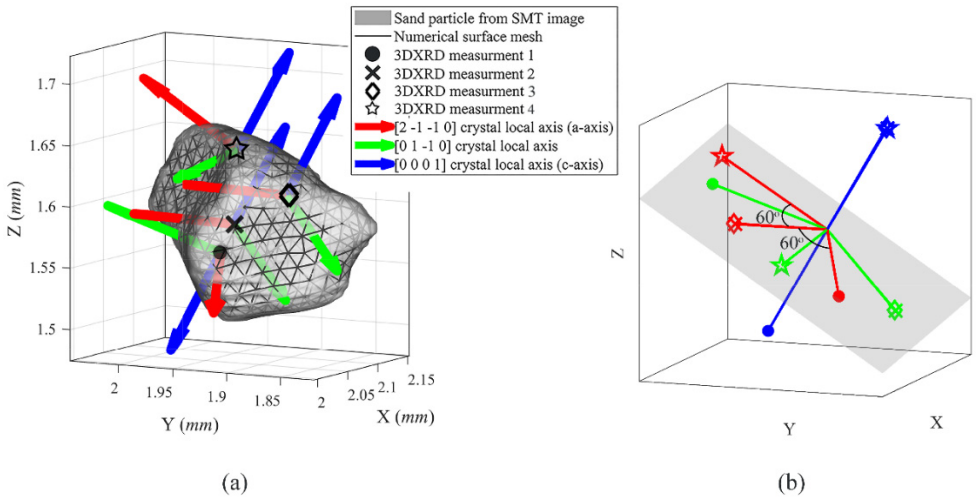


Figure 5-21. Illustrative examples of sand particles with poly crystal structures.

CHAPTER SIX

INFLUENCE OF MICRO- AND CRYSTALLINE- SCALE PROPERTIES ON THE FRACTURE OF SILICA SAND PARTICLES USING 3D FINITE ELEMENT ANALYSIS

A version of this chapter is currently under review as Imseeh, W. H. & Alshibli, K. A. “Influence of Micro- and Crystalline- Scale Properties on the Fracture of Silica Sand Particles Using 3D Finite Element Analysis”. *ASCE International Journal of Geomechanics*

Abstract: Particle fracture significantly influences the constitutive behavior of sands and impacts many geotechnical engineering applications such as hydraulic fracturing, pile driving, blast loading, and stability of dams. When a confined specimen of sand is loaded in 1D compression, particles ultimately fracture, causing permanent micro-scale deformations that contribute to the yielding behavior of the sand. The most common constituent of sand particles is silica mineral (quartz), which is well-known for its natural abundance and high compressive strength. Such excellent properties make silica sand particles an excellent proppant for high-pressure hydraulic fracturing in the oil and gas industry and many other applications. This chapter investigates the fracture characteristics of silica sand particles using 3D finite element (FE) simulations of single particle crushing and confined 1D compression experiments. The 3D FE simulations were generated using digital image processing of in-situ synchrotron micro-computed tomography (SMT) scans, unique 3D meshing algorithms, and coding development in ABAQUS FE software. In-situ SMT images were processed to produce 3D meshes that accurately resemble the complex morphology of the natural sand particles. A material point user-subroutine was developed and implemented in ABAQUS to simulate the constitutive and fracture behaviors of the 3D meshed particles. The user-subroutine incorporates the anisotropic linear elastic behavior of silica mineral and models particle fracture using the principles of continuum damage mechanics. In single particle crushing, the fracture stress of the sand particle was mostly dependent on the nature of contact between the particle and loading platens. The fracture pattern of the sand particle was mainly influenced by micro-structural imperfections and the direction of loading relative to the crystal lattice orientation of the sand particle. In confined 1D compression, the fracture stress of the sand particles correlated well with the particle coordination number and the aspect ratio. Sand particles within the specimen were found to fracture at higher stress-levels when they established more contacts with their neighboring particles and exhibit mostly spherical shapes rather than elongated. The chapter demonstrates the fundamental contribution of micro- and crystalline-scale properties to determine the constitutive and fracture behaviors of silica sand particles.

Keywords: **Brittle fracture, silica sand, finite element, particle morphology, quartz crystal.**

Introduction

Unlike the consolidation behavior of clay, the compressibility of sand is highly influenced by the fracture of particles under high effective stresses (Lee and Farhoomand, 1967). In the literature, many experimental studies have demonstrated that particle fracture in sand contributes to the stress-dilatancy relationship (Bolton, 1986), as well as the development of the critical state and normal compression lines (Coop and Lee, 1993, McDowell and Bolton, 1998a). Nakata et al. (1999) conducted single particle crushing experiments of sand and statistically compared the results with those obtained for individually marked particles placed within sand specimens that were tested in conventional triaxial compression (CTC). They found the size of the yield surface to be related to the amount of particle crushing within the sand specimen. Chuhan et al. (2002) used the oedometer experiment to test loose sand specimens composed of particles with fine- and coarse-grained sizes, as well as lithic and mono-crystalline silica composition. They reported a more significant reduction in particle sizes and specimen porosity for coarse-grained and lithic sands in comparison with the fine-grained and mono-crystalline sands. Russell and Khalili (2004) introduced a bounding surface constitutive model that was able to produce a uniquely-shaped critical state line when considering the permanent micro-scale deformations of sand specimens, such as particle fracture and rearrangements. Karimpour and Lade (2010) observed a unique pattern of response in CTC experiments on sand specimens that indicated the importance of particle fracture for axial and volumetric strains. In contrast, particle rearrangement and frictional sliding had less effect on the specimen's stress-strain behavior and volume change. Reduction in hydraulic conductivity of sand specimens was also attributed to the fracture of particles and the associated decrease in porosity of compressed specimens (Zheng and Tannant, 2016).

Relating the fracture of sand particles to conventional soil measurements such as effective mean stress and void ratio failed to provide unified correlations for different types of soil testing procedures (Lade et al., 1996). From a micro-scale point of view, sand specimens consist of crushable particles that exhibit complex interaction, morphology, and mineralogy. The complexity in the micro-scale characterization of sands has motivated many innovative testing techniques and procedures in a quest for a comprehensive understanding of particle fracture. Guimaraes et al. (2007) conducted extensive literature research and laboratory experiments to assess the role of particle mineralogy and fracture patterns in fines production during single particle crushing of aggregates, as well as the fracture of aggregates within granular specimens loaded in confined 1D compression. In both single particle crushing and confined 1D compression experiments, point loading generated "clean-fractures" in the particles and produced a small percentage of

fines. On the contrary, high inter-particle load contacts resulted in “micro-fractures” and a large production of fines. Todisco et al. (2017) utilized a high-speed magnifying camera to investigate the effect of multiple contacts on the fracture strength of single sand particles that were crushed between multiple support particles. They found the fracture strength of particles significantly influenced by the coordination number and the nature of contacts, which are fundamentally controlled by particles’ morphology. In the context of sand, the coordination number represents the number of contacts per particle. Xiao et al. (2020) conducted single particle crushing experiments on rockfill granular materials to investigate the effect of particle size on the fracture strength, as well as the relationship between the characteristic stress and probability of non-failure. They also used the results to predict the yield stress of granular specimens that were tested in confined 1D compression.

X-ray computed tomography (CT) has recently provided an accurate 3D characterization of the microstructure of sand specimens and state-of-the-art insights into the mechanisms of particle fracture. Parab et al. (2014) investigated the fracture of single wet and dry sand particles loaded at different strain-rates using x-ray CT and high-speed x-ray phase-contrast imaging. Under dynamic loading conditions, pulverization was observed as the sole mode of failure for dry sand particles, while wet particles fractured into relatively large sub-particles and then pulverized, similar to what occurred under quasi-static loading conditions. Zhao et al. (2015) collected in-situ x-ray CT images for single particle crushing experiments of sand and found the morphology of particles as well as their initial microstructure to be essential factors affecting the fracture patterns of sand particles. Afshar et al. (2017) examined the effects of sand particle shapes on their fracture mechanisms in single particle crushing and 1D compression of confined specimens using scanning electron microscopy, energy-dispersive x-ray spectroscopy, and the discrete element method (DEM). They reported that spherical particles exhibit higher resistance to particle fracture. Karatza et al. (2018) acquired in-situ x-ray CT images for specimens of sand loaded in high-confinement CTC to explore the effects of particle fracture on localized shear and volumetric strains. Opposed to the overall compaction behavior of the specimen, they observed dilative volumetric strains associated with localized regions of intensive shear where a high amount of particle fracture also occurred. Wu and Wang (2019) developed a tracking procedure that identified fragments from the crushing of a single sand particle through the application of the point cloud registration technique and the help of in-situ x-ray CT.

In recent years, 3D x-ray diffraction (3DXRD) has enabled the measurement of lattice strains within individual sand particles to expose their fracture strength (Alshibli et al., 2013). Cil et al. (2014) utilized 3DXRD and synchrotron micro-computed tomography (SMT) to examine the propagation of fracture in a column specimen composed of three silica sand particles loaded in confined 1D compression. As loading progressed, they found the lattice stress of the particles to exhibit a nearly linear increase in the normal component that was aligned with

the direction of loading, whereas shear stress components were relatively small with no clear systematic trend. A dual in-situ scanning technique that combines SMT and 3DXRD was also employed to investigate particle fracture in sand specimens loaded under confined 1D compression and composed of natural silica sand (Cil et al., 2017), as well as synthetic silica particle with spherical shapes (Hurley et al., 2018a). However, the results of this dual scanning technique are broadly challenged by the difficulty in identifying and tracking the many fragments from individual particles that fractured within the granular assembly.

In addition to the experimental characterization of particle fracture in sands, many DEM models were developed to evaluate the effect of particle morphology and fracture on the mechanical behavior of sand specimens. The particle fracture in DEM was introduced by modeling sand particles as agglomerates of small spheres (Potyondy and Cundall, 2004, Hanley et al., 2011) or rigid blocks (Nicksiar and Martin, 2014, Jarrar et al., 2020) that were bonded together using appropriate contact models. The rigid blocks in DEM offered the advantage of improving the numerical resemblance of the complex morphology of natural sand particles. The morphology of sand was also modeled in DEM using rigid clumps that were composed of small pebbles joined together (Gao et al., 2012, Li and McDowell, 2018). Accordingly, particle fracture was introduced by substituting the clumps that reached a pre-defined failure criterion with a group of smaller clumps (Lobo-Guerrero and Vallejo, 2005a, Zhou et al., 2016). The implementation of level-set functions in DEM was also powerful in modeling the complex morphology of sand particles (Kawamoto et al., 2018), and particles that fulfilled a failure criterion were split along fractured surfaces defined by the level set functions (Harmon et al., 2020). Nonetheless, the rigid particle assumption in DEM failed to quantify stress concentrations and fracture onset within individual sand particles, and the fracture criteria were instead established using the average stress of the particle calculated from its boundary contact forces. This DEM limitation has motivated recent efforts to mesh individual sand particles based on their actual 3D shape into solid finite elements (Druckrey and Alshibli, 2015). Consequently, the finite elements within an individual particle can deform according to an appropriate constitutive material model, as well as fracture based on continuum damage mechanics (Imseeh and Alshibli, 2018, Turner et al., 2019, Wei et al., 2019, Thakur and Penumadu, 2020). Yet, this finite element (FE) method has only considered the isotropic linear elastic behavior of silica mineral to model single particle crushing experiments or confined 1D compression tests with very a limited number of sand particles (less than 50 particles).

This chapter investigates the fracture characteristics of silica sand particles using 3D FE simulations with the help of rich experimental data from in-situ SMT and 3DXRD. The chapter adopts a new material user-subroutine that can numerically predict the fracture of sand particles assuming anisotropic linear elastic behavior of silica mineral. To the best knowledge of the authors, the user-subroutine reported in this chapter is the first attempt in the geotechnical research community

to model particle fracture in silica sands using properties that exist at the crystal scale-level of the constituent mineral.

Formulation of the Material User-Subroutines for Silica Mineral

Sand is a granular material composed of finely weathered rock and mineral particles. The most common constituent of sand particles is silica mineral which is composed of α –quartz crystal. The building block (unit cell) of the quartz crystal is silicon oxide tetrahedra (SiO_4) where each oxygen atom is shared between two tetrahedra. This composition gives quartz an overall chemical formula of silicon dioxide (SiO_2), which is commonly known as silica. In crystallography and material science, quartz crystal is known to possess a hexagonal lattice system, trigonal crystal system, and rhombohedral unit cell. The trigonal crystal system of quartz is spanned by a local coordinate system of four axes: a_1,a_2, a_3, and c. The three a axes correspond to a and b lattice parameters that have equal lengths, span the hexagonal lattice plane, intersect at 60^o angles, and are commonly referred to as the a-axis for simplification. The c-axis runs perpendicular to the hexagonal lattice plane and corresponds to the c lattice parameter, which is 1.1 times the length of a or b. This non-trivial crystal structure of quartz produces anisotropy in the constitutive behavior of silica particles. Namely, the stress-strain response of silica particles is altered by the direction of external loads relative to the crystal orientation of the particle. This section presents the formulation of a material user-subroutine that can numerically model the crystalline-scale anisotropy in the constitutive behavior of silica sand particles. The user-subroutine also incorporates a material point damage model to simulate the brittle fracture in silica sand particles.

The local crystal orientations are defined using the Miller-Bravais four-index system $(a_1\ a_2\ a_3\ c)$, in which parentheses and brackets describe the local crystal planes and axes, respectively. For example, $[0\ 0\ 0\ 1]$ represents the c-axis of the quartz crystal and $(0\ 0\ 0\ 1)$ refers to the crystal plane perpendicular to the c-axis. Bold symbols in the equations represent tensors/vectors whereas regular text symbols denote scaler quantities. The sign convention of stress and strain is positive for compression and negative for tension.

Constitutive Relationship

In single particle crushing experiments, the uniaxial load-displacement curves prior to fracture exhibit a linear relationship for silica sand particles. Therefore, the appropriate constitutive model for the behavior of intact silica sand particles is governed by the framework of anisotropic linear elasticity theory. In crystallography, α –quartz is known to possess trigonal symmetry (point group 32) and six independent elastic constants $(C_{1111}, C_{1122}, C_{1133}, C_{1123}, C_{3333}, C_{2323})$:

$$[\boldsymbol{\sigma}] = [\boldsymbol{C}][\boldsymbol{\epsilon}] \tag{6-1}$$

$$\begin{bmatrix}\sigma_{11}\\ \sigma_{22}\\ \sigma_{33}\\ \sigma_{23}\\ \sigma_{13}\\ \sigma_{12}\end{bmatrix} = \begin{bmatrix} C_{1111} & C_{1122} & C_{1133} & C_{1123} & 0 & 0 \\ C_{1122} & C_{1111} & C_{1133} & -C_{1123} & 0 & 0 \\ C_{1133} & C_{1133} & C_{3333} & 0 & 0 & 0 \\ C_{1123} & -C_{1123} & 0 & C_{2323} & 0 & 0 \\ 0 & 0 & 0 & 0 & C_{2323} & C_{1123} \\ 0 & 0 & 0 & 0 & C_{1123} & \frac{1}{2}(C_{1111}-C_{1122}) \end{bmatrix} \begin{bmatrix}\epsilon_{11}\\ \epsilon_{22}\\ \epsilon_{33}\\ 2\epsilon_{23}\\ 2\epsilon_{13}\\ 2\epsilon_{12}\end{bmatrix} \quad (6\text{-}2)$$

where $[\boldsymbol{\sigma}]$, $[\boldsymbol{\epsilon}]$, and $[\boldsymbol{C}]$ denote the Cauchy stress, strain, and elastic-stiffness tensors expressed in the conventional Voigt notation, respectively. In the published literature, the values of the elastic constant for α –quartz were measured using resonance-ultrasound spectroscopy (Heyliger et al., 2003). The constitutive relationship defined by Equation 6-2 principally worked in the local coordinate system associated with the material point (integration point) of the FE and spanned by the orthogonal orientation matrix $\boldsymbol{R}$:

$$\boldsymbol{R} = \begin{bmatrix} x_1 & x_2 & x_3 \\ y_1 & y_2 & y_3 \\ z_1 & z_2 & z_3 \end{bmatrix} \quad (6\text{-}3)$$

where (x_1, y_1, z_1), (x_2, y_2, z_2), and (x_3, y_3, z_3) are unit vectors expressed in the global coordinate system and span the [2 -1 -1 0] (a-axis), [0 1 -1 0], and [0 0 0 1] (c-axis) crystal local axes. Accordingly, the user-subroutine included rotational transformations of strain/stress tensors between the global and local coordinate systems:

$$\boldsymbol{\epsilon} = \boldsymbol{R}\,\boldsymbol{\epsilon}'\,\boldsymbol{R}^{\boldsymbol{T}} \quad (6\text{-}4)$$

$$[\boldsymbol{\sigma}] = [\boldsymbol{C}][\boldsymbol{\epsilon}] \quad (6\text{-}5)$$

$$\boldsymbol{\sigma}' = \boldsymbol{R}^{\boldsymbol{T}}\,\boldsymbol{\sigma}\,\boldsymbol{R} \quad (6\text{-}6)$$

where $\boldsymbol{\epsilon}$ and $\boldsymbol{\sigma}$ are the Cauchy strain and stress tensors expressed in symmetric component format (3×3) and the crystal local coordinate system, while $\boldsymbol{\epsilon}'$ and $\boldsymbol{\sigma}'$ refer to the same tensors but are transformed into the global coordinate system. At the beginning of the user-subroutine, $\boldsymbol{R}$ was updated to account for the rigid rotation at the material point, which was calculated from the polar decomposition of the deformation gradient.

In another user-subroutine, $[\boldsymbol{C}]$ in Equation 2 was substituted with the isotropic approximation $[\boldsymbol{C}]_{iso}$ to compare the isotropic and anisotropic linear elastic behaviors:

$$[\boldsymbol{C}]_{iso} = \frac{E}{(1+v)(1-2v)} \begin{bmatrix} 1-v & v & v & 0 & 0 & 0 \\ v & 1-v & v & 0 & 0 & 0 \\ v & v & 1-v & 0 & 0 & 0 \\ 0 & 0 & 0 & \frac{1-2v}{2} & 0 & 0 \\ 0 & 0 & 0 & 0 & \frac{1-2v}{2} & 0 \\ 0 & 0 & 0 & 0 & 0 & \frac{1-2v}{2} \end{bmatrix} \quad (6\text{-}7)$$

where E and v are the modulus of elasticity and Poisson's ratio, respectively, which were obtained using Voigt-Reuss-Hill approximation for an anisotropic linear elastic material. Since the latter material model is isotropic, $[\boldsymbol{C}]_{iso}$ was invariant for all orthogonal coordinate systems. Therefore, the rotational stress/strain transformations (Equations 4-6) were redundant and thus eliminated from the user-subroutine algorithm.

Failure Criterion

From single particle crushing experiments, the fracture patterns of silica sand particles manifest breakage into relatively large fragments due to tensile stresses, disintegrating into several small fragments and fines due to compressive stresses, or a combination of both tensile and compressive failure. Furthermore, silica mineral is known to possess a much higher compressive strength than tension. These experimental insights can be addressed through a frictional failure surface similar to Drucker-Prager yield criterion that activates the onset of fracture at the element material point:

$$\sigma_{vf} = \alpha + \beta\sigma_{hf} \tag{6-8}$$

$$\sigma_v = \sqrt{\frac{1}{2}[(\sigma_{11} - \sigma_{22})^2 + (\sigma_{22} - \sigma_{33})^2 + (\sigma_{33} - \sigma_{11})^2 + 6(\sigma_{23}^2 + \sigma_{31}^2 + \sigma_{12}^2)]} \tag{6-9}$$

$$\sigma_h = \frac{1}{3}(\sigma_{11} + \sigma_{22} + \sigma_{33}) \tag{6-10}$$

where α and β are material failure parameters, σ_v is the von Mises stress, and σ_h is the hydrostatic mean stress. In Equation 6-8, subscript "f" was appended to σ_v and σ_h to denote failure (yield surface). The material parameters α and β can be related to the uniaxial tensile and compressive strength (σ_t and σ_c, respectively) of the silica mineral as:

$$\alpha = \frac{2\sigma_c\sigma_t}{\sigma_c + \sigma_t} \tag{6-11}$$

$$\beta = \frac{3(\sigma_c - \sigma_t)}{\sigma_c + \sigma_t} \tag{6-12}$$

Figure 6-1a illustrates a typical example of the failure criterion represented by Equation 8, where it shows that a tension cutoff limit was introduced to the failure criterion in which σ_{vf} remained constant when σ_{hf} in tension extended beyond the cutoff limit. The cutoff limit eliminated numerical instabilities associated with the failure near the stress state of hydrostatic tension ($\sigma_{vf} \to 0$). The failure condition for the cutoff limit in tension is defined as:

$$\sigma_{vf} = 0.1\alpha \;\forall\; \sigma_{hf} < -0.9\left(\frac{\alpha}{\beta}\right) \tag{6-13}$$

Degradation of Stiffness and Damage Evolution

Continuum damage mechanics is the principal framework that governs the numerical modeling of fracture in brittle materials such as sand particles, rock, concrete, and ceramics. The framework postulates the sudden collapse in the stress-strain behavior at fracture through progressive degradation in the stiffness associated with the material point, assuming the damaged and undamaged states have equivalent strains (Lemaitre and Chaboche, 1978). One way to model the amount of degradation in stiffness is by using a scalar damage parameter (d) that ranges between 0 and 1. A value of $d = 0$ represents an undamaged section whereas a value of $d = 1$ indicates a fully-damaged section. Accordingly, the elastic constants of the damaged material point can be computed (Clayton and Knap, 2015):

$$C_{ijkl} = C^o_{ijkl}[\zeta + (1-\zeta)(1-d)^2] + k_0\delta_{ij}\delta_{kl}[1-\zeta-(1-\zeta)(1-d)^2]\langle \mathrm{tr}(\boldsymbol{\epsilon})\rangle \quad (6\text{-}14)$$

where C^o_{ijkl} denotes the elastic constants of the undamaged material point (Table 6-1), δ_{ij} is the Kronecker delta, $\mathrm{tr}(\boldsymbol{\epsilon})$ is the trace of the Cauchy strain tensor (local volume change), and the operation $\langle \mathrm{x}\rangle = 1 \forall x \leq 0$ or $\langle \mathrm{x}\rangle = 1 \forall x > 0$. ζ is a constant with magnitude much less than unity ($0.001 \leq \zeta \leq 0.01$) that introduced a small amount of residual stiffness for numerical stability of a fully-damage material point. k_0 is the bulk modulus of the undamaged material point that was calculated for the trigonal crystal system (quartz) as:

$$k_0 = \frac{(C^o_{1111} + C^o_{1122})C^o_{3333} - (C^o_{1133})^2}{C^o_{1111} + C^o_{1122} + 2C^o_{3333} - 4C^o_{1133}} \quad (6\text{-}15)$$

Equation 14 represents a damage model that permitted degradation of the bulk modulus only when volume change was tensile and degradation of the shear modulus regardless of whether the volume change was tensile or compressive. This damage approach was anisotropic in the sense of different degradation in the stiffness of the material point under tensile versus compressive loading, and appropriately modeled the constitutive damage in brittle materials like silica sand particles.

From single particle crushing experiments of silica sands, the load-displacement relationship exhibits a rapid softening behavior (brittle) close to being instantaneous. Similar to what was proposed by Cervera and Chiumenti (2006), the brittle softening behavior can be numerically modeled using an exponential function (rapid rate of decay) that governs the evolution of d after the material point fails:

$$d(\bar{\bar{\sigma}}_v) = 1 - \frac{\sigma_{vf}}{\bar{\bar{\sigma}}_v}\exp\left[-2H_s\left(\frac{\bar{\bar{\sigma}}_v - \sigma_{vf}}{\sigma_{vf}}\right)\right] \quad (6\text{-}16)$$

where $\bar{\bar{\sigma}}_v$ is an equivalent von Mises stress at the damaged material point which was calculated using the undamaged stiffness (C^o_{ijkl}) and H_s is the damage softening modulus which controlled the rate of degradation in stiffness. To alleviate the concerns of damage dependency on mesh refinement, H_s was related to the characteristic length of the element (l_{ch}):

$$H_s = \frac{\overline{H}_s l_{ch}}{1 - \overline{H}_s l_{ch}} \geq 0 \quad (6\text{-}17)$$

$$\overline{H}_s = \frac{\sigma_y E}{G_f} \quad (6\text{-}18)$$

where G_f is mode I fracture energy, and σ_y is the uniaxial strength of the material (i.e., σ_t if the material point failed in tension or σ_c if in compression). Note that l_{ch} represents the size of the element, defined as a typical length of a line across a first-order element or half of the same length for a second-order element. Lastly, the internal local constraint $\Delta d \geq 0$ was imposed on the evolution of d to ensure the irreversibility of damage. If the latter constraint was not enforced, then the fracture of the silica sand particles can heal upon unloading. Table 6-1 lists input parameters that were used in the material user-subroutines to simulate the constitutive and fracture behaviors of silica mineral.

Implementation of User-Subroutines for Silica Material

The material user-subroutines were developed and implemented in ABAQUS FE software through FORTRAN scripts to simulate the constitutive and fracture behaviors of natural silica sand particles. The FE simulations operate on 3D meshes of linear tetrahedral elements that closely resemble the morphology of natural sand particles. The 3D meshes were generated via digital image processing of in-situ SMT images that were acquired by the authors in previous studies for two single particle crushing experiments and a confined 1D compression test on a sand specimen composed of 2705 particles. The SMT images were acquired using Beamlines 1-ID and 13-BMD of the Advanced Photon Source (APS), Argonne National Laboratory (ANL), IL, USA. Table 6-2 summarizes the simulated experiments, including information about the tested silica sands, x-ray scanning resources, resolution of the SMT images, experimental loading rates, and the source studies from which the SMT images were adopted. The SMT images were processed through a sequence of interactive modules in AVIZO commercial computer code, developed by Thermo Fisher Scientific group. The image processing procedure involved several modules such as anisotropic diffusion filtering, watershed segmentation, particle labeling, and 3D surface meshing. The in-situ scanning technique for the 1D compression experiment combined both SMT and 3DXRD. In their previous studies, the authors developed algorithms to analyze the SMT images and 3DXRD measurements [see Amirrahmat et al. (2020) for more details] and characterize the local crystal orientation of each particle within the specimen [see Imseeh et al. (2020)]. These local orientations for individual particles were adopted in this chapter to provide experimental input data for the $\boldsymbol{R}$ matrix defined in the material user-subroutine (Equation 3).

2D triangular rigid elements were used to model the experiments' loading platens as well as the surrounding mold in the confined 1D compression experiment. Rigid elements in ABAQUS experience no deformation, but instead, they are associated

with a reference node such that the element kinematics are entirely determined by the boundary conditions imposed at the reference point. The FE simulations also employed the general contact module in ABAQUS to model the particle-to-particle, particle-to-platen, and particle-to-mold interactions. Surface elements of individual sand particles, loading platens, and confining mold were extracted into element sets and included in the domain of the general contact module. When elements of the general contact module domain are in contact, shear and normal forces are transmitted across the contact interface to resist node-into-face, node-into-rigid surface, and edge-into-edge penetration. The default hard contact model of ABAQUS was used to relate the normal contact forces to penetration distances through the bulk element stiffness at the contact interface where the allowed nodal penetration at contact interfaces was insignificant during the simulations. The Coulomb frictional model was adopted to simulate the transmission of tangential forces at the contact interfaces with a friction coefficient of 0.38, which is a typical value for the true angle of friction of silica mineral surface ($\tan 21^o = 0.38$).
The primary computational challenge in the intended FE simulations emerged from the large number of nodal contacts, especially in the simulations of the confined 1D compression test. Therefore, the explicit dynamic solver in ABAQUS was used to conduct the FE simulations in this chapter. The assumption of nodal lumped masses in this specific solver produced a diagonal mass matrix ($\boldsymbol{M}$), which was used to balance the equation of motion. The explicit central-difference time integration rule was then used to advance the nodal kinematic state (nodal displacement, velocity, and acceleration) over time. The key advantage of this solver is the use of explicit balance equations and the fast inversion of $\boldsymbol{M}$ (diagonal) versus the Newton-Raphson procedure, which is executed at every time increment of the static implicit solver to iterated equilibrium. Although the explicit dynamic solver was originally designated for problems with impact loading (i.e., high strain rate), the use of uniform mass scaling limited the speed of stress wave propagation, allowing for the utilization of the explicit dynamic solver in quasi-static analyses. Moreover, the mass scaling offered the advantage of drastically reducing the simulation runtime by increasing the size of the minimum stable time increment.

Single particle Crushing FE Simulations

Description of FE Simulations
3D FE simulations were developed for two single particle crushing experiments that were conducted on ASTM 20-30 Ottawa sand (99.9% silica sand). Table 6-3 lists information about the two experiments, including micro-scale measurements from the SMT images such as the particle 3D length, width, equivalent diameter, aspect ratio (AR = 3D length/3D width), and initial distance between the loading platens. The particle in the processed SMT image at the initial-state (unloaded) was projected on 2D planes at a specific angle, and the distance between the outermost tangents of projections was calculated to represent the 3D Feret diameter of that angle. Multiple 3D Feret diameters were computed with a sampling

of 31 angles regularly spaced in 3D space around the upper part of a unit sphere. Accordingly, the 3D length and width were determined as the longest and shortest of the 3D Feret diameters, respectively. AR was then calculated as the ratio between 3D length to width. The equivalent diameter was computed as the diameter of a sphere with equal volume to the sand particle. As listed in Table 6-3, both particles had almost the same equivalent diameter of ~0.850 mm with a difference less than 0.005 mm. For baseline analyses to compare results, simulations of the single particle crushing experiment were also executed on a sphere with a diameter of 0.850 mm (~equivalent diameter of the crushed sand particles). Figure 6-2 presents 3D volume rendering of the SMT images for the two single particle crushing experiments and their counter FE simulation, as well as the analogous simulations conducted on the sphere. As depicted in Figure 6-2, "Particle-1" and "Particle-2" refer to the two single particle crushing experiments, whereas the simulations of the sphere are denoted as "Sphere-Eq".

For each particle, both sand and sphere, three simulations were conducted and given the labels of "Isotropic", "Strong", and "Weak". In the Isotropic case, the simulations executed the material user-subroutine that assumed isotropic linear approximation of silica constitutive behavior (Equation 6-7). On the other hand, the Strong and Weak simulations executed the material user-subroutine that was developed using the anisotropic linear model for silica mineral (Equation 6-2). In the Strong and Weak simulation, $\boldsymbol{R}$ matrices were oppositely assigned to the elements' material points:

$$\boldsymbol{R} = \begin{bmatrix} 1 & 0 & 0 \\ 0 & 1 & 0 \\ 0 & 0 & 1 \end{bmatrix} \rightarrow \text{Strong simulations} \tag{6-19}$$

$$\boldsymbol{R} = \begin{bmatrix} 0 & -1 & 0 \\ 0 & 0 & -1 \\ 1 & 0 & 0 \end{bmatrix} \rightarrow \text{Weak simulations} \tag{6-20}$$

It can be seen from Figure 6-2 that the direction of uniaxial compression run parallel to the Z-axis of the global coordinate system. Accordingly, the idea of assigning $\boldsymbol{R}$ matrices per Equations 6-19 and 6-20 was to examine the difference in the constitutive and fracture behaviors when the particle was loaded against its crystal c-axis in the Strong simulations versus the a-axes in the Weak simulations. Note that compression against the c-axis was denoted as Strong since the crystal c-axis possesses larger stiffness (105.8 MPa) than the a-axis (87.28 MPa).

Figure 6-3a presents the evolution curves of vertical crushing load (F_Z) versus displacement (U_Z) of the top loading platen. Namely, U_Z represents the movement of the top platen and F_Z is the summation of reaction forces acting against the platen. The single particle crushing apparatus had the capability of measuring F_Z and U_z during the experiment via a load cell and stepper motor readings, which were used to plot the solid curves in Figure 6-3a. It can be seen from Figure 6-3a that the numerical prediction of the experimental curves (solid lines) improved when the material user-subroutine implemented the anisotropic linear elastic model of silica mineral (Strong and Weak curves), in comparison to the isotropic approximation (isotropic curves). When comparing the $F_Z - U_Z$ responses for

individual particles (set of curves with the same color), the Strong curves (dashed line) display a stiffer response compared to the Weak (double dashed line) and Isotropic curves (dotted line), respectively. The latter remark aroused from aligning the loading direction in the Strong simulations with the stiff crystal c-axis. Figure 6-3a also demonstrates a significant variation in the $F_Z{-}U_Z$ responses between Particle-1 and Particle-2. Relative to the response of Sphere-Eq, Particle-2 fractured at about half F_Z whereas Particle-1 at almost half U_Z. Both Particles were selected from Ottawa ASTM 20-30 sand, which is a standard type of sand that has been widely used in geotechnical testing and is known for having silica constituent (> 99.9%) as well as a uniform grain size distribution. Similar variation in $F_Z - U_Z$ response was also reported by Cil et al. (2013) for 87 particles of the same sand that were tested using the same testing apparatus. The following sub-section uses the 3D FE simulations to investigate the variation in the fracture and constitutive behaviors between Particles 1 and 2.

Variation in the Constitutive and Fracture Behaviors of Single particle Crushing Experiments

The material user-subroutines provided numerical estimates of σ_{ij} and ϵ_{ij} for the material point at the center of each element within the particle. These element-level estimates were averaged into particle-level Cauchy stress ($\overline{\sigma}_{ij}$) and strain ($\overline{\epsilon}_{ij}$) tensors as:

$$\overline{\sigma}_{ij} = \frac{\sum_{el=1}^{N} \sigma_{ij} V_{el}}{\sum_{el=1}^{N} V_{el}} \tag{6-21}$$

$$\overline{\epsilon}_{ij} = \frac{\sum_{el=1}^{N} \epsilon_{ij} V_{el}}{\sum_{el=1}^{N} V_{el}} \tag{6-22}$$

where V_{el} is the element volume and the summation runs on all of the elements (N) within the particle. Accordingly, the Eigenvalues of $\overline{\sigma}_{ij}$ and $\overline{\epsilon}_{ij}$ were computed to represent particle's major ($\overline{\sigma}_1$ or $\overline{\epsilon}_1$), intermediate ($\overline{\sigma}_2$ or $\overline{\epsilon}_2$), and minor ($\overline{\sigma}_3$ or $\overline{\epsilon}_3$) principal stresses and strains. Figure 6-3b displays the evolution of $\overline{\sigma}_1$ versus $\overline{\epsilon}_1$ for the simulations of Particle-1, Particle-2, and Sphere-Eq. The Strong simulations manifested stiffer behavior than Weak and Isotropic simulations. Furthermore, the curves of Particle-1 and Particle-2 simulations in Figure 6-3b exhibited less variation than the curves shown in Figure 6-3a. Recall that $F_Z - U_Z$ curves in Figure 6-3a represented the constitutive response of the particle as postulated by the load-displacement of the top loading platen, whereas $\overline{\sigma}_1 - \overline{\epsilon}_1$ curves in Figure 6-3b were the stress-strain that was experienced by the particle. Referring to Figure 6-2, it can be seen that Particle-2 exhibited soft contact with the loading platens, which caused the particle to rotate slightly between $F_Z = 0$ and $F_Z = 20$ N. Conversely, Particle-1 lacked this rotation due to its firm contact with the two loading platens. The difference in the nature of particle-to-platen contacts can explain the long stretch in the blue curves in Figure 6-3a relative to the red curves. Rotation of Particle-1 produced rigid motion, and eliminating this rigid

motion brought curves of Particle-1 and Particle-2 closer to each another in Figure 6-3b.

Figure 6-4 displays the distribution of σ_v within Particle-1, Particle-2, and Sphere-Eq at fracture. For the FE simulations of Particle-1 (Figure 6-4a), it can be seen that fracture patterns in the three FE simulations (Strong, Weak, and Isotropic) mainly occurred near a surface depression that penetrated through the micro-structure of Particle-1 (see the SMT scans in Figure 6-1a). Such material imperfections are well-known to exist in natural sand particles and create weak points in the particle micro-structure that give rise to fracture onset. Particle-2 and Sphere-Eq were free of micro-structural imperfections and exhibited different fracture modes in the strong simulations when compared to weak simulations. The latter finding clearly challenged the DEM and isotropic FE simulations, which falsely presume the same fracture and constitutive behaviors for two particles with identical morphology and particle-to-plate interaction. Differences in the constitutive and fracture behaviors of identical particles can fundamentally arise from properties beyond the micro-scale and exist at the crystal scale-level of silica sand.

The X-Y views of fractured particles in Figure 6-4 clearly illustrate a broader spread of red area in Sphere-Eq and Particle-1 than Particle-2. This red area represents the highly stressed region within the particle that interacted with the top loading platen. The difference in the particle-to-plate interaction area can explain the fracture of Particle-2 at a much lower F_Z in Figure 6-3a relative to Particle-1 and Sphere-Eq. Namely, F_Z in Particle-2 acted on a smaller region that caused high-stress concentrations within the particle, and thus Particle-2 fractured at a low F_Z. Another observation from Figure 6-4c is the shattering fracture manifested by the Isotropic simulations of Sphere-Eq. Such behavior was attributed to the regularity in the sphere geometry accompanied by the presumed isotropy in the constitutive response.

Imseeh et al. (2020) utilized 3DXRD and 3D FE to examine the evolution of lattice stress within synthetic silica cubes loaded in unconfined 1D compression tests. They concluded (i) the lattice stress uniformly distributed along the height of the cube in the direction of compression, and (ii) $\overline{\sigma}_1$ of the cube was equal to the applied force divided by the cube cross-sectional area. These two findings were fundamentally attributed to the regular geometry of the cube that established a full interaction between its cross-sectional area and the loading platens. In an attempt to investigate similar insights, Figure 6-5 displays $\overline{\sigma}_1$ versus $F_Z/(\frac{\pi d_c}{4})$ for the conducted simulations of Particle-1, Particle-2, and Sphere-Eq. As demonstrated in Figure 6-1a and b, d_c represents an equivalent diameter for the cross-sectional area (A_c) of Particle-1 and Particle-2 that was computed from a central axial (X-Y) slice through the particle. Note that d_c for the Sphere-Eq simulations also represents the diameter of the sphere. Interestingly, the $\overline{\sigma}_1 - F_Z/(\frac{\pi d_c}{4})$ relationships in Figure 6-5 converged to a slope of ~1.2 for all conducted simulations. The 1.2 slope suggests that F_Z acts on an effective axial cross-sectional area $A_e = 0.83A_c$

or, in other words, an effective diameter of $d_e \cong 0.9d_c$. Figure 6-6a-c demonstrates the interpretation of d_e with respect to d_c for the Sphere-Eq simulations through displaying the stress field distribution (σ_v) within the sphere. The stress fields explicitly show a blue portion toward the sphere sides that extended beyond $0.9d_c$ and exhibited very low stress (unloaded portion). Figure 6-6d also displays the distribution of σ_1 and σ_3 along the axial loading direction for the three simulations of Sphere-Eq. The solid black curves in Figure 6-6d represent the theoretical (closed-form) solution calculated by Hiramatsu and Oka (1966) for an isotropic linear elastic sphere. The theoretical solution has an excellent agreement with the Isotropic simulations of Sphere-Eq.

3D FE Simulations of a Confined 1D Compression Experiment

Description of FE Simulations

3D FE simulations were developed for a confined 1D compression experiment that was conducted on a specimen of natural silica sand known as Ottawa F-75 (Table 6-2). The confined specimen had a diameter of 1.6 mm, an initial height of 3.7 mm, and contained 2705 sand particles. As depicted in Figure 6-7, in-situ SMT images for the sand specimen were processed to produce 3D meshes that closely resembled the natural morphology of each particle within the specimen. Referring to Figure 6-7b, the meshed specimen consisted of 1,113,478 nodes and 4,712,134 elements. In addition to SMT, 3DXRD measurements were acquired for the simulated specimen, which experimentally quantified the local crystal orientation for each particle within the specimen. These local orientations were used to assign initial $\boldsymbol{R}$ matrices (Equation 6-3) for the group of elements meshing each particle.

In preliminary trials, FE simulations suffered from numerical instabilities when the meshed specimen in Figure 6-7b was confined inside a rigid mold and loaded in 1D compression using two rigid platens. The numerical instabilities were attributed to deficiencies in the contact establishment between the 3D particle meshes. These numerical instabilities were alleviated by applying gravity forces to the specimen before loading it in 1D compression. When gravity forces were applied, the initial height of the specimen decreased by 0.7 mm (2.3%), and the initial contact fabric of the specimen was slightly altered. Furthermore, the confining mold in the experiment consisted of a nylon tube, housed inside another acrylic tube with thick walls (Amirrahmat et al., 2020). The in-situ SMT images exposed bulging and deformation in the inner nylon tube as the 1D compression experiment progressed, unlike the rigid mold in the simulations. These minor mismatches between the experimental and simulated conditions made it difficult to perform an accurate particle-to-particle comparison between the results. For the purpose of comparison between the simulated and experimental response, an oedometer test was conducted on a laboratory-sized specimen composed of the same simulated sand. The specimen had a diameter of 50 mm, an initial height of 25 mm, and was confined inside a thick-wall steel mold (rigid).

Four different FE simulations were executed on the meshed specimen: FEM-Isotropic, FEM-Strong, FEM-Weak, and FEM-Experimental. In the FEM-Isotropic

simulations, the constitutive behavior of the 3D particle meshes was modeled using the material user-subroutine that assumed an isotropic linear elastic approximation of silica mineral (Equation 6-7). The other three FE simulations were performed using the material user-subroutine that considered the anisotropic linear elastic behavior of silica mineral (Equation 6-3). In the FEM-Experimental simulations, the elements meshing each sand particle were assigned $\boldsymbol{R}$ matrices that represented the experimental local crystal orientation of the particle, as quantified by 3DXRD. Figure 6-8 displays the evolution of 1D compression in the FEM-Experimental simulations. Prior to extensive particle fracture (Figure 6-8a), $\bar{\sigma}_{ij}$ was determined for each particle and was used to calculate the principal stresses $\bar{\sigma}_1$, $\bar{\sigma}_2$, and $\bar{\sigma}_3$, as well as their directions $\overline{\boldsymbol{V}}_{\boldsymbol{1}}$, $\overline{\boldsymbol{V}}_{\boldsymbol{2}}$, and $\overline{\boldsymbol{V}}_{\boldsymbol{3}}$. For the group of elements meshing each particle, $\boldsymbol{R}$ matrices were initialized as $[\overline{\boldsymbol{V}}_{\boldsymbol{3}}\ \overline{\boldsymbol{V}}_{\boldsymbol{2}}\ \overline{\boldsymbol{V}}_{\boldsymbol{1}}]$ in the FEM-Strong simulations wherase the FEM-Weak simulations assumed initial $\boldsymbol{R}$ matrices as $[\overline{\boldsymbol{V}}_{\boldsymbol{1}}\ \overline{\boldsymbol{V}}_{\boldsymbol{2}}\ \overline{\boldsymbol{V}}_{\boldsymbol{3}}]$. These configurations of initial $\boldsymbol{R}$ matrices sought to compare the constitutive response of the sand specimen when the crystal c-axis (stiff) of individual particles was aligned with the direction of $\bar{\sigma}_1$ in FEM-Strong simulations versus the opposite case of the crystal a-axis (less stiff) in FEM-Weak simulations. Figure 6-9 shows the local crystal orientations assigned for each particle in the FEM-Strong, FEM-Weak, and FEM-Experimental simulations. Although one local orientation was plotted per particle in Figure 6-9, these orientations were assigned to each element meshing the particle.

Figure 6-10 shows the evolution of the specimen void ratio (e) versus vertical compressive stress (σ_Z) for the four FE simulations of the 1D compression experiment. The solid black curve in Figure 6-10 displays the response of the laboratory-sized specimen. The four FE simulations yielded very close $e - \sigma_Z$ responses that had an excellent agreement with the response of the laboratory-sized specimen. The FE simulation curves in Figure 6-10 exhibited yielding at slightly larger σ_Z than the laboratory-sized experiment because of the residual stiffness $(\zeta = 0.01)$ possessed by the completely failed elements. Although a value of $\zeta < 0.01$ would bring the experiment and simulation curves closer to one another, the failed elements exhibited excessive deformations when using $\zeta < 0.01$. These excessive deformations drastically reduced the minimum required stable time increment, and the simulations became very slow and inefficient computationally. The dotted curves in Figure 6-10 display the FE simulated response of the specimen when the damage criterion was deactivated from the material user-subroutines algorithm (no particle fracture). Clearly, modeling particle fracture is essential to simulate sand yielding behavior in the confined 1D compression experiment.

Influence of Particle Morphology and Coordination on Fracture Stress

The evolution of $\bar{\sigma}_{ij}$ versus $\bar{\epsilon}_{ij}$ for FE simulations was determined in the course of 1D compression for each particle within the specimen. Out of the 2705 sand particles, the $\bar{\sigma}_{ij} - \bar{\epsilon}_{ij}$ relationships were examined to describe fractures of 1115 particles. Figure 6-11 presents the $\bar{\epsilon}_1 - \bar{\sigma}_1$ relationships for 6 fractured particles

that were selected from different regions within the specimen. It can be noticed from Figure 6-11 that the stress-strain response and fracture stress were influenced by the local crystal orientation of the particle, as well as whether the material user-subroutine uses the isotropic or anisotropic linear elastic model for silica mineral. As demonstrated in Figure 6-11, the fracture stress was determined as the peak in the stress-strain curves and the particle von Mises ($\bar{\sigma}_{vf}$) versus hydrostatic mean stress ($\bar{\sigma}_{hf}$) at fracture are plotted in Figure 6-12 which shows a linearly increasing correlation between $\bar{\sigma}_{vf}$ and $\bar{\sigma}_{hf}$ that was fundamentally inherited from the frictional failure criterion used to model the onset of fracture at the element-level (Figure 6-1a).

The simulated FE results were used to evaluate the influence of coordination number (CN) and AR on fracture stress of particles. The histogram depicted in Figure 6-13a displays the distribution of CN for 1115 fractured particles and Figures 13b-f correlate the particle CN to the principal stresses at fracture ($\bar{\sigma}_{1f}$, $\bar{\sigma}_{2f}$, and $\bar{\sigma}_{3f}$) as well as $\bar{\sigma}_{vf}$ and $\bar{\sigma}_{hf}$. The error bars in Figures 13b-f represent the interquartile range (IQR) in the fracture stress of each histogram bin, the curves passed through the mean fracture stress, and different colors denoted the four FE simulations (FEM-Isotropic, FEM-Strong, FEM-Weak, and FEM-Experimental). Note that CN for the fractured particles was the same in the four FE simulations since the simulations were conducted on the same meshed specimen. Figures 13b-f demonstrate a linear increase in fracture stress of particles with higher CN. Particles with a higher CN exhibited more contacts with their neighboring particles that provided a higher degree of confinement; therefore, $\bar{\sigma}_{hf}$ would be greater for fractured particles with higher CN. A higher $\bar{\sigma}_{hf}$ implied that the particle would fracture at a higher stress-level since the material user-subroutines implemented a frictional failure criterion. A similar assessment was also performed for the influence of AR on fracture stress of particles. Figure 6-14 presents a histogram plot of AR for the fractured particles and correlates AR to $\bar{\sigma}_{1f}$, $\bar{\sigma}_{2f}$, $\bar{\sigma}_{3f}$, $\bar{\sigma}_{vf}$ and $\bar{\sigma}_{hf}$, which shows that the particle fracture stress decreased with higher AR. In other words, the resistance to fracture was less for particles with shapes that tended to be elongated rather than spherical. A higher value of AR indicated the particle had a relatively short length that possessed less inertia to resist fracture. The significant correlations of CN and AR to fracture stress of particles advocated for the fundamental importance of micro-scale properties in sand specimens.

Summary and Conclusions

The chapter examined the constitutive and fracture behaviors of silica sand particles using 3D FE simulations and in-situ SMT images. The SMT images were processed to calibrate and develop 3D FE simulations for a single particle crushing and a confined 1D compression experiment. The 3D FE simulation executed a material point user-subroutine that numerically modeled the anisotropic linear elastic behavior of silica mineral, as well as the isotropic behavior approximation. Particle fracture was simulated using anisotropic degradation in the material point

stiffness. Numerical estimates of the material user-subroutine were then used to investigate micro- and crystalline-scale properties that influenced the fracture characteristics of silica sand particles. Comparison and assessment of the simulated FE results yielded the following conclusions:

I. In a single particle crushing, the load-displacement response and fracture stress are highly influenced by the nature of contacts between the particle and loading platens. Imperfections in the particle micro-structure create weak points that would give rise to the onset of fracture. For particles with intact micro-structure, the fracture patterns are affected by the direction of loading relative to the crystal lattice orientation of the particle.

II. In a confined 1D compression, particle fracture is of fundamental importance for the specimen yielding behavior. Changing the crystal lattice orientation of individual particles has an insignificant effect on the boundary stress-strain response. The use of the isotropic approximation for silica constitutive behavior would produce a boundary stress-strain response close to the case when the anisotropic linear elastic behavior is considered. Still, the local crystal orientations influence the particle strength and stress-strain response prior to fracture. Resistance to fracture is higher for particles that exhibit more contact interfaces with their neighboring particles, as well as for particles that have spherical shapes rather than elongated.

Acknowledgments

This material was partially funded by the US National Science Foundation (NSF) under Grant No. CMMI-1362510. Any opinions, findings, conclusions, and recommendations expressed in this chapter are those of the authors and do not necessarily reflect the views of the NSF. The SMT and 3DXRD scans were collected using the x-Ray Operations and Research Beamline Stations 13-BMD and 1-ID of the Advanced Photon Source (APS), a US Department of Energy (DOE) Office of Science User Facility operated by the Argonne National Laboratory (ANL) under Contract No. DE-AC02-06CH11357. We acknowledge the support of GeoSoilEnviroCARS (Sector 13), which is funded by the NSF Earth Sciences (EAR-1128799), and the DOE Geosciences (DE-FG02-94ER14466). We thank Dr. Mark Rivers and Dr. Peter Kenesei for their guidance at APS. We also thank Zaher Jarrar for his valuable comments during manuscript preparation

References

Hiramatsu, Y. & Oka, Y. (1966) Determination of the tensile strength of rock by a compression test of an irregular test piece. In *International Journal of Rock Mechanics and Mining Sciences & Geomechanics Abstracts*.) Elsevier, vol. 3, pp. 89-90.

Lee, K. L. & Farhoomand, I. (1967) Compressibility and crushing of granular soil in anisotropic triaxial compression. *Canadian Geotechnical Journal* **4(1)**:68-86.

Lemaitre, J. & Chaboche, J.-L. (1978) Aspect phénoménologique de la rupture par endommagement. *J Méc Appl* **2(3)**.

Bolton, M. D. (1986) The strength and dilatancy of sands. *Geotechnique* **36**:65-78.

Coop, M. & Lee, I. (1993) The behavior of granular soils at elevated stresses. *Predictive soil mechanics*:186-198.

Lade, P. V., Yamamuro, J. A. & Bopp, P. A. (1996) Significance of particle crushing in granular materials. *Journal of Geotechnical Engineering* **122(4)**:309-316.

Mcdowell, G. & Bolton, M. (1998) On the micromechanics of crushable aggregates. *Geotechnique* **48(5)**:667-679.

Nakata, A., Hyde, M., Hyodo, H. & Murata (1999) A probabilistic approach to sand particle crushing in the triaxial test. *Geotechnique* **49(5)**:567-583.

Chuhan, F. A., Kjeldstad, A., Bjørlykke, K. & Høeg, K. (2002) Porosity loss in sand by grain crushing—Experimental evidence and relevance to reservoir quality. *Marine and Petroleum Geology* **19(1)**:39-53.

Heyliger, P., Ledbetter, H. & Kim, S. (2003) Elastic constants of natural quartz. *J. Acoust. Soc. Am* **114**:644.

Potyondy, D. O. & Cundall, P. (2004) A bonded-particle model for rock. *International journal of rock mechanics and mining sciences* **41(8)**:1329-1364.

Russell, A. R. & Khalili, N. (2004) A bounding surface plasticity model for sands exhibiting particle crushing. *Canadian Geotechnical Journal* **41(6)**:1179-1192.

Lobo-Guerrero, S. & Vallejo, L. E. (2005) Analysis of crushing of granular material under isotropic and biaxial stress conditions. *Soils and Foundations* **45(4)**:79-87.

Cervera, M. & Chiumenti, M. (2006) Mesh objective tensile cracking via a local continuum damage model and a crack tracking technique. *Computer Methods in Applied Mechanics and Engineering* **196(1-3)**:304-320.

Guimaraes, M., Valdes, J., Palomino, A. & Santamarina, J. (2007) Aggregate production: fines generation during rock crushing. *International journal of mineral processing* **81(4)**:237-247.

Karimpour, H. & Lade, P. V. (2010) Time effects relate to crushing in sand. *Journal of Geotechnical and Geoenvironmental Engineering* **136(9)**:1209-1219.

Hanley, K. J., O'sullivan, C., Oliveira, J. C., Cronin, K. & Byrne, E. P. (2011) Application of Taguchi methods to DEM calibration of bonded agglomerates. *Powder Technology* **210(3)**:230-240.

Gao, R., Du, X., Zeng, Y., Li, Y. & Yan, J. (2012) A new method to simulate irregular particles by discrete element method. *Journal of Rock Mechanics and Geotechnical Engineering* **4(3)**:276-281.

Alshibli, K., Cil, M., Kenesei, P. & Lienert, U. (2013) Strain tensor determination of compressed individual silica sand particles using high-energy synchrotron diffraction. *Granular Matter*:1-14.

Cil, M., Alshibli, K., Mcdowell, G. & Li, H. (2013) Discussion: 3D assessment of fracture of sand particles using discrete element method. *Géotech. Lett* **3(3)**:13-15.

Cil, M. B., Alshibli, K., Kenesei, P. & Lienert, U. (2014) Combined high-energy synchrotron X-ray diffraction and computed tomography to characterize constitutive behavior of silica sand. *Nuclear Instruments and Methods in Physics Research Section B: Beam Interactions with Materials and Atoms* **324**:11-16.

Nicksiar, M. & Martin, C. (2014) Factors affecting crack initiation in low porosity crystalline rocks. *Rock mechanics and rock engineering* **47(4)**:1165-1181.

Parab, N. D., Claus, B., Hudspeth, M. C., Black, J. T., Mondal, A., Sun, J., Fezzaa, K., Xiao, X., Luo, S. & Chen, W. (2014) Experimental assessment of fracture of individual sand particles at different loading rates. *International Journal of Impact Engineering* **68**:8-14.

Clayton, J. & Knap, J. (2015) Phase field modeling of directional fracture in anisotropic polycrystals. *Computational Materials Science* **98**:158-169.

Druckrey, A. M. & Alshibli, K. A. (2015) 3D finite element modeling of sand particle fracture based on in situ X-Ray synchrotron imaging. *International Journal for Numerical and Analytical Methods in Geomechanics*.

Zhao, B., Wang, J., Coop, M., Viggiani, G. & Jiang, M. (2015) An investigation of single sand particle fracture using X-ray micro-tomography. *Geotechnique* **65(8)**:625-641.

Zheng, W. & Tannant, D. (2016) Frac sand crushing characteristics and morphology changes under high compressive stress and implications for sand pack permeability. *Canadian Geotechnical Journal* **53(9)**:1412-1423.

Zhou, W., Yang, L., Ma, G., Chang, X., Lai, Z. & Xu, K. (2016) DEM analysis of the size effects on the behavior of crushable granular materials. *Granular Matter* **18(3)**:64.

Afshar, T., Disfani, M. M., Arulrajah, A., Narsilio, G. A. & Emam, S. (2017) Impact of particle shape on breakage of recycled construction and demolition aggregates. *Powder Technology* **308**:1-12.

Cil, M. B., Alshibli, K. A. & Kenesei, P. (2017) 3D Experimental Measurement of Lattice Strain and Fracture Behavior of Sand Particles Using Synchrotron X-Ray Diffraction and Tomography. *Journal of Geotechnical and Geoenvironmental Engineering* **143(9)**.

Todisco, M., Wang, W., Coop, M. & Senetakis, K. (2017) Multiple contact compression tests on sand particles. *Soils and Foundations* **57(1)**:126-140.
Hurley, R., Lind, J., Pagan, D., Akin, M. & Herbold, E. (2018) In situ grain fracture mechanics during uniaxial compaction of granular solids. *Journal of the Mechanics and Physics of Solids* **112**:273-290.
Imseeh, W. H. & Alshibli, K. A. (2018) 3D Finite Element Modelling of Force Transmission and Particle Fracture of Sand. *Computers and Geotechnics* **94**:184-195.
Karatza, Z., Ando, E., Papanicolopulos, S.-A., Ooi, J. & Viggiani, G. (2018) Evolution of deformation and breakage in sand studied using X-ray tomography. *Geotechnique* **68(2)**:107-117.
Kawamoto, R., Andò, E., Viggiani, G. & Andrade, J. E. (2018) All you need is shape: Predicting shear banding in sand with LS-DEM. *Journal of the Mechanics and Physics of Solids* **111**:375-392.
Li, H. & Mcdowell, G. R. (2018) Discrete element modelling of under sleeper pads using a box test. *Granular Matter* **20(2)**:26.
Turner, A. K., Sharma, A., Penumadu, D. & Herbold, E. B. (2019) Finite element analyses of single particle crushing tests incorporating computed tomography imaging and damage mechanics. *Computers and Geotechnics* **115**:103158.
Wei, D., Zhao, B., Dias-Da-Costa, D. & Gan, Y. (2019) An FDEM study of particle breakage under rotational point loading. *Engineering fracture mechanics* **212**:221-237.
Wu, M. & Wang, J. (2019) Registration of point cloud data for matching crushed sand particles. *Powder Technology* **347**:227-242.
Amirrahmat, S., Imseeh, W. H., Alshibli, K. A., Kenesei, P., Jarrar, Z. A. & Sharma, H. (2020) 3D Experimental Measurements of Evolution of Force Chains in Natural Silica Sand. *Journal of Geotechnical and Geoenvironmental Engineering* **146(5)**:04020027.
Harmon, J. M., Arthur, D. & Andrade, J. E. (2020) Level set splitting in DEM for modeling breakage mechanics. *Computer Methods in Applied Mechanics and Engineering* **365**:112961.
Imseeh, W. H., Alshibli, K. A., Moslehy, A., Kenesei, P. & Sharma, H. (2020) Influence of Crystal Structure on Constitutive Anisotropy of Silica Sand at Particle-Scale. *Computers and Geotechnics*.
Jarrar, Z. A., Alshibli, K. A. & Al-Raoush, R. I. (2020) Three-Dimensional Evaluation of Sand Particle Fracture Using Discrete-Element Method and Synchrotron Microcomputed Tomography Images. *Journal of Geotechnical and Geoenvironmental Engineering* **146(7)**:06020007.
Thakur, M. M. & Penumadu, D. (2020) Triaxial compression in sands using FDEM and micro-X-ray computed tomography. *Computers and Geotechnics* **124**:103638.

Xiao, Y., Meng, M., Daouadji, A., Chen, Q., Wu, Z. & Jiang, X. (2020) Effects of particle size on crushing and deformation behaviors of rockfill materials. *Geoscience Frontiers* **11(2)**:375-388.

Appendices

Appendix A: Tables

Table 6-1. Input parameters adopted in the material user-subroutines for silica mineral.

Elastic Constants of Undamaged Material *(Heyliger et al., 2003)*	
C_{1111}	87.26 *GPa*
C_{1122}	6.57 *GPa*
C_{1133}	11.95 *GPa*
C_{1123}	-17.18 *GPa*
C_{3333}	105.8 *GPa*
C_{2323}	57.15 *GPa*
Modulus of elasticity, E *	99.45 *GPa*
Poisson's ratio, ν *	0.06
Damage Parameters	
Uniaxial compressive strength, σ_c	1600 *MPa*
Uniaxial tensile strength, σ_c	120 *MPa*
Mode I fracture energy per unit area, G_f	100 *J/m²*
Coefficient of residual stiffness, ζ	0.01

** Isotropic approximations obtained by Voigt-Reuss-Hill Averaging*

Table 6-2. Summary of the experiments that were simulated using 3D FE.

Experiment	Tested Sand	Grain Sizes: US Sieve # (mm)	Scanning Beamline	Image Resolution: μm/pixel	Loading Rate: mm/minute	Source of Scans
Single particle Crushing	Ottawa ASTM 20-30	#20(0.841)-#30(0.595)	13-BMD, APS, ANL	1.98	0.001	(Druckrey and Alshibli, 2016)
Confined 1D Compression	Fraction of F75 Ottawa sand	#100(0.149)-#140(0.105)	1-ID, APS, ANL	1.17	0.2	(Amirrahmat et al., 2020)

Table 6-3. Micro-scale properties of the two particles that were tested and simulated in single particle crushing, as well as the simulated equivalent sphere.

Label of Experiment/ FE Simulation	3D Length: mm	3D Width: mm	Equivalent Diameter: mm	Aspect Ratio (AR)	Initial Distance Between Loading plates: mm
Paricle-1	1.041	0.669	0.850	1.56	0.652
Particle-2	1.067	0.733	0.855	1.46	0.775
Sphere-Eq	0.850	0.850	0.850	1.00	0.850

Appendix B: Figures

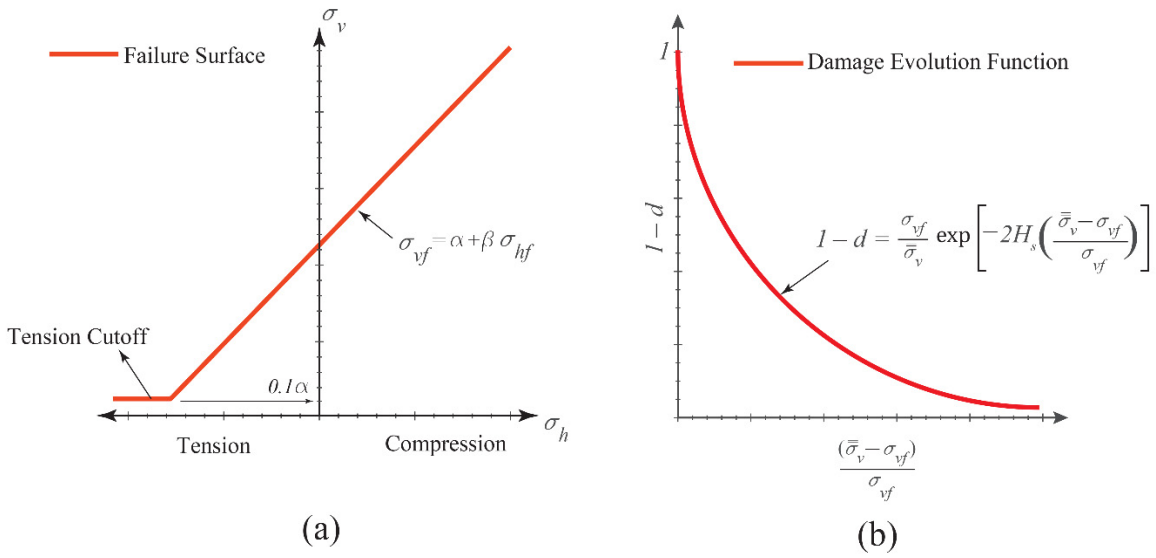


Figure 6-1. (a) Illustration of the failure criterion and (b) damage evolution that were implemented in the material user-subroutines to model the brittle fracture of silica sand particles.

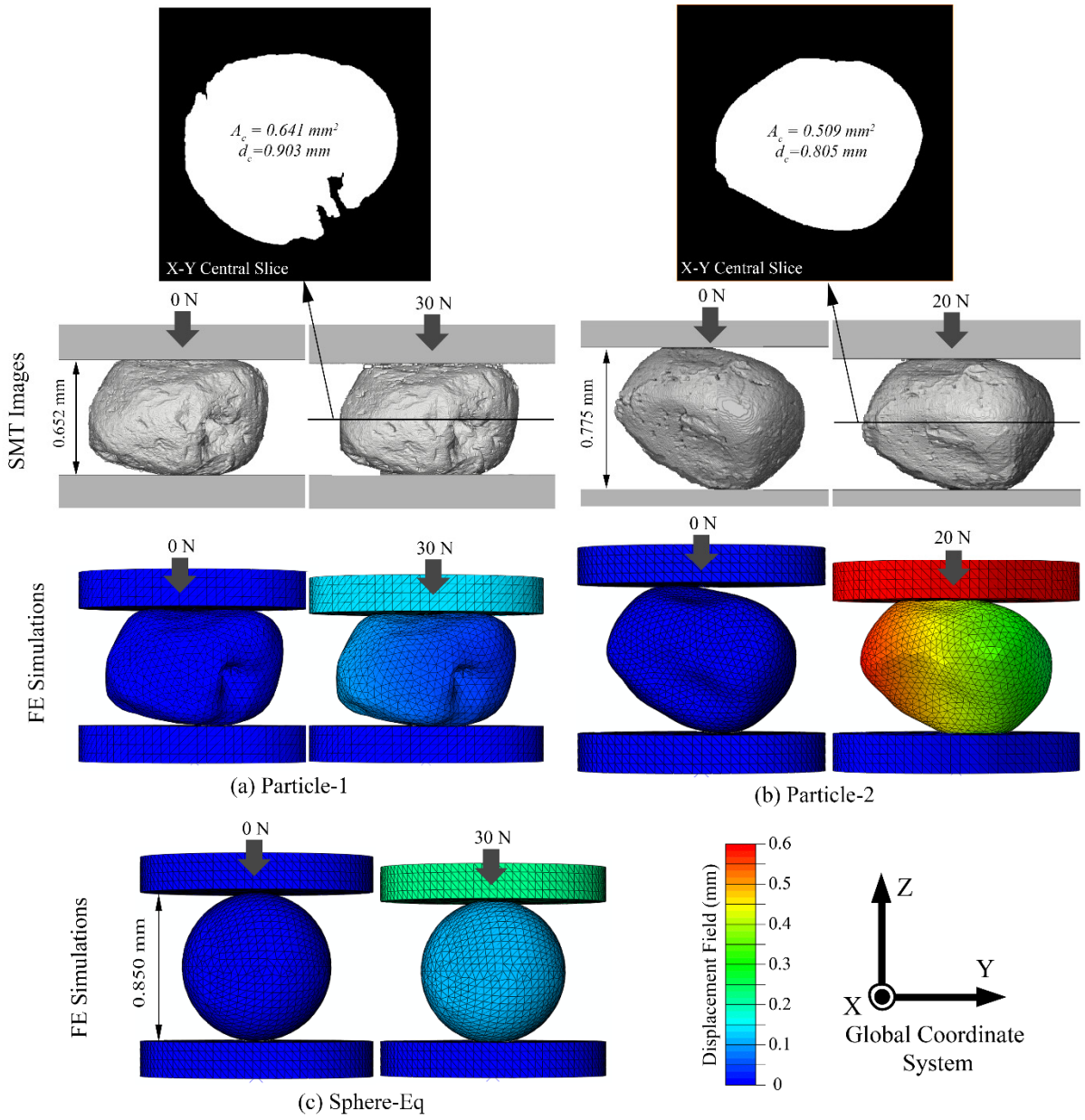
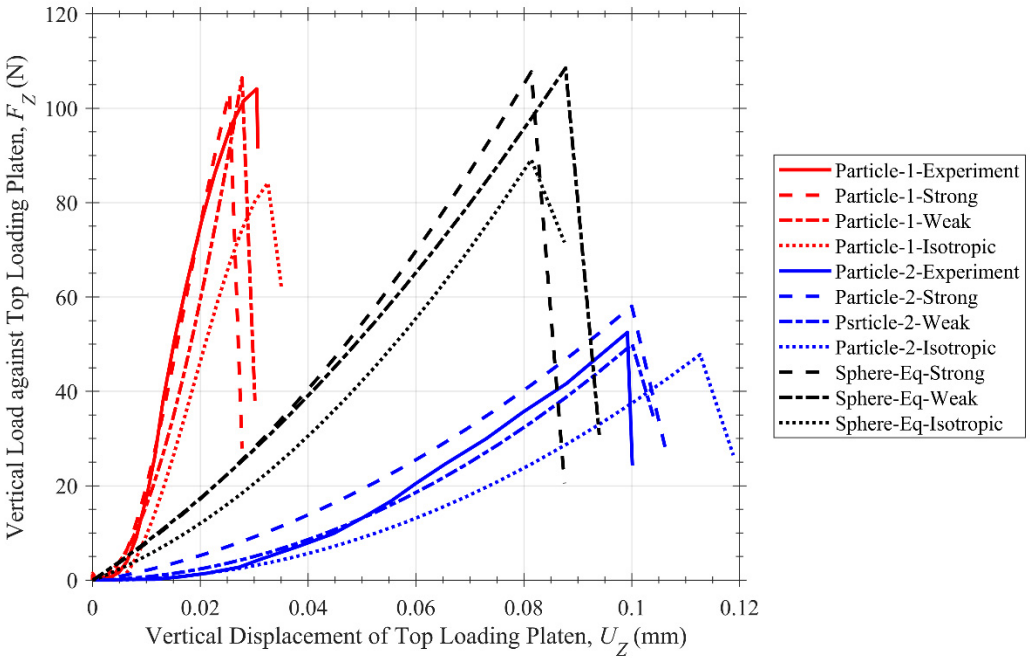
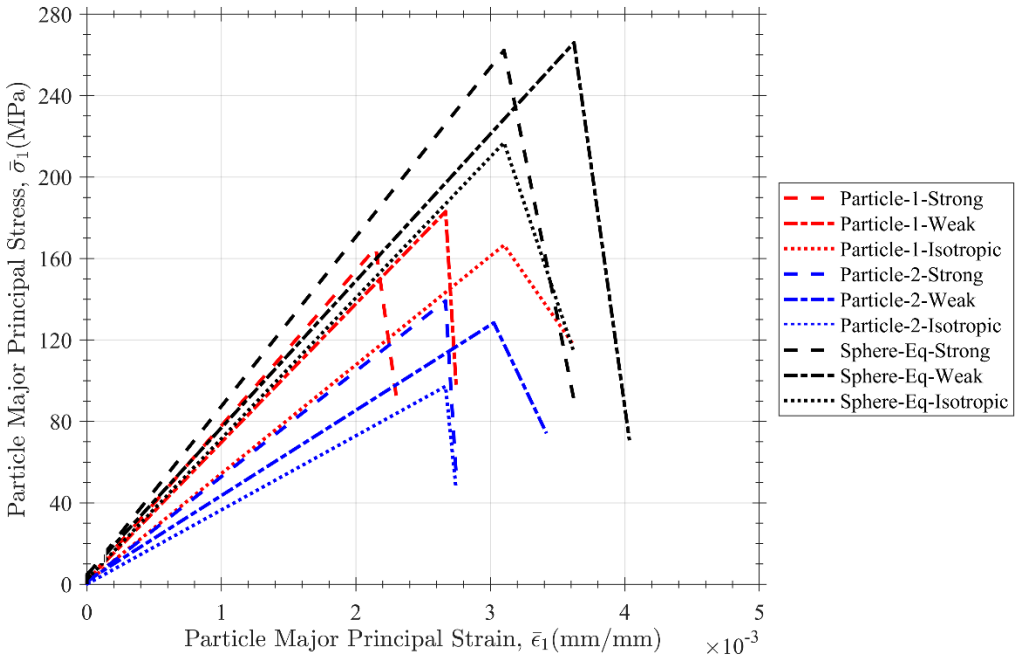


Figure 6-2. Illustration of the acquired in-situ SMT scans and conducted FE simulations for (a) Particle-1; (b) Particle-2; and (c) Sphere-Eq.



(a)



(b)

Figure 6-3. (a) Evolution of vertical load (F_z) versus displacement (U_Z) at the top loading platen for the single particle crushing simulations and experiments; and (b) evolution of the particle major principal stress ($\overline{\sigma_1}$) versus strain ($\overline{\epsilon_1}$).

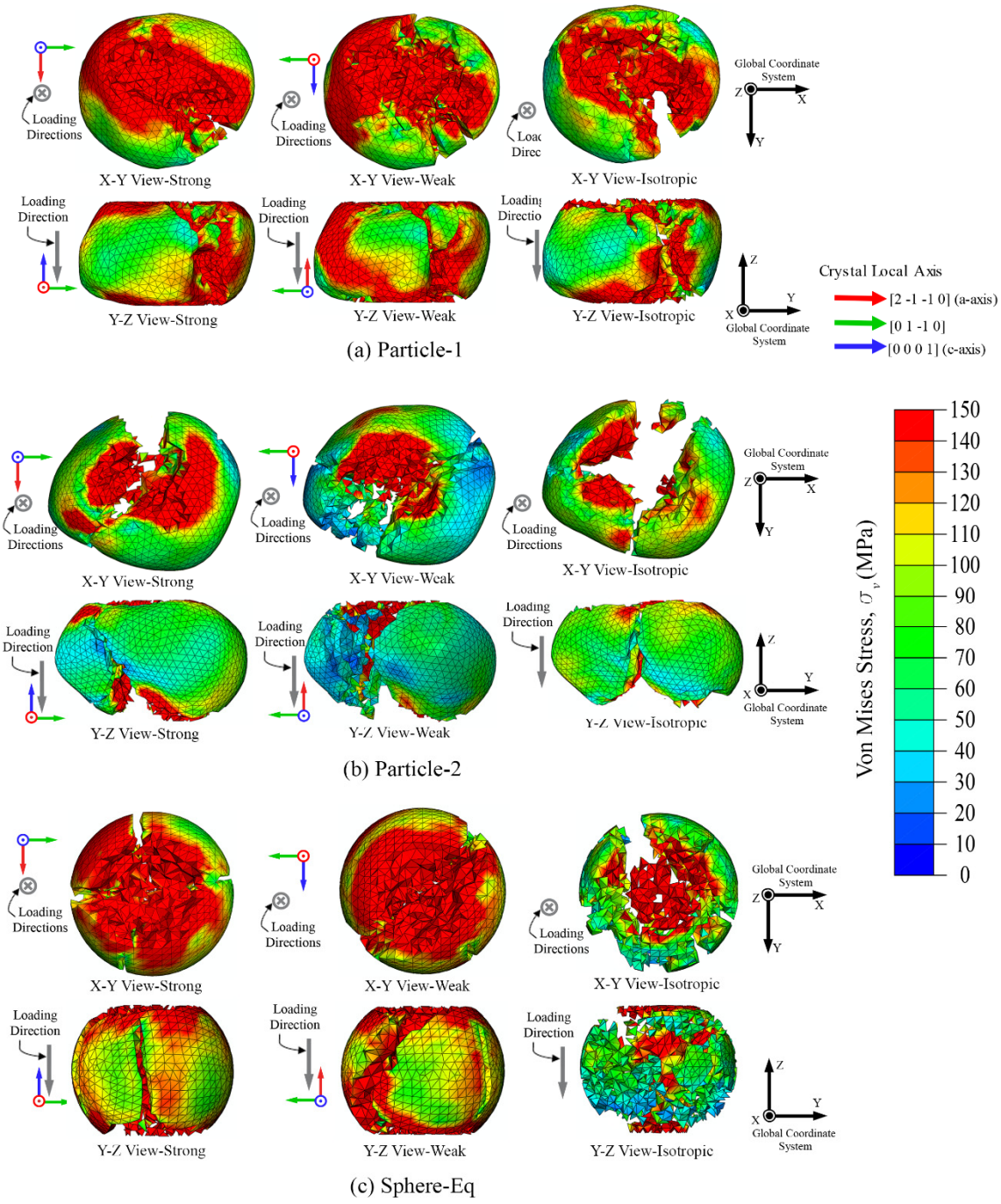


Figure 6-4. Fracture patterns in the FE simulations of (a) Particle-1; (b) Particle-2; and (c) Sphere-Eq.

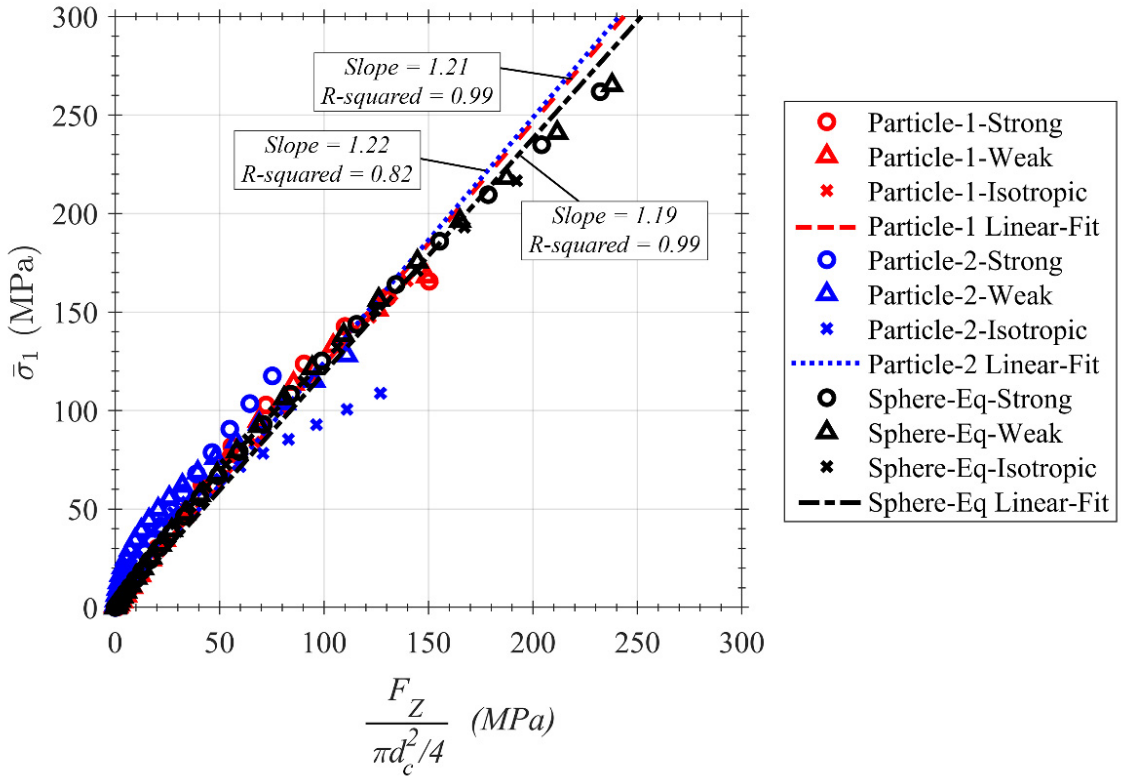


Figure 6-5. Relationship between the particle major principal stress ($\bar{\sigma}_1$) and applied vertical load (F_Z) prior to fracture in the single particle crushing FE simulations.

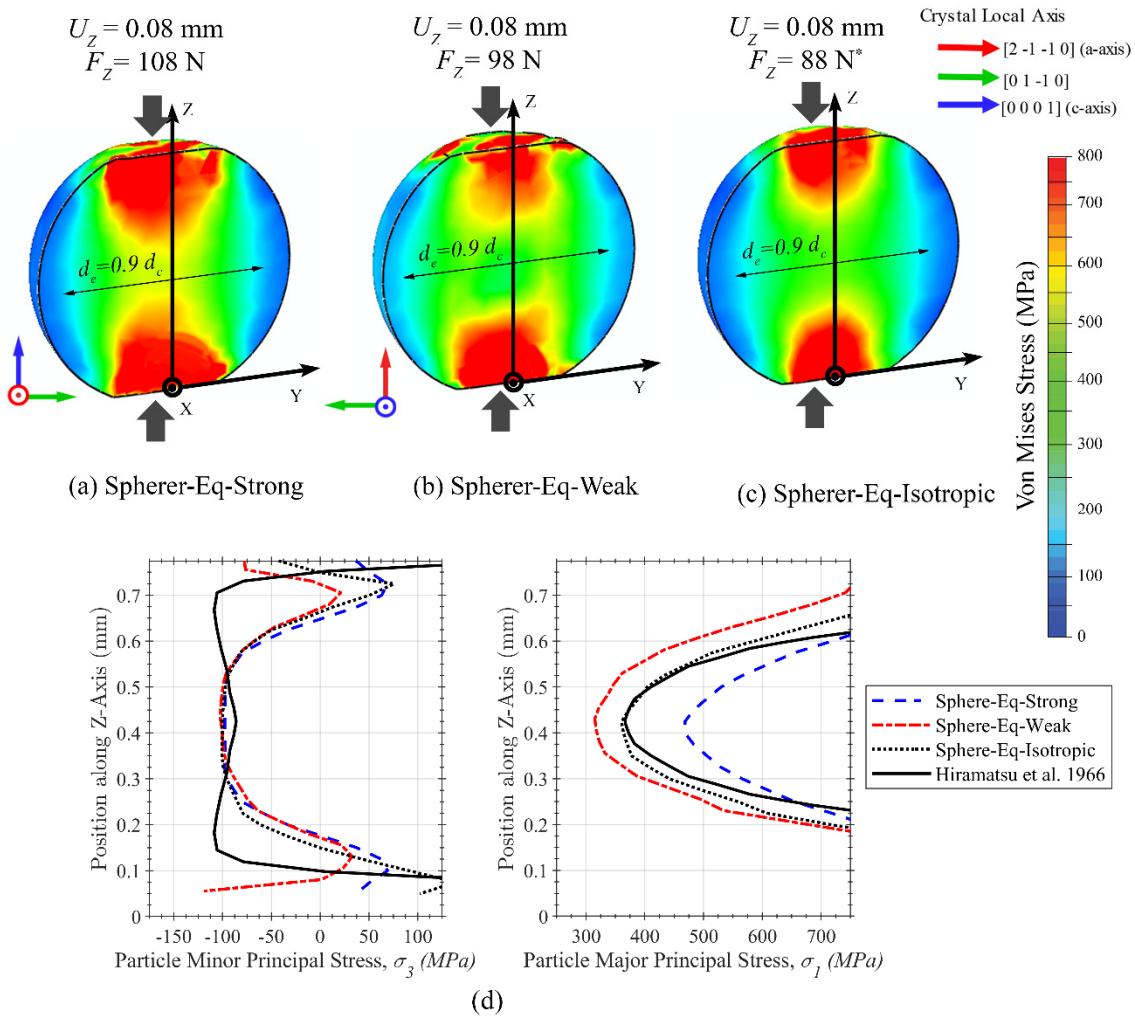


Figure 6-6. Distribution of stress within the Sphere-Eq simulations prior to fracture. *Value of force used to evaluate the theoretical closed-form solution per Hiramatsu and Oka (1966).

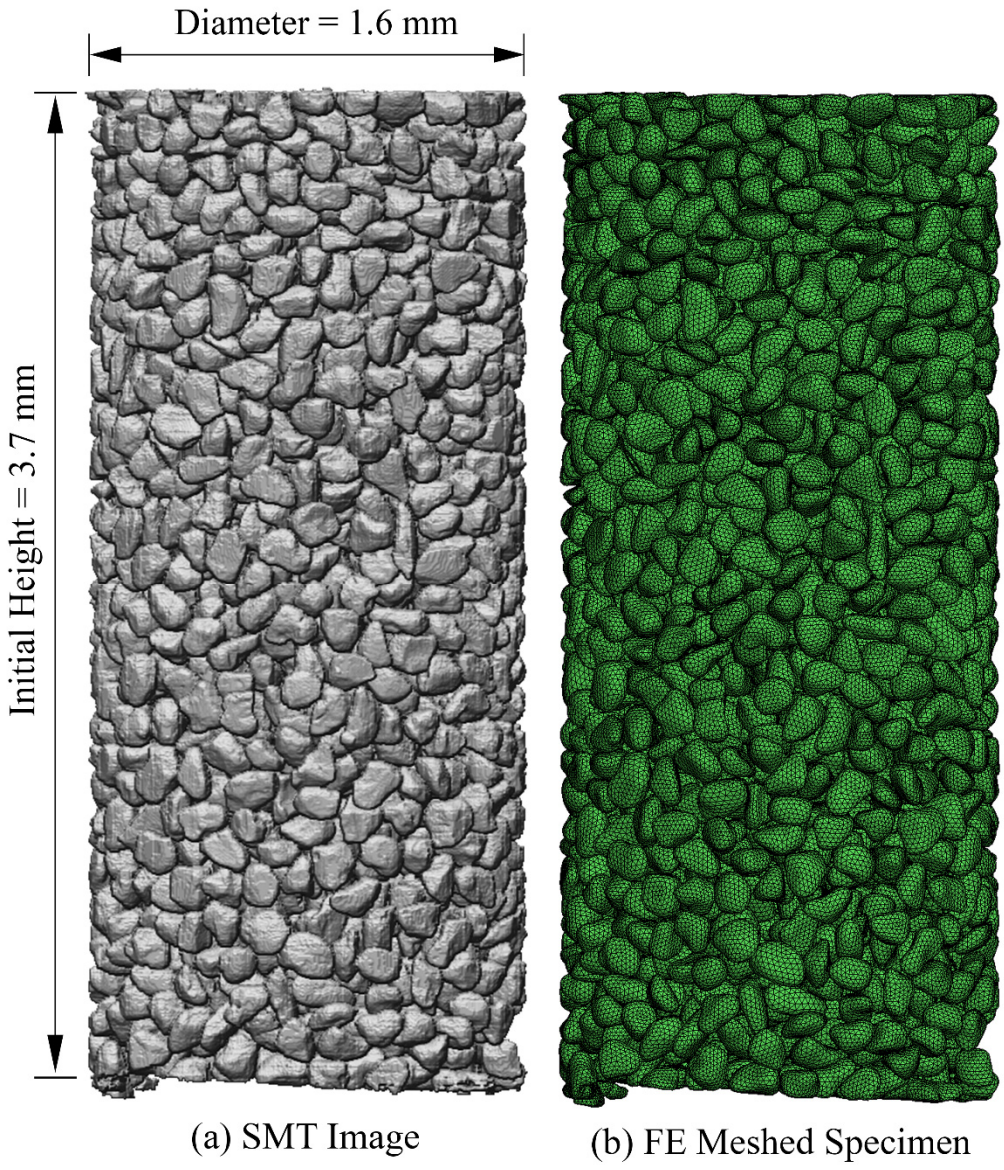


Figure 6-7. (a) 3D SMT image and (b) 3D FE numerical meshes of the sand specimen tested in confined 1D compression.

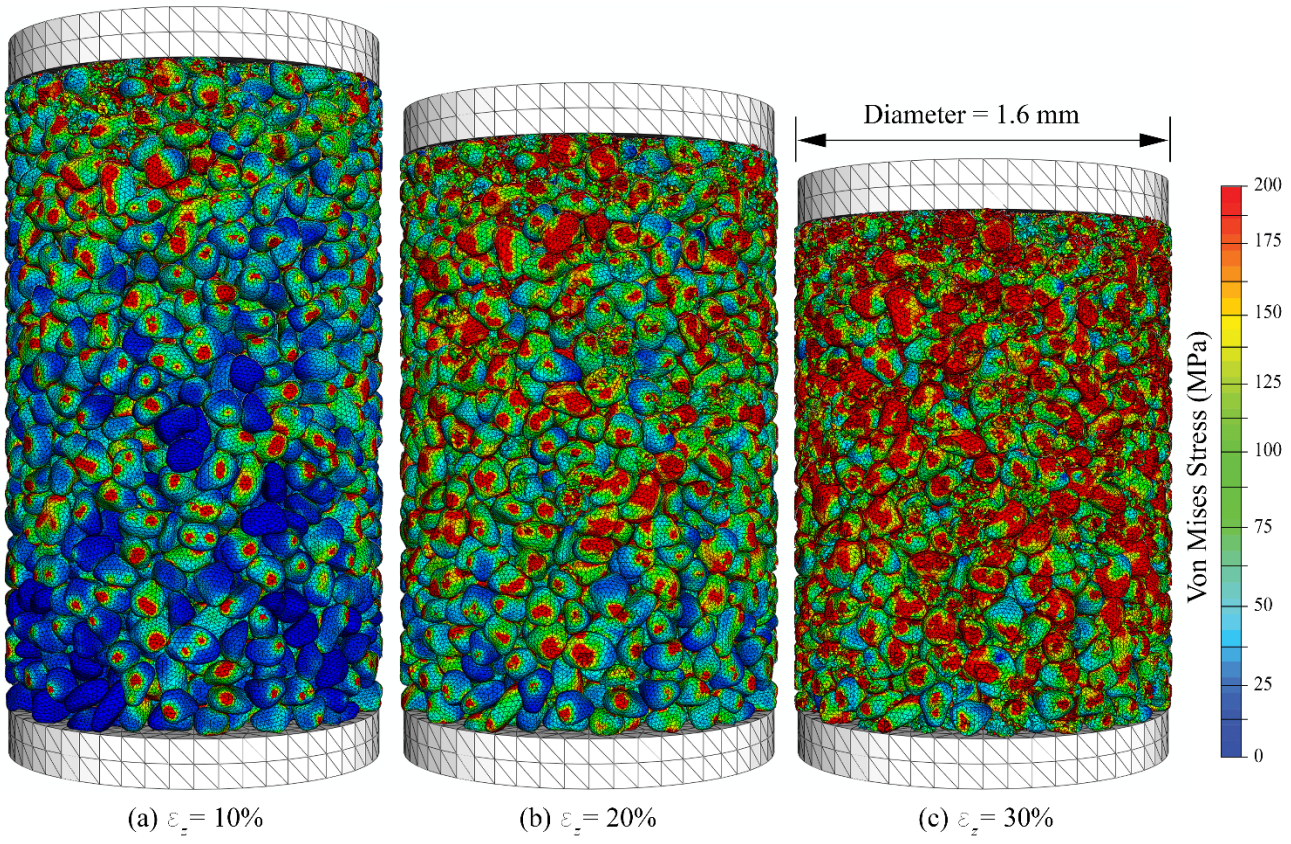


Figure 6-8. Illustration of the FEM-Experimental simulations at vertical axial strain (ε_Z) of (a) 10%; (b) 20%; and (c) 30%.

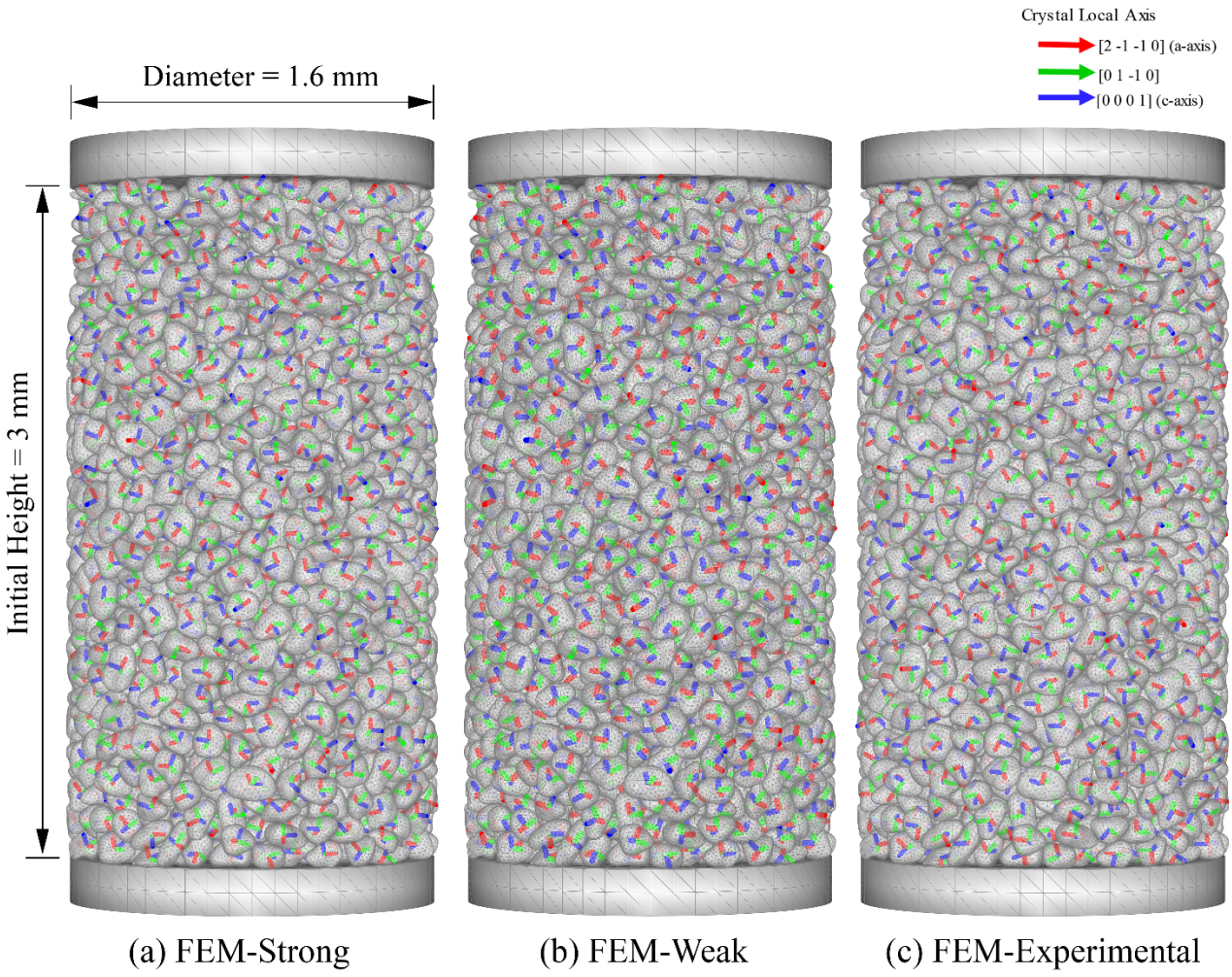


Figure 6-9. Configurations of local crystal orientations assigned to each particle in the FE simulations of (a) FEM-Strong; (b) FEM-Weak; and (c) FEM-Experiment.

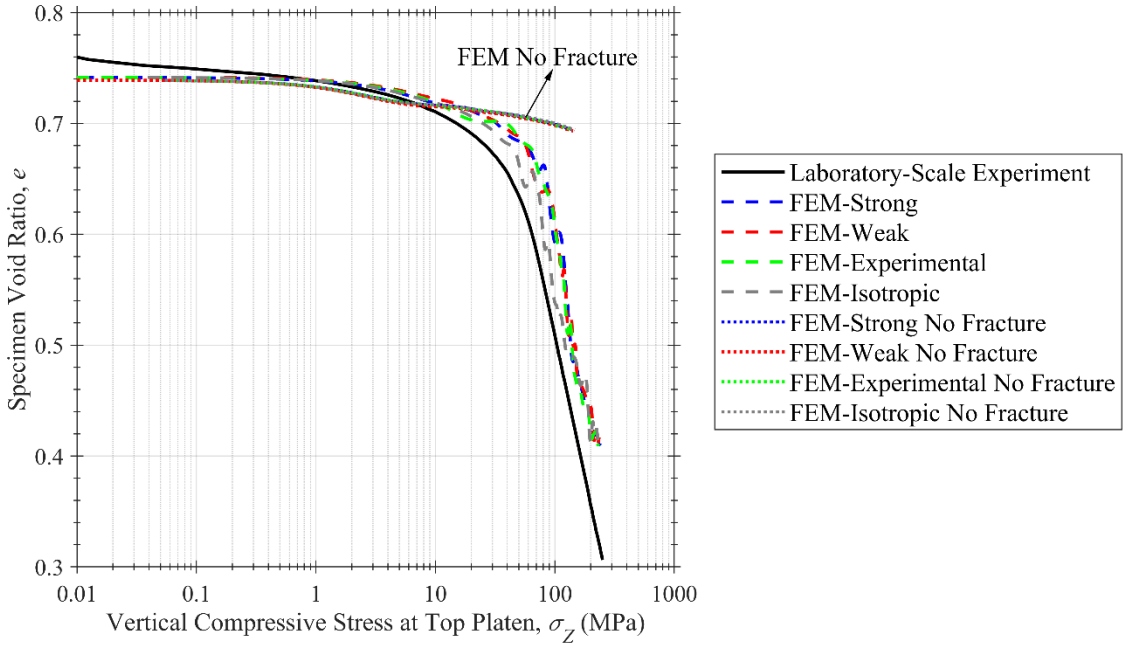


Figure 6-10. Evolution of the specimen void ratio (e) versus vertical compressive stress (σ_Z) for the confined 1D compression FE simulations and experiment.

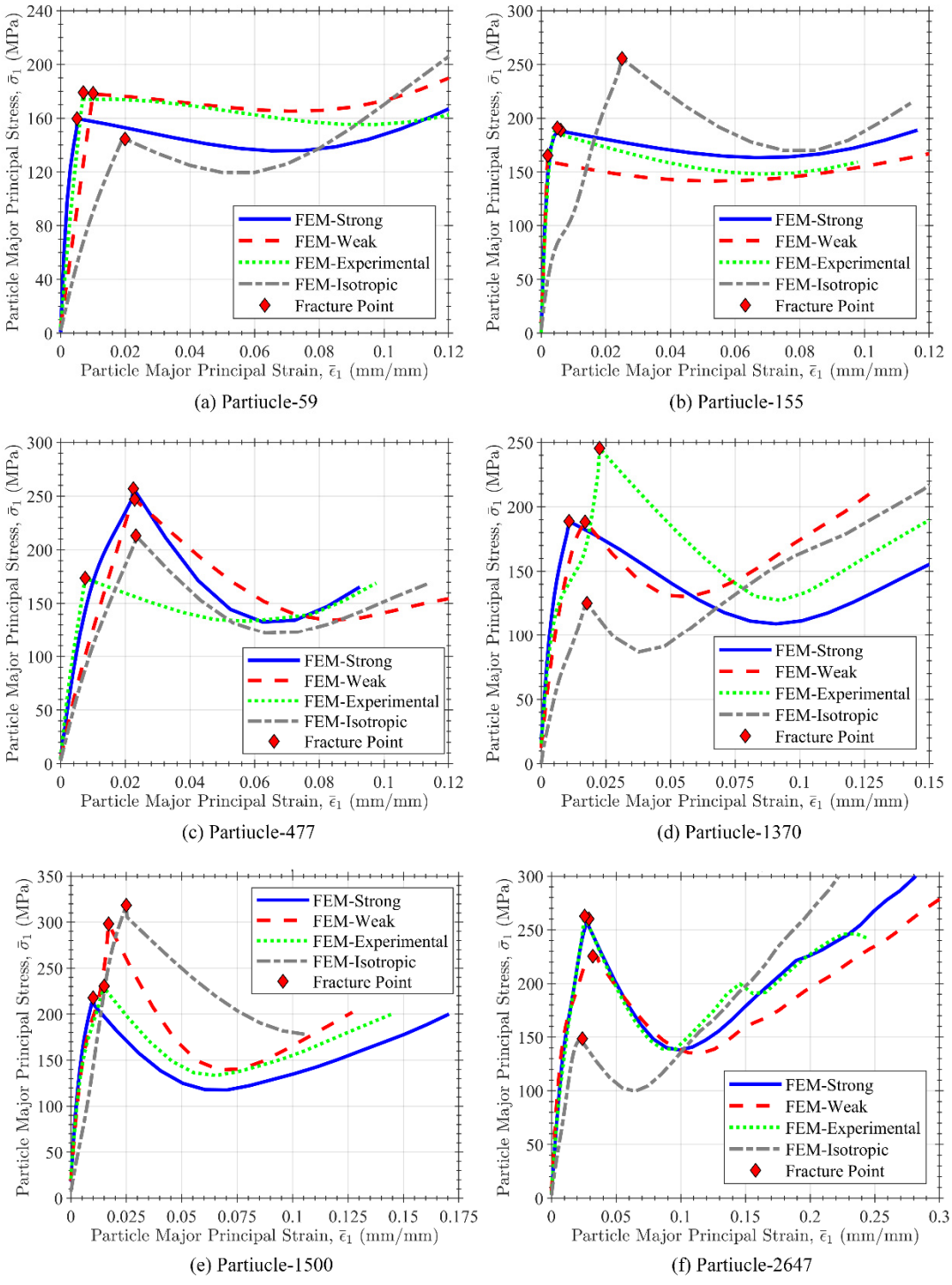


Figure 6-11. Examples of stress-strain relationships for 6 fractured particles that were selected from different regions within the specimen.

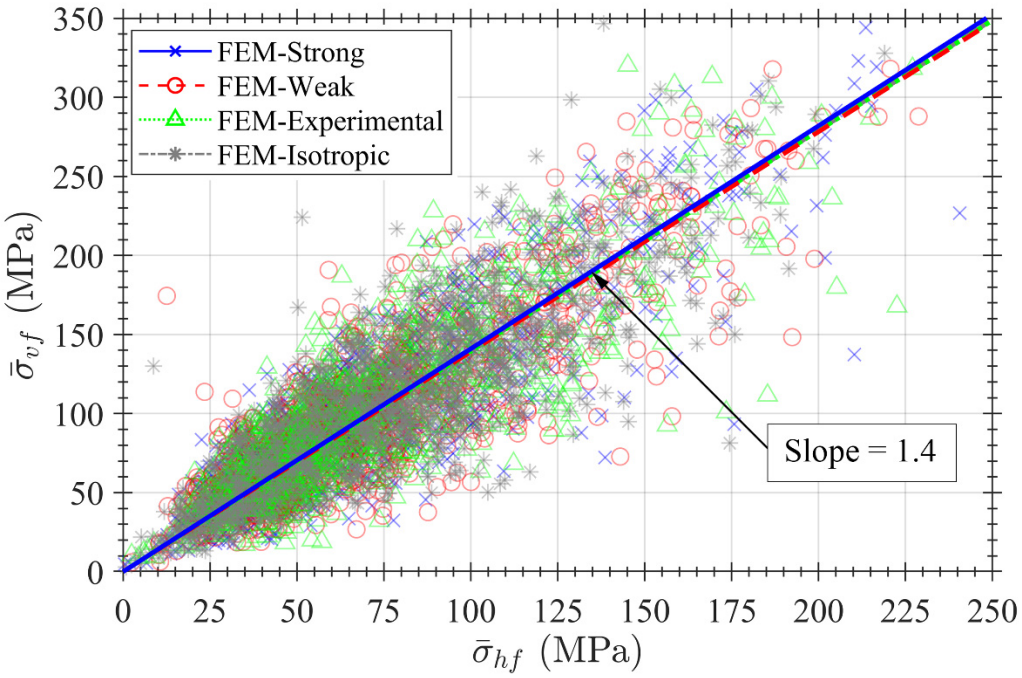


Figure 6-12. Relationships between particle von Mises ($\bar{\sigma}_{vf}$) and hydrostatic mean stress ($\bar{\sigma}_{hf}$) at fracture.

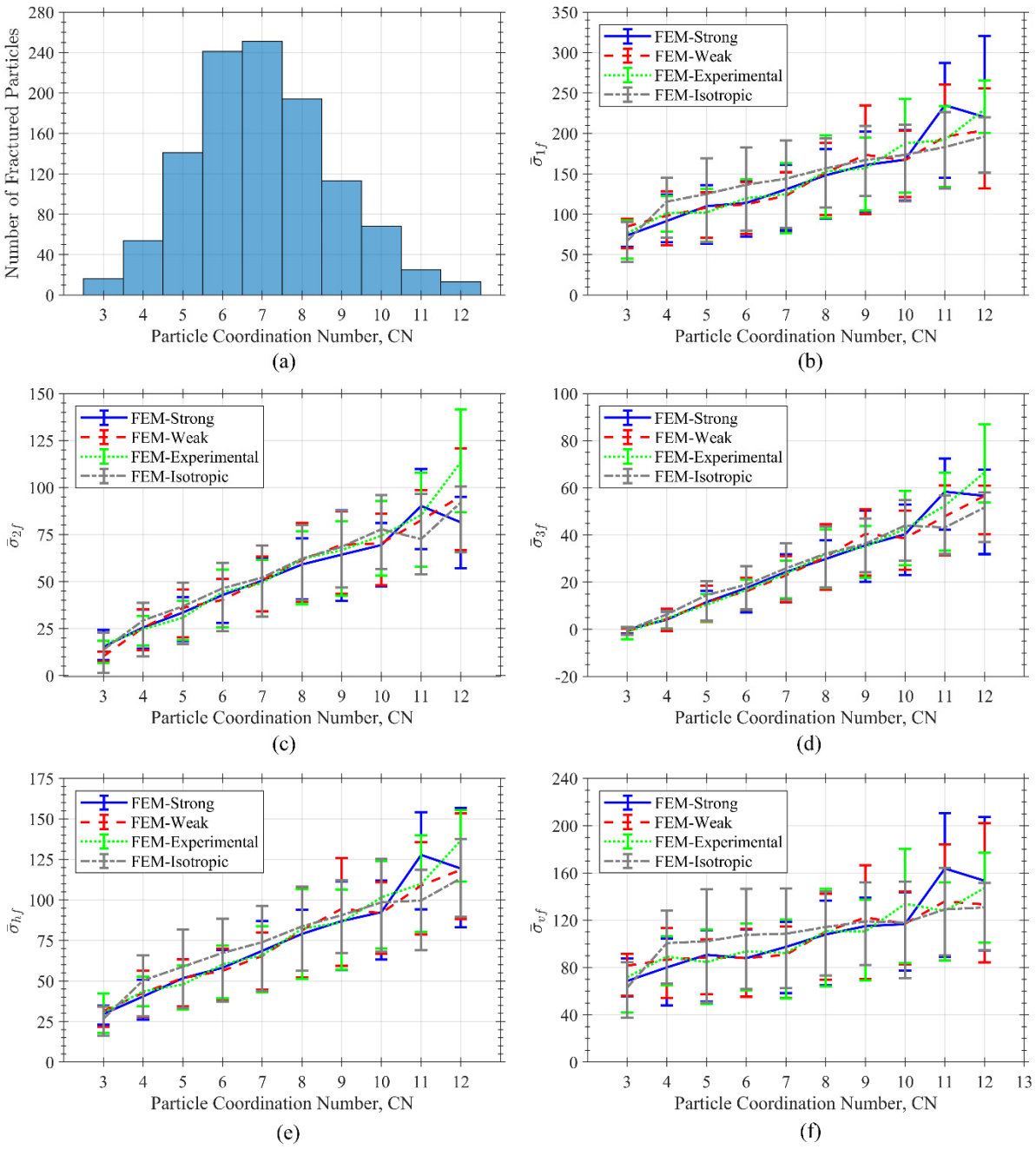


Figure 6-13. Correlation between the particle coordination number (CN) and fracture stress.

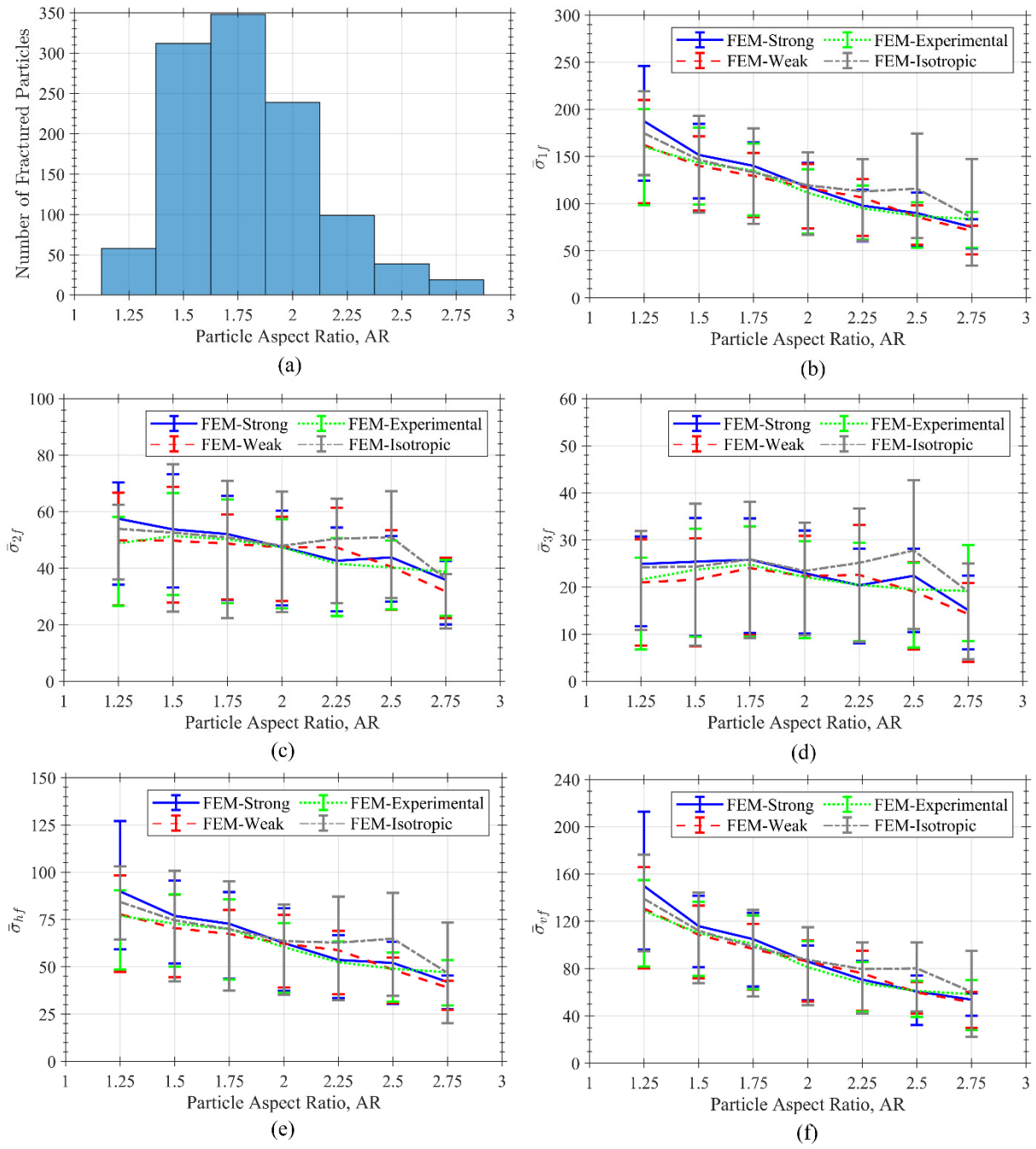


Figure 6-14. Correlation between the particle aspect ratio (AR) and fracture stress.

CHAPTER SEVEN

CONCLUSIONS AND RECOMMENDATIONS

Summary of Major Conclusions

The study reported in this dissertation investigated the 3D constitutive behavior of silica sand particles using in-situ synchrotron micro-computed tomography (SMT), 3D x-ray diffraction (3DXRD), high-performance digital image processing, and 3D finite element (FE) analysis. The constitutive behavior of silica sand particles was found to be highly influenced by the complex contribution of fundamental properties that exist among different scale levels, such as particle kinematics, morphology, coordination, and mineralogy. The following findings were concluded from this dissertation:

1. Applications of the critical state (CS) theory to sand are challenged by the complex characterization of micro-scale deformations within sheared sand specimens. In the conventional triaxial compression (CTC) apparatus, monitoring the global change in the volume of sand specimens fails to provide a unique CS locus in the compression plane. This deficiency is attributed to the high dilatation that occurs locally within internal shear bands (shear strain localization within the CTC sand specimen); however, this high dilation is averaged out when global measurements of the specimen volume are collected. In confined 1D compression, the oedometer test inhibits lateral deformation of the specimen and hinders the development of internal shear bands. Therefore, the CS locus in the compression plane can be established more accurately from the results of the oedometer test rather than CTC.
2. Natural sand morphology and particle-to-particle interactions play a significant role in the mechanisms leading to the fracture of particles within silica sand specimens. The brittle fracture of sand particles may occur due to the concentration of tensile stresses in elongated particles as they bridge over their neighboring particles. Sand particles also experience crushing into several fragments due to high compressive stresses associated with a high inter-particle contacts.
3. Natural sand morphology improves the embracement and interlocking between the particles within granular specimens loaded in confined 1D compression. These improvements make natural sand specimens manifest a stiffer response when recorded at specimen boundary (i.e., load-displacement at the loading platens), compared to the behavior of specimens containing spherical particles. Furthermore, the enhanced interlocking between natural sand particles causes force chains to evolve toward the center of the specimen. In contrast, force chains brace mostly by the confining mold within granular specimens composed of spherical particles.
4. Crystalline quartz is the constituent mineral of silica sand particles and possesses a hexagonal lattice system and trigonal symmetry. These properties

at the crystal scale-level can alter the constitutive behavior of silica sand particles. For instance, silica sand particles exhibit stiffer constitutive behavior when the applied major principal stress acts against the (0 0 0 1) local crystal plane of the particle, compared to (2 -1 -1 0) plane. This anisotropy in the material behavior can be modeled numerically using special user-subroutines for the constitutive behavior of silica minerals.

5. The fracture characteristics of silica sand particles are influenced by multiple properties that exist at different scale-levels. The fracture patterns of silica sand particles are affected by the imperfections that may occur within the particle micro-structural, as well as the direction of applied stresses relative to the crystal planes of the particle. Furthermore, fracture strength increases with higher inter-particle coordination and for particles with more spherical shape than elongated. These significant correlations can be explored using the powerful 3D FE simulations and special user-subroutines that were developed in this dissertation.

Recommendations for Future Work

Based on the findings reported in this dissertation, the following recommendations are suggested for future work:

1. In Chapter 1, data analyses of few in-situ SMT images exposed the possible notion of unique CS locus when evaluated for regions of intensive shear deformation (shear bands) within the CTC specimen. Additional in-situ images must be acquired and analyzed for more CTC experiments in search of a proof whether the CS theory is valid within a certain scale-range. The recommended additional images must incorporate many CTC experiments on loose and dense specimens of sand, as well as low and high confining pressures.
2. The 3D FE simulations developed in this dissertation are suitable for problems with dynamic and high-strain impact loading conditions, such as projectile or pile penetration through a sand deposit. The proposed 3D FE simulation would provide in-depth insights into the fracture mechanisms and characteristics of sand particles under the loading conditions of such specific engineering applications.
3. In Chapter 4, interlocking between sand particles has proven significant for the evolution of force chains within confined specimens loaded in 1D compression. Similarly, particle interlocking within CTC specimens is also expected to influence the evolution of shear bands. The latter hypothesis can be examined through the development of 3D FE simulations for CTC experiments. In the proposed CTC simulations, the flexible membrane can be modeled using deformable elastic elements, and confining stress can be applied as an external surface pressure on the membrane elements.
4. In Chapter 5, a significant portion of silica sand particles was characterized to possess Dauphiné twins and poly-crystal structure. These crystal characteristics are recognized to impact stress concentrations and the onset of fracture near the boundaries of crystal grains. Furthermore, the fracture of silica

sand particles composed of mono-crystals is fundamentally caused by the successive breakage in molecular bonds along specific slip systems in crystal quartz (closed-packed planes). Further coding development on the user-subroutines in this dissertation can prove properties at the crystal scale-level in silica sand much more influential in the mechanisms leading to particle fracture. For instance, these subroutines can incorporate the recent concepts of phase-field damage with the explicit staggered algorithm to efficiently model the preferred directions of fracture in light of the slip systems of mono-crystal quartz.

VITA

Wadi H. Imseeh was born in the holy city of Jerusalem. He attended Birzeit University in the State of Palestine, where in June 2015, he graduated with a Bachelor of Science degree in Civil Engineering. In July 2015, he moved to the United States of America and joined the University of Tennessee-Knoxville for graduate studies. In December 2017, he was granted a Concurrent Master of Science degree in Civil Engineering with a major in Geotechnical and Materials engineering and Interdisciplinary Graduate Minor in Computational Science. Wadi pursued his Ph.D. work at the University of Tennessee-Knoxville under the supervision of Prof. Khalid Alshibli. His research explored the micro- and crystal-scale mechanics of granular silica geo-materials using advanced 3D x-ray experiments, digital image processing, and finite element analysis.